Theoretical Investigations of Surface Oxides on Platinum and Platinum Alloy Catalysts for Fuel Cell Applications

Oluwakemi Adeola Otegbade

Department of Earth Sciences
University College London
and
Johnson Matthey Technology Centre

Thesis submitted for the degree of Doctor of Engineering (EngD)

January 2012

Declaration

I, Oluwakemi Adeola Otegbade, confirm that the work presented in this thesis is the result of my own investigations. Where information has been derived from other sources, I confirm that this has been indicated in the thesis.

Oluwakemi A. Otegbade

January 2012

Abstract

The interaction of oxygen with metal surfaces can lead to various structures; these include surface oxide films, oxygen penetration in the subsurface region and bulk oxides, at certain partial pressures and temperatures. This research focuses on the oxygen reduction reaction (ORR) within the proton exchange membrane fuel cell (PEMFC).

PEMFC are believed to be kinetically limited for the ORR due to a loss of surface area at the cathode as a result of oxidation. One explanation for this phenomenon is the "so called place exchange mechanism" which leads to a thin surface oxide being formed. In an attempt to understand and verify this hypothesis, Pt and Pt/Ni alloys have been modelled in order to determine the relative propensity of surface oxide film formation.

Density functional theory (DFT) has been used to model various facets of the catalyst particles, in particular the (111) and (100) surfaces. In addition, a range of oxygen coverages at high symmetry sites and oxide thin films have also been modelled as intermediates in the place exchange mechanism. The DFT data obtained from these calculations have been used in a statistical thermodynamics model. This allows one to bridge the temperature and pressure gap between the technological relevant conditions of the PEMFC and the electronic structure calculations.

Acknowledgements

I would like to express my gratitude towards all the people who have provided me with invaluable help, support and advice throughout this work. Without them, it would be impossible to finish this thesis at all. Specifically, I would like to thank Prof. Dario Alfè, my principal supervisor, for kindly offering me the opportunity to learn and study in an excellent environment of his group in UCL. Without his support, encouragement and guidance, I would not be able to achieve this.

I would like to thank my industrial supervisor Dr. Sam French for giving me the opportunity at Johnson Matthey. I would also like to acknowledge a number of people from Johnson Matthey; Dr. Glenn Jones, Dr. Misbah Sarwar, Dr. Dave Thompsett and Dr. Alejandro Martinez-Bonastre for the immense support, vaulable advice and useful discussions provided throughout the years. Futhermore, I am grateful to EPSRC and Johnson Matthey for the financial support.

I would like to mention my friends from UCL and Johnson Matthey who have made these years enjoyable. In addition, I would like to give my sincerest appreciation to my family (my parents and siblings) and friends for their endless support and encouragement given throughout. YOU ALL HAVE BEING AMAZING, THANK YOU SO MUCH!!!

Finally, I am grateful to the Almighty God beyond measure for giving me the grace, wisdom, courage and vigorous health in completing this thesis. I am grateful to Him for being the Rock of my life through everything I do.

Contents

1 Introduction **1**

1.1 Fuel Cells 1
1.2 Proton exchange membrane fuel cells (PEMFCs) 4
1.3 Performance loss in PEMFCs 5
1.4 PEMFC issues and challenges 9
1.4.1 Polymer electrolyte membrane 9
1.4.2 Catalyst 10
1.5 Oxygen Reduction Reaction 11
1.6 Platinum Catalysts 12
1.7 Parameters Affecting the Catalyst Performance 15
1.8 Pt-Alloy Catalysts 17
1.9 Theoretical studies of ORR 20
1.10 Project aims and Objectives 21
1.11 References 23

2 Theoretical Methodology **30**

2.1 Introduction 30
2.2 Electronic Structure Theory 31
2.2.1 The Schrödinger Equation/ Born-Oppenheimer approximation 31
2.2.2 Density Functional Theory 32
2.2.3 Exchange-Correlation Functionals 37
2.2.3.1 Local Density Approximation (LDA) 37
2.2.3.2 Generalised gradient approximation (GGA) . . 38

2.2.4 DFT Implementation in the VASP Code 39
2.2.4.1 Periodic Boundary Conditions and Bloch's Theorem 39
2.2.4.2 Brillouin Zone (BZ) Sampling 41
2.2.4.3 Plane Wave Basis Sets 42
2.2.4.4 Pseudopotentials 43
2.3 Output from the *ab-initio* Calculation 44
2.3.1 Binding and Segregation Energies 44
2.3.2 Work-function 45
2.3.3 Surface dipole moment 47
2.3.4 Charge Density differences 47
2.3.5 Density of States 48
2.3.6 *d*-band Centre Model 48
2.3.7 Bader Analysis 49
2.4 Statistical Thermodynamic Model 49
2.4.1 Free Energy as a Function of Potential 51
2.4.2 Limitation of the Statistical Thermodynamics Model . . . 52
2.5 References 53

3 Atomic Oxygen Coverage effects on Pt Surfaces 56
3.1 Introduction 56
3.2 Computational Methods 58
3.2.1 Density Functional Theory Calculations 58
3.3 Results and Discussion 59
3.3.1 Bulk Pt, Clean Pt (111) and (100) surfaces and the oxygen molecule 59
3.3.2 On-surface Adsorption of Atomic Oxygen on Pt Surfaces . 62
3.3.3 On-surface Mixed Sites Adsorption of Atomic Oxygen on Pt Surfaces 65
3.3.4 Sub-surface Absorption of Atomic Oxygen on Pt Surfaces 67
3.3.5 Interaction of Oxygen with the On/sub-surface Phases . . 71
3.4 Statistical Thermodynamic Model 78
3.4.0.1 Free Energy as a Function of Potential 81
3.5 Electronic Properties 83

3.5.1 Change in Work function, Dipole Moment and ***d***-band Centre 83
3.5.2 Electron density difference and Bader Analysis 86
3.6 Conclusions and Implications to PEMFC 90
3.7 References 92

4 Coverage effects on Pt/Ni-Monolayer Bimetallic Alloy Surfaces 98
4.1 Introduction 98
4.2 Computational Methods 100
4.3 Results and Discussion 101
4.3.1 Clean Ni-Pt-Pt and Pt-Ni-Pt structures on the (111) and (100) surfaces 101
4.3.2 Oxygen Interactions on Ni-Pt-Pt Monolayer Bimetallic Alloy Surfaces 104
4.3.2.1 On-surface Adsorption of Atomic Oxygen on Ni-Pt-Pt Surfaces 104
4.3.2.2 On-surface Mixed Sites Adsorption of Atomic Oxygen on Ni-Pt-Pt Surfaces 107
4.3.2.3 Sub-surface Absorption of Atomic Oxygen on Ni-Pt-Pt Surfaces 108
4.3.2.4 Interaction of Oxygen with the On/sub-surface Phases on Ni-Pt-Pt surfaces 110
4.3.3 Oxygen Interactions on Pt-Ni-Pt Monolayer Bimetallic Alloy Surfaces 116
4.3.3.1 On-surface Adsorption of Atomic Oxygen on Pt-Ni-Pt Surfaces 116
4.3.3.2 On-surface Mixed Sites Adsorption of Atomic Oxygen on Pt-Ni-Pt Surfaces 118
4.3.3.3 Sub-surface Absorption of Atomic Oxygen on Pt-Ni-Pt Bimetallic Surfaces 120
4.3.3.4 Interaction of Oxygen with the On/sub-surface Phases on Pt-Ni-Pt surfaces 122
4.3.4 Statistical Thermodynamic Model 129
4.3.4.1 Free Energy as a Function of Potential 134

4.3.5 Electronic Properties 136
4.3.5.1 Change in Work function, Dipole Moment and *d*-band Centre 136
4.3.5.2 Electron density difference and Bader Analysis . 141
4.3.6 Comparison between Ni-Pt-Pt and Pt-Ni-Pt surfaces . . . 145
4.4 Conclusions and Implications to PEMFC 147
4.5 References 149

5 Coverage effects on Pt_3Ni and Pt_3Ni-Pt_{skin} (111) surfaces 152
5.1 Introduction 152
5.2 Computational Methods 153
5.3 Results and Discussion 154
5.3.1 Clean Pt_3Ni and Pt_3Ni-Pt_{skin} structures on the (111) surfaces 154
5.3.2 On-surface Adsorption of Atomic Oxygen on the (111) surfaces of Pt_3Ni and Pt_3Ni-Pt_{skin} Alloys 156
5.3.3 On-surface Mixed Sites Adsorption of Atomic Oxygen on Pt_3Ni and Pt_3Ni-Pt_{skin} Surfaces 160
5.3.4 Sub-surface Absorption of Atomic Oxygen on Pt_3Ni and Pt_3Ni-Pt_{skin}Surfaces 162
5.3.5 Interaction of Oxygen with the On/sub-surface Phases . . 164
5.3.6 Statistical Thermodynamic Model 172
5.3.6.1 Free Energy as a Function of Potential 175
5.3.7 Electronic Properties 177
5.3.7.1 Change in Work function, Dipole Moment and d-band Centre 177
5.3.7.2 Electron density difference, Bader Analysis and Density of States 180
5.3.8 Surface Segregation 183
5.4 Conclusions and Implications to PEMFC 185
5.5 References 186

6 Conclusions and Implications to PEMFC 188
6.1 Future Research Work 191

6.2 References 194

Appendices

A Convergence Tests **195**

List of Figures

1.1 Schematic diagram of a proton exchange membrane fuel cell (PEMFC). 5
1.2 The main contributions associated with the PEMFC overpotential.[18] 7
1.3 Chemical structure of Nafion ®. 10
1.4 The reaction pathways for oxygen reduction reaction.[28] 11
1.5 Trends in oxygen reduction activity plotted as a function of the oxygen binding energy.[33] 13
1.6 A nanoparticle showing the (111) and (100) crystal facets, edge and corner site. 16
1.7 Relationship between the catalytic properties and electronic structure of Pt_3M alloys.[66] 19

2.1 Representation of the self-consistency cyclic loop. 36
2.2 Periodic unit cell 40
2.3 Schematic energy diagram of a bulk metal. 46

3.1 Adsobates at adsorption sites on (a) Pt (111) and (b) Pt(100) surfaces (top view). 62
3.2 On-surface adsorption binding energies of oxygen on Pt surfaces . 63
3.3 Binding energies for the on-surface mixed adsorption sites for oxygen adsorbed on Pt surfaces 66
3.4 Sub-surface absorption sites on Pt surfaces 68
3.5 Binding energies for the sub-surface oxygen absorption on Pt surfaces 69
3.6 Converged sub-surface structures on Pt surfaces 70
3.7 The binding energies for the on/sub-surface phases on Pt surfaces 72

3.8 Top and side views of the most stable oxygen on/sub-surface configurations on the Pt(111) surface 74
3.9 Top and side views of the most stable oxygen on/sub-surface configurations Top and side views of the most stable oxygen on/sub-surface configurations 76
3.10 Phase diagram of Pt surfaces 79
3.11 Free energy as a function of potential for the thermodynamically stable structures on Pt surfaces 82
3.12 Electronic properties of Pt surfaces 84
3.13 Calculated electron density differences for Pt surfaces 87
3.14 Projected density of states (PDOS) for O/Pt systems at 0.25 ML oxygen coverage 89

4.1 Pt/Ni Ni Monolayer Bimetallic Alloys (MBA) Surfaces; Ni-Pt-Pt (left) and Pt-Ni-Pt (right) 102
4.2 Adsobates at adsorption sites on (a) Ni-Pt-Pt (111) and (b) Ni-Pt-Pt (100) surfaces (top view). 104
4.3 On-surface binding energies of oxygen on Ni-Pt-Pt surfaces 105
4.4 Binding energies for the on-surface mixed adsorption sites for oxygen adsorbed on Ni-Pt-Pt surfaces 107
4.5 Binding energies for the sub-surface oxygen absorption on Ni-Pt-Pt surfaces 109
4.6 The binding energies for the on/sub-surface phases on Ni- Pt-Pt surfaces 111
4.7 Top and side views of the most stable oxygen on/sub-surface configurations on the Ni-Pt-Pt (111) surface 112
4.8 Top and side views of the most stable oxygen on/sub-surface geometric structures on the Ni-Pt-Pt (100) surface 114
4.9 On-surface binding energies of oxygen on Pt-Ni-Pt surfaces 116
4.10 Binding energies for the on-surface mixed adsorption sites for oxygen adsorbed on Pt-Ni-Pt surfaces 119
4.11 Subsurface binding energies of oxygen on Pt-Ni-Pt surfaces 120
4.12 Graph showing the binding energies of the stable on-surface fcc site and sub-surface tetra-i site on the Pt-Ni-Pt (111) surface. . . . 121

4.13 The binding energies for the on/sub-surface phases on Pt- Ni-Pt surfaces 123
4.14 Top and side views of the most stable oxygen on/sub-surface configurations on the Pt-Ni-Pt (111) surface 125
4.15 Top and side views of the most stable oxygen on/sub-surface structures on the Pt-Ni-Pt (100) surface 127
4.16 Phase diagram of Ni-Pt-Pt surfaces 130
4.17 Phase diagram of Pt-Ni-Pt surfaces 132
4.18 Free energy as a function of potential for the thermody- namically stable structures on monolayer bimetallic surfaces 135
4.19 Electronic properties of Ni-Pt-Pt surfaces 137
4.20 Electronic properties of Pt-Ni-Pt surface 138
4.21 Calculated electron density differences for Ni-Pt-Pt (111) surface . 141
4.22 Calculated electron density differences for Pt-Ni-Pt (111) surface . 142
4.23 Projected density of states (PDOS) for O/Ni-Pt-Pt systems at 0.25 ML oxygen coverage 144
4.24 Projected density of states (PDOS) for O/Pt-Ni-Pt systems at 0.25 ML oxygen coverage. 144
4.25 The segregation energies between Ni-Pt-Pt and Pt-Ni-Pt for the (111) and (100) surfaces 146

5.1 Two models of the Pt_3Ni alloy surfaces. Pt_3Ni bulk alloy (left) and Pt_3Ni-$Pt_{\mathbf{skin}}$ alloy (right). 155
5.2 Adsobates at adsorption sites on (a) Pt_3Ni (111) and (b) Pt_3Ni-$Pt_{\mathbf{skin}}$(111) surfaces (top views). 157
5.3 On-surface adsorption binding energies of oxygen on Pt_3Ni(111) alloys 157
5.4 Converged 1.00 ML oxygen coverage at the top site and on Pt_3Ni-$Pt_{\mathbf{skin}}$ surfaces. 159
5.5 Mixed sites binding energies of oxygen adsorbed on Pt_3Ni(111) alloys 161
5.6 Sub-surface Absorption sites on (a) Pt_3Ni(111) and (b) Pt_3Ni-$Pt_{\mathbf{skin}}$(111) surfaces. 163
5.7 Subsurface Absorption sites on Pt_3Ni alloys 163

5.8 The binding energies for the on/sub-surface phases on Pt_3Ni alloys 165
5.9 Top and side views of the most stable oxygen on/sub-surface configurations on the Pt_3Ni surface 168
5.10 Top and side views of the most stable oxygen on/sub-surface configurations on the Pt_3Ni-$Pt_{\mathbf{skin}}$ surface 170
5.11 Phase diagram of Pt_3Ni alloys 173
5.12 Free energy as a function of potential for the thermody- namically stable structures on Pt_3Ni alloys 176
5.13 Electronic properties of the most stable structures identified on the Pt_3Ni alloys 178
5.14 Calculated electron density differences for structures on the Pt_3Ni surface 181
5.15 Projected density of states (PDOS) of O/Pt_3Ni alloys at 0.25 ML oxygen coverage 183
5.16 Segregation energies between $Pt_3Ni(111)$ and Pt_3Ni-$Pt_{\mathbf{skin}}(111)$ surfaces 184

6.1 Segregation energies between the alloying elements 192
6.2 On-surface adsorption binding energies of oxygen adsorbed at the fcc site on the bimetallic monolayer alloy surfaces 193

A.1 Convergence test for the *k*-point grid. 196
A.2 Convergence test for the vacuum gap. 197

List of Tables

1.1 Comparison of different fuel cells and their operating characteristics. Data from[9] 3

3.1 Properties of bulk Pt 60
3.2 Change in interlayer spacings of Pt surfaces 61
3.3 Average Pt-O bond lengths and interlayer spacings of atomic oxygen on Pt 64
3.4 The calculated (average) bond lengths for the most stable on/sub-surface configurations on the Pt(111) surface 75
3.5 The calculated (average) bond lengths for the most stable on/sub-surface configurations on the Pt(100) surface 77
3.6 The temperatures (K) at which the oxygen coverage changes phase from the (T , p) thermodynamic phase diagram on the Pt surfaces . 80
3.7 Average Bader charges for the top two Pt layers on the Pt surfaces 88

4.1 The average bond lengths, interlayer spacings and workfunction of clean monolayer bimetallic surfaces 102
4.2 Average Ni-O bond lengths and interlayer spacings of atomic oxygen on Ni-Pt-Pt surfaces 106
4.3 Binding energies (eV) of on-surface and sub-surface sites for the Ni-Pt-Pt surfaces 110
4.4 The calculated (average) bond lengths for the most stable on/sub-surface configurations on the Ni-Pt-Pt(111) surface 113
4.5 The calculated (average) bond lengths for the most stable on/sub-surface geometric structures on the Ni-Pt- Pt(100) surface 115

4.6 Average Pt-O bond lengths and change in interlayer spacing of atomic oxygen on Pt-Ni-Pt surfaces 117
4.7 The average Pt-O and Ni-O bond lengths and the change in interlayer spacing 122
4.8 The calculated (average) bond lengths for the most stable on/sub-surface configurations on the Pt-Ni-Pt(111) surface 126
4.9 The calculated (average) bond lengths for the most stable on/sub-surface configurations on the Pt-Ni-Pt(100) surface 128
4.10 The temperatures (K) at which the oxygen coverage changes phase from the (T, p) thermodynamic phase diagram on the Ni-Pt-Pt surfaces 131
4.11 The temperatures (K) at which the oxygen coverage changes phase from the (T, p) thermodynamic phase diagram on the Pt-Ni-Pt surfaces 133
4.12 Average Bader charges of the top two layers on the (111) and (100) for Ni-Pt-Pt, Pt-Ni-Pt and Pt surfaces. 143

5.1 The average change in interlayer spacings (%) and workfunction (eV) of $Pt_3Ni(111)$, $Pt_3Ni\text{-}Pt_{\mathbf{skin}}(111)$ and Pt(111) surfaces. . . . 156
5.2 Average bond lengths and interlayer spacings of atomic oxygen on Pt_3Ni alloys 160
5.3 The most stable on/sub-surface phases on all studied (111) surfaces 167
5.4 The calculated (average) bond lengths for the most stable on/sub-surface configurations on the Pt_3Ni surface 169
5.5 The calculated (average) bond lengths for the most stable on/sub-surface configurations on the $Pt_3Ni\text{-}Pt_{\mathbf{skin}}$ surface 171
5.6 The temperatures (K) at which the oxygen coverage changes phase from the (T, p) thermodynamics phase diagram on the Pt_3Ni and $Pt_3Ni\text{-}Pt_{\mathbf{skin}}$ surfaces 174
5.7 Average Bader charges (e) of the top two layers on the Pt_3Ni alloys 182

Chapter 1

Introduction

The world's energy consumption has been increasing continually for many years, and it is expected to increase by a further 50 % by the year 2035.[1] Fossil fuels such as oil, coal and natural gas are currently the main sources of the world's energy demand. However, there are two major issues associated with fossil fuels, which are a) the depletion of natural resources and b) the emission of green house gases that causes global warming.[2] In order to solve these issues, cleaner sources of energy are required to conserve the natural resources and reduce the pollution. This has led to the research and development of alternative energy generation applications such as fuel cells. Fuel cells have emerged as a promising new technology due to their use of non-depleting, non-fossil and clean sources of fuel.

1.1 Fuel Cells

The discovery of the fuel cell began in 1839 by a Swiss scientist Christian Schoenberg. However, his friend William Grove constructed the first working fuel cell.[3] A fuel cell is an electrochemical device that requires a source of fuel to produce

electricity. The electricity is produced from a direct conversion of chemical energy[4] that takes place within the cell as long as there is a constant supply of fuel. A wide variety of fuels can be used to directly or indirectly generate the electricity. In addition to the generated electricity, other by-products including water and heat are also produced as the output. A fuel cell is an efficient system that does not require any moving part to function. It is, however, very expensive to manufacture on a large scale. For this reason, research was slowed down until the last twenty years where interest was dramatically increased with the aim of commercialisation in the near future.[5]

A fuel cell works similarly to a battery and so can be used for a number of applications that require current. Some of these applications are stationary power (*e.g.* power generating stations and auxiliary units), transportation (*e.g.* buses and cars) and portable electronics (*e.g.* laptops and mobile phones).[6] The key components in a fuel cell are two electrodes embedded with catalysts and separated by an electrolyte. The electrodes are electrical conductors that allow current to flow through the cell, and are classified as the negatively charged cathode (where reduction takes place) and the positively charged anode (where oxidation takes place). The electrolyte is an ion-conducting material which transports charged particles from one electrode to the other while the catalyst is coated onto the electrode to speed up the electrochemical half-cell reactions. The key components are then placed between a pair of flow field plates to give a single cell, known as a membrane electrode assembly (MEA).[7] This MEA can generate a limited amount of power. However, to achieve a higher voltage output, several MEAs are electrically connected in series to form a so called fuel cell stack.

There are different types of fuel cells, which are classified by the type of electrolyte and fuel employed. This electrolyte and fuel also determines the working operating temperature of the system. Generally, all the different types of fuel cell can be grouped into three main operating temperature regimes: high, medium and low temperatures. The high temperature fuel cells operate between 800-1000 °C, the medium temperature fuel cells operate between 120-250 °C and the low tem-

perature fuel cells operate between 80-120 °C.[8] Table 1.1 gives an overview of the various kinds of fuel cells and their associated reactions, operating temperature, electrolyte types, fuels and their applications.

Table 1.1: Comparison of different fuel cells and their operating characteristics. Data from[9]

Fuel cell type	Anode reaction Cathode reaction Overall reaction	Operating temperature [°C]	Electrolyte Material	Fuel	Application
Solid oxide (SOFC)	$2H_2 + 2O^{2-} \rightarrow 2H_2O + 4e^-$ $O_2 + 4e^- \rightarrow 2O^{2-}$ $2H_2 + O_2 \rightarrow 2H_2O$	750-1000	Yttrium stabilized zirconia oxide	H_2, CO, and CH_4	Stationary power plants, transportation
Molten carbonate (MFC)	$2H_2 + 2CO_3^{2-} \rightarrow 2CO_2 + 2H_2O + 4e^-$ $O_2 + 2CO_2 + 4e^- \rightarrow 2CO_3^{2-}$ $H_2 + 1/2O_2 + CO_2 \rightarrow H_2O + CO_2$	~650	Lithium and potassium carbonate	H2, CO, and CH_4	Stationary power plants
Phosphoric acid (PAFC)	$H_2 \rightarrow 2H^+ + 2e^-$ $O_2 + 4H^+ + 4e^- \rightarrow 2H_2O$ $2H_2 + O_2 \rightarrow 2H_2O$	~220	Phosphoric acid	Pure H_2	Stationary power plants
Alkaline (AFC)	$2H_2 + 4OH^- \rightarrow 4H_2O + 4e^-$ $O_2 + 2H_2O + 4e^- \rightarrow 4OH^-$ $2H_2 + O_2 \rightarrow 2H_2O$	90-120	Potassium hydroxide	Pure H_2	Apollo space mission vehicles
Direct methanol (DMFC)	$CH_3OH + H_2O \rightarrow CO_2 + 6H^+ + 6e^-$ $3/2O_2 + 6H^+ + 6e^- \rightarrow 3H_2O$ $CH_3OH + 3/2O_2 \rightarrow CO_2 + 2H_2O$	80-90	Proton-conducting membrane	CH_3OH	Portable power transportation
Proton exchange membrane (PEMFC)	$H_2 \rightarrow 2H^+ + 2e^-$ $2H^+ + 1/2O_2 + 2e^- \rightarrow H_2O$ $H_2 + 1/2O_2 \rightarrow H_2O$	80-100	Proton-conducting membrane	Pure H_2	Transportation portable power

This thesis focuses solely on the proton exchange membrane fuel cell (PEMFC) [a] and therefore, the following discussions will be limited to this type of fuel cell system. For a more detailed overview of the other types of fuel cell systems summarised in Table 1.1, the reader is referred to numerous textbooks.[9–13]

[a] Proton exchange membrane fuel cell (PEMFC) also known as polymer electrolyte membrane fuel cells.

1.2 Proton exchange membrane fuel cells (PEMFCs)

Proton exchange membrane fuel cells (PEMFCs), developed by General Electric Company, were the first type of fuel cell to find an application-power source, used in the NASA's Gemini space flights in the 1960's.[9] They have now become one of the most promising technologies for the future, as a replacement for combustion powered engines, e.g. vehicles. The PEMFC is a low temperature fuel cell, operating at a temperature range of 80-100 °C and requires a short warm-up before use and cool-down after use.[14] It has high power density and energy conversion efficiency.[15]

PEMFCs use hydrogen as fuel, oxygen (usually air) as the oxidant and hydrogen protons (H^+) from the fuel act as the mobile charge carrier. The membrane is a solid polymer electrolyte layer which is bound to the catalysed porous electrodes (anode and cathode) placed on each side. The membrane is thin (20-200 μm), flexible and transparent, and it is both chemically and thermally stable.[16] Both the anode and the cathode are usually composed of a platinum (Pt) containing catalyst on conductive carbon support. Figure 1.1 shows a schematic diagram of a PEMFC. The oxidation of hydrogen at the anode splits the molecule into protons and electrons. The protons drift through the electrolyte to the cathode, and the electrons flow around the external circuit to generate electricity. The protons and electrons then combine at the cathode to reduce the oxygen. Water and heat are produced as the waste products.

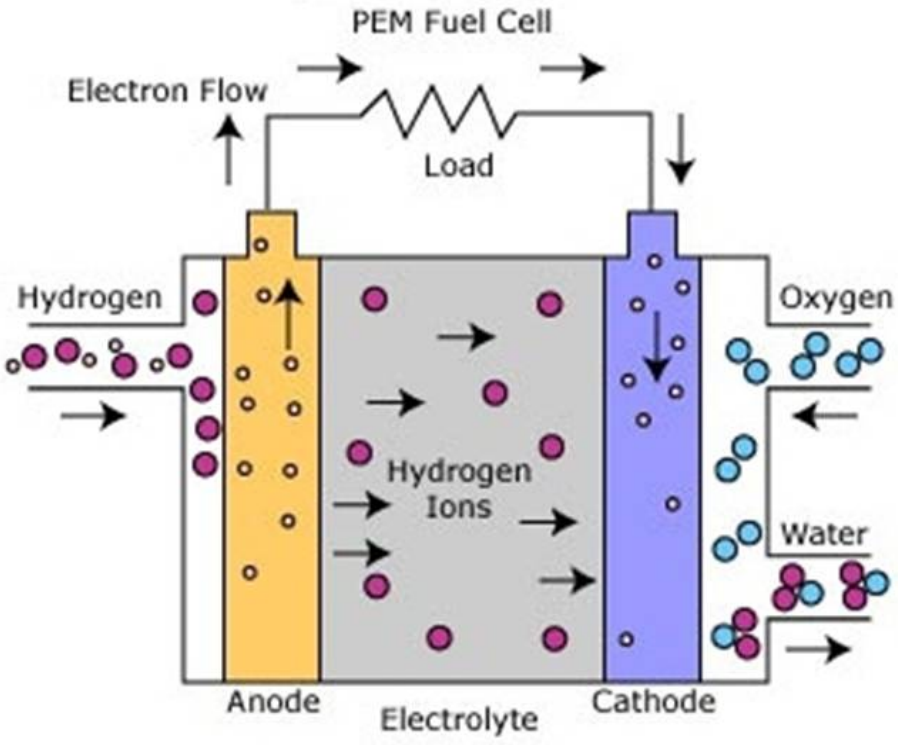

Figure 1.1: Schematic diagram of a proton exchange membrane fuel cell (PEMFC). Adapted from.[17]

1.3 Performance loss in PEMFCs

The maximum work other than the pressure-volume work that can be obtained from any system is given by the change in free energy (also called Gibbs energy, ΔG). In a PEMFC, ideally, all the free energy change is available in the form of electrical energy. Thus, the maximum electrical work obtained is defined as:

$$\Delta G = -nFE^o \tag{1.1}$$

where n is the number of electrons in the electrochemical reaction, F is the Faraday constant (F=96485.34 C mol^{-1}) and E^o is the standard reversible open circuit voltage potential.

The standard reversible open circuit voltage is given by:

$$E^o = -\frac{\Delta G^o}{nF} \tag{1.2}$$

where ΔG^o is the Gibbs free energy change of the reaction at standard temperature and pressure (STP; T = 298.15 K, p=1 atm) which is also dependent on the change in enthalpy and entropy.

$$\Delta G^o = \Delta H - T\Delta S \tag{1.3}$$

where ΔH is the reaction enthalpy change and ΔS is the reaction entropy change. At STP, the maximum theoretical voltage potential for a reversible open circuit cell is 1.23 V. In an ideal (reversible) fuel cell, the cell voltage is independent of the current drawn. However, a voltage drop is experienced in practice even under open-circuit (zero current) conditions due to various irreversible loss mechanisms. At a given current density, the difference between the maximum voltage potential and the generated operating potential is commonly referred to as the potential loss or overpotential. Generally, the overpotential can be classified into three categories: (a) ohmic loss, (b) concentration loss, and (c) activation loss. Figure 1.2 shows how these main contributions can affect the overpotential.

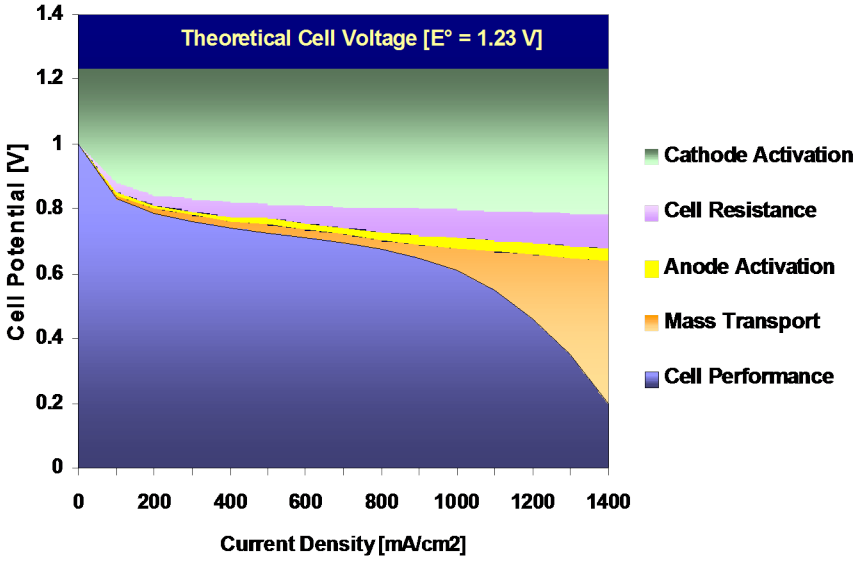

Figure 1.2: The main contributions associated with the PEMFC overpotential.[18]

a) Ohmic loss, η_{ohm} is caused by the internal resistance of the fuel cell components such as the flow of ions in the electrolyte, flow of electrons through the electrodes and the various interconnections. These losses can be reduced by using electrolytes with high ionic conductivity, electrodes with high electronic conductivity and reducing the space between the electrodes. This loss can be expressed mathematically as

$$\eta_{\text{ohm}} = IR \tag{1.4}$$

where, I is the current flowing through the cell and R is the total internal resistance.

b) Concentration loss, η_{conc} occurs due to a decrease in the concentration of the reactants at the electrode-electrolyte interface. A steady supply of the reactants is required at the electrode-electrolyte interface to maintain the flow of electric current. However, due to diffusion in the electrolyte, the concentration of the reactants is not maintained at the initial level. Reaction product accumulation

can also cause dilution of reactants. This mass transport loss can be described as

$$\eta_{\text{conc}} = \frac{RT}{nF}\, ln\left(1 - \frac{I}{I_L}\right) \tag{1.5}$$

where I_L is the limiting current, the maximum rate at which a reactant can be supplied to an electrode.

c) Activation loss, η_{act} is mainly due to charge transfer within the catalysts. This occurs from the sluggish oxygen reduction kinetics at the cathode surface. The nature of the surface, the species formed during the reaction and the intrinsic characteristics of the catalyst also influence the activation. The increase in temperature and the active surface area of the catalyst improves the cell performance. The corresponding voltage drop can be expressed by the Tafel equation defined as

$$\eta_{\text{act}} = \frac{RT}{\alpha nF}\, ln\left(\frac{I}{I_o}\right) \tag{1.6}$$

where, I_o is the exchange current density, which is the maximum current that can be extracted at negligible polarisation ($\eta = \eta_o$) and α is the electron transfer coefficient of the reaction at the electrode being studied.

The combined contributions of these overpotential losses cause the cell voltage output to decrease at low and high current densities. At the low current density, the activation loss is predominant while at the high current density, the concentration loss is the major cause. In an operating PEMFC, the voltage attained is 0.9 V.

1.4 PEMFC issues and challenges

1.4.1 Polymer electrolyte membrane

The polymer electrolyte membrane is an important component of the PEMFC and has two main functions: proton conduction from the anode to the cathode and the effective separation of the anode and cathode gases.[19] In addition it must have the following criteria to be an effective membrane.

- Good thermal stability (preferred temperature $>$100 °C for $\sim$5000 hours)
- High protonic conductivity under high-humidity conditions
- High mechanical strength
- Good chemical stability (especially the oxidative stability)

Currently, the most common polymer electrolyte membrane employed is Nafion®, a solid ion conducting perfluorinated polymer. It consists of a hydrophobic poly (tetrafluoroethylene) (PTFE) backbone that is sulphonated with side chains of perfluorinated vinyl ethers terminated by sulfonic acid groups (Figure 1.3).[20] The ionic nature of the sulphonic acid group makes it highly hydrophilic. It fulfills most of the above criteria but requires constant hydration. Another limitation of Nafion® is the operating temperature: when the temperature increases above 100 °C, without increasing the pressure, the polymer membrane dehydrates and thus loses proton conductivity. Further research has been performed to develop a well equipped polymer electrolyte membrane that can achieve all the above criteria. One of the membrane materials proposed is a non-fluorinated polymer made from sulfonated aromatic hydrocarbon.[21] Several different polymers have been proposed but the most promising is poly [2,2'-(m-phenylene)-5,5'-bibenzimidazole]/sulphuric acid (PBI/H_2SO_4), an acid-base complex that operates at a high temperature and can be manufactured cheaply.[19,22]

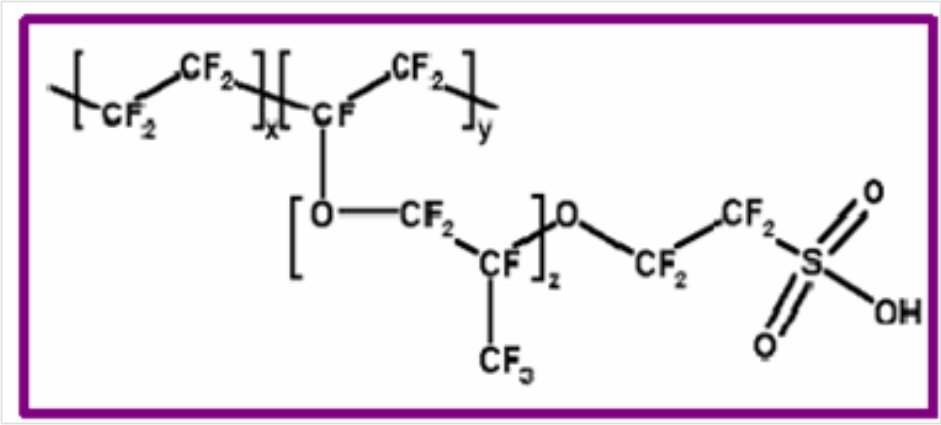

Figure 1.3: Chemical structure of Nafion ®.

1.4.2 Catalyst

The catalyst layer is responsible for the half-cell reactions that occur within the fuel cell. It is a thin surface ($\sim 3\mu$m) that is located between the membrane and the gas diffusion layer. This gives the catalyst particles (platinum or platinum alloys) easy access to the membrane. The particle loading on the surface, reactant diffusion, ionic and electrical conductivity and the diffusion path must all be balanced to achieve maximum operation.[23]

Often the catalyst employed for both the cathode and anode is platinum, an expensive metal. Higher loading of platinum particles is required for the cathode because the oxygen reduction reaction (ORR) has slower kinetics than the hydrogen oxidation reaction (HOR).[24] On the contrary to the high platinum loading, carbon monoxide poisoning occurs at the anode when reformed hydrogen is employed for the hydrogen fuel. This is due to traces of carbon monoxide ($\sim$4 ppm) generated along with the required hydrogen fuel. For these reasons, it is necessary to find alternative materials that can increase the oxygen reaction kinetics at the cathode and tolerate the carbon monoxide poisoning at the anode. This has led to the development of platinum alloys, especially carbon supported alloys. The carbon support allows full dispersion of the metals onto the catalyst surface, lead-

ing to increased reactant contact.[9] It has been reported that platinum-chromium or platinum-nickel supported on carbon for the cathode and platinum-ruthenium for the anode, are able to demonstrate high reaction activity, stability and tolerate the carbon monoxide respectively.[7,25,26]

1.5 Oxygen Reduction Reaction

A major problem identified from the overpotential of the PEMFC, is the relatively slow kinetics of the oxygen reduction reaction (ORR) at the cathode. This has led to extensive studies performed for the last 40 years to ascertain the fundamental complexity of the ORR and sensitivity to the electrode surface. The ORR is a complex multi-electron process involving several reaction intermediates and a number of elementary steps, which further depend on the electrode material, catalyst and the electrolyte. In an acid electrolyte, the most accepted overall reaction may proceed via one of two reaction pathways (Figure 1.4).[27] These reaction pathways are either the direct four-electron process, where oxygen is reduced to water (Eq. 1.7) or the indirect two-electron process, where oxygen initially reduces to hydrogen peroxide, followed by the formation of water (Eq. 1.8 and 1.9).

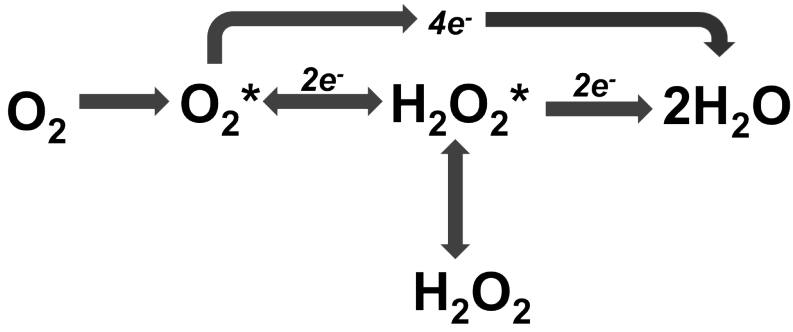

Figure 1.4: The reaction pathways for oxygen reduction reaction.[28] $*$ denotes as the surface site.

The reaction pathways can be written as:[27]

Direct four-electron process:

$$O_2 + 4H^+ + 4e^- \rightarrow 2H_2O \qquad E^0_{(O_2/H_2O)} = 1.23V \tag{1.7}$$

Indirect two-electron process:

$$O_2 + 2H^+ + 2e^- \rightarrow H_2O_2 \qquad E^0_{(O_2/H_2O_2)} = 0.67V \tag{1.8}$$

$$H_2O_2 + 2H^+ + 2e^- \rightarrow 2H_2O \qquad E^0_{(H_2O_2/H_2O)} = 1.77V \tag{1.9}$$

The standard potentials correspond to the values vs the normal hydrogen electrode at 25 °C.[29] A desired feature for a PEMFC ORR catalyst, is to reduce the oxygen molecules through the direct four-electron process. This is because the indirect two-electron process generates hydrogen peroxide (H_2O_2) which causes damage to the polymer membrane leading to low energy conversion efficiency. Using an experimental technique called the rotating ring-disk electrode (RRDE), studies have shown that the direct four-electron process dominates on noble metal catalysts such as Pt[27,30] while the indirect two-electron process prevails on less active metals like Au and non-metals like carbon.

1.6 Platinum Catalysts

An effective catalyst must be selective to the intermediate reaction and can follow the Sabatier's principle.[31] Sabatier's principle is when the catalyst is reaction specific and its interaction with intermediates are neither too strong nor too weak. If the interaction is too weak, the intermediate will fail to bind to the catalyst, and no reaction will take place. On the other hand, if the interaction is too strong, the catalyst gets blocked by the intermediate and further catalytic reactions are im-

peded.[32] In order to find an efficient catalyst for the ORR, a correlation between pure transition metal catalyst surfaces and its maximal catalytic activities were established theoretically by Nørskov.[33] The results generated a volcano curve of activity as a function of oxygen adsorption energies (Figure 1.5).

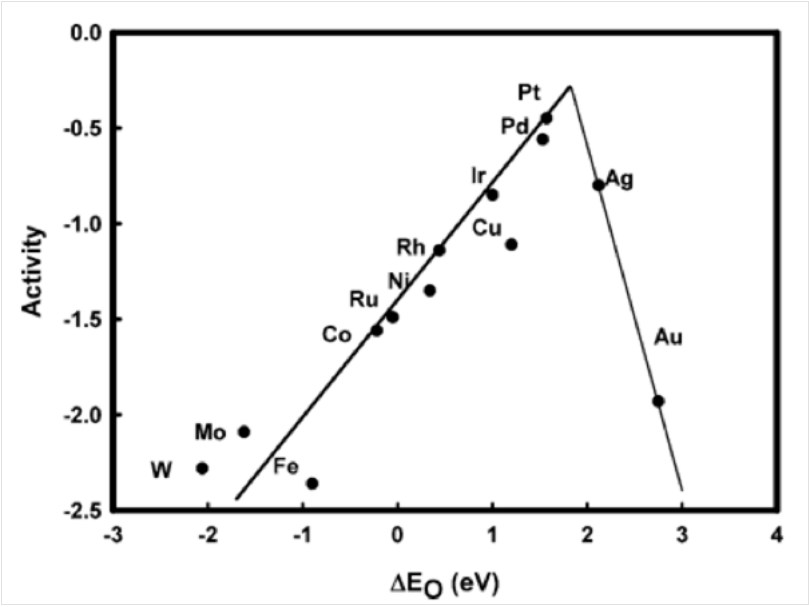

Figure 1.5: Trends in oxygen reduction activity plotted as a function of the oxygen binding energy.[33]

In good agreement with experiment, Figure 1.5 shows that Pt is the preferred metal catalyst because it sits on top of the volcano and has the highest catalytic activity under the operating conditions. Pt catalysts will adsorb oxygen with an optimal strength to generate intermediates when combined with hydrogen from the anode to form the final product, water (H_2O). As mentioned earlier, the direct four-electron reaction pathway is favoured on Pt but the exact reaction mechanism is still under debate.[34] Theoretical calculations based on density functional theory (DFT) have, however, been used to investigate the reaction mechanism and two accepted mechanisms were proposed.[33–35]

The first is the *dissociative* mechanism:

$$\frac{1}{2}O_2 + * \rightarrow O* \tag{1.10}$$

$$O* + H^+ + e^- \rightarrow HO* \tag{1.11}$$

$$HO* + H^+ + e^- \rightarrow H_2O + * \tag{1.12}$$

and the second is the *associative* mechanism:

$$O_2 + * \rightarrow O_2* \tag{1.13}$$

$$O_2* + (H^+ + e^-) \rightarrow HO_2* \tag{1.14}$$

$$HO_2* + (H^+ + e^-) \rightarrow H_2O + O* \tag{1.15}$$

$$O* + (H^+ + e^-) \rightarrow HO* \tag{1.16}$$

$$HO* + (H^+ + e^-) \rightarrow H_2O + * \tag{1.17}$$

where * denotes a site on the surface. Both mechanisms illustrate the direct four-electron process. However, the associative mechanism is capable of generating the H_2O_2 if the O-O bond is not broken when O_2 is adsorbed on the surface (Eq. 1.14). In the dissociative mechanism, the molecular oxygen dissociates to form adsorbed atomic O, which further gains two electrons in the two consecutive steps, forming water (Eq. 1.10 - 1.12).[10] The dissociation of O_2 is believed to be the rate-limiting step (rls) in the dissociative mechanism, and the proton transfer is thought to follow rather than being involved in the rls.[36] On the other hand, in the associative mechanism, the adsorption of molecular oxygen and the proton/electron transfer in the rls occur simultaneously (Eq. 1.13 - 1.17).[24] According to general views, the sluggish kinetics of ORR may be due to the following reasons:

i. the strong O-O bond and the formation of strongly bound Pt-O or Pt-OH intermediates, causing an accumulation on the surface and the blockage of active sites[37–39]

ii. the possible formation of a partially oxidised H_2O_2 intermediates and

iii. the difficulty in determining the rate-limiting step for the reactions.

Norskov *et al.*[33] demonstrated that there was a relationship between oxygen reduction activity and the binding ability of O and OH. They proposed that the origin of the overpotential for Pt was the O and OH adsorption, and both dissociative and associative reaction paths may contribute to the ORR depending on the metal and the electrode potential.

1.7 Parameters Affecting the Catalyst Performance

Essential criteria for good catalyst performance is the availability of active sites for the reactions and intermediates during the reduction process, high electronic conductivity and the chemical and structural stability under the operating temperature and oxygen partial pressure. The catalytic activity is controlled by all these intrinsic chemical activities on the surface. In a fuel cell, the Pt catalyst is made up of nanoparticles (ranging from 3-6 nm) typically dispersed on a high surface area carbon support, which considerably increases the available catalytic surface area and hence the catalytic activity.[40] These nanoparticles are generally represented as cubo-octahedral structures consisting of Pt atoms arranged on eight (111) and six (100) facets bounded by edge and corner atoms (Figure 1.6).[10] It has been observed that the (111) and (100) crystal facets are the active sites for the oxygen reduction with the (111) facets being thermodynamically more stable.[10,28] However, when the nanoparticle size increases, the number of Pt atoms on the (100)

facets increases and thus the oxygen reduction becomes facile and more catalytically active.[41]

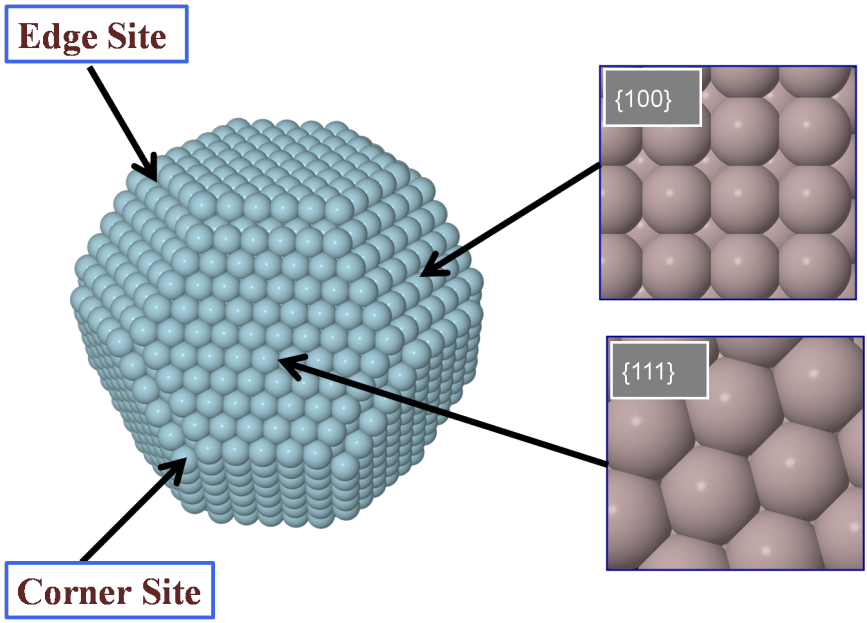

Figure 1.6: A nanoparticle showing the (111) and (100) crystal facets, edge and corner site.

Besides the active crystal facets, the size of the nanoparticle also affects the catalytic activity. According to studies performed by Kinoshita, the catalytic activity decreases with decreased Pt particle size.[42,43] One explanation for this, is the dissolution of platinum in the acidic environment and the migration of these soluble platinum species on to the carbon support, leading to loss of surface area and corrosion.[44,45] In addition, cyclic voltammetry (CV) experiments indicated that the concentration of the dissolved platinum increases when the voltage potential increases from 0.65 to 1.1 V and decreases at voltage potentials greater than 1.1 V.[46] The observed potential dependence can be explained by the complex oxidation behaviour of platinum. Between the voltage potential region of 0.85 and 1.2 V, quartz crystal nanobalance studies have shown that 0.5 monolayer (ML) of chemisorbed oxygen atoms are formed (at a potential region of 0.85 V and 1.15

V) and further formation of chemisorbed oxygen is explained in terms of a place-exchange mechanism of 0.3 ML of the chemisorbed oxygen with platinum.[46] This place-exchange mechanism between the oxygen and platinum eventually leads to the formation of a thin surface oxide film on the catalyst surface. The surface oxide film is thought to have a detrimental effect on the mechanism and kinetics of the catalysts such as the changing of the electronic properties of the catalyst surface, influencing the adsorption behaviour of reaction intermediates and/or products at the catalytic surface and restricting the flow of current within the cell.[47] For these reasons, Pt alone does not present satisfactory activity for the ORR and a number of strategies to improve the catalytic activity have been reported.

1.8 Pt-Alloy Catalysts

The alloying of Pt with a secondary transition metal (Pt-M alloy catalyst) is a prime approach for enhancing the catalytic activity of the ORR while reducing cost. A wide variety of Pt-M alloy catalysts and a range of atomic compositions have been investigated, both experimentally and theoretically, for their use in low temperature fuel cells. They have been shown to exhibit improved catalytic activity by a factor of 2 to 4 in comparison to pure Pt.[48,49] He *et al.*[50] classified these Pt-M alloy catalysts into four categories depending on their ability to reduce oxygen and their tolerance to chemical corrosion:[50] (*i*) highly active and highly corrosive (M = Fe, Co, V and Mn); (*ii*) highly active and corrosive (M = Zn, Cu, Mo and Ni); (*iii*) less active but stable (M = Zr, Cr and Ta) and (*iv*) active and stable (M = W and Ti). Investigations have also indicated that the catalytic activity of the Pt-M alloy catalysts is related to the atomic ordering between Pt and the alloying element M and the highest activity displayed for the Pt:M ratio is 3:1.[51]

The catalytic activity enhancement that occurs when Pt is alloyed with other metals are mainly attributed to the following:

Structural and geometric effects: Jalan and Taylor suggested that the enhanced catalytic activity of the Pt-M alloys catalysts are due to changes in the geometrical structures (i.e. bond distance, number of nearest neighbour and the surface atom position).[52] The Pt-Pt bond distance can be changed when Pt is alloyed with other metals. Alloying Pt with a smaller metal, causes a contraction in the Pt lattice, which has been shown to improve catalytic acitivity.[53] Experimentally, the heat-treatment temperature used for the alloy preparation also controls the Pt-Pt bond distance.[54] Additionally, it was observed that Pt atoms segregate to the catalyst surface in the presence of certain alloying elements (such as Ni, Co, Ir, *etc.*), which leads to a Pt-skin surface with higher concentration of active sites for the ORR.[55,56] Stamenkovic *et al.* showed that the $Pt_3Ni(111)$ with a Pt-skin layer is 10 times more active than the corresponding Pt(111) surface and 90 times more than the current state-of-the-art carbon supported catalysts[26].

OH_{ads} inhibition effect and oxide formation: X-ray absorption spectrocopy (XAS),[57–59] X-ray photoelectron spectroscopy (XPS)[60,61] and CV[26,62–66] experiments have shown that certain Pt-M alloy catalysts inhibit the formation of OH species and that the amount of oxide formed decreases when the alloying element present is increased. These occur because the competitive binding species are reduced, leading to an increase in the number of free active sites for the ORR[67].

Electronic effect: Alloying with different metals modifies the electronic structure which is caused by a shift in the d-band vacancies. These d-band vacancies are the degree to which the d-band is filled with electrons within the alloy.[68] Mukherjee *et al.*[57] used *in-situ* x-ray absorption near-edge structure (XANES), extended x-ray absorption fine structure (EXAFS) and *ex-situ* x-ray powder diffraction (XRD) experiments to investigate the electronic effect of Pt alloys. They observed lower d-band vacancies on the Pt-M alloys compared to Pt depending on the alloying element. This is

because the $5d$ vacancies on the alloy surface are increased, leading to an increased coupling between the oxygen $2p$ states and the alloying metal d-states.[69,70] This results in a stronger metal-O interaction, and the weakening of the O-O bonds.[69]

A d-band model approach was developed by Nørskov *et al.* that links the catalytic activity of the alloy with the fundamental surface properties of the catalyst surface.[71–74] These surface properties, contributing to this model are the surface d-band centre, ε_d, the degree of filling the d-band, $\mathrm{f_d}$ and the coupling between the absorbate states and the metal d-states, $\mathrm{V_{ad}}$. All these properties are expected to change the electronic effect of the alloy systems and also the catalytic activities. According to this model, as the alloy d-states (d-band centre, ε_d) shifts up, a distinctive antibonding state appears above the Fermi level, thereby causing a stronger activity. Therefore, in order to have an active alloy for the ORR, the shift in the ε_d must not cause a very strong or too weak activity. A volcano-type behaviour was observed when the d-band centre of the Pt_3M alloys was correlated with the catalytic activity (Figure 1.7).[57,66,70,75,76]

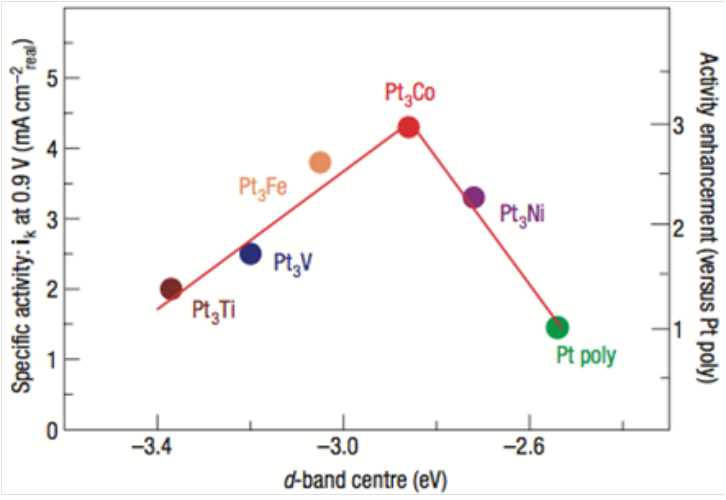

Figure 1.7: Relationship between the catalytic properties and electronic structure of Pt_3M alloys.[66]

As discussed, the Pt-M alloy catalyst can have increased benefits compared to pure Pt. However, they do not fully resolve all the problems associated with pure Pt. One of the biggest issues observed is the stability of the Pt-M alloys. A durability test performed by Colòn-Mercado and Popov[51] noticed a decay in performance of the Pt-M alloy catalysts caused by the dissolution of the alloying metal and Pt particles into the electrolyte, leading to the loss of active surface area and eventually the formation of thin surface oxide. Nonetheless, the presence of thin surface oxide is relatively low compared to the pure Pt.[60]

1.9 Theoretical studies of ORR

Theoretical modelling, especially with the present-day computer hardware capabilities has enhanced the understanding and development of the ORR processes and accelerated the pace for the discovery of a better catalyst. Predicted catalysts with enhanced catalytic activity and stability could then be validated by careful synthesis and experimental tests, leading to an overall reduction in costs. Several theoretical techniques have been employed to study the ORR but the most popular of these is the density functional theory [b] (DFT), a quantum mechanical method that can reproduce with a good degree of accuracy a variety of structural and electronic properties of the system (*e.g.* bond lengths, crystal lattice constant, binding energies, vibrational frequencies, *e.t.c.*).

Using DFT, the key elements in understanding the catalytic activities of the alloy catalysts are the adsorbate's structure, bonding type and the binding energy. For example, several theoretical studies have shown that atomic oxygen adsorbs on Pt(111) and Pt(100) at the three-fold face centred cubic (fcc) and two-fold bridge binding sites respectively.[77–79] In addition, it was observed that on both surfaces, the adsorption energies decrease when the atomic oxygen coverage increases. Furthermore, the absorption of atomic oxygen at 0.25 ML occurs at the tetrahedral

[b] Discussed further in Chapter 2.

site, underneath the hcp hollow site on the Pt(111) and tetrahedral site underneath the bridge site on the Pt(100).[78] Légaré[80] examined structures with a mixture of surface and sub-surface oxygen and predicted that sub-surface oxygen becomes favoured on Pt(111) at an oxygen coverage between 0.50 and 0.75 ML. On the other hand, Hawkin *et al.*[81] discovered the initiation of oxide growth on Pt(111) proceeded by an unexpected clustering of the oxygen atoms beyond 0.50 ML with a pronounced surface buckling. As for the Pt-M alloys, different compositions of alloys have been probed. One of these compositions is the monolayer bimetallic alloys (MBAs) where the alloying metal is present in the outer surface layers (mostly in the first two layers) of the alloy. One study predicted that MBAs of Pt will bind oxygen weaker than pure Pt and that the induced segregation energy will play a vital role in the relative stability of the surface and sub-surface monolayer structures.[82,83] The absorption energy barrier was investigated on both MBAs and Pt_3M alloys, and it was found that the alloying metal and alloy compositions does have an effect on the atomic oxygen absorption kinetics.[84]

Nonetheless, in-depth investigations of oxygen coverage on Pt-M alloys are still insufficient, a topic which, this thesis will attempt to address.

1.10 Project aims and Objectives

A brief overview of fuel cell technology presented in this chapter has outlined the current inadequacy of PEMFCs for future commercialisation. One of the major issues, is to find a more efficient catalyst for the poor cathode performance associated with the ORR. Platinum-based alloy catalysts have been identified as a means of improving both the activity and the stability. The work presented in this thesis will attempt to gain detailed understanding of the catalyst surface oxidation on platinum-nickel (Pt-Ni) alloy catalysts compared to pure Pt. The aim of this research is to determine the relative propensity of surface oxide film forming on Pt and Pt-Ni alloys. The DFT technique will be employed to investigate how atomic oxygens bind to the surface. Furthermore, to bridge the temperature

and pressure gap between DFT and technological relevant conditions, a statistical thermodynamic model is applied.

The rest of the thesis will be presented as follows: Chapter 2 describes the theoretical methodology used for this research. The examination of atomic oxygen coverage effects on pure Pt was carried out in Chapter 3. Both the active Pt(111) and (100) surfaces were explored to determine their tendency of forming thin surface oxide. It was found that surface oxide film is more likely to form on the Pt(111) surface compared to the Pt(100) surface. However, at the PEMFC operating conditions, the adsorbed oxygens were present on the two surfaces. Next, different compositions of Pt-M alloy were investigated, starting with MBAs in Chapter 4 and Pt_3M in Chapter 5. Chapter 4 focused on Pt-Ni-Pt (underlayer) and Ni-Pt-Pt (overlayer) structures for the (111) and (100) surfaces, whereas Chapter 5 considered Pt_3Ni and Pt_3Ni-$Pt_{\mathbf{skin}}$ at the (111) surface. It was discovered that, at the PEMFC operating conditions, thin surface oxide film is more likely to form on the MBAs compared to the Pt_3Ni and Pt_3Ni-$Pt_{\mathbf{skin}}$ surfaces. Finally, Chapter 6 presents preliminary results on the other alloying element and summarises the outcomes of the research.

References

[1] http://www.eia.doe.gov/oiaf/ieo/world.html.

[2] http://www.eia.doe.gov/oiaf/1605/ggccebro/chapter1.html.

[3] http://www.fuelcellmarkets.com/ceramic_fuel_cells/news_and_information/3,1,443,1,7900.html.

[4] Ruettinger, W.; Ilinich, O.; Farrauto, R. J. *Journal of Power Sources* **2003**, *118*, 61–65, Conference on Scientific Advances in Fuel Cell Systems, Amsterdam, Netherlands, Sep 25-26, 2002.

[5] Schultz, T.; Zhou, S.; Sundmacher, K. *Chemical Engineering and Technology* **2001**, *24*, 1223–1233.

[6] Hoogers, G. *Fuel Cell Technology Handbook*; Society of Automotive Engineers,U.S., 2003.

[7] Ralph, T. R.; Hogarth, M. P. *Platinum Metals Review* **2002**, *46*, 3–14.

[8] Appleby, A. *Energy* **1996**, *21*, 521–653.

[9] Larminie, J.; Dicks, A. *Fuel Cell Systems Explained*, 2nd ed.; John Wiley and Sons Ltd: West Sussex, England, 2003.

[10] Kinoshita, K. *Electrochemical Oxygen Technology*; Wiley-Interscience, 1992; Vol. 30.

[11] *Handbook of Fuel Cells: Fundamentals, Technology, Applications*; Vielstich, W., Lamm, A., Gasteiger, H. A., Eds.; Wiley-Blackwell, 2003; Vol. 1.

[12] *Handbook of Fuel Cells: Fundamentals, Technology, Applications*; Vielstich, W., Lamm, A., Gasteiger, H. A., Eds.; Wiley-Blackwell, 2003; Vol. 3 & 4.

[13] Steele, B. C. H.; Heinzel, A. *Nature* **2001**, *414*, 345–352.

[14] Young, J. B. *Annual Review of Fluid Mechanics* **2007**, *39*, 193–215.

[15] Gottesfeld, S.; Zawodzinski, T. A. *Polymer Electrolyte Fuel Cells, in Advances in Electrochemical Science and Engineering*; Wiley-VCH Verlag GmbH, Weinheim, Germany., 1997; Vol. 5, pp 195–301.

[16] O'Hayre, R.; et.al, *Fuel cells fundamentals*; John Wiley and Sons Inc.: Hoboken, New Jersey, 2006.

[17] http://www.rcs.bham.ac.uk/hydrogenproject/whatis/fuelcells.shtml.

[18] Acres, G. J. K.; Frost, J. C.; Hards, G. A.; Potter, R. J.; Ralph, T. R.; Thompsett, D.; Burstein, G. T.; Hutchings, G. J. *Catalysis Today* **1997**, *38*, 393–400, Conference on Fuel Cells and Catalysis, London, England, Jan, 1996.

[19] Rozière, J.; Jones, D. J. *Annual Review of Materials Research* **2003**, *33*, 503–555.

[20] Souzy, R. *Solid State Ionics* **2005**, *176*, 2839–2848.

[21] Li, Q. F.; et. al, *Chemistry of Materials* **2003**, *15*, 4896–4915.

[22] Smitha, B.; Sridhar, S.; Khan, A. A. *Journal of Membrane Science* **2005**, *259*, 10–26.

[23] Litster, S.; McLean, G. *Journal of Power Sources* **2004**, *130*, 61–76.

[24] Wang, B. *Journal of Power Sources* **2005**, *152*, 1–15.

[25] Bryikoglu, A. *International Journal of Hydrogen Energy* **2005**, *30*, 1181–1212.

[26] Stamenković, V. R.; Fowler, B.; Mun, B. S.; Wang, G.; Ross, P. N.; Lucas, C. A.; Marković, N. M. *Science* **2007**, *315*, 493–497.

[27] Yeager, E. *Electrochimica Acta* **1984**, *29*, 1527–1537.

[28] Marković, N. B.; Schmidt, T. J.; Stamenković, V.; Ross, N. M. *Fuel Cells* **2001**, *1*, 105–116.

[29] Hoare, J. *Standard Potentials in Aqueous Solution*; Marcel Dekker, New York, 1985.

[30] Shih, Y.; Sagar, G. V.; Lin, S. D. *Journal of Physical Chemistry C* **2008**, *112*, 123–130.

[31] Bligaard, T.; Norskov, J. K.; Dahl, S.; Matthiesen, J.; Christensen, C. H.; Sehested, J. *Journal of Catalysis* **2004**, *224*, 206–217.

[32] Rothenberg, G. *Catalysis: Concepts and Green Applications*, 1st ed.; Wiley-VCH, 2008.

[33] Nørskov, J.; Rossmeisl, J.; Logadottir, A.; Lindqvist, L.; Kitchin, J.; Bligaard, T.; Jonsson, H. *Journal of Physical Chemistry B* **2004**, *108*, 17886–17892.

[34] Shi, Z.; Zhang, J. J.; Liu, Z. S.; Wang, H. J.; Wilkinson, D. P. *Electrochimica Acta* **2006**, *51*, 1905–1916.

[35] Zhdanov, V. P.; Kasemo, B. *Electrochemistry Communications* **2006**, *8*, 1132–1136.

[36] Yeager, E. B.; Razaq, M.; Gervasio, D.; Razaq, A.; Tryk, D. *Journal of the Serbian Chemical Society* **1992**, *57*, 819.

[37] Lamas, E. J.; Balbuena, P. B. *Journal of Chemical Theory and Computation* **2006**, *2*, 1388–1394.

[38] Wang, J. X.; Markovic, N. M.; Adzic, R. R. *Journal of Physical Chemistry B* **2004**, *108*, 4127–4133.

[39] Zhang, J. L.; Vukmirovic, M. B.; Sasaki, K.; Nilekar, A. U.; Mavrikakis, M.; Adzic, R. R. *Journal of the American Chemical Society* **2005**, *127*, 12480–12481.

[40] Xie, J.; Wood, D. L.; Wayne, D. M.; Zawodzinski, T. A.; Atanassov, P.; Borup, R. L. *Journal of the Electrochemical Society* **2005**, *152*, A104–A113.

[41] Beard, B. C.; Ross, P. N. *Journal of the Electrochemical Society* **1990**, *137*, 3368–3374.

[42] Takasu, Y.; Ohashi, N.; Zhang, X. G.; Murakami, Y.; Minagawa, H.; Sato, S.; Yahikozawa, K. *Electrochimica Acta* **1996**, *41*, 2595–2600.

[43] Kinoshita, K. *Journal of Electrochemical Society* **1990**, *137*, 845–848.

[44] Sasaki, K.; Shao, M.; Adzic, R. *Catalysts: Dissolution and Stabilization of Platinum in Oxygen Cathodes*; Springer, 2009; pp 7–28.

[45] Ferreira, P. J.; La O', G. J.; Shao-Horn, Y.; Morgan, D.; Makharia, R.; Kocha, S.; Gasteiger, H. A. *Journal of the Electrochemical Society* **2005**, *152*, A2256–A2271.

[46] Wang, X.; Kumar, R.; Myers, D. *Electrochemical and Solid State Letters* **2006**, *9*, A225–A227.

[47] Jerkiewicz, G.; Vatankhah, G.; Lessard, J.; Soriaga, M.; Park, Y. *Electrochimica Acta* **2004**, *49*, 1451–1459, 197th Meeting of the Electrochemical-Society, Toronto, Canada, May, 2000.

[48] Mukerjee, S.; Srinivasan, S. *Journal of Electroanalytical Chemistry* **1993**, *357*, 201–224.

[49] Paulus, U.; Wokaun, A.; Scherer, G.; Schmidt, T.; Stamenkovic, V.; Radmilovic, V.; Markovic, N.; Ross, P. *Journal of Physical Chemistry B* **2002**, *106*, 4181–4191.

[50] He, T.; Kreidler, E.; Xiong, L.; Luo, J.; Zhong, C. J. *Journal of the Electrochemical Society* **2006**, *153*, A1637–A1643.

[51] Colón-Mercado, H. R.; Popov, B. N. *Journal of Power Sources* **2006**, *155*, 253–263.

[52] Jalan, V.; Taylor, E. J. *Journal of the Electrochemical Society* **1983**, *130*, 2299–2301.

[53] Appleby, A. J. *Energy, The International Journal* **1986**, *11*, 13–94.

[54] Min, M. K.; Cho, J. H.; Cho, K. W.; Kim, H. *Electrochimica Acta* **2000**, *45*, 4211–4217, 3rd Electrocatalysis Meeting (ECS 99), Portoroz, Slovenia, 1999.

[55] Salgado, J. R. C.; Antolini, E.; Gonzalez, E. R. *Journal of Physical Chemistry B* **2004**, *108*, 17767–17774.

[56] Ma, Y.; Balbuena, P. B. *Surface Science* **2008**, *602*, 107–113.

[57] Mukerjee, S.; Srinivasan, S.; Soriaga, M. P.; McBreen, J. *Journal of the Electrochemical Society* **1995**, *142*, 1409–1422.

[58] Roques, J.; Anderson, A. B.; Murthi, V. S.; Mukerjee, S. *Journal of the Electrochemical Society* **2005**, *152*, E193–E199.

[59] Mukerjee, S.; McBreen, J. *Journal of Electroanalytical Chemistry* **1998**, *448*, 163–171.

[60] Aricó, A. S.; Shukla, A. K.; Kim, H.; Park, S.; Min, M.; Antonucci, V. *Applied Surface Science* **2001**, *172*, 33–40.

[61] Shukla, A. K.; Neergat, M.; Bera, P.; Jayaram, V.; Hegde, M. S. *Journal of Electroanalytical Chemistry* **2001**, *504*, 111–119.

[62] Paulus, U.; Wokaun, A.; Scherer, G.; Schmidt, T.; Stamenkovic, V.; Markovic, N.; Ross, P. *Electrochimica Acta* **2002**, *47*, 3787–3798.

[63] Kuzume, A.; Herrero, E.; Feliu, J. M. *Journal of Electroanalytical Chemistry* **2007**, *599*, 333–343.

[64] Stamenković, V.; Schmidt, T. J.; Ross, P. N.; Marković, N. M. *Journal of Electroanalytical Chemistry* **2003**, *554*, 191–199.

[65] Stamenković, V.; Schmidt, T. J.; Ross, P. N.; Marković, N. M. *Journal of Physical Chemistry B* **2002**, *106*, 11970–11979.

[66] Stamenković, V. R.; Mun, B. S.; Arenz, M.; Mayrhofer, K. J. J.; Lucas, C. A.; Wang, G.; Ross, P. N.; Markovic, N. M. *Nature Materials* **2007**, *6*, 241–247.

[67] Lima, F. H. B.; Zhang, J.; Shao, M. H.; Sasaki, K.; Vukmirovic, M. B.; Ticianelli, E. A.; Adzic, R. R. *Journal of Physical Chemistry C* **2007**, *111*, 404–410.

[68] Sinfelt, J. H. *Accounts of Chemical Research* **1977**, *10*, 15–20.

[69] Antolini, E.; Passos, R. R.; Ticianelli, E. A. *Electrochimica Acta* **2002**, *48*, 263–270.

[70] Stamenković, V.; Mun, B. S.; Mayrhofer, K. J. J.; Ross, P. N.; Markovic, N. M.; Rossmeisl, J.; Greeley, J.; Nørskov, J. K. *Angewandte Chemie-International Edition* **2006**, *45*, 2897–2901.

[71] Hammer, B.; Nørskov, J. *Advances in Catalysis* **2000**, *45*, 71–129.

[72] Hammer, B.; Nørskov, J. K. *Surface Science* **1995**, *343*, 211–220.

[73] Kitchin, J.; Norskov, J.; Barteau, M.; Chen, J. *Journal of Chemical Physics* **2004**, *120*, 10240–10246.

[74] Mavrikakis, M.; Hammer, B.; Nørskov, J. K. *Physical Review Letters* **1998**, *81*, 2819–2822.

[75] Ruban, A.; Hammer, B.; Stoltze, P.; Skriver, H. L.; Nørskov, J. K. *Journal of Molecular Catalysis A-Chemical* **1997**, *115*, 421–429, 1st Francqui Colloquium on Molecular Heterogeneous Catalysis, Brussels, Belgium, Feb 19-20, 1996.

[76] Zhang, J.; Vukmirovic, M.; Xu, Y.; Mavrikakis, M.; Adzic, R. *Angewandte Chemie-International Edition* **2005**, *44*, 2132–2135.

[77] Ford, D. C.; Xu, Y.; Mavrikakis, M. *Surface Science* **2005**, *587*, 159–174.

[78] Gu, Z.; Balbuena, P. *Journal of Physical Chemistry C* **2007**, *111*, 9877–9883.

[79] Moussounda, P. S.; Haroun, M. F.; Legare, P. *Physica Scripta* **2010**, *81*, 045603.

[80] Légaré, P. *Surface Science* **2005**, *580*, 137–144.

[81] Hawkins, J.; Weaver, J.; Asthagiri, A. *Physical Review B* **2009**, *79*, 125434.

[82] Greeley, J.; Mavrikakis, M. *Journal of Physical Chemistry B* **2005**, *109*, 3460–3471.

[83] Chen, J. G.; Menning, C. A.; Zellner, M. B. *Surface Science Reports* **2008**, *63*, 201–254.

[84] Gu, Z.; Balbuena, P. B. *Journal of Physical Chemistry C* **2008**, *112*, 5057–5065.

Chapter 2

Theoretical Methodology

2.1 Introduction

One of the main goals of modelling a solid material is the determination of its total energy, which can further lead to the evaluation of other physical properties such as the cohesion energy, equation of state, vibration frequencies, *etc*. To achieve accurate total energies, it is necessary to use electronic structure methods based on quantum mechanics.

This chapter provides a general introduction to the many-body problem of electronic structure theory and the other practicalities involved in performing a total energy calculation. These include the electronic structure theory itself, how the theory is implemented and finally, the statistical thermodynamic model, which bridges the temperature and pressure gap. For a detailed description of other simulation methods, the reader is referred to numerous textbooks.[1–5]

2.2 Electronic Structure Theory

2.2.1 The Schrödinger Equation/ Born-Oppenheimer approximation

In quantum mechanics, the energy of a non-relativistic system is determined through the approximate solution of the time-independent Schrödinger equation.[6]

$$\hat{H}\Psi = E\Psi \quad . \tag{2.1}$$

where $\hat{H}$ is the Hamiltonian operator, Ψ is the wavefunction and E is the total energy of the system. The Hamiltonian operator is the sum of the kinetic energy operator, $\hat{T}$, (that is the kinetic energy of the electrons and nuclei separately) and the potential energy operator, $\hat{V}$, (that is the attractive electrostatic interaction between the electrons and nuclei and the repulsive potential due to the electron-electron and nucleus-nucleus interactions).

In reality, the Schrödinger equation (Eq. 2.1) can only be solved for a limited number of systems (*e.g.* hydrogen atom). In order to solve Eq. 2.1 for solids, which contain many interacting atoms, approximations are employed. The most fundamental approximation is the Born-Oppenheimer approximation (adiabatic approximation)[7] that separates the motions of the nuclei and electrons. It assumes that the nuclei are infinitely heavy compared to the electrons and so move much more slowly than the electrons. Hence the nuclei can be assumed to be at stationary positions (*i.e.* fully localised about a single point) with respect to the electron movement that is more rapid. Therefore, within this approximation, as the nuclei are stationary, the kinetic energy of the nuclei is neglected and the potential energy of the nucleus-nucleus repulsion interaction is treated as a constant.

Thus, the nuclear and electronic wavefunctions are decoupled and the Schr-ödinger equation is solved only for the electronic wavefunction. The Hamiltonian operator within the Born-Oppenheimer approximation becomes the sum of the kinetic energy of the electrons (T_{e}), the potential energy due to electron-electron interaction (V_{ee}), and the attractive potential energy between the electrons and nuclei, known as the external potential (V_{ext}).

$$\hat{H}_{\mathrm{elec}}\Psi_{\mathrm{elec}} = (T_{\mathrm{e}} + V_{\mathrm{ee}} + V_{\mathrm{ext}})\ \Psi_{\mathrm{elec}} = E_{\mathrm{elec}}\Psi_{\mathrm{elec}} \quad . \tag{2.2}$$

The V_{ee} is the quantity that contains all the many-body physics of the electronic structure problem because too many degrees of freedom are involved. Since most practical systems contain lots of electrons, it is still a major challenge to solve the Schrödinger equation using the Born-Oppenheimer approximation. Hence, further approximations are required to solve Eq. 2.2 accurately and efficiently.

2.2.2 Density Functional Theory

A fundamental approach to the electronic structure problem relies on the *Density Functional Theory* (DFT) method. This method is a powerful *ab-initio* [a] method used for describing the structural and electronic properties of a practical system especially solids and their surfaces. Furthermore, it is currently one of the most popular and robust theoretical methods available as it is computationally more efficient than other theoretical methods with similar accuracy. [1,2] The development of the DFT method started as far back as the late 1920's by Thomas and Fermi. [8,9] However, 30 years later, in 1964, Hohenberg and Kohn proved two key theorems that are stated below.

[a] *ab-initio* (synonymous to first-principles) calculations involve no adjustable parameters.

The first theorem states that the ground state total energy of a system of interacting electrons is a unique functional [b] of the ground state electron density, $n_0(\mathbf{r})$.[10,11] In addition, all the ground state properties (the potential, wavefunction, Hamiltonian) are functionals of the electron density, $n(\mathbf{r})$, by a one to one correspondence between the ground state electron density and the external potential, V_{ext}. Therefore, all the physical properties of a system can be calculated if the $n(\mathbf{r})$ is known.

The second theorem (also called the variational principle) states that the ground state electron density, $n_0(\mathbf{r})$, and the total energy for a given external potential, V_{ext}, can be calculated exactly (at least, in principle) by successfully minimising the energy functional with respect to the $n(\mathbf{r})$. This is subject to the constraint of describing the correct number of electrons as:

$$N = \int n(\mathbf{r}) dr \quad . \tag{2.3}$$

According to these theorems, the ground state total energy, $E_0[n(\mathbf{r})]$, of an electronic system at a given V_{ext} can be written as a functional of the $n(\mathbf{r})$:

$$E[n(\mathbf{r})] = \min_{n(r)} \langle \Psi | T_{\text{e}}[n(\mathbf{r})] + V_{\text{ee}}[n(\mathbf{r})] + V_{\text{ext}}[n(\mathbf{r})] | \Psi \rangle \quad , \tag{2.4}$$

where $\min_{n(r)}$ is the minimum $E[n(\mathbf{r})]$ with respect to all the possible electron density, $n(\mathbf{r})$ and

$$E[n(\mathbf{r})] \geq E_0[n_0(\mathbf{r})] \quad . \tag{2.5}$$

Unfortunately, the above Hohenberg-Kohn theorems do not provide a way of finding the ground state density. This led to a significant discovery by Kohn and Sham

[b] A functional is a function whose argument is itself a function.

(1965), where they showed that the problem of the many interacting electrons in an external potential can be mapped exactly to a set of non-interacting electrons in an effective external potential.[12,13] The Kohn-Sham (KS) total energy for the system can be written as:

$$E[n(\mathbf{r})] = T[n(\mathbf{r})] + V_{\text{ext}}[n(\mathbf{r})] + E_{\text{Hartree}}[n(\mathbf{r})] + E_{\text{xc}}[n(\mathbf{r})] \quad . \tag{2.6}$$

where $T[n(\mathbf{r})]$ is the kinetic energy functional of the non-interacting electron system which has the same $n(\mathbf{r})$ as the real system, given as:

$$T = -\frac{1}{2}\sum_{i=1}^{N}\int \varphi_i^*(\mathbf{r})\nabla^2\varphi_i(\mathbf{r})d^3\mathbf{r} \quad , \tag{2.7}$$

where φ_i are the single-particle KS orbitals. The $V_{\text{ext}}[n(\mathbf{r})]$ is given as:

$$V_{\text{ext}}[n(\mathbf{r})] = \int V(\mathbf{r})n(\mathbf{r})d^3\mathbf{r} \quad , \tag{2.8}$$

E_{Hartree} is the Hartree energy describing the (classical) electron-electron Coulomb repulsion given by:

$$E_{\text{Hartree}}[n(\mathbf{r})] = \frac{1}{2}\iint \frac{n(\mathbf{r})n(\mathbf{r}')}{|\mathbf{r}-\mathbf{r}'|}d^3\mathbf{r}d^3\mathbf{r}' \quad , \tag{2.9}$$

And the final term, $E_{\text{xc}}[n(\mathbf{r})]$, is the exchange and correlation energy functional, which accounts for all the important quantum-mechanical many-body interactions between the electrons. The next step in the electronic structure problem is to

define the effective potential, $V_{\text{eff}}(\mathbf{r})$, which consists of the electrostatic potentials (that is the external potential), Hartree potential and the exchange-correlational potential. The $V_{\text{eff}}(\mathbf{r})$ is defined as:

$$\begin{aligned} V_{\text{eff}}(\mathbf{r}) &= V_{\text{ext}}(\mathbf{r}) + V_{\text{Hartree}}[n(\mathbf{r})] + V_{\text{xc}}[n(\mathbf{r})] \quad , \\ &= \frac{\delta \left\{ \int V(\mathbf{r}) n(\mathbf{r}) d^3\mathbf{r} + E_{\text{Hartree}}[n(\mathbf{r})] + E_{\text{xc}}[n(\mathbf{r})] \right\}}{\delta n(\mathbf{r})} \quad , \\ &= V(\mathbf{r}) + \int \frac{n(\mathbf{r}')}{|\mathbf{r} - \mathbf{r}'|} d^3\mathbf{r}' + \frac{\delta E_{\text{xc}}[n(\mathbf{r})]}{\delta n(\mathbf{r})} \quad . \end{aligned} \tag{2.10}$$

The ground-state electron density is obtained in practice by solving the N electron Schrödinger-like one-particle equation, given by:

$$\left\{ -\frac{1}{2}\nabla^2 + V_{\text{eff}}(\mathbf{r}) \right\} \varphi_i(\mathbf{r}) = \epsilon_i \varphi_i(\mathbf{r}) \quad , \tag{2.11}$$

which yields the KS orbitals, φ_i, and the electron density of the non-interacting electron system is given as:

$$n(\mathbf{r}) = \sum_{i=1}^{N} |\varphi_i(\mathbf{r})|^2 \quad . \tag{2.12}$$

The Kohn-Sham equations yield the mathematical framework for finding the ground state density, $n_0(\mathbf{r})$, and the energy, $E[n(\mathbf{r})]$, of a many-body electron problem. The Hartree and exchange-correlation potentials depend on the density, $n(\mathbf{r})$, which further relies on the KS orbitals, φ_i, and in turn depends on the $V_{\text{eff}}(\mathbf{r})$.

Therefore, the problem of solving the Kohn-Sham equations (Eqs. 2.10, 2.11 and 2.12) has to be done in a self-consistent (iterative) way. The general procedure is schematically shown in Figure 2.1. Usually, the first step is to start with an initial guess for the $n(\mathbf{r})$, calculate the corresponding $V_{\text{eff}}(\mathbf{r})$ and then solve the Kohn-Sham equations for the φ_i, which in turn define a new density and total energy. This process is repeated using the new density and total energy, until convergence is reached to within the chosen numerical accuracy.[1]

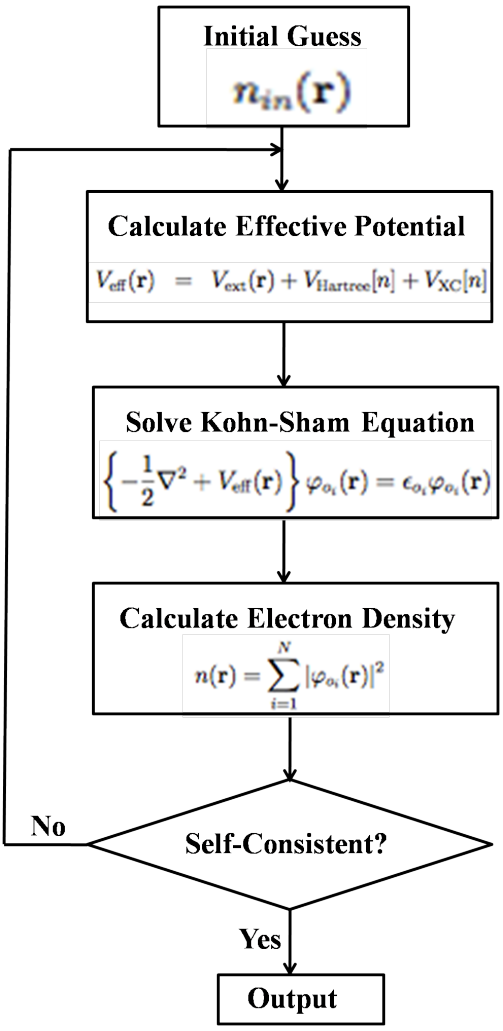

Figure 2.1: Representation of the self-consistency cyclic loop used in solving the Kohn-Sham equations in numerical calculations.[1]

2.2.3 Exchange-Correlation Functionals

In principle, the ground state total energy (Eq. 2.6) is exact for the considered system and contains no approximations, as long as the exchange-correlation functional can be derived exactly. Unfortunately, this has not been possible and the precise form for the $E_{\rm xc}[n(\mathbf{r})]$ and $V_{\rm xc}(\mathbf{r}) = \frac{\delta E_{\rm xc}[n(\mathbf{r})]}{\delta n(\mathbf{r})}$ are still not known and will therefore be approximated. So far, there are a variety of approximations for the exchange-correlation functional but the most widely used ones in condensed matter physics are the local density approximation (LDA) and the generalised gradient approximation (GGA).

2.2.3.1 Local Density Approximation (LDA)

This is the simplest approximation originally introduced by Kohn and Sham,[12] valid only for slowly varying electron densities. Within LDA, the $E_{\rm xc}[n(\mathbf{r})]$ is assumed to be the same as that of a homogeneous electron gas of the same density, $\epsilon_{\rm xc}^{\rm hom}(n(\mathbf{r}))$,

$$E_{\rm xc}^{\rm LDA}[n(\mathbf{r})] = \int n(\mathbf{r})\ \epsilon_{\rm xc}^{\rm hom}\ (n(\mathbf{r}))\ d^3\mathbf{r} \quad , \tag{2.13}$$

where $\epsilon_{\rm xc}^{\rm hom}(n(\mathbf{r}))$ is the exchange-correlation energy per particle of the homogeneous electron gas of density, n. The exchange and correlation contributions are separated out as:

$$\epsilon_{\rm xc}^{\rm hom}(n(\mathbf{r})) = \epsilon_{\rm x}^{\rm hom}(n(\mathbf{r})) + \epsilon_{\rm c}^{\rm hom}(n(\mathbf{r})) \quad . \tag{2.14}$$

The exchange energy, $\epsilon_{\mathrm{x}}^{\mathrm{hom}}(n(\mathbf{r}))$ can be calculated exactly by using the Dirac expression,[14]

$$\epsilon_{\mathrm{x}}^{\mathrm{hom}}(n(\mathbf{r})) = -\frac{3}{4}\left(\frac{3}{\pi}\right)^{1/3}(n(\mathbf{r}))^{1/3} \quad , \tag{2.15}$$

while the correlation energy, $\epsilon_{\mathrm{c}}^{\mathrm{hom}}(n(\mathbf{r}))$ is obtained based on the highly accurate quantum Monte Carlo simulations of the free electron gas[15,16] and the numerical data are then fitted to a simple parameterised form. Common parameterisation forms are Perdew-Zunger (PZ),[17] Perdew- Wang (PW)[18] and Vosko-Wilk-Nusair (VWN).[19]

LDA works well for realistic systems such as solid state and metal systems but does badly for molecular systems. Furthermore, it typically underestimates the lattice constant and overestimates the binding energies compared to experimental values. To improve the shortcomings of the LDA, the gradient dependent functionals were introduced.

2.2.3.2 Generalised gradient approximation (GGA)

These are second generation functionals, where the gradient of the electron density, $\nabla n(\mathbf{r})$ as well as the density itself, are included in the $\epsilon_{\mathrm{xc}}^{\mathrm{hom}}(n(\mathbf{r}))$ as:

$$E_{\mathrm{xc}}^{\mathrm{GGA}}[n(\mathbf{r})] = \int n(\mathbf{r})\ \epsilon_{\mathrm{xc}}^{\mathrm{hom}}(n(\mathbf{r}))\ , \nabla n(\mathbf{r}))\ d^3\mathbf{r} \quad . \tag{2.16}$$

The GGA takes into account the inhomogeneity in the electron density gradient. They are "semi-local" functionals and generally yields more reliable results

than the LDA functional for molecular systems. However, the GGA results are not necessarily superior to the LDA results and errors can be identified for some properties such as the overestimation of the lattice constants. There are many different versions of GGAs but the most widely used in this thesis, as in many surface physics studies, is the Perdew, Burke, and Ernzerhof (PBE)[20,21] exchange-correlation functional. Several off-spring of PBE (revPBE,[22] RPBE[23] and PBE-WC[24]) and its close relative PW91[18,25] are also used for the simulations of solids and its surfaces. The PBE functional is chosen because it is well known to treat molecules interacting with metallic surfaces reasonable well.

2.2.4 DFT Implementation in the VASP Code

The implementation of DFT has been incorporated into several computational codes to perform quantum mechanical energy minimisation calculations on molecules, solids and surfaces. In this thesis, the VASP (Vienna *Ab-initio* Simulation Package) code has been used, developed at the Institut für Materialphysik of the University of Vienna.[5,26–28] VASP is a DFT-based code used to compute the electronic structure properties of systems, using periodic boundary conditions. It utilises plane-waves as the basis set to expand the Kohn-Sham orbitals and the projector-augmented-wave (PAW) method[29,30] to describe the electron-ion interactions. The following sections will briefly outline the most important aspects of the VASP implementations.

2.2.4.1 Periodic Boundary Conditions and Bloch's Theorem

Crystalline solids are periodic in three dimensions and contain lots of electrons that cannot be included in the calculation. To overcome this problem, periodic boundary conditions (PBC) are introduced to reduce the system to one particular unit cell, which is periodically repeated in three dimensions. For crystal surfaces, where the periodicity is in two dimensions, they are represented as slabs (several

layers of atoms) with a vacuum region. The vacuum region must be large enough to prevent any significant interaction between the adsorbate and the next periodic image (lateral interaction) or any subsequent slab respectively. The slab must also be thick enough to represent both the bulk and surface atoms (as shown in Figure 2.2).

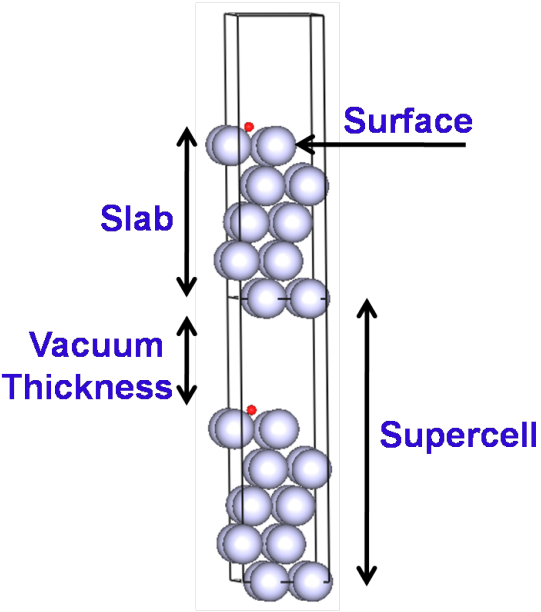

Figure 2.2: Periodic unit cell with a slab consisting of five atomic layers and one adsorbate, repeated in vertical direction.

The application of PBC allows Bloch's theorem[4,31] to be utilised. According to this theorem, due to the translational symmetry, each electronic wavefunction of the crystal, based on the unit cell can be expressed as:

$$\Psi_{\boldsymbol{k}}(\mathbf{r}) = e^{i\boldsymbol{k}.\mathbf{r}} u_{\boldsymbol{k}}(\mathbf{r}) \quad , \tag{2.17}$$

where $\Psi_{\boldsymbol{k}}(\mathbf{r})$ is the electronic states, $\mathbf{r}$ is a position vector, $\boldsymbol{k}$ is a wave vector

confined to the first Brillouin zone (BZ) [c] of the reciprocal lattice, $e^{i\boldsymbol{k}.\mathbf{r}}$ is a plane wave and $u_{\boldsymbol{k}}(\mathbf{r})$ is a periodic function of the crystal lattice, given by,

$$u_{\boldsymbol{k}}(\mathbf{r}) = u_{\boldsymbol{k}}(\mathbf{r} + \mathbf{L}) \quad . \tag{2.18}$$

where $\mathbf{L}$ is one of the lattice vectors of the periodic crystal.

2.2.4.2 Brillouin Zone (BZ) Sampling

When PBC are applied to the solid system, the infinitely extended integrals in real space are replaced by the finite integrals over the BZ in reciprocal space. These integrals are computed numerically by sampling the integrals at finite number of k-points in the BZ. To minimise the number of $\boldsymbol{k}$-points needed to integrate the BZ, a number of different methods have been devised for obtaining accurate approximations.[32–34] In this thesis, the method developed by Monkhorst and Pack is implemented. This method generates a uniform mesh of $\boldsymbol{k}$-points along the three lattice vectors in reciprocal space.[33] The number of $\boldsymbol{k}$-points is determined by three integers, q_i, along the coordinates. The integers generate a sequence of numbers according to

$$u_i = \frac{2r - q_i - 1}{2q_i} \tag{2.19}$$

where r varies from 1 to q_i . The grid size determined by the Monkhorst-Pack scheme is obtained according to

$$\boldsymbol{k}_{xyz} = \boldsymbol{u}_x\boldsymbol{t}_1 + \boldsymbol{u}_y\boldsymbol{t}_2 + \boldsymbol{u}_z\boldsymbol{t}_3 \tag{2.20}$$

[c]The first Brillouin zone is the collection of all points in reciprocal space that are closer to the origin (denoted as the Γ point) than to any other reciprocal lattice point.

where $\boldsymbol{t}_1$, $\boldsymbol{t}_2$ and $\boldsymbol{t}_3$ are the lattice vectors in reciprocal space.

A sufficiently high number of $\boldsymbol{k}$-points must be used, to reduce the magnitude of any error in the total energy calculation. However, the computational cost also increases with increased $\boldsymbol{k}$-point mesh. Therefore, it is important to test a varied set of $\boldsymbol{k}$-point mesh until convergence is reached to within the chosen accuracy. For insulators and semiconductors, only a very small number of $\boldsymbol{k}$-points is needed to obtain an accurate electronic potential and total energy. In contrast, metals require a dense $\boldsymbol{k}$-point mesh to define the Fermi surface and the total energy precisely.

2.2.4.3 Plane Wave Basis Sets

To solve the Kohn-Sham equations (Eq. 2.10, 2.11 and 2.12) in practice, the use of basis set functions are required to expand the one-particle orbital, $\varphi_i(\mathbf{r})$. The basis set functions are constructed from either atom-centred functions or non-atom-centred functions or a combination of both. The type of basis sets chosen is very important to the accuracy and computational time of an electronic structure calculation. For solid state simulations, VASP uses the non-atom-centred plane-wave basis set and implements efficient algorithms such as fast Fourier transforms (FFTs) to move between real and reciprocal space.[35]

The periodic function, $u_{\boldsymbol{k}}(\mathbf{r})$, in Eq. 2.17 can be expanded using a discrete set of plane waves with the wave vectors of the reciprocal lattice vectors,

$$u_{\boldsymbol{k}}(\mathbf{r}) = \sum_{\mathbf{G}} c_{\boldsymbol{k},\mathbf{G}}\, e^{i\mathbf{G}.\mathbf{r}} \quad , \tag{2.21}$$

where $\mathbf{G}$ represents the reciprocal lattice vectors (defined as $\mathbf{G} \,.\, \mathbf{L} = 2\pi m$, $\mathbf{L}$ is the lattice vector of the crystal in real space and m is an integer). The one-

particle orbital in the total energy calculation, $\varphi_{i,\boldsymbol{k}}(\mathbf{r})$ can be rewritten as the linear combination of plane waves:[4]

$$\varphi_{i,\boldsymbol{k}}(\mathbf{r}) = \sum_{\mathbf{G}} c_{i,(\boldsymbol{k}+\mathbf{G})}\, e^{[i\,(\boldsymbol{k}+\mathbf{G}).\mathbf{r}]} \quad . \tag{2.22}$$

To represent the orbitals exactly, an infinite number of plane waves would be required. However, the expansion coefficient, $c_{i,(\boldsymbol{k}+\mathbf{G})}$, for the plane waves with small kinetic energies are more important than those with large kinetic energies. Thus, within a practical simulation, the plane wave basis set is truncated to include only plane waves that have kinetic energies less than a particular energy cutoff, E_{cut}

$$\frac{1}{2}|\mathbf{k}+\mathbf{G}|^2 \leq E_{cut} \quad . \tag{2.23}$$

Therefore, the size of the plane wave basis set can be adjusted via E_{cut}. The truncation of the plane wave basis set to E_{cut} will ultimately lead to an error in the computed physical quantities, but this can be reduced by increasing E_{cut} until convergence within the required tolerance is reached.

2.2.4.4 Pseudopotentials

Electrons in a solid (or atom or molecule) can be divided into core and valence electrons, where the core electrons are localised and tightly bound to the nuclei, while the valence electrons are weakly bound. The physical properties of a material are mainly governed by the valence electrons. Thus, the core electrons are "frozen" using the pseudopotential (PP) approximation. Within this approximation, the strong Coulomb potential of the nucleus and the effects of the tightly

bound core electrons are replaced by an effective ionic potential acting on the valence electrons.[36] Using pseudopotentials to describe the electron-ion interaction leads to a reduced number of electrons that need to be described. Thus faster calculations and the treatment of bigger systems can be performed.

In all the calculations reported in this thesis, the *Projector-Augmented-Wave* (PAW) method[29,30] is utilised. This method is, in principle, a frozen-core all-electron method that combines ideas from the pseudopotential method and the all-electron linear augmented plane- wave (LAPW) method.[37] This means that the core electrons are frozen, but the valence electron wavefunctions are reconstructed to effectively have an all electron character.

2.3 Output from the *ab-initio* Calculation

The outputs generated from the DFT calculations contain sufficient information for evaluating physical and chemical properties of the system. This section gives a brief introduction of the selected properties considered in this thesis.

2.3.1 Binding and Segregation Energies

An energy minimisation is performed for an initial guessed structure until the lowest energy configuration is attained. From the output total energy, the binding energy can be calculated. Within this thesis, the binding energy, $\mathrm{E_b}$, per oxygen atom is defined as :

$$\mathrm{E_b} = \frac{1}{\mathrm{n_O}}[\mathrm{E_{slab/O}} - \mathrm{E_{slab}} - \mathrm{n_O E_O}] \tag{2.24}$$

where $\mathrm{n_O}$ is the number of oxygen atoms in the unit cell, $\mathrm{E_{O/slab}}$ is the energy of the slab with oxygen atoms, and $\mathrm{E_{slab}}$ is the energy of the clean slab. $\mathrm{E_O}$= $1/2\mathrm{E_{O_2}^{total}}$, where $\mathrm{E_{O_2}}$ is the energy of the isolated oxygen molecule in its ground state.

The next stage is to understand the composition and stability of interacting oxygen with the Pt-M alloy surfaces so as to determine which configuration is likely to be observed under oxidising conditions. It is believed that the M component will be enriched to the surface in the presence of oxygen.[38] To determine which surface composition is most stable, the surface segregation energy is calculated for all the Pt-M alloy surfaces in the presence of oxygen at the oxygen coverages studied. The surface segregation energy is defined as:

$$\Delta E_{\mathrm{seg}} = E_{[\mathrm{PtNi/O}]} - E_{[\mathrm{Pt_{skin}/O}]} \tag{2.25}$$

where $E_{[\mathrm{PtNi/O}]}$ is the total energy for non-$\mathrm{Pt_{skin}}$ configurations with oxygen, and $E_{[\mathrm{Pt_{skin}/O}]}$ is the total energy for $\mathrm{Pt_{skin}}$ structures with oxygen. In Chapter 3 of this thesis, $E_{[\mathrm{PtNi/O}]}$ and $E_{[\mathrm{Pt_{skin}/O}]}$ are Ni-Pt-Pt/O and Pt-Ni-Pt/O surfaces respectively while in Chapter 4, they are $\mathrm{Pt_3}$Ni/O and $\mathrm{Pt_3}$Ni-$\mathbf{Pt_{skin}}$/O configurations respectively. The segregation energy for the clean slab (that is the configuration without oxygen) is the difference in total energies between the two structures. Positive segregation energy indicates that a Ni-rich surface is favoured while negative segregation energy signifies a Pt-rich surface.

2.3.2 Work-function

The work-function (Φ) is the minimum energy required to remove an electron from the bulk metal at 0K. Therefore, the energy difference between the Fermi energy, E_{F} and the electrostatic potential in the middle of the vacuum level, E_{vac}, corresponds to the work-function (Eq. 2.26 and Figure 2.3).

$$\Phi = E_{\mathrm{F}} - E_{\mathrm{vac}} \tag{2.26}$$

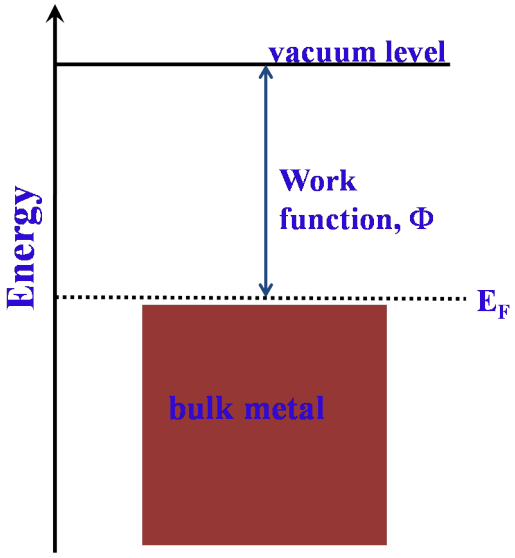

Figure 2.3: Schematic energy diagram of a bulk metal.

It is well-known that the surface environment will affect the work-function.[39] Therefore, the work-function change, $\Delta\Phi$, according to Eq. 2.27 can be used as a representation for the actual surface state when the reaction is taking place.

$$\Delta\Phi = \Phi(\Theta) - \Phi^{\mathrm{clean}} \tag{2.27}$$

where $\Delta\Phi$ is the work-function change in eV and Θ is the total oxygen coverage and Φ^{clean} is the work-function for the clean slab.

2.3.3 Surface dipole moment

The surface dipole moment[40] (in Debye) is evaluated by the using Helmholtz equation,

$$\mu = \frac{A\Delta\Phi}{12\pi\Theta} \tag{2.28}$$

where A is the surface area in Å^2 per (1x1) surface unit cell, $\Delta\Phi$ is the work-function change in eV and Θ is the total oxygen coverage.

2.3.4 Charge Density differences

An important output from electronic structure calculations is the electron density. By analysing the electron density, real space information can be obtained about the chemical bonds that have been formed or broken within the system. In this thesis, the charge density difference, $\Delta n(\mathbf{r})$, is defined as:

$$\Delta n(\mathbf{r}) = n^{\text{slab/O}}(\mathbf{r}) - n^{\text{slab}}(\mathbf{r}) - n^{\text{O}}(\mathbf{r}) \tag{2.29}$$

where $n^{\text{slab/O}}(\mathbf{r})$ is the total electron density for the converged slab with oxygen atoms. From the $n^{\text{slab/O}}(\mathbf{r})$, the electron density of both the clean surface, $n^{\text{slab}}(\mathbf{r})$ and the isolated oxygen layer, $n^{\text{O}}(\mathbf{r})$, are subtracted. The charge difference formed according to Eq. 2.29 describes the charge transfer between the adsorbates and the interacting surface. The final state geometries (*i.e.* the adsorbed or absorbed systems) are required to calculate the charge density differences.

2.3.5 Density of States

The density of states (DOS) is a common tool for interpreting the characteristics of the chemical bonding within quantum systems. These analyses provide very useful information about the distribution of electronic states in $\boldsymbol{k}$-space and at a given energy level. From the DOS, we can locate the Fermi level and the energy of the highest occupied state. Also, to determine the electronic state for a particular ion in a system, the partial density of states (PDOS) is analysed. This is when the DOS is projected onto the atomic orbitals. In this thesis, the average partial density of states (PDOS) for each layer in the surface slab system is analysed.

2.3.6 *d*-band Centre Model

The *d*-band centre, ε_{d}, model, developed by Hammer and Nørskov,[41,42] can predict the trends in the adsorption binding energies of various adsorbates on the metal surfaces. It has been shown that there is correlation between the *d*-band centre, referenced to the Fermi level and the structure reactivity. In general, the adsorbates bind to the surface of the transition metal strongly if the *d*-band centre of the surface atom is higher in energy. The *d*-band centre is calculated as the first moment of the projected *d*-band density of states on the surface atoms referenced to the Fermi level.[43]

$$\varepsilon_{\mathrm{d}} = \frac{\mu_1}{\mu_0} = \frac{\int E\, n(E) dE}{\int n(E) dE} \tag{2.30}$$

where μ_1 and μ_0 are the first and zero moment of the projected *d*-band density of states.

2.3.7 Bader Analysis

Bader analysis[44] is a useful tool for calculating the number of valence electrons associated with a particular ion in a periodic solid. This method involves analysing the topological features of the electron density around an atom (or ion), which is then divided into Bader basins associated with each atom. Inside the Bader basin, the electron density is summed up and the Bader charge for each atom is determined. Also, the technique can provide valuable results for magnetic systems where the electronic magnetic moments contained within the Bader basins can be integrated in the same manner as the charge.

2.4 Statistical Thermodynamic Model

DFT is usually denoted to be the theory at zero temperature and pressure. However, there is need to extrapolate the results to conditions at which industrial catalysts operate (*i.e.* real catalysts work under high pressures and temperatures). In order to bridge the temperature and pressure gap, statistical thermodynamics using classical ideal gas is implemented. In this approach, a clean platinum surface is in contact with an oxygen environment (reservoir) at a certain temperature, T, and pressure, p. At equilibrium, the oxygen molecules can be added to (or taken from) the platinum surface without changing either its temperature or pressure. The statistical thermodynamic properties of the system can be described by the Gibbs free energy, G, which is a function of the number of Pt (N_{Pt}) and O (N_{O}) atoms in the system, in addition to the T and p.

The most stable configuration is the one that minimises the surface free energy, $\gamma(T,p)$:[45,46]

$$\gamma(T,p) = \frac{1}{A}[\Delta G(T,p,N_{\mathrm{Pt}},N_{\mathrm{O}}) - N_{\mathrm{Pt}}\mu_{\mathrm{Pt}}(T,p) - N_{\mathrm{O}}\mu_{\mathrm{O}}(T,p)] \qquad (2.31)$$

where A is the surface area, N_{Pt} and N_{O} are the number of platinum and oxygen atoms respectively. μ_{Pt} is the platinum chemical potential, which is the total energy of a Pt atom in the bulk (*i.e.* μ_{Pt} = $E_{\mathrm{Pt}}^{\mathrm{bulk}}$). The T and p dependence is mainly given by μ_{O}, the oxygen chemical potential, (*i.e.*, the O_2 gas phase environment), defined as:

$$\mu_{\mathrm{O}}(T,p) = \frac{1}{2}\left[\mathrm{E}_{\mathrm{O_2}}^{\mathrm{DFT}} + \tilde{\mu}_{\mathrm{O_2}}(T,p^o) + k_B T \ln\left(\frac{p_{\mathrm{O_2}}}{p^o}\right)\right] \tag{2.32}$$

where p^o corresponds to the atmospheric pressure.
$\tilde{\mu}_{O_2}(T,p^o) = \mathrm{E}^{\mathrm{ZPE}} + \Delta\mathrm{H} - \mathrm{T}\Delta\mathrm{S}$ and includes the contributions from rotations and vibrations of the O_2 molecule, as well as the ideal-gas entropy at 1 atm.[47] This term can either be calculated or taken from experimental values (the choice made in this study)[48] listed in thermodynamic tables. $\mathrm{E}_{\mathrm{O_2}}^{\mathrm{DFT}}$ is the DFT total energy of the O_2 molecule.

From Eq. 2.31, ΔG is the Gibbs free energy difference between the surface slab with oxygen (slab/O system, *i.e.*, Pt/O system) and the clean slab (Pt). This is defined as:

$$\Delta G = G_{\mathrm{slab/O}} - G_{\mathrm{slab}} \tag{2.33}$$

where $G_{\mathrm{slab/O}}$ and G_{slab} is:

$$G = E^{\mathrm{DFT}} + F^{\mathrm{conf}} + F^{\mathrm{vib}} + pV \tag{2.34}$$

E^{DFT} is the total energy from the DFT calculations, F^{conf} is the configurational free energy, and F^{vib} is the vibrational free energy, which contains the zero point energy, E^{ZPE}, and the entropy-related contributions, S^{vib}. The largest contribu-

tion to Eq. 2.34 arises from the E^{DFT}. the contributions (F^{conf}, F^{vib} and pV) have not been included in the present study for the surface and bulk phases. This is because the present work has assumed that the F^{conf} and F^{vib} for the metal atoms in the clean surface is similar to that in the adlayer structure and that these contributions are rather small. As for the pV-term, according to literature, a simple dimensional analysis illustrates that the contribution will be less than 0.001 meV Å^{-2} for pressures up to 1 atm.

Therefore, the contributions (F^{conf}, F^{vib} and pV) have not been included in the present study for the surface and bulk phases.

2.4.1 Free Energy as a Function of Potential

In order to determine which surface structure is observed when applied potential is included, the oxygen chemical potential, μ_{O}, is extended as:

$$\mu_{\mathrm{O}}(T,p) = \frac{1}{2}\left[\mathrm{E}_{\mathrm{O_2}}^{\mathrm{DFT}} + \tilde{\mu}_{\mathrm{O_2}}(T,p^o) + k_B T \ln\left(\frac{p_{\mathrm{O_2}}}{p^o}\right) - eU\right] \tag{2.35}$$

where U is the applied potential. The Gibbs free energy, $G(T,p)$, is then calculated as:

$$G(T,p) = E_{\mathrm{slab/O}}^{\mathrm{DFT}} - E_{\mathrm{slab}}^{\mathrm{DFT}} - \mu_{\mathrm{O}} \tag{2.36}$$

where $E_{\mathrm{slab/O}}^{\mathrm{DFT}}$ and $E_{\mathrm{slab}}^{\mathrm{DFT}}$ is the DFT total energy of the slab with the oxygen system, (Pt/O) and the clean slab (Pt) respectively.

2.4.2 Limitation of the Statistical Thermodynamics Model

There are several limitations to the above statistical thermodynamics model. These limitations are discussed below.

1. The phase diagram is restricted to the structural configurations considered. This means that if there is a more stable phase and it is not included in the set of structures considered, the model will not find it.

2. The bulk oxidation of Pt is not considered in the model. This is important because in a more accurate model, the formation of bulk PtO_2 could be more stable than the oxygen adsorption, absorption or on/sub-surface phases.

3. The approach cannot describe disordered phases, which may become important e.g. at more elevated temperatures. If the disordered phases are found to be stable, then an explicit calculation of the configurational entropy contribution will become necessary, which can be addressed by equilibrium Monte Carlo simulations.

4. The presence of water on the catalyst surface is not included in the free energy as a function of potential model. This is because, a humid environment is required for a working PEMFC.

References

[1] Martin, R. M. *Electronic Structure: Basic Theory and Practical Methods*; Cambridge University Press, 2004.

[2] Parr, R. G.; Weitao, Y. *Density-Functional Theory of Atoms and Molecules*; Oxford University Press Inc, New York, USA, 1989.

[3] Koch, W.; Holthausen, M. C. *A Chemist's Guide to Density Functional Theory*, 2nd Edition ed.; Wiley VCH, 2001.

[4] Payne, M. C.; Teter, M. P.; Allan, D. C.; Arias, T. A.; Joannopoulos, J. D. *Reviews of Modern Physics* **1992**, *64*, 1045–1097.

[5] Kresse, G.; Furthmüller, J. *Computational Material Science* **1996**, *6*, 15–50.

[6] Schrödinger, E. *Annalen der Physik* **1926**, *384*.

[7] Born, M.; Oppenheimer, J. R. *Annalen der Physik* **1927**, *84*, 457–484.

[8] Thomas, L. H. *Proceedings of the Cambridge Philosophical Society* **1927**, *23*, 542–548.

[9] Fermi, E. *Rend. Accad. Naz. Lincei* **1927**, *6*, 602–607.

[10] Hohenberg, P.; Kohn, W. *Physical Review B* **1964**, *136*, B864.

[11] Levy, M. *Proceedings of the National Academy of Sciences of the United States of America* **1979**, *76*, 6062–6065.

[12] Kohn, W.; Sham, L. J. *Physical Review* **1965**, *140*, 1133.

[13] Kohn, W. *Reviews of Modern Physics* **1999**, *71*, 1253–1266.

[14] Dirac, P. A. M. *Proceedings of the Cambridge Philosophical Society* **1930**, *26*, 376 –385.

[15] Gell-mann, M.; Brueckner, K. A. *Physical Review* **1957**, *106*, 364–368.

[16] Ceperley, D. M.; Alder, B. J. *Physical Review Letters* **1980**, *45*, 566–569.

[17] Perdew, J. P.; Zunger, A. *Physical Review B* **1981**, *23*, 5048–5079.

[18] Perdew, J. P.; Wang, Y. *Physical Review B* **1992**, *45*, 13244–13249.

[19] Vosko, S. H.; Wilk, L.; Nusair, M. *Canadian Journal of Physics* **1980**, *58*, 1200–1211.

[20] Perdew, J.; Burke, K.; Ernzerhof, M. *Physical Review Letters* **1996**, *77*, 3865–3868.

[21] Perdew, J.; Burke, K.; Ernzerhof, M. *Physical Review Letters* **1997**, *78*, 1396.

[22] Zhang, Y. K.; Yang, W. T. *Physical Review Letters* **1998**, *80*, 890.

[23] Hammer, B.; Hansen, L. B.; Nørskov, J. K. *Physical Review B* **1999**, *59*, 7413–7421.

[24] Wu, Z. G.; Cohen, R. E. *Physical Review B* **2006**, *73*, 235116.

[25] Perdew, J. P.; Chevary, J. A.; Vosko, S. H.; Jackson, K. A.; Pederson, M. R.; Singh, D. J.; Fiolhais, C. *Physical Review B* **1992**, *46*, 6671–6687.

[26] Kresse, G.; Furthmüller, J. *Physical Review B* **1996**, *54*, 11169–11186.

[27] Kresse, G.; Hafner, J. *Physical Review B* **1993**, *47*, 558–561.

[28] Kresse, G.; Hafner, J. *Physical Review B* **1994**, *49*, 14251–14269.

[29] Blöchl, P. E. *Physical Review B* **1994**, *50*, 17953–17979.

[30] Kresse, G.; Joubert, D. *Physical Review B* **1999**, *59*, 1758–1775.

[31] Ashcroft, N. W.; Mermin, N. D. *Solid State Physics*; Brooks/Cole, 1976.

[32] Chadi, D. J.; Cohen, M. L. *Physical Review B* **1973**, *8*, 5747–5753.

[33] Monkhorst, H.; Pack, J. *Physical Review B* **1976**, *13*, 5188–5192.

[34] Pack, J. D.; Monkhorst, H. J. *Physical Review B* **1977**, *16*, 1748–1749.

[35] Pickett, W. E. *Computer Physics Reports* **1989**, *9*, 115–197.

[36] Troullier, N.; Martins, J. L. *Physical Review B* **1991**, *43*, 1993–2006.

[37] Andersen, O. K. *Physical Review B* **1975**, *12*, 3060–3083.

[38] Greeley, J.; Nørskov, J.; Mavrikakis, M. *Annual Review of Physical Chemistry* **2002**, *53*, 319–348.

[39] Attard, G.; Barnes, C. *Surfaces (Oxford Chemistry Primers)*; Oxford University Press Inc., 2006; pp 62–65.

[40] Li, W.; Stampfl, C.; Scheffler, M. *Physical Review B* **2002**, *65*, 075407.

[41] Hammer, B.; Nørskov, J. *Advances in Catalysis* **2000**, *45*, 71–129.

[42] Hammer, B.; Nørskov, J. K. *Surface Science* **1995**, *343*, 211–220.

[43] Kitchin, J.; Norskov, J.; Barteau, M.; Chen, J. *Journal of Chemical Physics* **2004**, *120*, 10240–10246.

[44] Bader, R. F. *Atoms in Molecules: A Quantum Theory*; Clarendon Press, 1994.

[45] Stampfl, C. *Catalysis Today* **2005**, *105*, 17–35.

[46] Li, W.; Stampfl, C.; Scheffler, M. *Physical Review B* **2003**, *68*, 165412.

[47] Reuter, K.; Scheffler, M. *Physical Review B* **2002**, *65*, 035406.

[48] Stull, D. R.; Prophet, H. *JANAF Thermochemical Tables*, 2nd Edition ed.; US Government Print. Office, Washington, D.C., 1971.

Chapter 3

Atomic Oxygen Coverage effects on Pt Surfaces

3.1 Introduction

Platinum is a noble metal that is widely used as a catalyst in many technologically important processes such as, in automotive exhaust gas systems and fuel cells. It is, therefore, essential to understand the mechanical and chemical properties involved in the oxidation of Pt surfaces. Extensive studies of oxygen adsorbed on low index Pt(111) and Pt(100) surfaces have been carried out theoretically [1–10] and experimentally using a variety of surface techniques. [11–20] Without the presence of oxygen, the Pt(100) surface is observed to reconstruct to a quasi-hexagonal structure that is not found on the Pt(111) surface. [21] However, it was discovered that the surface reconstruction on the Pt(100) surface is lifted upon the adsorption of oxygen and a p(2x2) overlayer is formed on the Pt(111) at low oxygen coverage. [22,23] The oxygen adsorption process on the surfaces resulted in different surface structures and depend greatly on temperature. [24,25] On the Pt(111) surface, three phases of adsorbed oxygen atoms were discovered, which are: (*i*) the molecular phase ($\sim$

160 K); (*ii*) atomic oxygen (desorbs $\sim$ 600 K and 1100 K) and (*iii*) surface oxide ($>$ 1250 K).[24]

It was observed that during the characterisation of the surface using cyclic voltammetry experiment, an oxide formation was detected within the Pt surface.[26–28] This is similar to other reports where the oxidation of other transition metals (TMs) in an oxygen-rich environment has resulted in the formation of surface oxides. Some of the TMs identified theoretically and experimentally to form surface oxides are Ru, Rh, Ir, Co, Pd, Ag, and Cu.[26,29–36] There is general agreement that the adsorption of oxygen to a catalyst surface involves the dissociation of adsorbed oxygen, followed by oxygen diffusion into the sub-surface region to form a surface oxide. The thermodynamics and kinetics of these steps depend on the partial pressure, temperature and the orientation of the metal surface.[37,38] It is believed that the surface oxide formation on the Pt surface poisons the catalyst during surface reactions, leading to significant loss of activity. Clearly, a more detailed atomistic understanding of the interactions of oxygen with Pt surfaces would be valuable, in particular, to investigate how easily the surface oxides will form. It is believed that a critical oxygen coverage is the key to the oxide formation and this critical oxygen coverage is thermodynamically, not kinetically determined.[39]

This chapter gives an extensive account of the interaction of the platinum catalyst with the oxidising environment using first-principles calculations. The focus of this study is on the low index Pt(111) and the unreconstructed Pt(100) surfaces. The results presented are for oxygen adsorption, incorporation of sub-surface oxygen and the stability of surface oxide. In addition, the pressure-temperature phase diagrams are determined for conditions extending from low pressure to technologically relevant conditions of finite temperature and pressure. Results from the present study show that the Pt(100) surface binds oxygen more strongly than the Pt(111) surface. Furthermore, the critical oxygen coverage required before the sub-surface incorporation of oxygen is 0.75 ML on the Pt(111) surface and above 1.00 ML on the Pt(100) surface. The statistical thermodynamic study also re-

vealed that at the PEMFC operating condition (300 K and 1 atm), the most likely structures to be found on the surfaces are 0.50 ML (fcc) and 0.75 ML (bridge) on the Pt(111) and Pt(100) surfaces respectively.

The rest of this chapter is organised as follows: Section 3.2 is devoted to the computational setup for the calculations, followed by section 3.3 and 3.4, which discusses the stability of oxygen within the considered environments and finally, section 3.5 contains the conclusion of this chapter.

3.2 Computational Methods

This section describes the computational methods used to collect and analyse the results of this chapter.

3.2.1 Density Functional Theory Calculations

All calculations were performed using DFT as implemented in the Vienna *ab-initio* simulation package (VASP) with the projector augmented wave (PAW)[40–43] method, generalised gradient approximation (GGA) of Perdew-Burke-Ernzerhof (PBE) for the exchange-correlation functional[44,45] and a plane-wave cut-off energy of 400 eV. The Monkhorst-Pack *k-point* sampling scheme was used to sample the Brillouin zone[46] and a Methfessel-Paxton method of order 1 with a smearing[47] of 0.2 eV was used for all relaxation calculations. The convergence criteria for the electronic self-consistent iteration and the ionic relaxation loop are set to 10^{-5} eV and 0.02 eV Å^{-1}, respectively.

Extensive convergence tests were carried out to determine the *k-point* mesh (reported in Appendix A) which gives confidence that the adsorption energies re-

ported herein are fully converged to 0.001 eV. The theoretical lattice constant for fcc Pt was calculated by performing total energy calculations on a Pt perfect crystal at various volumes, and fitting energy versus volume curves to a Birch-Murnaghan equation of state.[48] All surface calculations were performed within a (2x2) supercell and a five-layer slab consisting of four atoms in each layer. The positions of the atoms in the top three layers were allowed to relax, while the bottom two layers were fixed at the calculated bulk positions. A vacuum thickness of 8 Å separate each successive slab and a *k-point* mesh of 8x8x1 was used for all calculations, which generates energy convergence to within 0.01 meV.

For all calculations performed, the oxygen atoms were allowed to move freely in all directions during the energy minimisation until the lowest energy configuration was attained. The binding energy, E_b per oxygen atom was calculated as defined by Eq. 2.24.

3.3 Results and Discussion

This section details the results of the atomic oxygen interaction with the Pt(111) and Pt(100) surfaces. Firstly, the bulk properties are modelled, followed by the interactions of atomic oxygen with the surfaces. Finally, a statistical thermodynamic model is applied to assess the stability of the surfaces under realistic conditions.

3.3.1 Bulk Pt, Clean Pt (111) and (100) surfaces and the oxygen molecule

Before investigating oxygen adsorption on the Pt surfaces, the properties of bulk Pt, clean Pt (111) and (100) surfaces and the free oxygen molecule are considered. Table 3.1 illustrates the calculated properties of bulk Pt along with the

corresponding experimental and other theoretical values for comparison. Using a *k-point* grid of 16x16x16, the calculated bulk lattice constant, $\mathrm{a_o}$ is 3.98 Å (neglecting zero-point vibrations), the bulk modulus, $\mathrm{B_o}$ is 2.28 Mbar and the cohesive energy, $\mathrm{E_o}$ is -5.90 eV . The corresponding experimental values for the Pt lattice constant, cohesive energy and bulk modulus are 3.92 Å, -5.84 eV and 2.78 Mbar respectively.[49] The slight overestimation of the calculated $\mathrm{a_o}$ and the corresponding underestimation of the $\mathrm{B_o}$ is well known for the PBE functional.[50,51] The calculated lattice constant is in good agreement with other PBE results.[8,51] On the other hand, the calculated cohesive energy and bulk modulus are smaller than other PBE results.[51] This may be due to the different technical set-up been employed.

Table 3.1: Properties of bulk Pt and comparison with other *ab initio* calculations and experiment. $\mathrm{a_o}$(Å) is the lattice constant, $\mathrm{B_o}$(Mbar) is the bulk modulus, $\mathrm{E_{coh}}$(eV) is the cohesive energy.

	Present work [a]	Other *ab initio* calculations [b]	Experimental results [c]
a_o	3.98	3.97	3.92
B_o	2.28	2.41	2.78
E_{coh}	-5.90	-5.59	-5.84

[a] Present work using PBE
[b] FP-LAPW method, PBE[51]
[c] Experimental result[49]

The clean Pt(111) and Pt(100) surfaces were cleaved from the bulk and then allowed to relax to their lowest energy structures. The change in interlayer spacings, $\delta_{i,j}$, between layers i and j with respect to the bulk interlayer distance, δ_0, is listed in Table 3.2. For the Pt(111) surface, the changes observed for the first and second interlayer spacings are positive and negative respectively while the Pt(100) surface showed a negative change of the interlayer distance. These results are in good agreement with other *ab-initio* calculations[52] and experimental analyses determined by low energy electron diffraction (LEED) and high-energy ion scattering(HEIS).[53,54] The calculated workfunction for the clean Pt(111) and

Pt(100) surfaces are 5.67 eV and 5.69 eV respectively, in good agreement with the experimental values. The experimental values determined by photoelectron spectroscopy for Pt(111) is 5.82 $\pm$ 0.15 eV and for Pt(100) is 6.08 $\pm$ 0.15 eV.[55]

Table 3.2: Change in interlayer spacings of Pt(111) and Pt(100) surfaces and the comparison with other *ab initio* calculations and experiments. d_0(Å) is the bulk Pt interlayer distance, $\delta_{12}(\%)$ is the change in the interlayer spacing between the first and second layer and $\delta_{23}(\%)$ is the change in the interlayer spacing between the second and third layer spacing.

		Present	*ab initio*[a]	Exp
	d_o	2.30		
Pt(111)	δ_{12}	+0.53	+0.85	1.0 ± 0.1[b]
	δ_{23}	-1.40	-0.56	
	δ_o	1.99		
Pt(100)	δ_{12}	-3.02	-2.37	$+0.2 \pm 2.6$ [c]
	δ_{23}	-1.25	-0.55	

[a] USPP-PBE[52]
[b] LEED[53]
[c] HEIS and LEED[54]
USPP= Ultrasoft pseudopotentials
HEIS=high-energy ion scattering (HEIS) spectroscopy

A spin-polarised calculation was performed on the isolated O_2 molecule using a cubic unit cell of 12 Å. The binding energy and bond length for the gas-phase O_2 molecule are calculated to be 3.04 eV/ O atom and 1.23 Å respectively; both are larger than the experimental values (2.56 eV/ O atom and 1.21 Å[56]) but comparable with other theoretical results.[31,57] The differences between the theoretical and experimental values are due to the well-known overestimation of the PBE functional[31] and the theoretical binding energy does not include the zero-point energy. In the present work, the main interest is the relative stability of various structures and so the over-binding of O_2 is not expected to affect the overall trends and conclusions of this work.

3.3.2 On-surface Adsorption of Atomic Oxygen on Pt Surfaces

The most stable adsorption sites on both Pt(111) and Pt (100) surfaces have been explored by comparing the binding energies relative to the gas-phase O_2 molecule for the oxygen coverage range of $\theta_{\mathrm{tot}}(0.25 \leq \theta_{\mathrm{tot}} \leq 1.00\mathrm{ML})$. Figure 3.1. illustrates the high symmetry adsorption sites of an isolated O atom on both the (111) and (100) surfaces. On the (111) surface, the adsorption sites are three-fold fcc (where there is no Pt atom in the second layer) and hcp (where Pt is present in the second layer), two-fold bridge and one-fold top while on the (100) surface, there are four-fold hollow, two-fold bridge and one-fold top sites. Figure 3.2 summarises the DFT adsorption energies as a function of oxygen coverage on the Pt surfaces at 0 K. The binding energies reported are the non zero-point corrected energies.

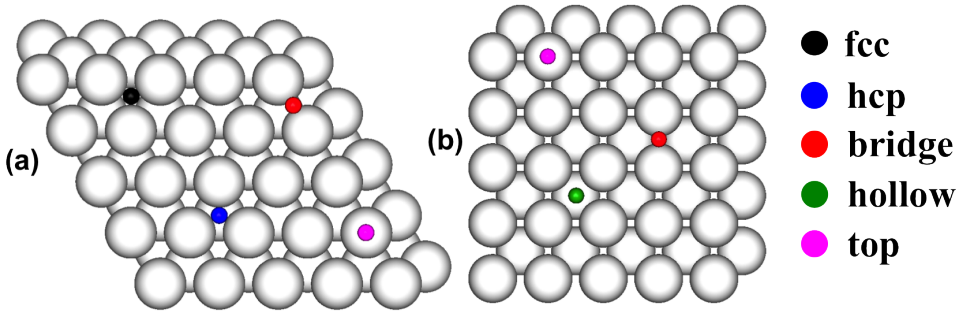

Figure 3.1: Adsobates at adsorption sites on (a) Pt (111) and (b) Pt(100) surfaces (top view).

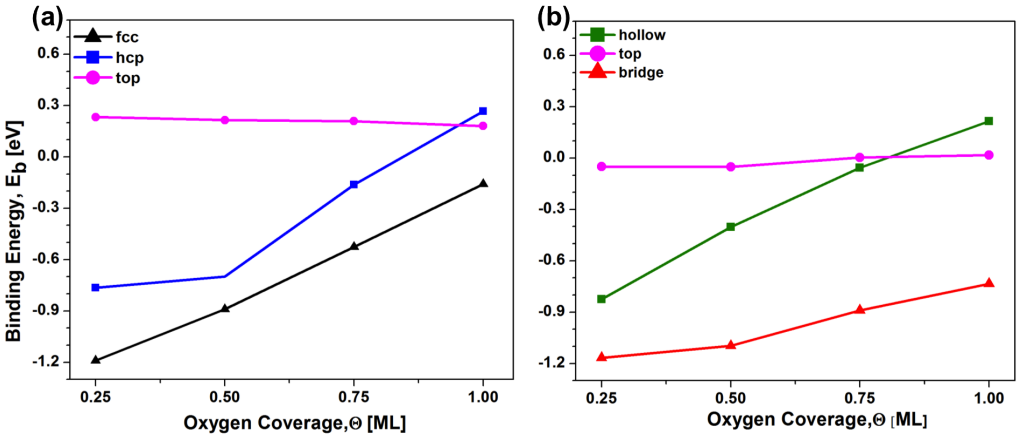

Figure 3.2: On-surface adsorption binding energies of oxygen on (a) Pt(111) and (b) Pt(100) surfaces at various oxygen coverages.

Figure 3.2a illustrates that on the (111) surface, oxygen prefers to bind to the high-coordinated three-fold fcc site. This is in agreement with experimental scanning tunnelling microscopy (STM) and low energy electron diffraction (LEED) studies as well as other DFT calculations that give a p (2x2) superstructure.[10,11,58] The fcc preference for adsorbed oxygen has also been observed on the (111) surfaces of several other fcc transition metals (TM) such as Ir, Rh.[59,60] In addition, on the (111) surface, the bridge site is unstable and oxygen adsorbed on that site relaxes into the neighbouring fcc site. For the (100) surface, (shown in Figure 3.2b), the two-fold bridge site is the most energetically favoured binding site for oxygen. This is also in line with other theoretical calculations.[9,22] Overall, the (100) surface binds oxygen more strongly than the higher coordinated (111) surface above 0.25 ML. At 0.25 ML, the binding energies of oxygen for both the (111) and (100) surfaces are similar. The (111) surface at low oxygen coverage is however, slightly more favoured with a small energy difference of 0.03 eV.

Looking closely at both figures, it can be seen that the binding energies decrease steadily as the oxygen coverage is increased except for the top site. Similar trends have also been observed for other transition metals such as Cu,[36,61] Ag,[57] Au,[62] Rh[30] and Pd,[63] when oxygen coverage increases. The reason the binding energies

decrease with increased oxygen coverage is because each Pt atom interacts with more oxygen atoms, leading to reduced binding energies *e.g.* at the fcc site and at 0.25 ML, oxygen is coordinated to three Pt atoms. This is still the case at a higher oxygen coverage, however, the Pt atom is interacting with more than one oxygen atom. As for the top site, the binding energies are essentially constant as the oxygen coverage is increased on both surfaces. This is because at the top site, each oxygen atom interacts directly with only one Pt atom even when the oxygen coverage increases.

The binding energy difference between 0.25 ML and 1.00 ML oxygen coverage at the most stable adsorption site for the (100) surface is 0.43 eV while for the (111) surface is 1.03 eV, suggesting that the (100) surface binds oxygen more tightly. It is observed that, for both the (111) and (100) surfaces, the 1.00 ML oxygen coverage at the top site is more stable than the hcp and hollow site respectively.

Table 3.3: Average Pt-O bond lengths (Å) and interlayer spacings (%) of atomic oxygen on Pt(111) and Pt(100) surfaces at 0.25ML. $d_{\mathrm{Pt-O}}$(Å) is the bond length between O and the nearest neighbour belonging to the top-layer Pt atoms, $\delta_{12}(\%)$ is the change in the interlayer spacing between the first and the second layer and $\delta_{23}(\%)$ is the change in the interlayer spacing between the second and the third layer.

	Pt (111)			Pt (100)		
	fcc	hcp	top	bridge	hollow	top
$d_{\mathrm{Pt-O}}$	2.05	2.06	1.83	1.95	2.27	1.81
δ_{12}	+1.19	+1.93	-0.14	-0.98	-0.48	-1.95
δ_{23}	-0.44	-0.86	-1.13	-0.98	-0.46	-1.16

Table 3.3 shows the Pt-O bond lengths and the change in interlayer spacings of all the studied adsorption sites at 0.25 ML oxygen coverage. Further analysis of the geometric structures show that the Pt-O bond lengths for the (111) and (100) surfaces are constant as the oxygen coverage is increased. This suggests that the bond length is not coverage dependent at any specific adsorption site. The bond lengths on the high coordinated adsorption sites are longer on both surfaces. These results are in good agreement with calculations performed by Gu and Balbuena.[8] In addition, it is interesting to note that on the (100) surface, the favourable bridge site has a shorter bond length compared to the fcc site on the (111) surface. The reason for this, could be that the (100) surface is an open and less coordinated surface and therefore binds oxygen more strongly. The magnitude of the interlayer spacings is different on the two surfaces and at each adsorption sites. On the (111) surface, positive changes are observed for the first interlayer spacing at the fcc and hcp sites and a negative change is noticed at the top site while on the (100) surface and at all the adsorption sites, the changes are negative. Furthermore, on the two surfaces and at all adsorption sites, small negative changes in the second interlayer spacings are observed.

3.3.3 On-surface Mixed Sites Adsorption of Atomic Oxygen on Pt Surfaces

To examine the effect of multiple surface interactions with oxygen, mixed sites configurations were considered for both surfaces. The oxygen atoms are adsorbed at two different high symmetry adsorption sites at the same time. These configurations include various combinations of oxygen atoms binding on the (111) surface at the fcc and hcp sites while on the (100) surface at the hollow and bridge sites. The top adsorption site was excluded in the study because it is an unfavourable binding site for all coverages except at 1.00 ML for the two surfaces studied. The oxygen coverage range was extended to 2.00 ML, in order to fully explore all the possible mixed configurations on the (2x2) surface.

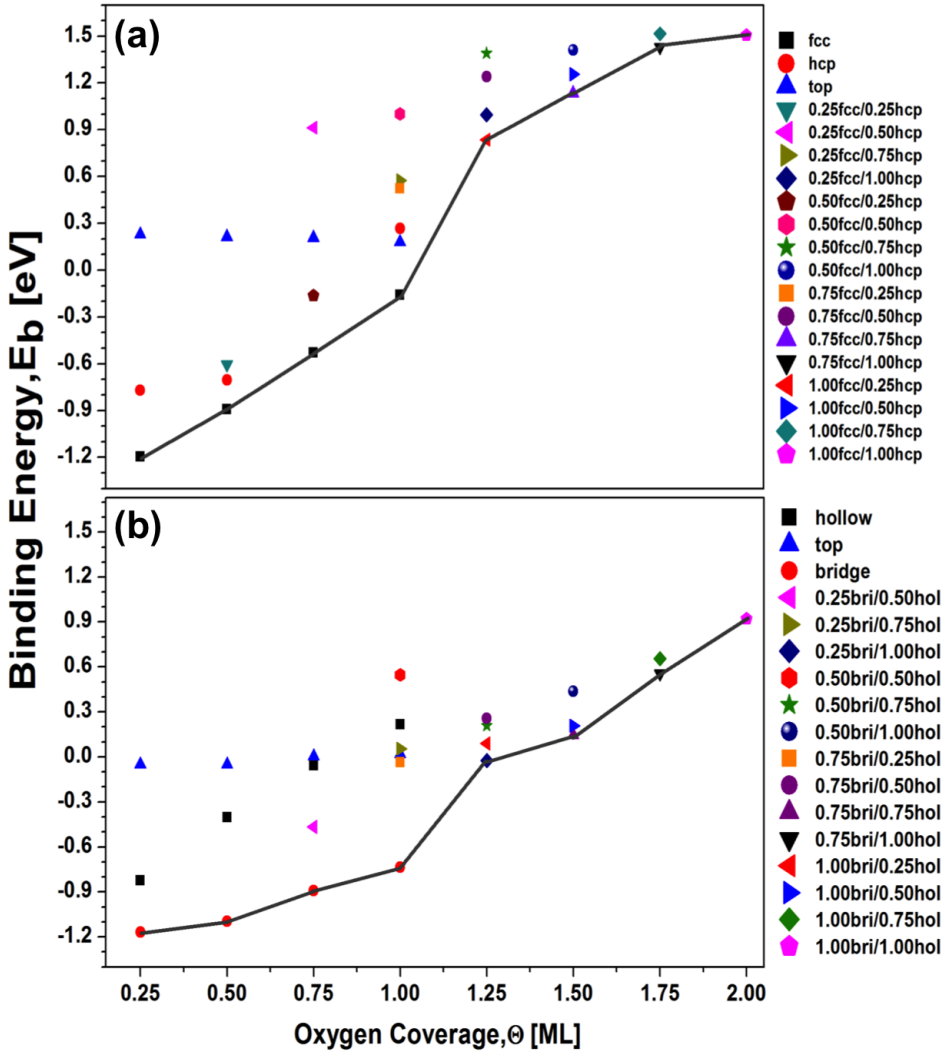

Figure 3.3: Binding energies for the on-surface mixed adsorption sites for oxygen adsorbed on (a) Pt (111) and (b) Pt (100) surfaces at various oxygen coverages. Solid black lines highlight the most stable mixed sites at each oxygen coverage.

Figure 3.3 illustrates the binding energies of the most stable mixed sites configurations along with the on-surface adsorption. Between 0.25 ML and 1.00 ML coverage, the high-symmetry on-surface fcc and bridge sites are the favoured adsorption sites for the (111) and (100) surface respectively. This is in agreement with work carried out by Lagare and Hawkin *et al.* who demonstrated that the fcc site is more favoured compared to the mixed-site configuration on the (111) surface.[7,64] Above 1.00 ML oxygen coverage, low binding energies are observed for all the considered configurations on both surfaces. This is because the interactions between the Pt atoms and adsorbed oxygens increase with oxygen coverage, thereby leading to an unstable overlayer. It is evident that the on-surface mixed sites configuration is unfavourable for the adsorption of oxygen above 1.00 ML.

3.3.4 Sub-surface Absorption of Atomic Oxygen on Pt Surfaces

As mentioned earlier, sub-surface oxygen has been detected during surface oxidation for a number of TMs including Ru, Rh, Ir, Pd, Ag, and Cu.[26,29–36] These sub-surface oxygen atoms are believed to poison the surface leading to the formation of a surface oxide. This has prompted the present work to investigate the incorporation of oxygen sub-surface on Pt surfaces.

The stability of incorporating oxygen sub-surface without the presence of on-surface oxygen, is examined theoretically on both the (111) and (100) surfaces at the oxygen coverage range of $\theta_{\mathrm{sub_{tot}}}(0.25 \leq \theta_{\mathrm{sub_{tot}}} \leq 1.00$ ML). This involves placing the oxygen atoms between the top two Pt layers. Figure 3.4 shows the high symmetry absorption sites for oxygen incorporation on both surfaces. On the (111) surface, there are three different absorption sites, the octahedral (octa) and two tetrahedral sites described as tetra-i and tetra-ii. The octa site is where oxygen is located underneath the fcc site while for tetra-i and tetra-ii, oxygen is located underneath the top and hcp site respectively. On the other hand, the (100) surface, has only the octahedral and one tetrahedral site present, where oxygen is

positioned beneath the top and bridge sites respectively.

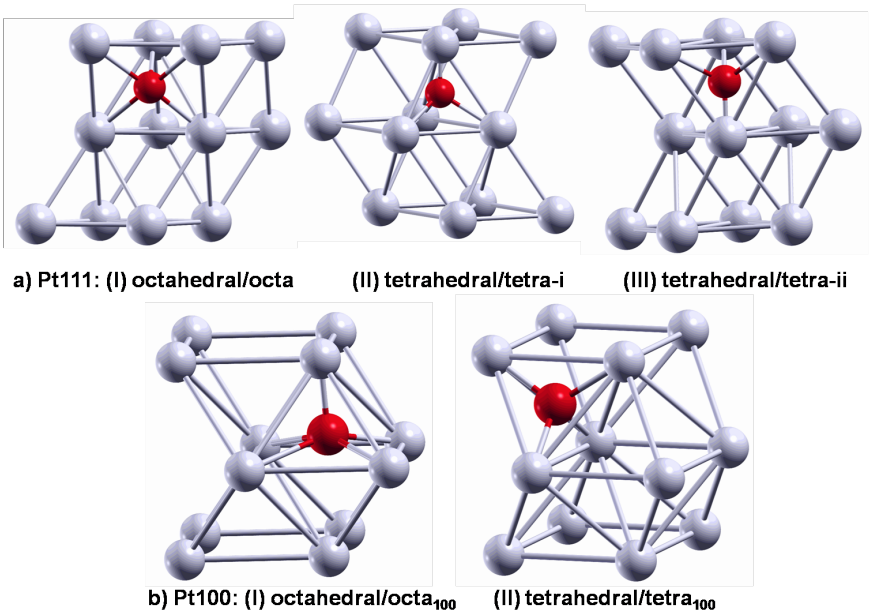

Figure 3.4: Sub-surface absorption sites on Pt (111) and Pt (100). Red represent oxygen and light blue represent Pt.

Figure 3.5 shows the binding energies of oxygen absorption at each sub-surface site for both surfaces. For both surfaces, the incorporation of oxygen into the sub-surface region is very unstable compared to the on-surface adsorption. On the (111) surface and at the oxygen coverage between 0.25 ML and 0.50 ML, oxygen prefers to absorb at the tetrahedral (tetra-ii) site where oxygen is located underneath the hcp site. This is in agreement with the theoretical calculations performed by Gu *et al.* on Pt(111) surface.[8] Above 0.50 ML, the favoured absorption site switches to the tetra-i site where oxygen is positioned underneath the top site. As for the (100) surface, the tetrahedral ($tetra_{100}$) site with oxygen located beneath the bridge site is the favoured absorption site at all considered oxygen coverage. The octahedral site ($octa_{100}$) is very unstable with a binding energy difference of about 2.0 eV at the 0.25 ML oxygen coverage.

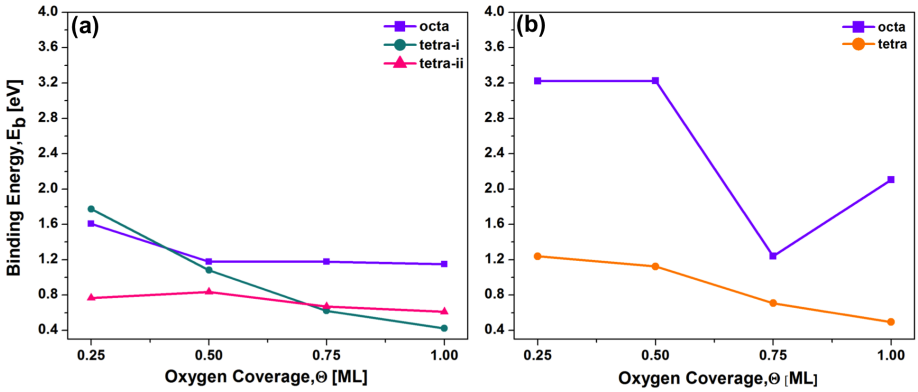

Figure 3.5: Binding energies for the sub-surface oxygen absorption on (a) Pt (111) and (b) Pt (100) at various oxygen coverages.

As the sub-surface oxygen coverage increases, the sub-surface incorporation becomes more favoured, indicating that there is attraction between the oxygen atoms which stabilise the sub-surface structures.[65] At 0.25 ML sub-surface oxygen coverage for all the studied sub-surface sites, the binding energy is significantly lower compared to the on-surface adsorption. This is because additional energy is required to distort the lattice.[32] Figure 3.6 shows the converged structures and the interlayer spacings of the sub-surface oxygen at 0.25 ML and 1.00 ML on the (111) and (100) surfaces. It can be seen that as the sub-surface oxygen coverage increases, the δ_{12} increases from 14 to 52 % and from 13 to 58 % on the (111) and (100) surface respectively. In addition, there is a small contraction of the δ_{23} on the two surfaces. This further illustrates the large expansion between the top two Pt layers as the sub-surface oxygen increases so as to accommodate the increasing number of sub-surface oxygen atoms.

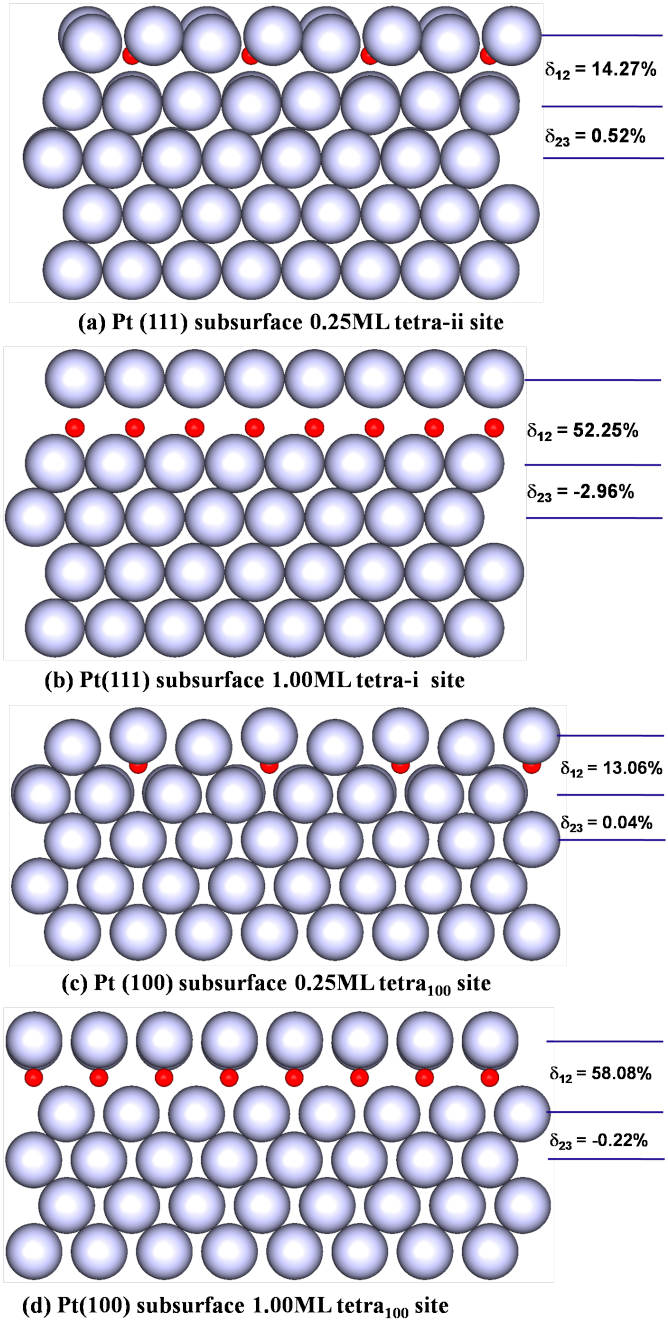

Figure 3.6: Converged sub-surface structures at (a) 0.25ML and (b) 1.00ML on Pt(111) and (c) 0.25ML and (d) 1.00ML on Pt(100) surfaces. Red represent oxygen and light blue represent Pt.

3.3.5 Interaction of Oxygen with the On/sub-surface Phases

To understand the initial formation of surface oxides, it is important to examine the interaction between the on-surface and sub-surface oxygens. This can be done by studying the combined interaction of the on-surface and sub-surface oxygen. There is a vast number of possible structural combinations that can be examined on the two surfaces. Here, the configurations considered on the (111) surface are: (*i*) fcc/tetra-i; (*ii*) fcc/tetra-ii; (*iii*) fcc/octa; (*iv*) hcp/tetra-i; (*v*) hcp/tetra-ii and (*vi*) hcp/octa while on the (100) surface are: (*i*) bridge/tetra; (*ii*) bridge/octa; (*iii*) hollow/tetra and (*iv*) hollow/octa. A total oxygen coverage, θ_{tot} of 2.00 ML was considered. The formation of a thin surface oxide will appear when the on/sub-surface phases become energetically more stable than having pure on-surface or sub-surface structures at the same total oxygen coverage θ_{tot}.

The configuration where the sub-surface oxygen is located directly below an on-surface oxygen is significantly less stable than other structures. These configurations are fcc/octa and hcp/tetra-ii on the (111) surface and bridge/tetra on the (100) surface. The reason these configurations are unstable is due to the strong repulsion between the electronegative oxygen atoms located on the top and directly below the Pt atom.[63] Also, the structures in which the oxygen atoms are located further away from each other are found to be more stable because the electrostatic repulsion between the oxygens are reduced.

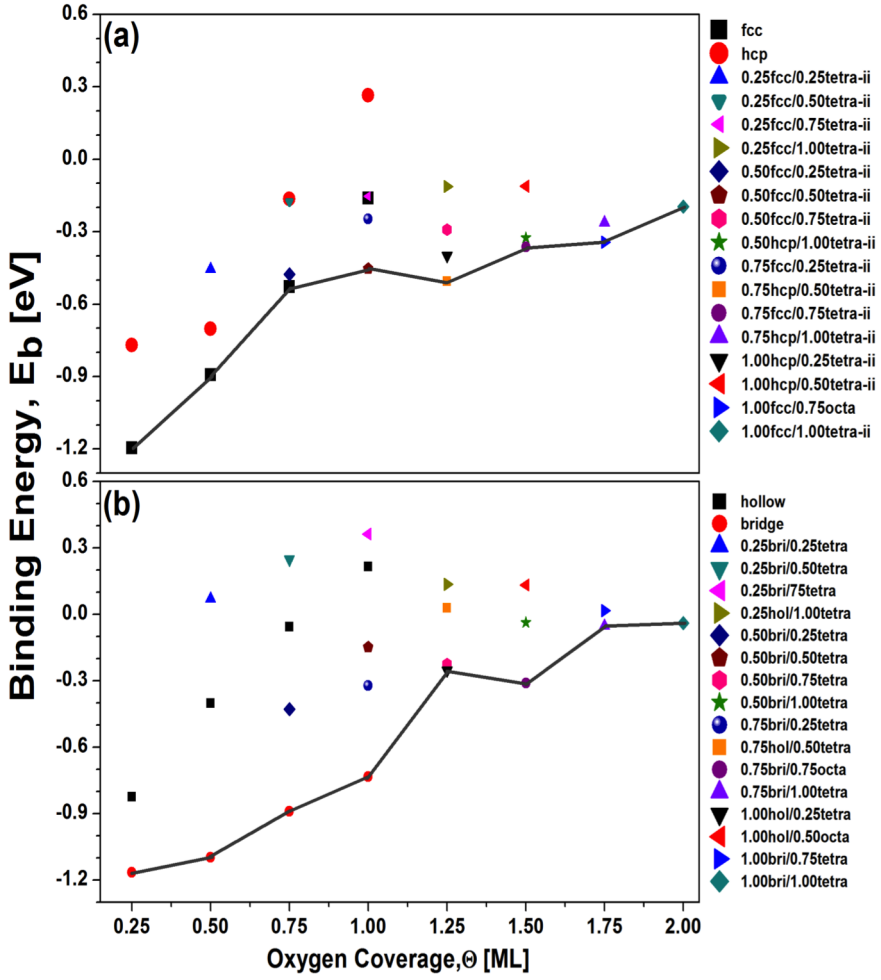

Figure 3.7: The binding energies for the on/sub-surface phases on (a) Pt (111) and (b) Pt (100) surfaces at various oxygen coverages. Solid black lines highlight the most stable on/sub-surface structures at each oxygen coverage.

Within the limits of the on/sub-surface phases considered, the main geometries that were found to be stable between the θ_{tot} of 0.50 ML and 2.00 ML are the fcc/tetra-ii and bridge/tetra structures on the (111) and (100) surface respectively. Figure 3.7 shows the binding energies of the most stable on/sub-surface phases along with the on-surface adsorption on both surfaces.

On the (111) surface and at the θ_{tot} of 0.25 and 0.5 ML, the on-surface fcc site is still the most stable geometry. As θ_{tot} increases to 0.75 ML, the fcc site is also favourable but the difference in binding energies between the (0.75 O_{fcc}) and (0.50 O_{fcc} + 0.25 $O_{\mathrm{tetra-ii}}$) is only 0.05 eV. This means that there is a possible coexistence of the (fcc/-) and (fcc/tetra-ii) structures at 0.75 ML, suggesting that the formation of surface oxide film will begin at this oxygen coverage. Above 0.75 ML, the on/sub-surface configurations are energetically favourable (as shown in Figure 3.7 (top)). At 1.00 ML and 1.25 ML, the preferred geometries are (0.50 O_{fcc} + 0.50 $O_{\mathrm{tetra-ii}}$) and (0.75 O_{hcp} + 0.50 $O_{\mathrm{tetra-ii}}$) respectively. It is interesting to notice that at 1.00 ML, the binding energy difference between the (1.00 O_{fcc}) and (0.50 O_{fcc} + 0.50 $O_{\mathrm{tetra-ii}}$) structure is quite large, being 0.29 eV. Furthermore, the binding energy at 1.25 ML is much lower when compared to 0.75 ML and 1.00 ML oxygen coverage. This further suggests that a coexistence of on/sub-surface phases will begin to form at 0.75 ML and then a phase transition from on-surface adsorption to the reconstructed surface oxide-like structure from 1.00 ML. These results are in agreement with DFT calculations performed by Hawkins *et al.* who found that the crossover between surface and sub-surface configurations occurs at a coverage above 0.75 ML.[64] In addition to the DFT calculation, experimental studies using TPD, XPS, EELS and LEED observed a coexistence of ordered and disordered domains for oxygen coverages from about 0.40 to 0.75 ML.[13] In the same experimental study performed by Weaver *et al.* Pt surface oxides were observed and significant disruption of the surface layers was detected above 0.75 ML.[13]

For the θ_{tot} between 1.50 ML and 2.00 ML, the on/sub-surface configurations are stable as the binding energies are exothermic. This indicates that a surface oxide-like structure will continue to grow on the surfaces as the oxygen coverage increases. In addition, it is observed that the binding energies at these total oxygen coverages are more stable compared to the full monolayer (1.00 O_{fcc}) on-surface structure.

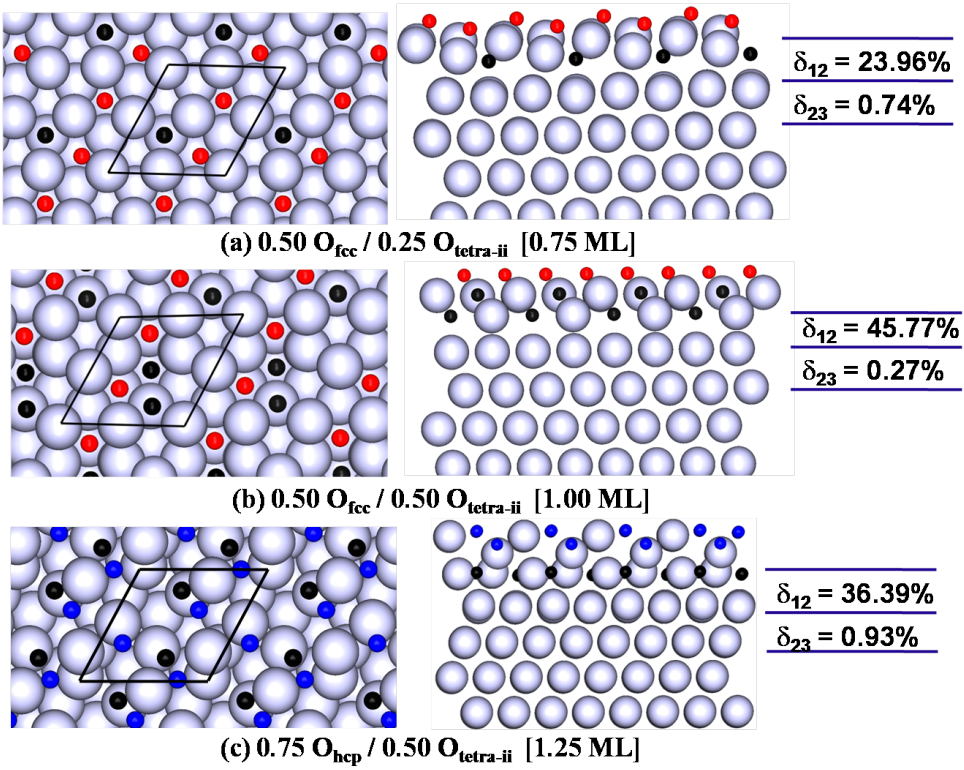

Figure 3.8: Top and side views of the most stable oxygen on/sub-surface configurations calculated using a (2x2) surface unit cell on the Pt(111) surface at the θ_{tot} of (a) 0.75 ML, (b) 1.00 ML and (c) 1.25 ML. The average change in interlayer spacing, (%), δ_{12}, between the first and second layer and δ_{23}, between the second and third layer, with respect to the bulk Pt interlayer distance is given to the right of the figures. The large sky blue sphere represents Pt atoms, the small red and blue spheres represent on-surface O atoms at the fcc and hcp sites and the small black sphere represents the sub-surface O atoms at the tetra-ii site.

Table 3.4: The calculated (average) bond lengths (Å) for the most stable on/sub-surface configurations on the Pt(111) surface at the θ_{tot} of 0.75 ML, 1.00 ML and 1.25 ML. $d_{\mathrm{O_{onsurf}-Pt_1}}$ (Å) is the distance between the on-surface oxygen and the nearest-neighbour first layer Pt atom, $d_{\mathrm{Pt_1-O_{sub}}}$ (Å) is the distance between the nearest-neighbour first layer Pt atom and sub-surface oxygen, $d_{\mathrm{O_{sub}-Pt_2}}$ (Å) is the distance between the sub-surface oxygen and the nearest-neighbour second layer Pt atom and $d_{\mathrm{Pt_1-Pt_2}}$ (Å) is the distance between the top two Pt atoms layers

	0.75 ML	1.00 ML	1.25 ML
$d_{\mathrm{O_{onsurf}-Pt_1}}$	2.04	2.01	2.01
$d_{\mathrm{Pt_1-O_{sub}}}$	2.03	2.06	2.96
$d_{\mathrm{O_{sub}-Pt_2}}$	2.04	2.15	2.04
$d_{\mathrm{Pt_1-Pt_2}}$	3.27	3.75	3.43

Next, the geometric structures of the stable on/sub-surface phases are analysed in more detail. The most stable configurations and the structural details for the θ_{tot} at 0.75, 1.00 and 1.25 ML are displayed in Figure 3.8 and Table 3.4. The stable structures at these θ_{tot} are: (*i*) (0.50 $\mathrm{O_{fcc}}$ + 0.25 $\mathrm{O_{tetra-ii}}$); (*ii*) (0.50 $\mathrm{O_{fcc}}$ + 0.50 $\mathrm{O_{tetra-ii}}$) and (*iii*) (0.75 $\mathrm{O_{hcp}}$ + 0.50 $\mathrm{O_{tetra-ii}}$). From all these geometric structures, a significant amount of Pt buckling was observed in the first layer of the surface. This Pt buckling is more pronounced on the (0.50 $\mathrm{O_{fcc}}$ + 0.50 $\mathrm{O_{tetra-ii}}$) phase. The average positions of the top two Pt layers are used to calculate the interlayer spacings, δ_{12} and δ_{23}. It can be seen that the first interlayer spacing, δ_{12}, for (0.50 $\mathrm{O_{fcc}}$ + 0.25 $\mathrm{O_{tetra-ii}}$) and (0.50 $\mathrm{O_{fcc}}$ + 0.50 $\mathrm{O_{tetra-ii}}$) doubles from 24 to 46 % as the θ_{tot} increases while the (0.75 $\mathrm{O_{hcp}}$ + 0.50 $\mathrm{O_{tetra-ii}}$) configuration decreases back to 36 % (Figures 3.8). As for the bond lengths, the Pt-O bond lengths for the on-surface and sub-surface oxygens are around 2 Å for all three structures while the Pt-Pt bond lengths for the top two Pt layers are above 3 Å.

Proceeding onto the (100) surface, the on-surface bridge site is still the energetically favoured site at the θ_{tot} of 0.25 ML up until 1.00 ML (Figure 3.7b). Above 1.00 ML, the binding energies for the on/sub-surface phases are considerably lower compared to the pure on-surface adsorption. With the lower binding energies observed, it is predicted that the surface oxide will be difficult to form on

the surface. At 1.25 ML and 1.50 ML, the binding energies are slightly exothermic and the geometric structures are illustrated in Figure 3.9. The stable structures are (1.00 O_{hollow} + 0.25 O_{tetra}) and (0.75 O_{bridge} + 0.75 O_{octa}). From the (1.00 O_{hollow} + 0.25 O_{tetra}) structure (Figure 3.9a), it can be seen that the top Pt layer splits into two layers. This is illustrated as Pt_{1_a} and Pt_{1_b} and a large interlayer spacing of 16.4 % between this split layer is observed. As for the (0.75 O_{bridge} + 0.75 O_{octa}) structure (Figure 3.9b), there is a significant gap between the top Pt layers, with an expansion of 60 % for the δ_{12}. Table 3.5 illustrates the bond lengths of the stable geometric structures. On the two structures, the Pt-O bond lengths for the on-surface oxygens are shorter than the sub-surface oxygens. Furthermore, the Pt-Pt bond length for the split Pt layers on (1.00 O_{hollow} + 0.25 O_{tetra}) is shorter than the two Pt layers on the (0.75 O_{bridge} + 0.75 O_{octa}).

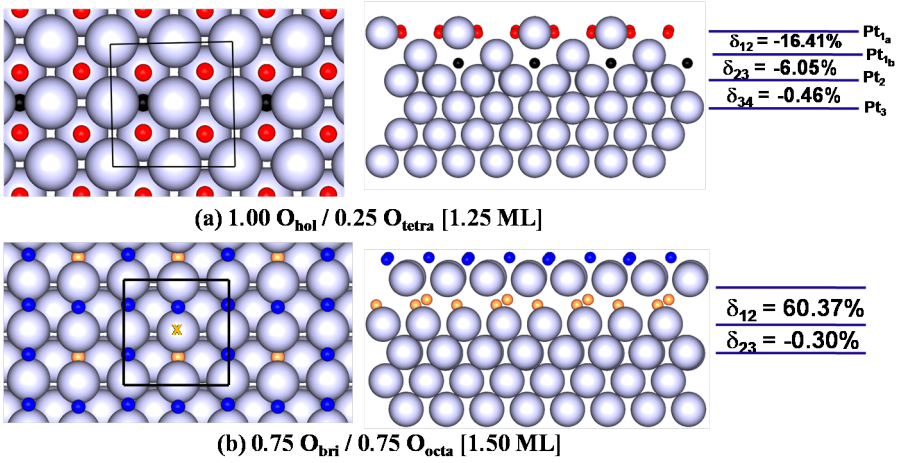

Figure 3.9: Top and side views of the most stable oxygen on/sub-surface configurations calculated using a (2x2) surface unit cell on the Pt(100) surface at the θ_{tot} of (a) 1.25 ML and (b) 1.50 ML. The average change in interlayer spacing, (%), δ_{12}, between the first and second layer and δ_{23}, between the second and third layer, with respect to the bulk Pt interlayer distance is given to the right of the figures. The large sky blue sphere represent Pt atoms, the small red and blue spheres represent on-surface O atoms at the hollow and bridge sites and the small black and orange spheres represent the sub-surface O atoms at the tetra and octa.

Table 3.5: The calculated (average) bond lengths (Å) for the most stable on/sub-surface configurations on Pt(100) surface. $d_{\mathrm{O_{onsurf}-Pt_1}}$ (Å), $d_{\mathrm{O_{onsurf}-Pt_{1_a}}}$ (Å) and $d_{\mathrm{O_{onsurf}-Pt_{1_b}}}$ (Å) are the distances between the on-surface oxygens and the nearest-neighbour first layer platinum atoms or split platinum atoms; $d_{\mathrm{Pt_1-O_{sub}}}$ (Å), $d_{\mathrm{Pt_{1_a}-O_{sub}}}$ (Å) and $d_{\mathrm{Pt_{1_b}-O_{sub}}}$ (Å) are the distances between the nearest-neighbour first layer platinum atom or split platinum atoms and sub-surface oxygen; $d_{\mathrm{O_{sub}-Pt_2}}$ (Å) is the distance between the sub-surface oxygen and the nearest-neighbour second layer platinum atom; $d_{\mathrm{Pt_{1_a}-Pt_{1_b}}}$ (Å) and $d_{\mathrm{Pt_{1_b}-Pt_2}}$ (Å) are the distances between the split top platinum layer and $d_{\mathrm{Pt_1-Pt_2}}$ (Å) is the distance between the top two platinum atoms layers.

	1.25 ML	1.50 ML
$d_{\mathrm{O_{onsurf}-Pt_1}}$	-	1.95
$d_{\mathrm{O_{onsurf}-Pt_{1_a}}}$	1.99	-
$d_{\mathrm{O_{onsurf}-Pt_{1_b}}}$	2.65	-
$d_{\mathrm{Pt_1-O_{sub}}}$	-	2.67
$d_{\mathrm{Pt_{1_a}-O_{sub}}}$	2.65	-
$d_{\mathrm{Pt_{1_b}-O_{sub}}}$	3.22	-
$d_{\mathrm{O_{sub}-Pt_2}}$	1.95	2.09
$d_{\mathrm{Pt_{1_a}-Pt_{1_b}}}$	3.27	-
$d_{\mathrm{Pt_{1_b}-Pt_2}}$	2.73	-
$d_{\mathrm{Pt_1-Pt_2}}$	-	3.89

From the results discussed above, it can be concluded that a threshold oxygen adsorption coverage, θ_{c}, is required before oxygen starts penetrating sub-surface to form a thin surface oxide-like structure. This θ_{c} within the (2x2) surface unit cell structures considered is 0.75 ML on the (111) surface and above 1.00 ML on the (100) surface. A larger surface unit cell will be required to accurately determine the θ_{c}. Nevertheless, the θ_{c} is compared to other late transition metals calculated on the (111) surface. The θ_{c} for Ru, Rh, Pd, Ag and Ir are 0.89, 0.59, 0.50, 0.24 and 1.5 ML respectively.[31,32] This result suggests that it will be difficult for surface oxide to form on the (100) surface because of the high binding energies observed. There is no available information from literature to confirm the formation of surface oxide on the (100) surface.

When oxygen interacts with the two surfaces, the (100) surface is more reactive than the (111) surface. In addition, the fact that thin surface oxide-like structure can form on the (111) surface suggests that a gradual poisoning of the catalyst may occur. This will eventually lead to a degradation of the catalyst, hence a decreased power output.

The next section discusses the thermodynamically stable structures that may be observed on the catalyst surfaces during a PEMFC operation.

3.4 Statistical Thermodynamic Model

The effect of temperature and pressure on the (111) and (100) surfaces are investigated using a statistical thermodynamic model on the stability of the various oxygen coverage structures. The statistical thermodynamic model discussed in Section 2.4 is implemented to calculate the surface free energies. This generates the (T, p) phase diagram that describes the most stable phase from low pressure right up to real catalysis conditions. The surface free energies are calculated for the most stable adsorption energies for oxygen coverages from $\theta_{\mathrm{tot}}(0.25 \leq \theta_{\mathrm{tot}} \leq 2.00\mathrm{ML})$ over a temperature range from 100 K to 1000 K and a pressure range from 10^{-5} atm to 10^{5} atm. Figure 3.10 shows the (T, p) phase diagram of the (111) and (100) surfaces.

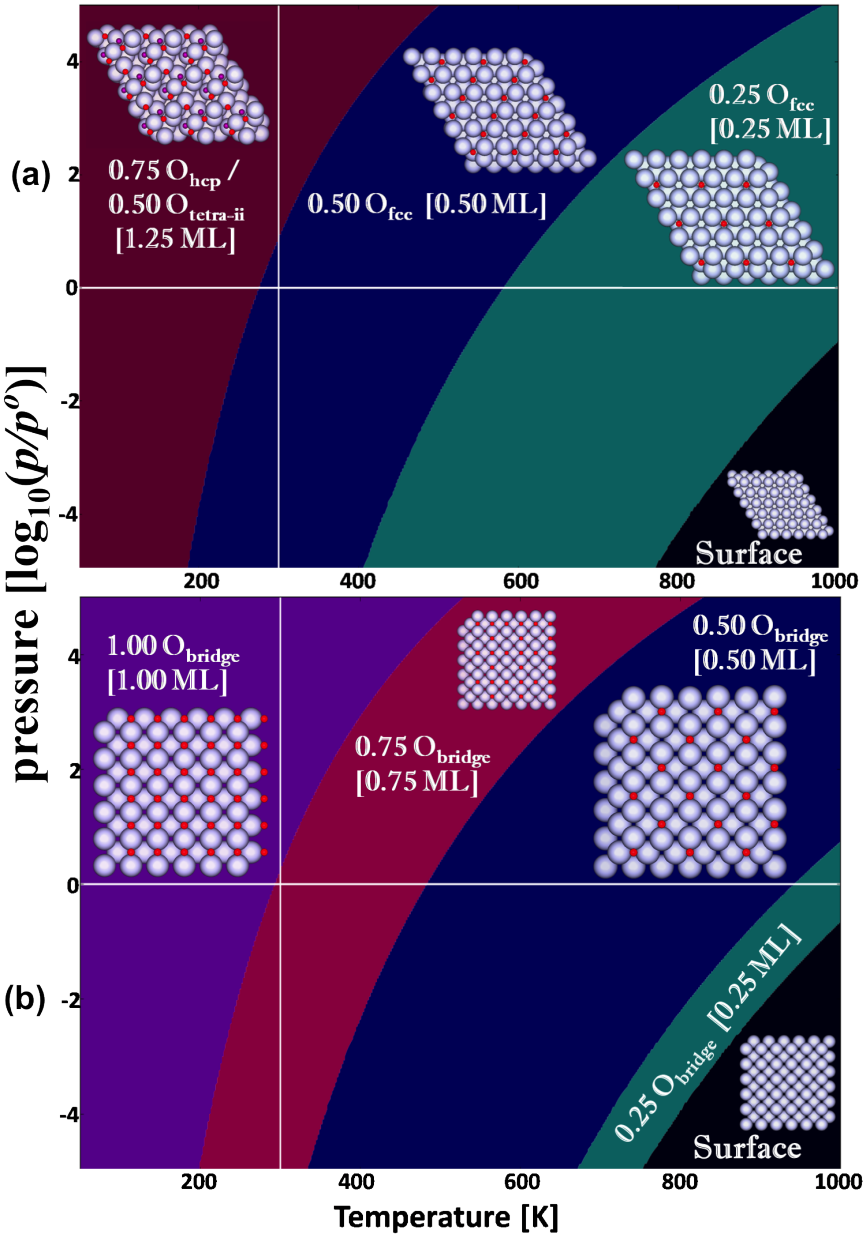

Figure 3.10: Phase diagram of (a) Pt(111) and (b) Pt(100) surfaces in equilibrium with O_2 gas phase. PEMFC operating conditions are labelled as 1 atm (horizontal white line) and 300 K (vertical white line).

Table 3.6: The temperatures (K) at which the oxygen coverage changes phase from the (T, p) thermodynamic phase diagram on the Pt(111) and Pt(100) surfaces at low pressure (10^{-5} atm), real catalytic condition (1 atm) and high pressure (10^{5} atm).

		pressure [atm]		
	phase change [ML]	10^{-5}	1	10^{5}
		Temperature [K]		
Pt (111)	1.25 → 0.50	184	274	500
	0.50 → 0.25	404	580	982
	0.25 → surface	766	> 1000	> 1000
Pt (100)	1.00 → 0.75	198	292	528
	0.75 → 0.50	334	482	830
	0.50 → 0.25	670	942	> 1000
	0.25 → surface	752	>1000	-

Three different oxygen coverage structures were identified on the (111) surface while there were four identified structures on the (100) surface. The thermodynamically stable structures on the (111) surface are: (*i*) 1.25 ML on/sub-surface configuration (0.75 O_{hcp} + 0.50 $O_{tetra-ii}$); (*ii*) on-surface fcc adsorption 0.50 ML and (*iii*) on-surface fcc adsorption 0.25 ML. Table 3.6 summarises the temperatures at which the oxygen coverage changes phase on the (111) and (100) surfaces at low, real catalytic condition and high pressures. On the (111) surface and at low pressure (10^{-5} atm), oxygen desorbs off the surface at 766 K. The experimental oxygen desorption temperature was determined by Gland *et al.* to be 700 K.[11] In addition, both the experimental and theoretical calculations have observed a p(2x2) structure of 0.25 ML oxygen coverage at 670 K and a high density p(2x1) structure of 0.50 ML at 480 K.[3,23,24,66] This is in agreement with the current theoretical results which also identified the (2x1) and (2x2) structures as the most stable at 0.50 ML and 0.25 ML respectively. Experimental UHV and TPD studies showed that at 300 K and 1.2 ML, the disordering of the Pt surface occurs, caused by either the sub-surface oxygen or the nucleation of platinum oxide particles.[67] These experimental results are similar to present study, which identified

the on/sub-surface structure $(0.75\mathrm{O_{fcc}} + 0.50\mathrm{O_{tetra-ii}})$ but at a reduced desorption temperature of 184 K. Furthermore, the on/sub-surface structure also showed a disordering of the surface atoms. At the operating pressure of a realistic catalyst, 1 atm (as indicated by the thick horizontal white line), 0.25 ML is the lowest oxygen coverage observed on the (111) surface and desorbs off the surface above 1000 K. It is evident that 0.50 ML will be observed on the surface at the operating temperature of a realistic catalyst at 300 K (as indicated by the thick vertical white line).

As for the (100) surface, all the on-surface bridge adsorption sites (from 0.25 ML to 1.00 ML oxygen coverage) were the thermodynamically most stable structures. At the low pressure (10^{-5}) atm, oxygen desorbs from the (100) surface at 752 K. The UHV experiment performed by Weaver *et al.* indicated a 0.63 ML oxygen coverage at 573 K with a LEED pattern of disordered (3x1) domains.[16] This oxygen coverage cannot be modelled on the current (2x2) surface and therefore, a (3x1) surface is required to address this experimental observation. Even though oxide growth has been reported on the (111) surface,[13,67] none has been detected on the (100) surface. This suggests that the observed on-surface oxygen adsorptions are most likely to be formed on the surface. At the operating pressure of a realistic catalyst, 1 atm (as indicated by the thick horizontal white line), all the on-surface oxygen adsorption coverages, 1.00 ML, 0.75 ML, 0.50 ML and 0.25 ML are observed on the surface while at the operating temperature of the realistic catalyst at 300 K (as indicated by the thick vertical black line), only 0.75 ML will be detected.

3.4.0.1 Free Energy as a Function of Potential

As discussed in Section 2.4.1, the free energy as a function of potential is obtained for the PEMFC operating conditions of 300 K and 1 atm. The thermodynamically stable structures identified above for the (111) and (100) surfaces are analysed using Eqs. 2.35 and 2.36, to determine the most likely structures that would be

observed on the catalyst surface when potential (between 0.00 V and 1.50 V) is applied to the statistical thermodynamic model. Figure 3.11 displays the free energy as a function of potential for the (111) and (100) surfaces.

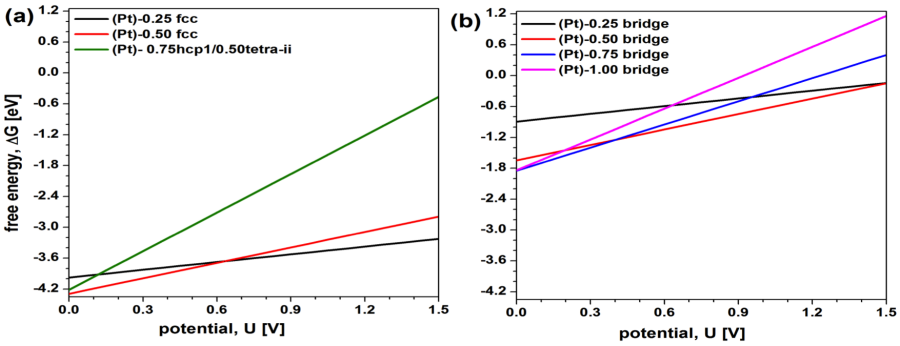

Figure 3.11: Free energy as a function of potential for the thermodynamically stable structures on (a) Pt(111) and (b) Pt (100) surfaces.

In general, as the potential is increased, the free energies observed on the (111) surface is considerably more stable than the (100) surface. Furthermore, the surface composition changes on the two surfaces as the potential is increased. The structures predicted on the (111) surface are 0.50 ML at low applied potential and 0.25 ML at high applied potential, with the oxygen coverage switching at 0.63 V. As for the (100) surface, 0.75 ML and 0.50 ML oxygen coverages are expected at low and high applied potentials respectively, with the oxygen coverage changing at 0.40 V. At low applied potentials, the structures observed are the same as those predicted in the above statistical thermodynamic model at 300 K and 1 atm (Figure 3.10). These results suggest that pure on-surface adsorptions will be expected on the two surfaces regardless of the applied potential.

3.5 Electronic Properties

3.5.1 Change in Work function, Dipole Moment and *d*-band Centre

The work function change, $\Delta\Phi$, (defined in Eq. 2.27), surface dipole moment, μ, (Eq. 2.28), and the average d-band centre, ε_d, of the first Pt layer (described in section 2.3.6) are analysed with respect to oxygen coverage on the Pt(111) and Pt(100) surfaces. In addition, the plot between the average d-band centre, ε_d, of the first layer and the binding energies are shown for the studied oxygen coverages. These results are illustrated in Figure 3.12. The pure on-surface adsorption of oxygen at the fcc and bridge site on the Pt(111) and Pt(100) surfaces respectively are compared to the on/sub-surface configurations for the identified stable structures at the $\theta_{\mathrm{tot}}(0.25 \leq \theta_{\mathrm{tot}} \leq 2.00\mathrm{ML})$.

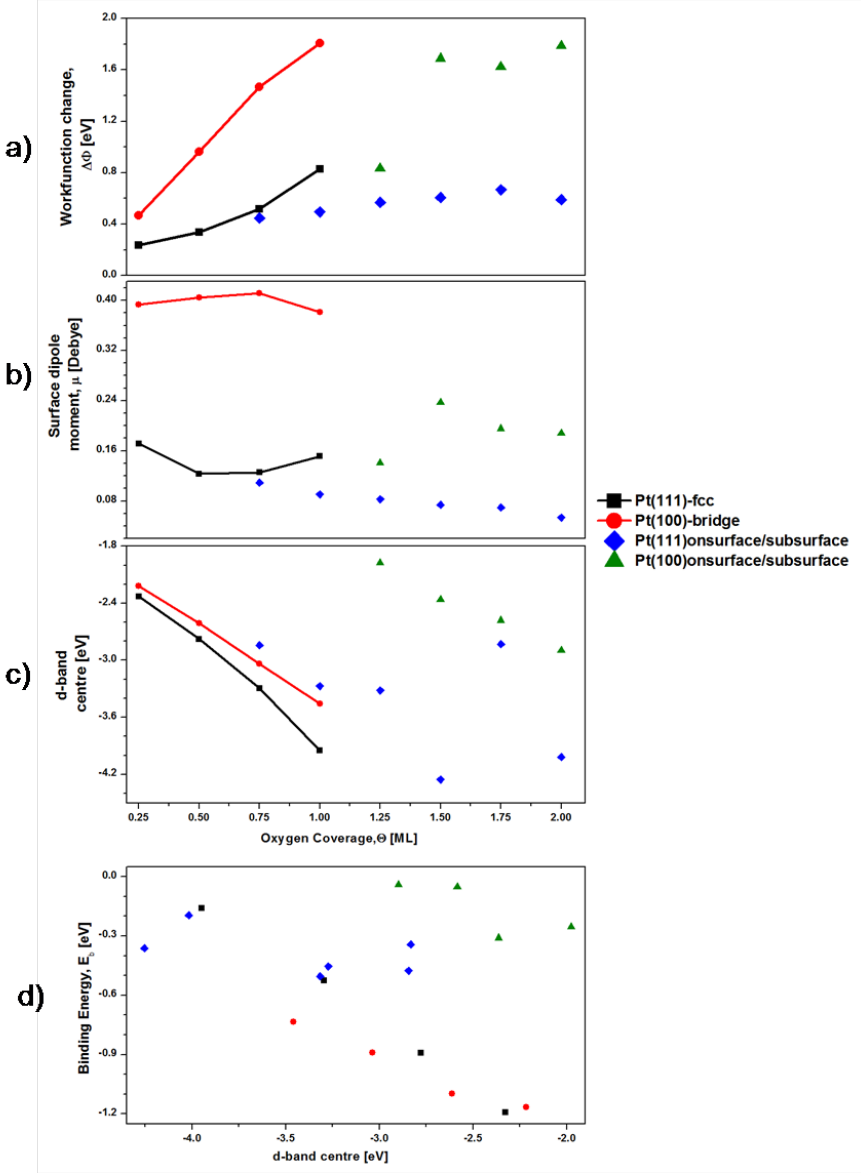

Figure 3.12: Electronic properties of Pt(111) and Pt(100) surfaces where a) change in the calculated work-function, $\Delta\Phi$, b) surface dipole moment, μ, c) average d-band centre of the top Pt layer as a function of oxygen coverage for the most stable structures and d) the average d-band centre, ε_d, of the top Pt layer plotted as a function of the binding energies at the studied oxygen coverages.

Figure 3.12a shows that on the Pt(111) and Pt(100) surfaces, the workfunction, $\Delta\Phi$, changes as the oxygen coverage increases up to 1.00 ML for the on-surface adsorption. This change is considerably larger on the Pt(100) surface compared to the Pt(111) surface. This general increase in work function change is mainly due to the electronegativity difference between Pt (2.28) and oxygen (3.44) which causes large charge transfer from the top-layer Pt atoms to the oxygen, resulting in a large inward pointing surface dipole moment (that is the oxygen negative charge at the vacuum side of the surface).[57,68,69] On the Pt(111) surface and at 0.75 ML and 1.00 ML, the workfunction changes are lower for the on/sub-surface structures compared to the on-surface adsorption at the same oxygen coverage. Above 1.00 ML oxygen coverage, the workfunction change for the Pt(111) on/sub-surface configurations is much lower than that of the Pt(100) on/sub-surface configurations. In addition, on the Pt(111) surface, a saturation value of 1.25 ML oxygen coverage is reached, which includes the on/sub-surface configurations. The lower workfunction change observed for the on/sub-surface configurations occurs because there is competition for the bonding charge of the top-layer Pt atoms that arise between the sub-surface and on-surface oxygen atoms, thereby making the on-surface oxygen less negatively charged.[70] Overall, the Pt(100) surface induces more charge transfer compared to the Pt(111) surface.

The surface dipole moment, μ, for the on-surface adsorption, on the two surfaces are different (Figure 3.12b). On the Pt(111) surface, μ decreases between 0.25 ML and 0.50 ML and then increases from 0.75 ML while on the Pt(100) surface, there is an increase between 0.25 ML and 0.50 ML and then a reduction from 0.75 ML. The observed μ is in agreement with those calculated by Pang *et al.*[71] With regards to the on/sub-surface configurations, there is a continuous decrease of the μ on the two surfaces as the oxygen coverage increases. The μ for Pt(100) surface is much higher than that of the Pt(111) surface. The decrease in the surface dipole moment is consistent with strong depolarisation that arises from the partial charge transfer of the oxygen atoms back on to the top-layer Pt atoms so as to reduce the repulsive dipole-dipole interactions between the oxygen atoms.[72]

Figure 3.12c shows that for the on-surface adsorption on the Pt(111) and Pt(100) surfaces, the average d-band centre of the top Pt layer becomes more negative as the oxygen coverage increases. In addition, the average d-band centre correlates with the adsorption energy which shows that the more negative the d-band centre, the weaker the adsorption energy (Figure 3.12d). This is in agreement with the DFT calculation performed on Pd(111).[73] The d-band centre for the Pt(100) surface at the bridge site is higher than the Pt(111) surface at the fcc site, suggesting that Pt(111) surface will bind oxygen more weakly at the fcc site. This is consistent with the work-function change and surface dipole observations. The d-band centre for the on/sub-configurations on the Pt(100) surface are reduced with oxygen coverage while on the Pt(111) surface, there is no correlation with oxygen coverage.

3.5.2 Electron density difference and Bader Analysis

To understand the bonding mechanism that occurs within the on-surface chemisorption and on/sub-surface configurations, the electron density differences, Bader charges and projected density of states (PDOS) are analysed on the Pt(111) and Pt(100) surfaces. The structures examined for the electron density differences on the Pt(111) surface are: (*i*) on-surface adsorption at 0.25 ML; (*ii*) on-surface adsorption at 1.00 ML and (*iii*) on/sub-surface structure, (0.75 O_{hcp} + 0.50 $O_{tetra-ii}$) and on the Pt(100) surface are: (*i*) on-surface adsorption at 0.25 ML and on-surface adsorption at 1.00 ML structures. The reason for choosing these configurations is because they are the thermodynamically stable structures. The Pt(111)-1.00 ML geometry is included for comparison with the Pt(100) counterpart.

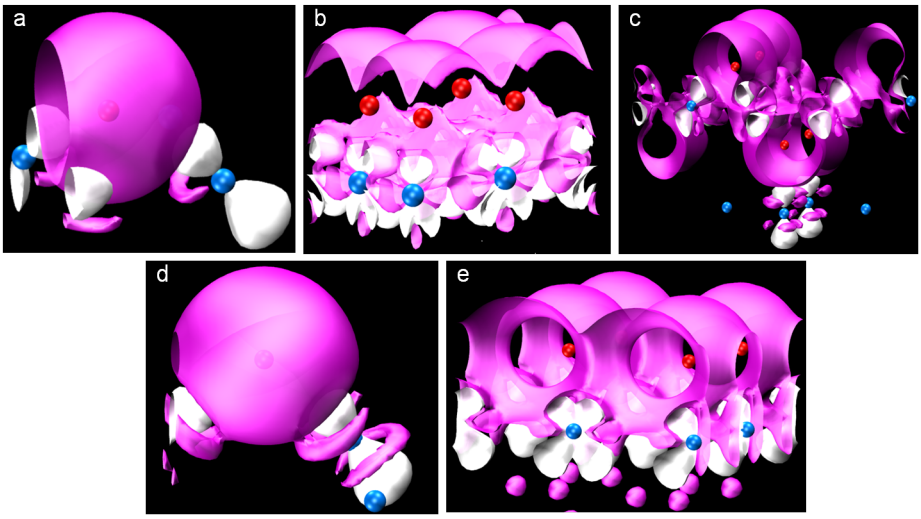

Figure 3.13: Calculated electron density differences for Pt(111) surface at a) 0.25 ML b)1.00 ML c) (0.75 O_{hcp} + 0.50 $O_{tetra-ii}$) and Pt(100) surface at d) 0.25 ML and e) 1.00 ML oxygen coverages. The pink and white isosurfaces represent positive and negative electron density differences respectively. The blue and red spheres are Pt and O atoms respectively and the isospheres value is $\pm 0.045\ e\text{Å}^{-3}$.

The electron density difference (Eq. 2.29) is the induced redistribution of the oxygen electron density that originates from the oxygen dipole moment. From Figure 3.13, it can be seen that in all cases, there is a large increase in the electron charge density on the oxygen atoms which has been transferred from the Pt atoms (showing a depletion of electron charge density). This reflects the accumulation of charge on the oxygens and the depletion of charge from the Pt 5d-orbitals. On Pt(111) and Pt(100) on-surface adsorption (0.25 ML and 1.00 ML oxygen coverage), the oxygens interact mainly with the top-layer Pt atoms and the electron density accumulates in the vacuum. At the 1.00 ML oxygen coverage, there is build-up of the electron density because each oxygen atom is coordinated to three Pt atoms. This increased electron density causes the low binding energy observed compared to the 0.25 ML oxygen coverage. On the Pt(100) surface, the observed electron charge density around the oxygen atoms, especially the on-surface 1.00 ML oxygen coverage, may be the major reason for the increased workfunction as the oxygen coverage increases.[68] Similar to the on-surface chemisorption, the on/sub-surface configuration, (0.75 O_{hcp} + 0.50 $O_{tetra-ii}$) (Figure 3.13c) has a

reduced electron density charge at the top-layer Pt atoms while the second-layer Pt atoms that are bonded to the O atoms have an enhanced electron charge density on the O atoms.

Table 3.7: Average Bader charges (e) for the top two Pt layers on the Pt(111) and Pt(100) surfaces. The average Bader charges for the on-surface oxygen layer, (O_{onsurf}) and the sub-surface oxygen layer ($O_{subsurf}$) layer are also included. The nominal valence charges for Pt and O are 10 and 6 electrons respectively.

		slab	0.25ML	1.00ML	1.25ML
Pt(111)	1^{st} layer	10.04	9.83	9.20	9.90
	2^{nd} layer	9.96	9.99	10.05	9.11
	O_{onsurf}	-	6.74	6.73	6.76
	$O_{subsurf}$	-	-	-	6.85
Pt(100)	Pt_1	10.05	9.85	9.28	
	Pt_2	9.97	9.98	10.06	
	O_{onsurf}	-	6.75	6.67	
	$O_{subsurf}$	-	-	-	

Table 3.7 illustrate the Bader charges of the top two layers on the Pt(111) and Pt(100) surfaces. On the two surfaces, the slabs show a small increase and decrease of charges between the first and second Pt layers respectively. This suggests that there are charge transfers between the Pt layers and the second Pt layer is donating charge to the first Pt layer. Moving on to the adsorbed oxygens at 0.25 ML and 1.00 ML on the two surfaces, there are charge transfer from the first Pt layer onto the oxygen atoms, causing a depletion of electrons on that Pt layer. As for the on/sub-surface configuration (1.25 ML), the increased charge transfer observed on the oxygen atoms are mostly being donated from the second Pt layer.

Figure 3.14 shows the PDOS plots (discussed in Section 2.3.5) for the clean Pt surfaces, the gas phase oxygen atom and the 0.25 ML oxygen coverage at the

fcc site on the Pt(111) surface and at the bridge site on Pt(100) surface. The interacting and non-interacting plots are the PDOS for the top Pt layer which is interacting and not interacting respectively with the O atom. The Pt-O/O plot illustrates the PDOS of the O atom interacting with the two surfaces. Finally, the gas phase O is showing the energy levels of the gas phase O atom and the Fermi level, ε_{F}, is determined by taking the experimental first ionisation energy of O atom from the highest occupied molecular orbital (HOMO).

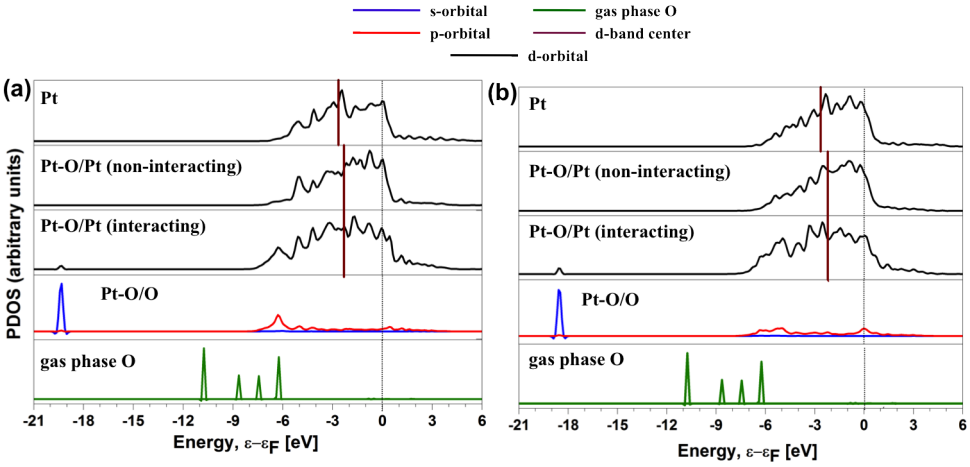

Figure 3.14: Projected density of states (PDOS) for (a) O/Pt(111) and (b) O/Pt(100) systems at 0.25 ML oxygen coverage. The Fermi energy is indicated by the vertical dotted line.

On the Pt(111) and Pt(100) surfaces, the O $2s$ orbital is observed on the PtO/O plot, as shown from the sharp DOS peak around 20 eV below the Fermi level. There is bonding hybridisation between the O $2p$ and the Pt $5d$ orbitals. This bonding hybridisation occurs because the O $2p$ orbital mixes strongly with the Pt $5d$ orbitals, thereby causing the broadening of the O $2p$ orbital (as shown in PtO/O plot). The oxygen energy levels (Pt-O/O) are split into two states, bonding and anti-bonding on both surfaces. The bonding states are located between the energy region of -7.5 eV and -5.5 eV, the lower part of the Pt $5d$ orbitals. The anti-bonding states are positioned just above the Fermi level for the Pt(111) surface and at the Fermi level for Pt(100) surface. On the two surfaces, the average d-band centre for the oxygen covered Pt surfaces is slightly lower than that of the clean Pt.

The PDOS for the Pt-O/O non-interacting is similar to the PDOS of the clean Pt surface. In addition, the average d-band centre for the Pt-O/O non-interacting is lower than the Pt-O/O interacting.

3.6 Conclusions and Implications to PEMFC

A theoretical investigation of interacting Pt surfaces with the oxidising environment was carried out. The study focused on the low index Pt(111) and unreconstructed Pt(100) surfaces using density functional theory and a statistical thermodynamic model. It was observed that for oxygen on-surface adsorption and at oxygen coverages between 0.25 ML and 1.00 ML, the fcc and bridge sites are the most stable adsorption sites for Pt(111) and Pt(100) surfaces respectively. In addition, it was shown that the Pt(100) surface binds oxygen more strongly than the Pt(111) surface except at 0.25ML, where the Pt(111) surface is favoured. The on-surface mixed sites were unfavourable on both Pt(111) and Pt(100) surfaces compared to the stable on-surface adsorption sites. This is because the interactions between the Pt atoms and adsorbed oxygens increase as the oxygen coverage increases. The incorporation of oxygen sub-surface on the two surfaces is endothermic. Furthermore, it was observed that the surface oxide-like structures are more likely to form on the Pt(111) surface and the oxygen coverage required before oxygen starts to penetrate sub-surface is 0.75 ML. As for the Pt(100) surface, lower binding energies were observed for the on-surface chemisorption compared to the on/sub-surface structures, suggesting that oxygen coverage of more than 1.00 ML will be required to form the surface oxide-like structure.

At the PEMFC operating condition (300 K and 1 atm), the statistical thermodynamics model revealed that the most likely structures to be found on the surfaces are 0.50 ML (fcc) on the Pt(111) surface and 0.75 ML (bridge) on the Pt(100) surface. As the temperature increases at 1 atm pressure, oxygen gradually desorbs off each of the surfaces studied. Overall, the Pt(100) surface is less able to form the thin surface-like structures compared to the Pt(111) surface. However,

because the Pt(100) surface binds oxygen more strongly, its suitability as a ORR catalyst will not be feasible. On the other hand, the Pt(111) surface is a better catalyst for the ORR but with prolonged exposure to the oxidising environment at high atmospheric pressure, will cause the catalyst to degrade.

In the next chapter, the stability and structural behaviour of Pt/Ni-monolayer bimetallic alloy surfaces will be investigated theoretically. The alloy compositions on the (111) and (100) surfaces will be explored along with their tendencies of forming surface oxide film in oxidising environment.

References

[1] Feibelman, P. *Physical Review B* **1997**, *56*, 10532–10537.

[2] Lynch, M.; Hu, P. *Surface Science* **2000**, *458*, 1–14.

[3] Tang, H.; Van der Ven, A.; Trout, B. *Physical Review B* **2004**, *70*, 045420.

[4] Feibelman, P. J.; Hafner, J.; Kresse, G. *Physical Review B* **1998**, *58*, 2179–2184.

[5] Eichler, A.; Mittendorfer, F.; Hafner, J. *Physical Review B* **2000**, *62*, 4744–4755.

[6] Jacob, T.; Muller, R. P.; Goddard, W. A. *Journal of Physical Chemistry B* **2003**, *107*, 9465–9476.

[7] Légaré, P. *Surface Science* **2005**, *580*, 137–144.

[8] Gu, Z.; Balbuena, P. *Journal of Physical Chemistry C* **2007**, *111*, 9877–9883.

[9] Moussounda, P. S.; Haroun, M. F.; Legare, P. *Physica Scripta* **2010**, *81*, 045603.

[10] Ford, D. C.; Xu, Y.; Mavrikakis, M. *Surface Science* **2005**, *587*, 159–174.

[11] Gland, J.; Sexton, B.; Fisher, G. *Surface Science* **1980**, *95*, 587–602.

[12] Zambelli, T.; Barth, J. V.; Wintterlin, J.; Ertl, G. *Nature* **1997**, *390*, 495–497.

[13] Weaver, J. F.; Chen, J. J.; Gerrard, A. L. *Surface Science* **2005**, *592*, 83–103.

[14] Devarajan, S. P.; Hinojosa Jr, J. A.; Weaver, J. F. *Surface Science* **2008**, *602*, 3116–3124.

[15] Kim, Y. S.; Bostwick, A.; Rotenberg, E.; Ross, P. N.; Hong, S. C.; Mun, B. S. *Journal of Chemical Physics* **2010**, *133*, 034501.

[16] Weaver, J. F.; Kan, H. H.; Shumbera, R. B. *Journal of Physics-Condensed Matter* **2008**, *20*, 184015.

[17] Norton, P.; Binder, P. E.; Griffiths, K. *Journal of Vacuum Science & Technology A- Vacuum Surfaces and Films* **1984**, *2*, 1028–1031.

[18] McMillan, N.; Lele, T.; Snively, C.; Lauterbach, J. *Catalysis Today* **2005**, *105*, 244–253.

[19] Rotermund, H. H.; Lauterbach, J.; Haas, G. *Applied Physics A-Materials Science & Processing* **1993**, *57*, 507–511.

[20] Shumbera, R. B.; Kan, H. H.; Weaver, J. F. *Surface Science* **2006**, *600*, 2928–2937.

[21] Yeo, Y. Y.; Wartnaby, C. E.; King, D. A. *Science* **1995**, *268*, 1731–1732.

[22] Ge, Q.; Hu, P.; King, D.; Lee, M.; White, J.; Payne, M. *Journal of Chemical Physics* **1997**, *106*, 1210–1215.

[23] Materer, N.; Starke, U.; Barbieri, A.; Doll, R.; Heinz, K.; Vanhove, M. A.; Somorjai, G. A. *Surface Science* **1995**, *325*, 207–222.

[24] Steininger, H.; Lehwald, S.; Ibach, H. *Surface Science* **1982**, *123*, 1–17.

[25] Gland, J. L. *Surface Science* **1980**, *93*, 487–514.

[26] Over, H.; Kim, Y. D.; Seitsonen, A. P.; Wendt, S.; Lundgren, E.; Schmid, M.; Varga, P.; Morgante, A.; Ertl, G. *Science* **2000**, *287*, 1474–1476.

[27] Stampfl, C.; Ganduglia-Pirovano, M.; Reuter, K.; Scheffler, M. *Surface Science* **2002**, *500*, 368–394.

[28] Wang, X.; Kumar, R.; Myers, D. *Electrochemical and Solid State Letters* **2006**, *9*, A225–A227.

[29] Blume, R.; Niehus, H.; Conrad, H.; Bottcher, A.; Aballe, L.; Gregoratti, L.; Barinov, A.; Kiskinova, M. *Journal of Physical Chemistry B* **2005**, *109*, 14052–14058.

[30] Ganduglia-Pirovano, M.; Reuter, K.; Scheffler, M. *Physical Review B* **2002**, *65*, 245426.

[31] Zhang, H.; Soon, A.; Delley, B.; Stampfl, C. *Physical Review B* **2008**, *78*, 045436.

[32] Todorova, M.; Li, W.; Ganduglia-Pirovano, M.; Stampfl, C.; Reuter, K.; Scheffler, M. *Physical Review Letters* **2002**, *89*, 096103.

[33] Gopinath, C. S.; Thirunavukkarasu, K.; Nagarajan, S. *Chemistry - An Asian Journal* **2009**, *4*, 74–80.

[34] German, E. D.; Sheintuch, M.; Kuznetsov, A. M. *Journal of Physical Chemistry C* **2009**, *113*, 15326–15336.

[35] Schnadt, J.; Knudsen, J.; Hu, X. L.; Michaelides, A.; Vang, R. T.; Reuter, K.; Li, Z.; Laegsgaard, E.; Scheffler, M.; Besenbacher, F. *Physical Review B* **2009**, *80*, 075424.

[36] Soon, A.; Todorova, M.; Delley, B.; Stampfl, C. *Physical Review B* **2006**, *73*, 165424.

[37] Reuter, K.; Stampfl, C.; Scheffler, M. *Handbook of Materials modelling: Fundamental Models, Methods*; Springer, 2005; Vol. 1.

[38] Lundgren, E.; Mikkelsen, A.; Andersen, J. N.; Kresse, G.; Schmid, M.; Varga, P. *Journal of Physics - Condensed Matter* **2006**, *18*, R481–R499.

[39] Carlisle, C.; Fujimoto, T.; Sim, W.; King, D. *Surface Science* **2000**, *470*, 15–31.

[40] Blöchl, P. E. *Physical Review B* **1994**, *50*, 17953–17979.

[41] Kresse, G.; Furthmüller, J. *Physical Review B* **1996**, *54*, 11169–11186.

[42] Kresse, G.; Furthmüller, J. *Computational Material Science* **1996**, *6*, 15–50.

[43] Kresse, G.; Joubert, D. *Physical Review B* **1999**, *59*, 1758–1775.

[44] Perdew, J.; Burke, K. *International Journal of Quantum Chemistry* **1996**, *57*, 309–319, 8th International Congress of Quantum Chemistry, Prague, Czech Republic, Jun 19-23, 1994.

[45] Perdew, J.; Burke, K.; Ernzerhof, M. *Physical Review Letters* **1996**, *77*, 3865–3868.

[46] Monkhorst, H.; Pack, J. *Physical Review B* **1976**, *13*, 5188–5192.

[47] Methfessel, M.; Paxton, A. *Physical Review B* **1989**, *40*, 3616–3621.

[48] Birch, F. *Physical Review* **1947**, *71*, 809–824.

[49] Kittel, C. *Introduction to Solid State Physics*, 8th ed.; John Wiley & Sons, 2004; pp 20, 50 and 52.

[50] Lee, I.; Martin, R. *Physical Review B* **1997**, *56*, 7197–7205.

[51] Da Silva, J. L. F.; Stampfl, C.; Scheffler, M. *Surface Science* **2006**, *600*, 703–715.

[52] Singh-Miller, N. E.; Marzari, N. *Physical Review B* **2009**, *80*, 235407.

[53] Adams, D. L.; Nielsen, H. B.; Van-Hove, M. *Physical Review* **1979**, *20*, 4789–4806.

[54] Davies, J. A.; Jackman, T. E.; Jackson, D. P.; Norton, P. R. *Surface Science* **1981**, *109*, 20–28.

[55] Salmerón, M.; Ferrer, S.; Jazzar, M.; Somorjai, G. A. *Physical Review B* **1983**, *28*, 6758–6765.

[56] Huber, K.; Herzberg, G. *Molecular spectra and molecular structure IV: constants of diatomic molecules*, 1st ed.; Van Nostrand, 1979.

[57] Li, W.; Stampfl, C.; Scheffler, M. *Physical Review B* **2002**, *65*, 075407.

[58] Mortensen, K.; Klink, C.; Jensen, F.; Besenbacher, F.; Stensgaard, I. *Surface Science* **1989**, *220*, L701–L708.

[59] Xu, Y.; Mavrikakis, M. *Journal of Chemical Physics* **2002**, *116*, 10846–10853.

[60] Ganduglia-Pirovano, M.; Scheffler, M. *Physical Review B* **1999**, *59*, 15533–15543.

[61] Duan, X.; Warschkow, O.; Soon, A.; Delley, B.; Stampfl, C. *Physical Review B* **2010**, *81*, 075430.

[62] Shi, H.; Stampfl, C. *Physical Review B* **2007**, *76*, 075327.

[63] Todorova, M.; Reuter, K.; Scheffler, M. *Journal of Physical Chemistry B* **2004**, *108*, 14477–14483.

[64] Hawkins, J.; Weaver, J.; Asthagiri, A. *Physical Review B* **2009**, *79*, 125434.

[65] Reuter, K.; Stampfl, C.; Ganduglia-Pirovano, M. V.; Scheffler, M. *Chemical Physics Letters* **2002**, *352*, 311–317.

[66] Jerdev, D.; Kim, J.; Batzill, M.; Koel, B. *Surface Science* **2002**, *498*, L91–L96.

[67] Saliba, N.; Tsai, Y. L.; Panja, C.; Koel, B. E. *Surface Science* **1999**, *419*, 79–88.

[68] Benesh, G. A.; Liyanage, L. S. G. *Surface Science* **1992**, *261*, 207–216.

[69] Lide, D. R. *CRC Handbook of Chemistry and Physics*, 89th Edition ed.; CRC Press, 2008.

[70] Li, W.; Stampfl, C.; Scheffler, M. *Physical Review B* **2003**, *67*, 045408.

[71] Pang, Q.; Zhang, Y.; Zhang, J.-M.; Xu, K.-W. *Applied Surface Science* **2011**, *257*, 3047–3054.

[72] Stampfl, C.; Scheffler, M. *Physical Review B* **1996**, *54*, 2868–2872.

[73] Kitchin, J. R. *Physical Review B* **2009**, *79*, 205412.

Chapter 4

Coverage effects on Pt/Ni-Monolayer Bimetallic Alloy Surfaces

4.1 Introduction

Proton exchange membrane fuel cells (PEMFCs) are a promising alternative power source to combustion for automobile applications.[1] Their long-term application is, however, hindered by several factors, which include the high-cost of the Pt-based electrocatalyst and the slow kinetics of the oxygen reduction reaction (ORR) at the cathode.[2] Hence, much research has been dedicated to the identification of a more stable and efficient catalyst that will increase the ORR activity and thereby reduce the Pt loading.[3]

Several alloy catalysts involving a combination of Pt and another $3d$ transition metal such as Co[4–7] and Ni[6,8–10] have been studied intensively in an attempt to

improve the catalytic activity and stability relative to pure Pt. The activity of these alloys has been shown to be dependent on how the atoms are arranged in the first two layers of the catalyst surface, which can be significantly different from the bulk composition.[11–14] There has been much focus on the monolayer bimetallic alloys (MBA) where the $3d$ alloying metal is incorporated either at the top layer ($3d$-Pt-Pt) or the sublayer (Pt-$3d$-Pt).[15–17] This arrangement effectively changes the electronic and chemical properties of the catalyst surface.[18] A theoretical investigation of adsorbing 0.50 ML of oxygen atoms on the MBA has shown that when certain alloying metal is placed at the sublayer (Pt-$3d$-Pt), there is an increase in the ORR activity which has been attributed to weaker oxygen binding energy compared to pure Pt.[8,19–21] Alternatively, when the same alloying metal is placed at the top layer ($3d$-Pt-Pt), the binding of oxygen is predicted to be stronger than pure Pt.[22] However, due to the surface segregation phenomenon, it has been shown that certain $3d$ metals come to the surface causing a decrease in the catalytic activity compared to Pt.[13,23,24] A number of $3d$ metals were studied for their stability in the presence of oxygen and the most promising of these metals, which was verified by AES and HREELS experiments, is the Pt-Ni-Pt surface.[22,25] This Pt-Ni-Pt surface also generated the smallest potential for surface segregation, indicating that it should be an effective surface catalyst towards the ORR.

For this reasons, it is important to understand the catalytic activity and stability of Pt/Ni MBA surfaces in an oxidising environment. Additionally, reports to date have not investigated the tendency of forming thin film surface oxides on the MBA surfaces when exposed to the oxidising environment for a long period of time. Hence, this chapter gives an extensive account of the first-principles calculations carried out on the low index MBA (111) and (100) surfaces. The results presented are similar to those presented for the Pt surfaces and include oxygen adsorption, incorporation of sub-surface oxygen and the stability of surface oxide. In addition, statistical thermodynamics is employed so that conditions ranging from low pressure to technological relevance can be described, leading to the (T, p) phase diagrams and free energy as a function of potential plots. It was discovered from the present study that the Pt-Ni-Pt surface was the stable MBA surface

when oxygen is adsorbed on the surface. However, when the amount of oxygen is increased, this surface becomes highly susceptible to the formation of thin film surface oxide-like structures. The Ni-Pt-Pt surface is also not an oxide resistant surface because it binds oxygen more strongly even when the oxygen coverage is increased.

4.2 Computational Methods

All calculations are performed using DFT as implemented in VASP with the same functional and parameters as the calculations presented in the previous chapter (Section 3.2.1).

The theoretical lattice constant for Pt (3.98 Å) was used for all calculations and the Ni atoms were incorporated by replacing the Pt atoms in the slabs. Spin polarisation was included in the calculations to take into account the presence of magnetic moments in the system due to the presence of Ni. All calculations were performed within a 2x2 supercell, a five-layer slab consisting of four atoms in each layer with a *k-point* mesh of 8x8x1, which converges the energy to within 0.01 meV. The positions of the atoms in the top three layers were allowed to relax, while the bottom two layers were fixed at the calculated bulk Pt positions and a vacuum thickness of 8 Å separates each successive slab.

For all calculations performed, the oxygen atoms were allowed to move freely in all directions during the energy minimisation until the lowest energy configuration was attained. The binding energy, $\mathrm{E_b}$ per oxygen atom is defined in Eq. 2.24. The convergence criteria for the electronic self-consistent iteration and the ionic relaxation loop are set to 10^{-5} eV and 0.02 eV $\mathrm{Å}^{-1}$ respectively.

4.3 Results and Discussion

4.3.1 Clean Ni-Pt-Pt and Pt-Ni-Pt structures on the (111) and (100) surfaces

In the current study, the DFT adsorption energies as a function of oxygen coverage were modelled on two configurations of the Pt/Ni MBA surfaces. These configurations are Ni-Pt-Pt (Ni-overlayer) and Pt-Ni-Pt (Ni-underlayer) (Figure 4.1). The Ni-Pt-Pt (Ni-overlayer) configuration is constructed with the first layer Pt atoms substituted for Ni atoms while the other four layers remain as Pt atoms. The other configuration, Pt-Ni-Pt (Ni-underlayer) is set up by inserting Ni atoms underneath the surface Pt atoms. Therefore, the first, third, fourth and fifth layers are still Pt atoms. In both configurations, the fourth and fifth layers are fixed to the calculated bulk Pt positions. The top three-layers that include the substituted Ni atoms are allowed to relax. The incorporation of Ni into the sub-surface is expected to contract the surface because Ni (3.52 Å) has a smaller lattice parameter.[26] As a result, any modification observed when the surfaces interact with oxygen could be due to the presence of Ni atoms.

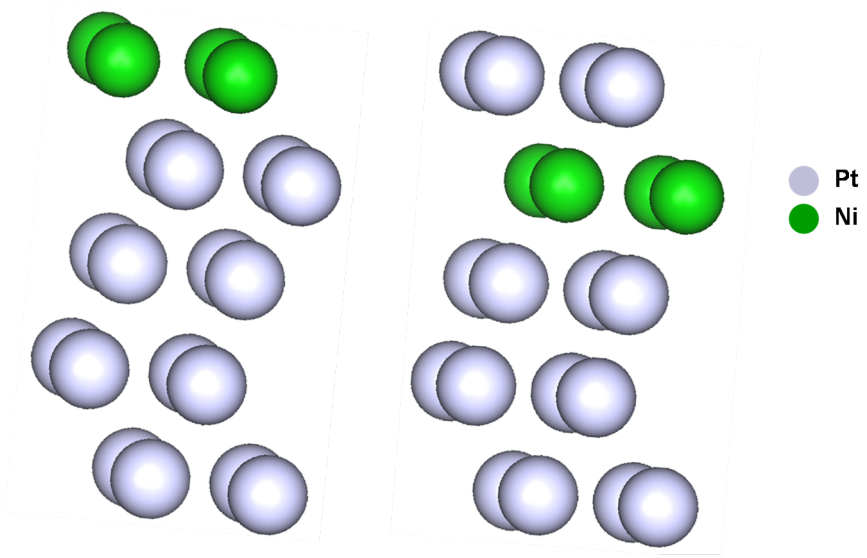

Figure 4.1: Pt/Ni Ni Monolayer Bimetallic Alloys (MBA) Surfaces; Ni-Pt-Pt (left) and Pt-Ni-Pt (right)

Table 4.1: The average bond lengths (Å), interlayer spacings (%) and workfunction (eV) of clean Ni-Pt-Pt (Ni-overlayer) and Pt-Ni-Pt (Ni-underlayer) for the (111) and (100) surfaces. The results are compared to pure Pt surfaces. d_{12}(Å) and d_{23}(Å) are the bond lengths between the nearest-neighbour first and second layer and between the nearest neighbour second and third layer respectively. $\delta_{12}(\%)$ and $\delta_{23}(\%)$ are the changes in the interlayer spacing between the first and the second layer and the second and the third layer, respectively. Φ(eV) is the workfunction.

	(111) surface			(100) surface		
	Ni-Pt-Pt	Pt-Ni-Pt	Pt	Ni-Pt-Pt	Pt-Ni-Pt	Pt
d_{12}	2.56	2.61	2.83	2.55	2.60	2.77
d_{23}	2.83	2.60	2.79	2.84	2.64	2.80
δ_{12}	-13.20	-10.93	+0.53	-19.90	-16.34	-3.02
δ_{23}	+0.76	-12.01	-1.40	+1.72	-13.02	-1.25
Φ	5.69	5.73	5.67	5.69	5.73	5.69

Table 4.1 lists the properties for the relaxed clean surface structures for both the (111) and (100) surfaces, compared to pure Pt surfaces. In general, the trends for the bond lengths and interlayer spacings of the Ni-Pt-Pt and Pt-Ni-Pt structures are similar for the (111) and (100) surfaces. For the first layer, the Pt-Ni bond lengths are shorter while there is a negative change of the interlayer distance for the considered MBA surfaces at the (111) and (100) surfaces with respect to pure Pt surfaces. This suggests that the first layer Pt-Ni bonding is strong, caused by the lattice mismatch between Pt and Ni.[27] Therefore, it is expected that the modification of the surface reactivity will be due to the geometric and electronic effects. Theoretical studies performed by Escaño *et al.* suggest that the geometric effect will dominate.[28] In addition, these results are similar to other magnetic alloying metals such as Cr, Mn and Fe,[27] where it was also found that the bond lengths are shorter compared to pure Pt surfaces.

On both the (111) and (100) surfaces, the bond lengths for the first and second layers of the Ni-Pt-Pt structure are shorter and longer respectively. For the Ni-Pt-Pt configuration, the changes observed are negative and positive for the δ_{12} and δ_{23} respectively while the Pt-Ni-Pt structures showed a negative change of the two interlayer distances. The magnitude of the change in interlayer spacings is slightly bigger for the (111) surface compared to the (100) surface while there is little difference for the bond lengths. Concerning the workfunction, Φ, it can be seen that for Pt-Ni-Pt and Ni-Pt-Pt and at the (111) and (100) surfaces, the Φ is identical. The workfunction difference between Pt-Ni-Pt and Ni-Pt-Pt surface is 0.04 eV, a small change. Compared to the pure Pt and on the (111) surface, the Φ for the Pt-Ni-Pt and Ni-Pt-Pt surfaces are bigger and smaller respectively. As for the (100) surface, the Φ for the Ni-Pt-Pt surface is the same as the Pt surface but smaller than the Pt-Ni-Pt surface.

The next section is divided into two parts, which discuss the interactions of atomic oxygen with these MBA surfaces on both Ni-Pt-Pt and Pt-Ni-Pt structures at the (111) and (100) surfaces. These will enable a detailed understanding of the relative propensity of forming surface oxides on these surfaces.

4.3.2 Oxygen Interactions on Ni-Pt-Pt Monolayer Bimetallic Alloy Surfaces

4.3.2.1 On-surface Adsorption of Atomic Oxygen on Ni-Pt-Pt Surfaces

The effect of increasing the oxygen coverage on the Ni-Pt-Pt surfaces was investigated in the same way as the Pt surface discussed in Chapter 3. The binding energies reported here, are the non zero-point corrected energies relative to the gas-phase O_2 molecule for the oxygen coverage range of $\theta_{\mathrm{tot}}(0.25 \leq \theta_{\mathrm{tot}} \leq 1.00\mathrm{ML})$. The high symmetry adsorption sites of the isolated O atom on the Ni-Pt-Pt (111) and Ni-Pt-Pt (100) surfaces are illustrated in Figure 4.2. The DFT adsorption energies as a function of oxygen coverage on the Ni-Pt-Pt surfaces at 0 K are summarised in Figure 4.3.

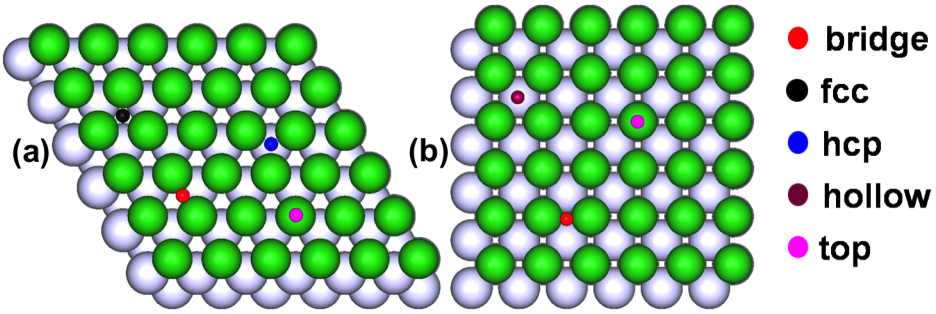

Figure 4.2: Adsobates at adsorption sites on (a) Ni-Pt-Pt (111) and (b) Ni-Pt-Pt (100) surfaces (top view).

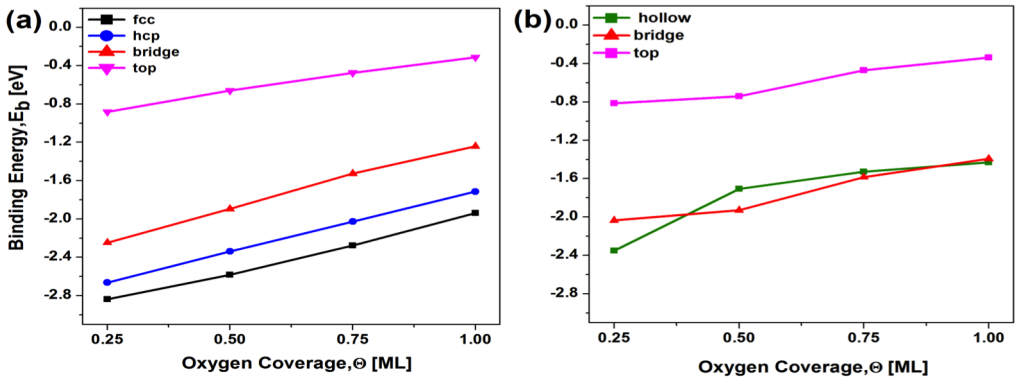

Figure 4.3: On-surface binding energies of oxygen on (a) Ni-Pt-Pt (111) and (b) Ni-Pt-Pt (100) surfaces at various oxygen coverage.

The binding energy graphs (Figure 4.3) indicate a decrease in binding energies as the oxygen coverage increases. This decrease in binding energies is mainly due to the lateral repulsion interaction between the negatively charged oxygen atoms. This is because, compared to the pure Pt surfaces, the top site on the Ni-Pt-Pt surfaces are dependent on the oxygen coverage. On the (111) surface (Figure 4.3a), oxygen prefers to occupy the three-fold fcc-hollow sites. In addition, it can be seen that a linear trend and a clear order for the adsorption sites were observed. The next stable adsorption site after the fcc site is the three-fold hcp site, followed by the two-fold bridge and then the top site. The (100) surface (Figure 4.3b), on the other hand, showed no favoured binding site for all the considered oxygen coverages. At 0.25 ML, the four-fold hollow site is stable, followed by the two-fold bridge sites at 0.50 ML and 0.75 ML and then back to the hollow site at the 1.00 ML. At 1.00 ML oxygen coverage, although the hollow site is favourable, the energy difference between the hollow and bridge site is small (0.04 eV). Overall, oxygen adsorbed on the (111) surface is more stable than that on the (100) surface.

Table 4.2: Average Ni-O bond lengths (Å) and interlayer spacings (%) of atomic oxygen on Ni-Pt-Pt (111) and Ni-Pt-Pt (100) surfaces at 0.25 ML. $d_{\mathrm{Ni-O}}$(Å) is the bond length between O and the nearest neigbour belonging to the top-layer Ni atoms, $\delta_{12}(\%)$ is the change in the interlayer spacing between the Ni first layer and the Pt second layer and $\delta_{23}(\%)$ is the change in the interlayer spacing between the Pt second layer and the Pt third layer. Pure Pt results at the (111) and (100) surfaces are also presented for comparison.

		(111) surface				(100) surface		
		fcc	hcp	top	bridge	bridge	hollow	top
Ni-Pt-Pt	$d_{\mathrm{Ni-O}}$	1.85	1.85	1.66	1.79	2.05	1.99	1.66
	δ_{12}	-11.47	-11.60	-9.64	-12.04	-16.56	-16.61	-17.88
	δ_{23}	+0.61	+0.53	+0.53	+0.53	+0.92	+2.17	+1.48
Pt	$d_{\mathrm{Pt-O}}$	2.05	2.06	1.83		1.95	2.27	1.81
	δ_{12}	+1.19	+1.93	-0.14		-0.98	-0.48	-1.95
	δ_{23}	-0.44	-0.86	-1.13		-0.98	-0.46	-1.16

Table 4.2 shows the Ni-O bond lengths and the first and second interlayer spacings of all the studied adsorption sites at 0.25 ML oxygen coverage and at the (111) and (100) surfaces. The results for the bond lengths and interlayer spacings for the oxygen adsorption on pure Pt surfaces are also presented for comparison. Further analysis of the geometric structures on the Ni-Pt-Pt surfaces have shown that the top-layer Ni-O bond lengths are not coverage dependent for both the (111) and (100) surfaces. Furthermore, at all adsorption sites, the Ni-O bond lengths for the (111) surface are shorter than those of the (100) surface expect at the top site, where they are both the same. Comparing these results with Pt (111) and (100) surfaces, the bond lengths for the Ni-Pt-Pt (111) and (100) surfaces and at all adsorption sites are shorter, apart from the bridge site on the (100) surface. This could be the influence of Ni because it is a smaller atom that causes a contraction within the surfaces. With respect to the interlayer spacings (Table 4.2), the changes are positive and negative for the δ_{12} and δ_{23} respectively at all studied adsorption sites and surfaces. In addition, the negative change for the first layer on the Ni-Pt-Pt surfaces is bigger compared to those on the Pt surfaces.

4.3.2.2 On-surface Mixed Sites Adsorption of Atomic Oxygen on Ni-Pt-Pt Surfaces

The interaction of oxygen atoms with the surfaces are investigated at two different high symmetry adsorption sites at the same time. This gives a detailed understanding of adsorbing oxygen at multiple adsorption sites. Consistent with the Pt surfaces, the high symmetry adsorption sites considered are the fcc and hcp sites on the (111) surface and the bridge and hollow sites on the (100) surface. All the possible mixed configurations on the (2x2) surface were explored at an oxygen coverage range of $\theta_{\mathrm{tot}}(0.25 \leq \theta_{\mathrm{tot}} \leq 2.00\mathrm{ML})$.

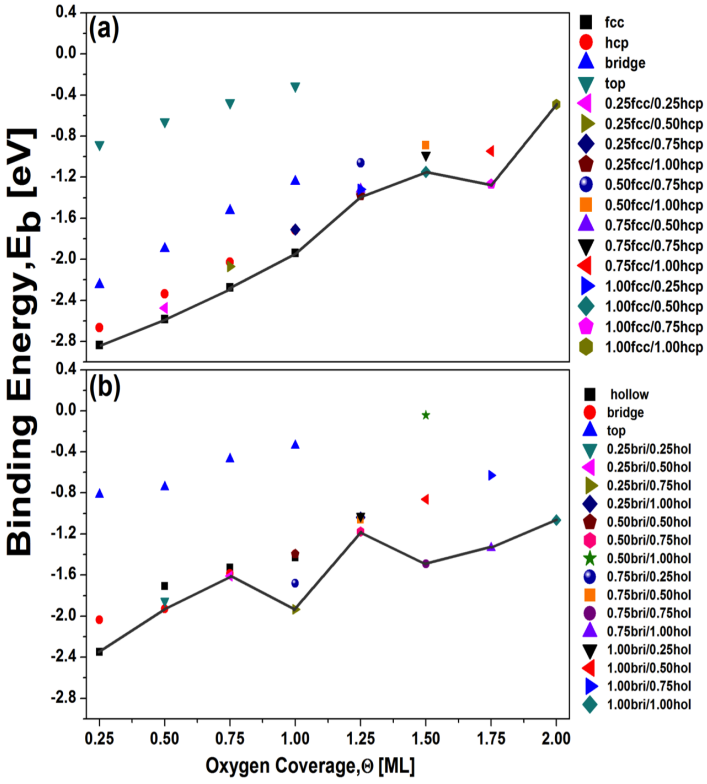

Figure 4.4: Binding energies for the on-surface mixed adsorption sites for oxygen adsorbed on (a) Ni-Pt-Pt (111) and (b) Ni-Pt-Pt (100) surfaces at various oxygen coverages. Solid black lines highlight the most stable mixed sites at each oxygen coverage.

The binding energies of the most stable mixed adsorption sites along with the on-surface binding energies at single adsorption sites are shown in Figure 4.4. On the (111) surface, the oxygen atoms prefer to occupy the high symmetry fcc sites at the oxygen coverage between 0.25 ML and 1.00 ML. In contrast, the mixed adsorption sites become favourable above 0.50 ML on the (100) surface. At the θ_{tot} of 0.75 ML on the (100) surface, there is a small binding energy difference of 0.03 V between the stable (0.25 O_{bri} + 0.50 O_{hol}) and (0.75 O_{bri}). Above 1.00 ML on the two surfaces, the binding energies for the stable mixed site configurations are lower compared to those below the 1.00 ML oxygen coverage. In addition, as the oxygen coverage increases, oxygen binds the (111) surface weaker than the (100) surface, due to O-O repulsion effect. According to this model, the binding energies for all the favoured mixed site configurations are exothermic indicating that they are likely to exist.

4.3.2.3 Sub-surface Absorption of Atomic Oxygen on Ni-Pt-Pt Surfaces

The stability of incorporating oxygen sub-surface is examined theoretically on both the (111) and (100) surfaces at the oxygen coverage range of $\theta_{sub_{tot}}(0.25 \leq \theta_{sub_{tot}} \leq 1.00$ ML). This involves placing the oxygen atoms at the high symmetry absorption sites between the top Ni layer and the second Pt layer (see Figure 3.4 for illustration).

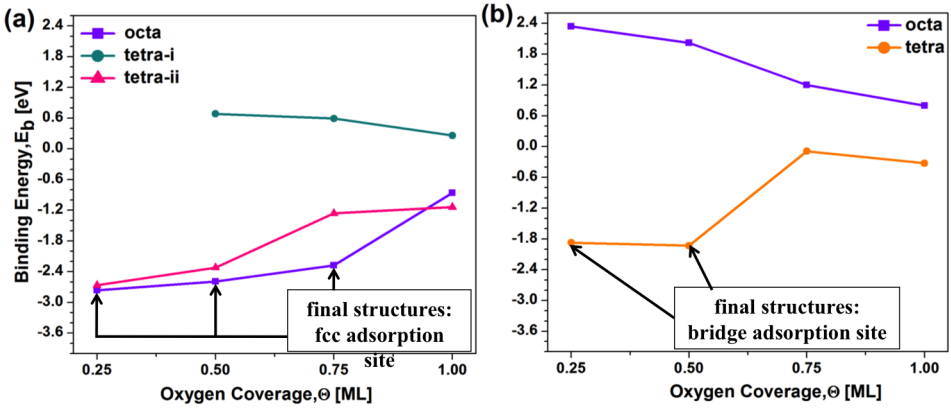

Figure 4.5: Binding energies for the sub-surface oxygen absorption on (a) Ni-Pt-Pt (111) and (b) Ni-Pt-Pt (100) surfaces at various oxygen coverages.

Figure 4.5 shows the relaxed binding energies of oxygen absorption at each sub-surface site for both surfaces. The incorporation of oxygen into the sub-surface is exothermic for the (111) and (100) surfaces at the studied oxygen coverages and at the stable absorption and adsorption sites. Analysis of the final relaxed structures show that at low oxygen coverage on both surfaces, the oxygen atoms do not remain sub-surface but return to the on-surface structures. On the (111) surface and at the oxygen coverage between 0.25 ML and 0.75 ML, the favoured structures are the on-surface fcc adsorption sites but switches to the sub-surface tetrahedral (tetra-ii) site, where oxygen is positioned below the hcp site at an oxygen coverage of 1.00 ML (Figure 4.5a). As for the (100) surface and at the oxygen coverage of 0.25 ML and 0.50 ML, the on-surface bridge adsorption sites are also favoured, which then converts back to the sub-surface tetrahedral ($tetra_{100}$) site where oxygen is placed underneath the bridge site at the 0.75 ML and 1.00 ML (Figure 4.5b). Table 4.3 tabulates the binding energies of the on-surface adsorption sites and the sub-surface absorption sites for the (111) and (100) surfaces. It can be seen that as the oxygen coverage increases to 1.00 ML on both surfaces, the oxygen atoms remain sub-surface and are significantly unstable. However, when compared to pure Pt surfaces, oxygen binds strongly to the Ni-Pt-Pt surfaces. This may be due to the high affinity of Ni for oxygen atoms.

Table 4.3: Binding energies (eV) of on-surface fcc site and sub-surface octa site for the Ni-Pt-Pt (111) surface and onsurface bridge site and sub-surface tetra_{100} site for the Ni-Pt-Pt (100) surface at oxygen coverages between 0.25 and 1.00 ML.

	Ni-Pt-Pt (111)		Ni-Pt-Pt (100)	
coverage (ML)	fcc	octa	bridge	tetra_{100}
	[eV]			
0.25	-2.83	-2.76	-2.03	-1.87
0.50	-2.58	-2.59	-1.93	-1.93
0.75	-2.28	-2.28	-1.58	-0.09
1.00	-2.28	-0.86	-1.39	-0.32

4.3.2.4 Interaction of Oxygen with the On/sub-surface Phases on Ni-Pt-Pt surfaces

The on/sub-surface configurations are investigated to determine the propensity of forming surface oxides on the Ni-Pt-Pt surfaces. Similar to the Pt surfaces, a number of possible structural combinations for the on-surface and sub-surface oxygen were studied. The configurations considered are the same as those modelled for pure Pt surfaces (Section 3.3.5), at the oxygen coverage range of θ_{tot}(0.25 $\leq \theta_{tot} \leq$ 2.00 ML). The thermodynamic tendency of forming thin surface oxide will then become evident when the on/sub-surface phases become energetically more stable than having pure on-surface or sub-surface structures at the same total oxygen coverage θ_{tot}.

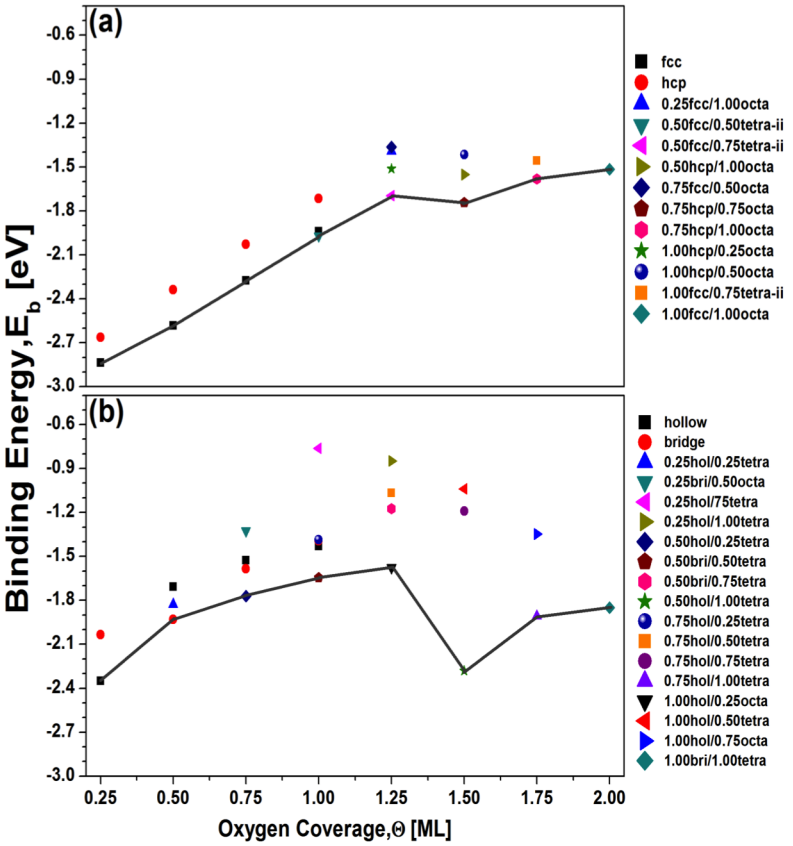

Figure 4.6: The binding energies for the on/sub-surface phases on (a) Ni-Pt-Pt (111) and (b) Ni-Pt-Pt (100) surfaces. Solid black lines highlight the most stable on/sub-surface phases at each oxygen coverage.

Figure 4.6 illustrates the binding energies of the most stable on/sub-surface phases along with the on-surface adsorption on both the (111) and (100) surfaces. On the (111) and between θ_{tot} of 0.25 and 0.75 ML, the on-surface fcc site is the most stable adsorption site. As the θ_{tot} increases to 1.00 ML, the (0.50 O_{fcc} + 0.50 $O_{\mathrm{tetra-ii}}$) is favoured. However, the binding energy difference between the on/sub-surface phase (0.50 O_{fcc} + 0.50 $O_{\mathrm{tetra-ii}}$) and the (1.00 O_{fcc}) is small, at only 0.03 eV. This suggests that there is a possible coexistence of the (fcc/-) and (fcc/tetra-ii) geometries at 1.00 ML, similar to the Pt (111) surface. Above 1.00 ML, the on/sub-surface configurations are relatively stable with lower binding energies, due to the O-O repulsion. The negative binding energies imply that the

surface oxide-like structure will continue to grow on the surface as the oxygen coverage increases. At all studied oxygen coverage, the stable fcc and on/sub-surface configurations are energetically favoured compared to those identified on the Pt(111) surface.

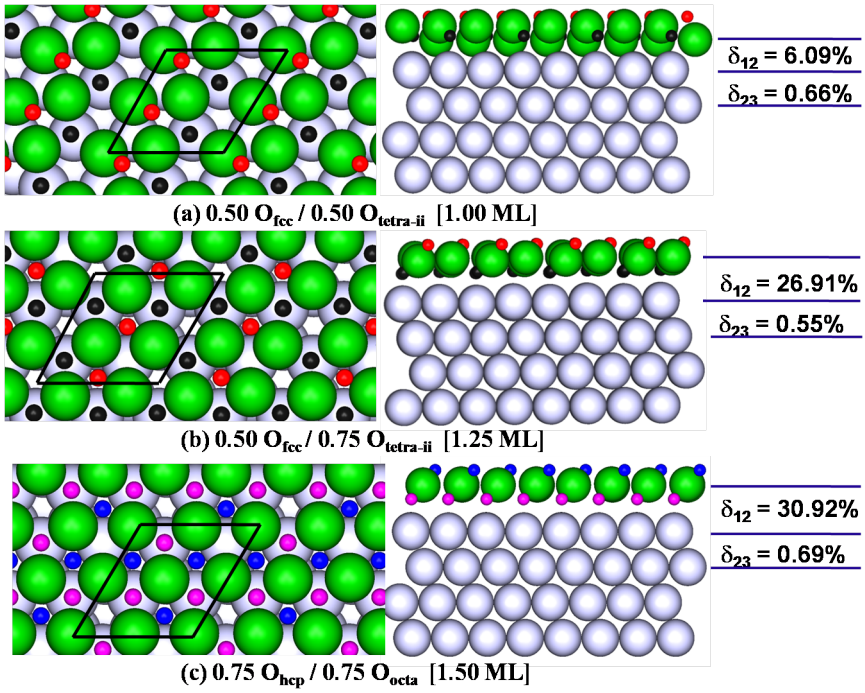

Figure 4.7: Top and side views of the most stable oxygen on/sub-surface configurations on the Ni-Pt-Pt (111) surface calculated using a (2x2) unit cell at the θ_{tot} of (a) 1.00 ML, (b) 1.25 ML and (c) 1.50 ML. The average change in interlayer spacing, (%), δ_{12}, between the first and second layer and δ_{23}, between the second and third layer, with respect to the bulk Pt interlayer distance is given to the right of the figures. The large sky blue and green spheres represent Pt and Ni atoms, the small red and blue spheres represent the on-surface O atoms at the fcc and hcp sites and the small black and purple spheres represent the sub-surface O atoms at the tetra-ii and octa sites.

Table 4.4: The calculated (average) bond lengths (Å) for the most stable on/sub-surface configurations on the Ni-Pt-Pt(111) surface at the θ_{tot} of 1.00 ML, 1.25 ML and 1.50 ML. $d_{\mathrm{O_{onsurf}-Ni}}$ (Å) is the distance between the on-surface oxygen and the nearest-neighbour first layer Ni atom, $d_{\mathrm{Ni-O_{sub}}}$(Å) is the distance between the nearest-neighbour first layer Ni atom and sub-surface oxygen, $d_{\mathrm{O_{sub}-Pt}}$(Å) is the distance between the sub-surface oxygen and the nearest-neighbour second layer Pt atom and $d_{\mathrm{Ni-Pt}}$ (Å) is the distance between the Ni and Pt layers.

	1.00 ML	1.25 ML	1.50 ML
$d_{\mathrm{O_{onsurf}-Ni}}$	1.80	1.88	1.86
$d_{\mathrm{Ni-O_{sub}}}$	1.83	1.89	1.90
$d_{\mathrm{O_{sub}-Pt}}$	2.23	2.07	2.08
$d_{\mathrm{Ni-Pt}}$	3.00	3.40	3.42

As seen previously for the Pt(111) surface, the geometric structures for the stable on/sub-surface phases at the θ_{tot} of 1.00, 1.25 and 1.50 ML are analysed. Figure 4.7 and Table 4.4 show the stable on/sub-surface structures along with the structural information. From all the considered configurations, the (0.50 $\mathrm{O_{fcc}}$ + 0.50 $\mathrm{O_{tetra-ii}}$) phase is the only structure showing a significant amount of buckling in the first layer of the surface. This buckling in the first layer of the (0.50 $\mathrm{O_{fcc}}$ + 0.50 $\mathrm{O_{tetra-ii}}$) structure causes the average Ni-Pt bond length to be shorter than the (0.50 $\mathrm{O_{fcc}}$ + 0.75 $\mathrm{O_{tetra-ii}}$) and (0.75 $\mathrm{O_{hcp}}$ + 0.50 $\mathrm{O_{octa}}$) structures. The δ_{23} for all the structures increases slightly, indicating a small disruption in the Pt layers. The Ni-O bond lengths for the on/sub-surface structures are shorter than the Pt-O bond lengths. The difference in bond lengths is due to Ni having a smaller lattice parameter compared to Pt. The Pt-O bond lengths for the on/sub-surface structures are similar to those observed on/sub-surface arrangements on the Pt(111) surface.

Continuing this discussion to the (100) surface, the on-surface hollow and bridge sites are the favoured adsorption sites at the θ_{tot} of 0.25 and 0.50 ML (Figure 4.6b). Beyond 0.50 ML oxygen coverage, the on/sub-surface phases are stable implying that the reconstructed surface oxide-like structures will begin to form above 0.50 ML. The binding energy differences between the stable surface oxide-

like structures and the on-surface adsorption geometries at the θ_{tot} of 0.75 ML and 1.00 ML are very large at 0.19 eV and 0.21 eV respectively. Also, at 1.50 ML, the binding energy for (0.50 O_{hol} + 1.00 O_{tetra}) is the lowest compared to all other oxide-like structures at the different oxygen coverages.

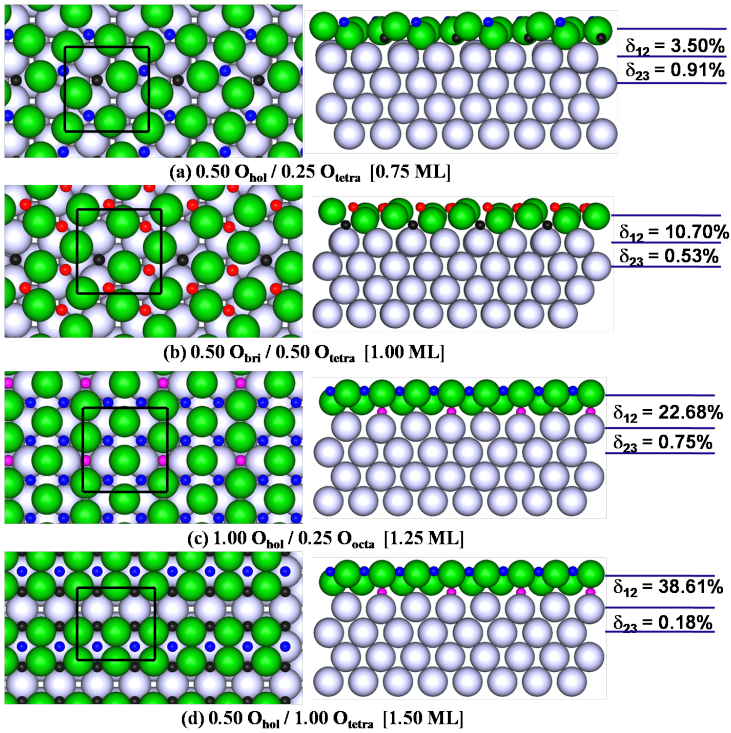

Figure 4.8: Top and side views of the most stable oxygen on/sub-surface geometric structures on the Ni-Pt-Pt (100) surface calculated using a (2x2) unit cell at the θ_{tot} of (a) 0.75 ML, (b) 1.00 ML, (c) 1.25 ML and (d) 1.50 ML. The average change in interlayer spacing, (%), δ_{12}, between the first and second layer and δ_{23}, between the second and third layer, with respect to the bulk Pt interlayer distance is given to the right of the figures. The large sky blue and green spheres represent Pt and Ni atoms, the small red and blue spheres represent the on-surface O atoms at the bridge and hollow sites and the small black and purple spheres represent the sub-surface O atoms at the tetra and octa sites.

Table 4.5: The calculated (average) bond lengths (Å) for the most stable on/sub-surface geometric structures on the Ni-Pt-Pt(100) surface at the θ_{tot} of 0.75 ML, 1.00 ML, 1.25 ML and 1.50 ML. $d_{\mathrm{O_{onsurf}-Ni}}$(Å) is the distance between the on-surface oxygen and the nearest-neighbour first layer Ni atom, $d_{\mathrm{Ni-O_{sub}}}$(Å) is the distance between the nearest-neighbour first layer Ni atom and sub-surface oxygen, $d_{\mathrm{O_{sub}-Pt}}$(Å) is the distance between the sub-surface oxygen and the nearest-neighbour second layer Pt atom and $d_{\mathrm{Ni-Pt}}$(Å) is the distance between the Ni and Pt layers.

	0.75 ML	1.00 ML	1.25 ML	1.50 ML
$d_{\mathrm{O_{onsurf}-Ni}}$	1.85	1.83	1.85	2.01
$d_{\mathrm{Ni-O_{sub}}}$	1.83	1.91	1.87	1.86
$d_{\mathrm{O_{sub}-Pt}}$	2.14	2.04	2.02	2.15
$d_{\mathrm{Ni-Pt}}$	2.84	2.79	2.98	3.42

Figure 4.8 and Table 4.5 show the geometric structures, interlayer spacings and the calculated bond lengths for the stable on/sub-surface phases at the θ_{tot} between 0.75 ML and 1.50 ML. A significant amount of buckling in the Ni first layer is observed in all the considered configurations, with the largest buckling found on (0.50 O_{hol} + 1.00 O_{tetra}) (Figure 4.8d). These bucklings are considerably bigger than those identified on the Pt(100) surface. Furthermore, the interlayer spacings for all the configurations show that the δ_{12} increases with oxygen coverage (Figure 4.8). The Ni-O bond lengths for both the on-surface and sub-surface oxygens are between 1.8 and 1.9 Å for all the studied structures except for 1.50ML where the on-surface Ni-O bond length is slightly longer at 2.01 Å. This longer Ni-O bond length observed on the 1.50 ML on/sub-surface structure is caused by the large buckling in the first layer.

4.3.3 Oxygen Interactions on Pt-Ni-Pt Monolayer Bimetallic Alloy Surfaces

4.3.3.1 On-surface Adsorption of Atomic Oxygen on Pt-Ni-Pt Surfaces

The investigation of atomic oxygen interactions is carried out on the Pt-Ni-Pt surfaces, where the Ni layer is positioned below the surface Pt layer. As in the case of the Ni-Pt-Pt and Pt surfaces, both the (111) and (100) surfaces are investigated. Figure 4.9 shows the binding energies of oxygen adsorption at the high symmetry adsorption sites on these surfaces, as a function of oxygen coverage.

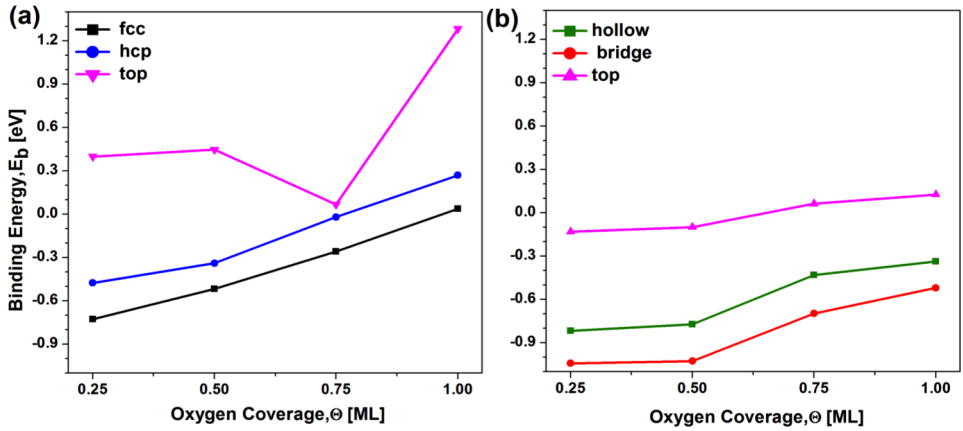

Figure 4.9: On-surface binding energies of oxygen on (a) Pt-Ni-Pt (111) and (b) Pt-Ni-Pt (100) surfaces at various oxygen coverages.

The results observed for the Pt-Ni-Pt surfaces are similar to those observed for the Pt surfaces. On the Pt-Ni-Pt surfaces, the most stable binding sites are the three-fold fcc-hollow site on the (111) surface and the two-fold bridge site on the (100) surface. As in the case of Pt (111) surface, the bridge site for the (111) surface is unstable because the oxygen falls into the nearest fcc site. Comparing both surfaces, oxygen binds the (100) surface more strongly than the (111) surface. Furthermore, in agreement with the Pt and the Ni-Pt-Pt surfaces, the binding

energies decrease steadily as the oxygen coverage increases for all the stable adsorption sites. Similarly to the Ni-Pt-Pt surfaces, the decrease in binding energies is mainly due to the repulsion effect between the negatively charged oxygen atoms adsorbed onto the surfaces.

Table 4.6: Average Pt-O bond lengths (Å) and change in interlayer spacing (%) of atomic oxygen on Pt-Ni-Pt (111) and Pt-Ni-Pt (100) surfaces at 0.25 ML. $d_{\mathrm{Pt-O}}$(Å) is the bond length between O and the top-layer Pt, $\delta_{12}(\%)$ is between the Pt first layer and the Ni second layer and $\delta_{23}(\%)$ is between the Ni second layer and the Pt third layer. Results for Ni-Pt-Pt and Pt at the (111) and (100) surfaces are also presented for comparison.

		(111) surface				(100) surface		
		fcc	hcp	top	bridge	bridge	hollow	top
Pt-Ni-Pt	$d_{\mathrm{Pt-O}}$	2.06	2.05	1.85		1.96	2.03	1.82
	δ_{12}	-10.04	-9.38	-12.14		-14.74	-13.13	-16.52
	δ_{23}	-11.97	-12.31	-11.73		-13.67	-13.91	-13.19
Ni-Pt-Pt	$d_{\mathrm{Ni-O}}$	1.85	1.85	1.66	1.79	2.05	1.99	1.66
	δ_{12}	-11.47	-11.60	-9.64	-12.04	-16.56	-16.61	-17.88
	δ_{23}	+0.61	+0.53	+0.53	+0.53	+0.92	+2.17	+1.48
Pt	$d_{\mathrm{Pt-O}}$	2.05	2.06	1.83		1.95	2.27	1.81
	δ_{12}	+1.19	+1.93	-0.14		-0.98	-0.48	-1.95
	δ_{23}	-0.44	-0.86	-1.13		-0.98	-0.46	-1.16

Table 4.6 shows the Pt-O bond lengths and the first and second interlayer spacings of all the studied adsorption sites at 0.25 ML oxygen coverage. Results for Ni-Pt-Pt and Pt at the (111) and (100) surfaces are also presented for comparison. Similar to the Pt and Ni-Pt-Pt surfaces, the top-layer Pt-O bond lengths are not coverage dependent for both the (111) and (100) surfaces at the studied adsorption sites. The high coordinated adsorption sites on the (111) and (100) surfaces have longer Pt-O bond lengths. The bond length for the energetically favoured bridge site on the (100) surface is shorter than that of the stable fcc site on the (111) surface. This is the same result observed for the Pt surfaces. The bond lengths for the Pt-Ni-Pt surfaces and at all adsorption sites, are comparable to the Pt surfaces but longer than the Ni-Pt-Pt surfaces. The reason for this observation may be

because the Ni sub-layer is not interacting with oxygen and the entire bonding interactions occur with the top Pt layer. As for the change in interlayer spacings, negative changes of the first two interlayer distances are observed on the Pt-Ni-Pt surfaces and at all adsorption sites. These interlayer spacings are different from those observed on the Ni-Pt-Pt and Pt surfaces.

4.3.3.2 On-surface Mixed Sites Adsorption of Atomic Oxygen on Pt-Ni-Pt Surfaces

The exploration of adsorbing oxygen at mixed high symmetry adsorption sites was carried out at the oxygen coverage range of $\theta_{\mathrm{tot}}(0.25 \leq \theta_{\mathrm{tot}} \leq 2.00\mathrm{ML})$. In the same way as the Pt and Ni-Pt-Pt surfaces, the fcc and hcp sites were examined on the (111) surface while the hollow and bridge sites were modelled on the (100) surface.

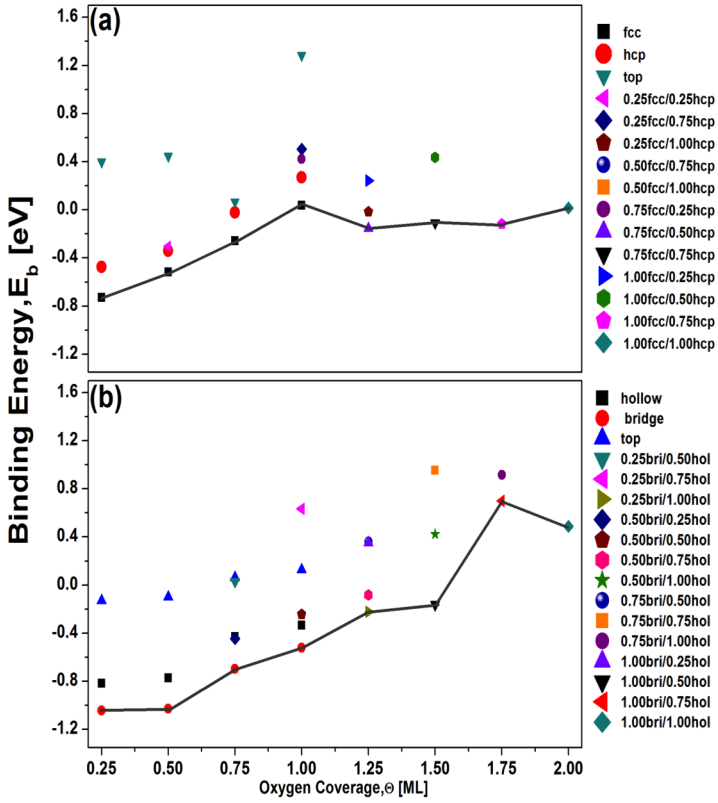

Figure 4.10: Binding energies for the on-surface mixed adsorption sites for oxygen adsorbed on (a) Pt-Ni-Pt (111) and (b) Pt-Ni-Pt (100) surfaces at various oxygen coverage. Solid black lines highlight the most stable mixed sites at each oxygen coverage.

The graph above (Figure 4.10) illustrates the binding energies of the most stable mixed adsorption sites along with the non-mixed on-surface binding energies. Similar to the Pt surfaces, the oxygen atoms prefer to occupy the non-mixed high symmetry fcc sites at the oxygen coverage between 0.25 ML and 1.00 ML on the (111) and (100) surfaces. On the (111) surface, there is a small decrease in binding energy at the 1.25 ML, which then levels off as the oxygen coverage increases. As for the (100) surface, the mixed adsorption sites are unstable as the oxygen coverage is increased, caused mainly by the O-O repulsion.

4.3.3.3 Sub-surface Absorption of Atomic Oxygen on Pt-Ni-Pt Bimetallic Surfaces

The stability of absorbing oxygen sub-surface are investigated at the oxygen coverage range of $\theta_{\mathrm{tot}}(0.25 \leq \theta_{\mathrm{tot}} \leq 1.00\mathrm{ML})$.

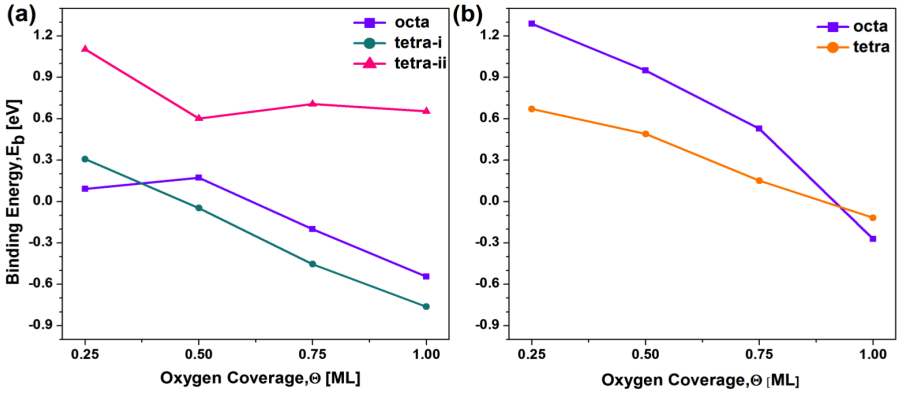

Figure 4.11: Subsurface binding energies of oxygen on (a) Pt-Ni-Pt (111) and (b) Pt-Ni-Pt (100) surfaces at various oxygen coverages.

Figure 4.11 illustrates the binding energies of the oxygen absorption at each sub-surface site on the two surfaces. On the (111) surface, the octahedral (octa) site (where oxygen is located beneath the fcc site) is favoured at 0.25 ML while the tetrahedral (tetra-i) sites (oxygen is positioned underneath the top site) are preferred at the oxygen coverages between 0.50 and 1.00 ML. Similarly to the Pt(100) surface, the tetrahedral (tetra_{100}) site (were oxygen is positioned beneath the bridge site) is stable at oxygen coverages between 0.25 and 0.75 ML on the (100) surface. As the oxygen coverage increases to 1.00 ML on the (100) surface, the stability switches to the octahedral (octa_{100}) (where oxygen is located below the top site) site.

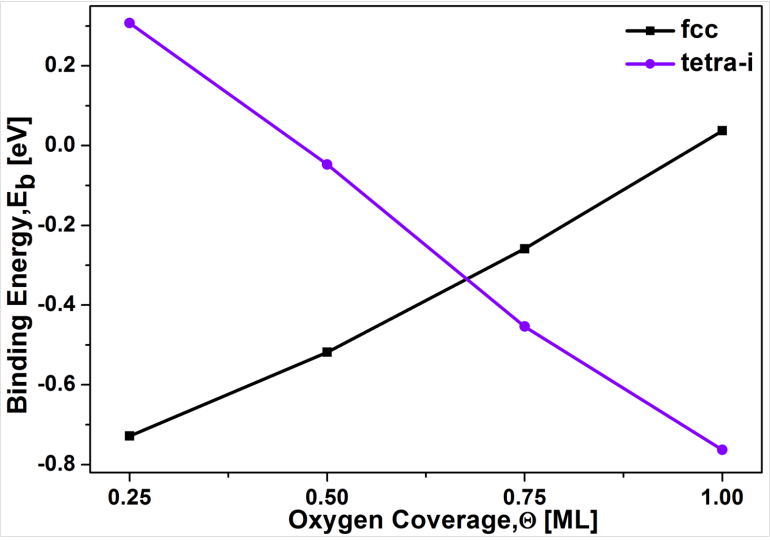

Figure 4.12: Graph showing the binding energies of the stable on-surface fcc site and sub-surface tetra-i site on the Pt-Ni-Pt (111) surface.

On the (111) and (100) surfaces, the binding energies increase as the sub-surface oxygen coverage increases. This trend is similar to those observed on the Pt surfaces, where it is observed that there is an attractive force that stabilises the sub-surface structure as the oxygen coverage increases. On (111) surface, the stable sub-surface tetra-i site is found to intersect the favoured on-surface fcc adsorption site at 0.68 ML (Figure 4.12). This suggests that oxygen will probably occupy the sub-surface region when the on-surface oxygen coverage reaches the critical oxygen coverage of 0.68 ML. Therefore, it is possible that a thin surface oxide will form on the (111) surface above 0.68 ML.

Table 4.7: The average Pt-O and Ni-O bond lengths (Å) and the change in interlayer spacing (%) at the θ_{tot} of 0.50 and 0.75 ML for the on-surface fcc adsorption and sub-surface tetra-i absorption sites. $d_{\mathrm{Pt-O}}$(Å) is the bond length between O and the top-layer Pt, $d_{\mathrm{O-Ni}}$(Å) is the bond length between O and the second-layer Ni, $\delta_{12}(\%)$ is between the Pt first layer and the Ni second layer and $\delta_{23}(\%)$ is between the Ni second layer and Pt third layer.

	on-surface fcc		subsurface tetra-i	
	0.5ML	0.75ML	0.5ML	0.75ML
$d_{\mathrm{O\text{-}Pt}}$	2.04	2.04	-	-
$d_{\mathrm{Pt\text{-}O}}$	-	-	2.02	2.06
$d_{\mathrm{O\text{-}Ni}}$	-	-	1.87	1.91
δ_{12}	-9.67	-10.31	+13.21	+29.85
δ_{23}	-11.64	-12.01	-9.96	-10.67

To understand the stability of the sub-surface tetra-i site and compare it to the on-surface fcc site, the Pt-O and Ni-O bond lengths and the first and second interlayer spacings are examined for the oxygen coverage at 0.50 and 0.75 ML (Table 4.7). It is between these oxygen coverages that the intersection occurs. Regardless of where the oxygen is placed (either on-surface or sub-surface), the Pt-O bond lengths are about 2 Å while the Ni-O bond lengths are slightly shorter for the sub-surface structures. Furthermore, a negative change of the interlayer distance is observed for the first two layers of the on-surface adsorption while the changes are postive and negative for the δ_{12} and δ_{23} for the sub-surface absorption. These results demonstrate that the location of the oxygen atoms does not have any effect on the O-metal bonding interaction.

4.3.3.4 Interaction of Oxygen with the On/sub-surface Phases on Pt-Ni-Pt surfaces

As mentioned in section 4.3.3.3, it is possible for oxygen to occupy the sub-surface region when the on-surface oxygen coverage reaches 0.68 ML. To validate

this result, a bigger unit cell would be required to investigate a greater range of oxygen coverages, so that the actual critical surface coverage can be determined. However, by using the (2x2) unit cell, the oxygen coverage at which the surface oxide-like layer is likely to form can be determined roughly. The configurations considered for the on/sub-surfaces are exactly the same as those examined for the Ni-Pt-Pt surfaces for both the (111) and (100) surfaces (section 4.3.2.1).

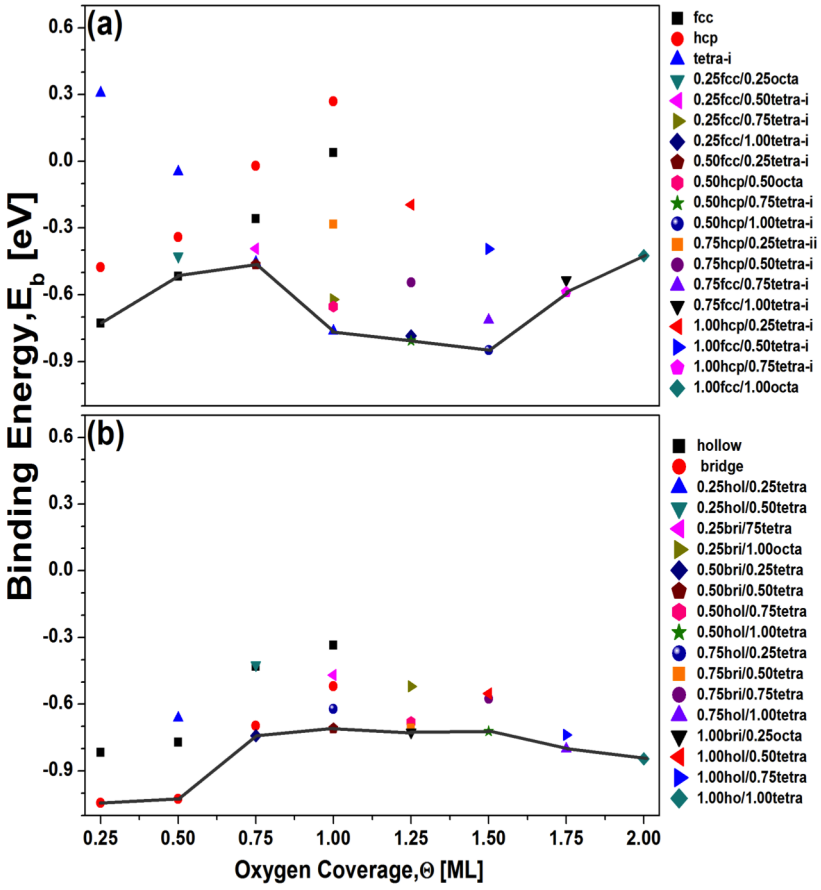

Figure 4.13: The binding energies for the on/sub-surface phases on (a) Pt-Ni-Pt (111) and (b) Pt-Ni-Pt (100) surfaces at various oxygen coverages. Solid black lines highlight the most stable on/sub-surface phases at each oxygen coverage.

Figure 4.13 shows the binding energies of the most stable on/sub-surface phases along with the on-surface adsorption energies. For the (111) surface, the sta-

ble sub-surface tetra-i absorption energies are also included for comparison with the on/sub-surface binding energies. From these graphs, it is clear that there is no dominant on/sub-surface configurations found at all the studied oxygen coverages. However, consistent sub-surface sites are found to be stable on the two surfaces. These sub-surface sites are tetra-i and tetra for the (111) and (100) surfaces respectively.

On the (111) surface, the on/sub-surface phases become stable from the θ_{tot} of 0.75 ML. At 0.75 ML, there is a small binding energy difference of 0.01 eV between the stable on/sub-surface (0.50 O_{fcc} + 0.25 $O_{\mathrm{tetra-i}}$) and the next favoured sub-surface (0.75 $O_{\mathrm{tetra-i}}$) structure. In addition, it is interesting to observe that at 1.00 ML, the pure sub-surface phase (1.00 $O_{\mathrm{tetra-i}}$) is favoured, thereby validating the stability of the pure sub-surface absorption at 0.68 ML (discussed in section 4.3.3.3). Therefore, these results illustrate that there is coexistence between the pure sub-surface and the surface oxide-like structures and they are likely to occur above 0.50 ML. The binding energies are unsteady as the oxygen coverage increases.

Comparing these results with Ni-Pt-Pt(111) and Pt(111) surfaces, Pt-Ni-Pt(111) will form surface oxide-like structures from 0.50 ML. This is much sooner than the other surfaces. Furthermore, the binding energy for the stable on/sub-surface structure at 0.75 ML on Pt-Ni-Pt(111) is similar to the favoured on/sub-surface structure at 1.00 ML on Pt(111) but lower than the stable on/sub-surface structure at 1.00 ML on the Ni-Pt-Pt(111) surface. Unlike Ni-Pt-Pt(111) and Pt(111), the binding energies do not decrease with the oxygen coverage.

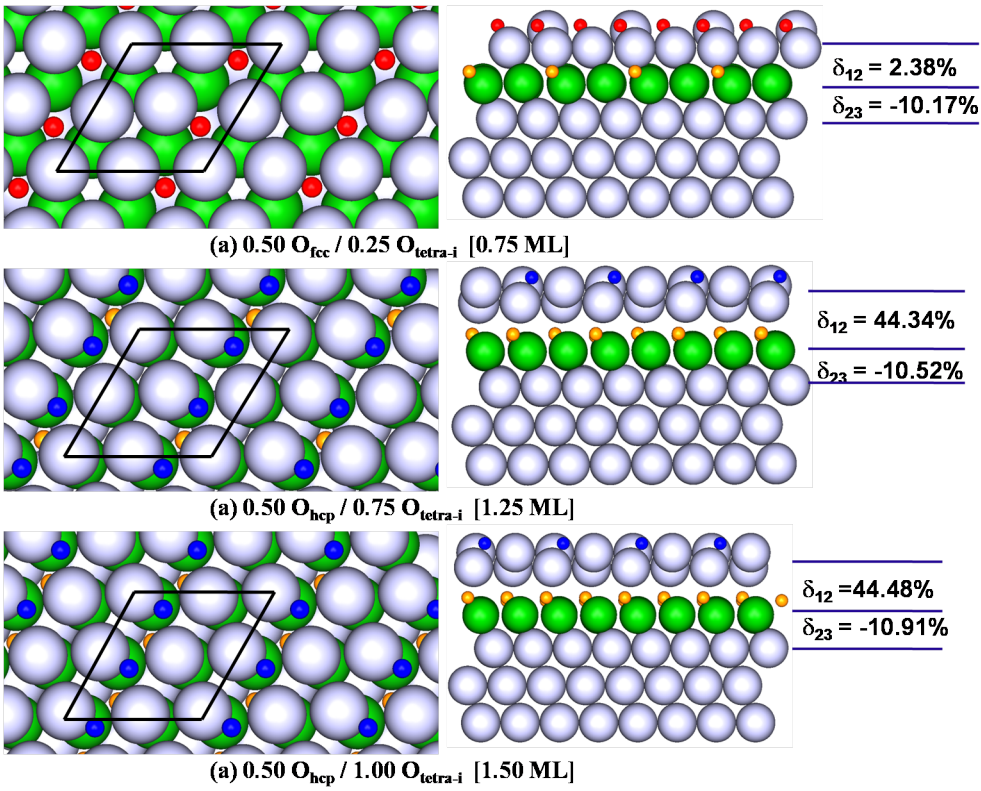

Figure 4.14: Top and side views of the most stable oxygen on/sub-surface configurations on the Pt-Ni-Pt (111) surface calculated using a (2x2) surface unit cell at the θ_{tot} of (a) 0.75 ML, (b) 1.25 ML and (c) 1.50 ML. The average change in interlayer spacing, (%), δ_{12}, between the first and second layer and δ_{23}, between the second and third layer, with respect to the bulk Pt interlayer distance is given to the right of the figures. The large sky blue and green spheres represent Pt and Ni atoms, the small red and blue spheres represent the on-surface O atoms at the fcc and hcp sites and the small orange sphere represents the sub-surface O atoms at the tetra-i site.

Table 4.8: The calculated (average) bond lengths (Å) for the most stable on/sub-surface configurations on the Pt-Ni-Pt(111) surface at the θ_{tot} of 0.75, 1.25 and 1.50 ML. $d_{\mathrm{O_{onsurf}-Pt}}$(Å) is the distance between the on-surface oxygen and the nearest-neighbour first layer Pt atom, $d_{\mathrm{Pt-O_{sub}}}$(Å) is the distance between the nearest-neighbour first layer Pt atom and sub-surface oxygen, $d_{\mathrm{O_{sub}-Ni}}$(Å) is the distance between the sub-surface oxygen and the nearest-neighbour second layer Ni atom and $d_{\mathrm{Pt-Ni}}$(Å) is the distance between the Pt and Ni layers.

	0.75 ML	1.25 ML	1.50 ML
$d_{\mathrm{O_{onsurf}-Pt}}$	2.06	2.01	2.01
$d_{\mathrm{Pt-O_{sub}}}$	2.45	2.77	2.90
$d_{\mathrm{O_{sub}-Ni}}$	1.83	1.90	1.90
$d_{\mathrm{Pt-Ni}}$	2.83	3.39	3.50

Figure 4.14 and Table 4.8 show the geometric structures, interlayer spacings and the calculated bond lengths for the stable on/sub-surface structures at the θ_{tot} of 0.75, 1.25 and 1.50 ML. A considerable amount of buckling is observed in the first layer of all the on/sub-surface structures. These observed bucklings are similar to those identified on the Pt(111) on/sub-surface structures. This suggests that sub-layer Ni atoms have little effect within the bonding mechanism. The Pt-O bond lengths for the sub-surface oxygens are slightly longer than those for the on-surface oxygens while the O-Ni bond lengths are shorter for all the considered oxygen coverages (Table 4.8). As for the Pt-Ni bond lengths, the higher the oxygen coverage, the longer the bond length. In addition, these Pt-O bond lengths are comparable to the top-layer Pt-O bond length for the Pt(111) while the Pt-Ni bond lengths are shorter than the Pt-Pt bond length. The Pt-Ni bond lengths are expected to be short because the Ni atoms are smaller than Pt.

With regards to the Pt-Ni-Pt (100) surface, the on/sub-surface phases become stable from the θ_{tot} of 0.75 ML (Figure 4.13b). In addition, difference in binding energies between the on/sub-surface structures is small when the oxygen coverage is increased. Similarly to the Ni-Pt-Pt(100), the surface oxide-like structures will begin to form above 0.50 ML, earlier than those on the Pt(100) surface. The binding energy for the on/sub-surface structure at 0.75 ML on the Pt-Ni-Pt (100)

surface is lower than that on the Ni-Pt-Pt (100) surface.

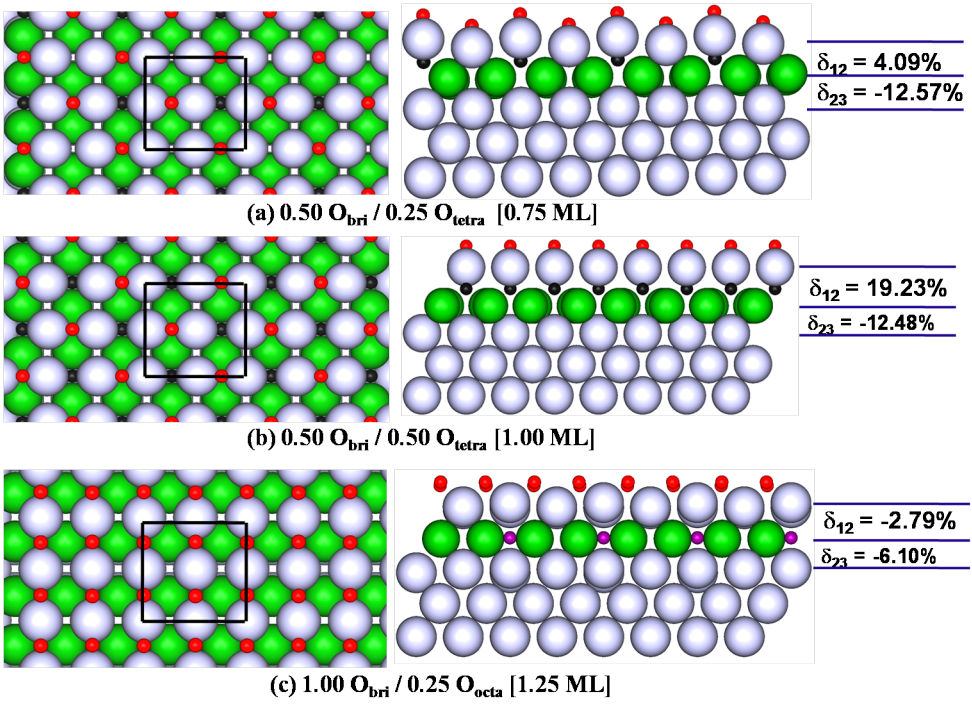

Figure 4.15: Top and side views of the most stable oxygen on/sub-surface structures on the Pt-Ni-Pt (100) surface calculated using a (2x2) surface unit cell at the θ_{tot} of (a) 0.75 ML, (b) 1.00 ML and (c) 1.50 ML. The average change in interlayer spacing, (%), δ_{12}, between the first and second layer and δ_{23}, between the second and third layer, with respect to the bulk Pt interlayer distance is given to the right of the figures. The large sky blue and green spheres represent Pt and Ni atoms, the small red sphere represents the on-surface O atoms at the bridge site and the small black and purple spheres represent the sub-surface O atoms at the tetra and octa sites respectively.

Table 4.9: The calculated (average) bond lengths (Å) for the most stable on/sub-surface configurations on the Pt-Ni-Pt(100) surface at the θ_{tot} of 0.75, 1.00 and 1.25 ML. $d_{\mathrm{O_{onsurf}-Pt}}$(Å) is the distance between the on-surface oxygen and the nearest-neighbour first layer Pt atom, $d_{\mathrm{Pt-O_{sub}}}$(Å) is the distance between the nearest-neighbour first layer Pt atom and sub-surface oxygen, $d_{\mathrm{O_{sub}-Ni}}$(Å) is the distance between the sub-surface oxygen and the nearest-neighbour second layer Ni atom and $d_{\mathrm{Pt-Ni}}$(Å) is the distance between the Pt and Ni layers.

	0.75 ML	1.00 ML	1.25 ML
$d_{\mathrm{O_{onsurf}-Pt}}$	1.94	1.93	2.01
$d_{\mathrm{Pt-O_{sub}}}$	1.99	2.01	2.07
$d_{\mathrm{O_{sub}-Ni}}$	1.86	1.87	1.80
$d_{\mathrm{Pt-Ni}}$	2.65	3.16	2.57

Subsequently, the geometric structures, interlayer spacings and the calculated bond lengths for the stable on/sub-surface phases at the θ_{tot} of 0.75, 1.00 and 1.25 ML are examined further. Figure 4.15 and Table 4.8 illustrate these stable on/sub-surface phases. There was no significant buckling observed in the first Pt layer of all the on/sub-surface structures. This is in contrast with the Ni-Pt-Pt (100) and Pt (100) surfaces, suggesting that the sub-layer Ni atoms are stabilising the surface structure. The Pt-O bond lengths for the on-surface and sub-surface oxygens are similar while the Ni-O bond lengths are shorter for all considered oxygen coverages (Table 4.9). These bond lengths are also comparable to the on/sub-surface structures on the Ni-Pt-Pt(100) surface.

To date, there is no literature data to compare with the binding energies of all the studied oxygen interactions. A general observation from the present work show that the (111) surface binds oxygen more strongly compared to the (100) surface. Overall, the interaction of oxygen with the Pt-Ni-Pt surfaces showed lower binding energies compared to the Ni-Pt-Pt and Pt at the (111) and (100) surfaces. These low binding energies occur because the sublayer Ni is influencing the Pt-O bond on the Pt-Ni-Pt surfaces. The Pt-O bond becomes weaker, thereby leading to reduced oxygen poisoning effect and enhanced ORR activity on the surfaces.[16]

4.3.4 Statistical Thermodynamic Model

The statistical thermodynamic model that yields the (T, p) phase diagrams are evaluated for both the Ni-Pt-Pt and Pt-Ni-Pt surfaces at the (111) and (100) surfaces and compared to the Pt surfaces. The surface free energies required for the thermodynamic model are calculated from low pressure to real catalytic conditions using the approximation discussed in Section 2.4. Similar to the Pt surfaces, the surface free energies are calculated for the most stable adsorption energies for the oxygen coverage range of $\theta_{\mathrm{tot}}(0.25 \leq \theta_{\mathrm{tot}} \leq 2.00\mathrm{ML})$ over a temperature range from 100 K to 1000 K and a pressure range from 10^{-5} atm to 10^{5} atm. The (T, p) phase diagram of Ni-Pt-Pt and Pt-Ni-Pt surfaces are illustrated in Figure 4.16 and Figure 4.17. On all these surfaces, the phase diagrams differ from each other and the temperatures at which the oxygen coverage changes phase were different across the examined conditions.

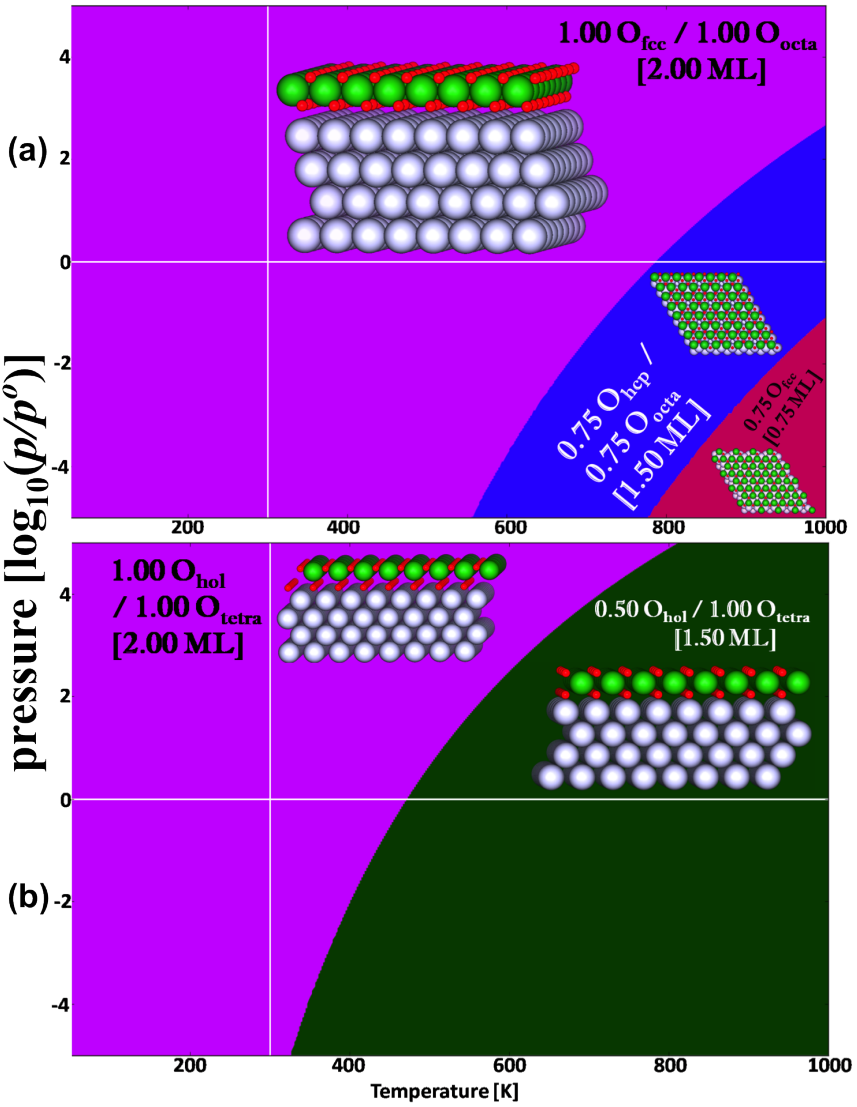

Figure 4.16: Phase diagram of (a) Ni-Pt-Pt(111) and (b) Ni-Pt-Pt(100) surfaces in equilibrium with O_2 gas phase. PEMFC operating conditions are labelled as 1 atm (horizontal white line) and 300 K (vertical white line).

Table 4.10: The temperatures (K) at which the oxygen coverage changes phase from the (T, p) thermodynamic phase diagram on the Ni-Pt-Pt(111) and Ni-Pt-Pt(100) surfaces at low pressure (10^{-5} atm), real catalytic condition (1 atm) and high pressure (10^{5} atm).

		pressure [atm]		
	phase change [ML]	10^{-5}	1	10^{5}
		Temperature [K]		
(111) surface	2.00 → 1.75	554	786	> 1000
	1.75 → 0.75	776	> 1000	-
(100) surface	2.00 → 1.50	355	470	810

On the Ni-Pt-Pt surfaces, the thermodynamically favoured structures on the (111) surface are the on/sub-surface configurations, (1.00 O_{fcc} + 1.00 O_{octa}) (2.00 ML) and (0.75 O_{hcp} + 0.75 O_{octa}) (1.50 ML) and the on-surface configuration, (0.75 O_{fcc}) (0.75 ML) while on the (100) surface, are the on/sub-surface configurations, (1.00 O_{hol} + 1.00 O_{tetra}) (2.00 ML) and (0.50 O_{hol} + 1.00 O_{tetra}) (1.50 ML) (Figure 4.16). Table 4.10 summarises the temperatures at which the oxygen coverage changes phase on the (111) and (100) surfaces at low pressure, real catalytic condition and high pressure. It can be seen that at low temperature and at all considered pressure, the on/sub-surface structures are likely to be seen on both the (111) and (100) surfaces. As the temperature increases, the on/sub-surface structure is favoured on the (100) surface while the surface structures changes with pressure on the (111) surface. In addition, a lower temperature range is noticed on the (100) surface compared to the (111) surface as the oxygen coverage changes phase. There is no complete desorption of oxygen from the Ni-Pt-Pt surfaces at all the considered pressures (10^{-5} to 10^{5} atm). At the operating temperature of a catalyst, 300 K (as indicated by the thick vertical white line), the 2.00 ML on/sub-surface structures will be observed on both surfaces. This signifies a rapid poisoning of the catalyst surface which will eventually lead to the instability of the PEM fuel cell.

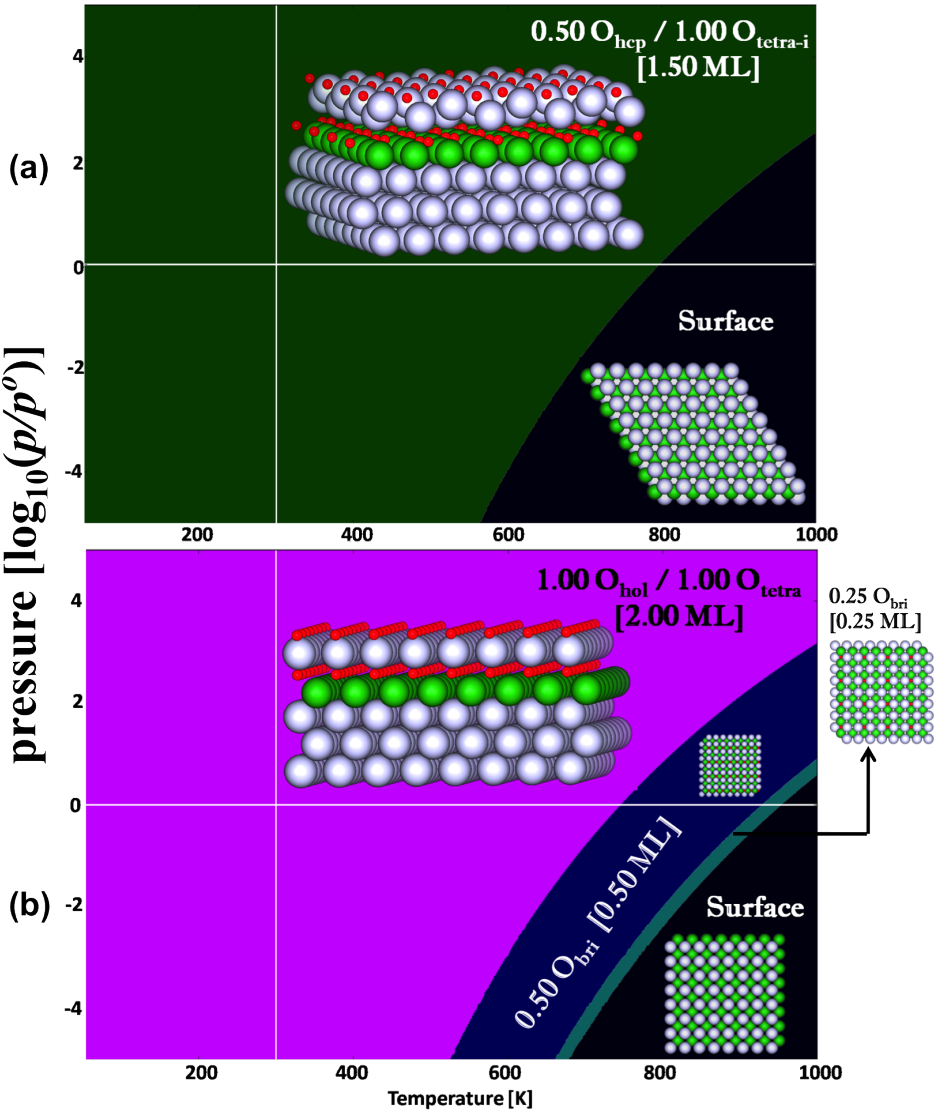

Figure 4.17: Phase diagram of (a) Pt-Ni-Pt(111) and (b) Pt-Ni-Pt(100) surfaces in equilibrium with O_2 gas phase. PEMFC operating conditions are labelled as 1 atm (horizontal white line) and 300 K (vertical white line).

Table 4.11: The temperatures (K) at which the oxygen coverage changes phase from the (T, p) thermodynamic phase diagram on the Pt-Ni-Pt(111) and Pt-Ni-Pt (100) surfaces at low pressure (10^{-5} atm), real catalytic condition (1 atm) and high pressure (10^{5} atm).

		pressure [atm]		
	phase change [ML]	10^{-5}	1	10^{5}
		Temperature [K]		
(111) Surface	1.50 → surface	562	796	>1000
(100) surface	2.00 → 0.50	524	742	>1000
	0.50 → 0.25	660	926	-
	0.25 → surface	678	952	-

Proceeding onto the Pt-Ni-Pt surfaces, the thermodynamically stable structure on the (111) surface is (0.50 O_{hcp} + 1.00 $O_{tetra-i}$) (1.50 ML) while the structures on the (100) surface are (1.00 O_{hol} + 1.00 O_{tetra}) (2.00 ML), (0.50 O_{bri}) (0.50 ML) and (0.25 O_{bri}) (0.25 ML) (Figure 4.17). Similar to the Ni-Pt-Pt surface, at low temperatures and all considered pressures, the on/sub-surface structures are stable but varies as the temperature is increased on the (111) and (100) surfaces. Table 4.11 indicates that the (111) surface changes phase at a lower temperature compared to the (100) surface. On both surfaces, it can be seen that oxygen will come off the surface at some point depending on the temperature and pressure. The desorption temperatures (at low pressure and standard operating pressures) identified on these surfaces are lower than those on the Pt surfaces (Figure 3.10). At the operating temperature of a catalyst, 300 K (as indicated by the thick vertical white line), the on/sub-surface structures will be observed on the two surfaces, similar to the Ni-Pt-Pt surfaces. Similarly to the Ni-Pt-Pt surfaces, the poisoning of the catalyst surface will occur due to the presence of the surface oxide-like structures.

There are no reported experimental or theoretical data where the thermodynamics of the Ni-Pt-Pt and Pt-Ni-Pt surfaces have been studied. However, it was found that between 298 K and 373 K, NiO islands ($\sim$2.00 ML thick) were formed on the Ag(100) surface.[29] This data was collected from LEIS, XPS, XPD, and LEED experiments. Other experimental results obtained by XPS and LEIS indicated a film of CoO growth on a $Pt_{80}Co_{20}$(100) surface, which also forms islands that relate to bulk cobalt monooxide.[30] This suggests that the current theoretical results are comparable with these experimental data and that the monolayer oxide films will most likely form on the catalyst surface during PEMFC operation. Overall, the presented phase diagrams for all the surfaces showed that the Ni-Pt-Pt surfaces will bind oxygen more strongly compared to the Pt-Ni-Pt and Pt surfaces. This agrees with the theoretical work presented by Menning *et al.* who predicted lower ORR activity on the Ni-Pt-Pt surfaces due to stronger bonds being formed between the surface metal and O atoms.[22] Therefore, the operation of the PEM fuel cell will degrade rapidly.

4.3.4.1 Free Energy as a Function of Potential

The free energy as a function of potential is obtained for the thermodynamically stable structures identified above for the Ni-Pt-Pt and Pt-Ni-Pt surfaces at the normal working conditions of a PEMFC, 300 K and 1 atm. The most likely structures on the catalyst surface are determined when potential (between 0.00 V and 1.50 V) is applied. Figure 4.18 shows the free energy as a function of potential for the Ni-Pt-Pt, Pt-Ni-Pt and Pt surfaces at the (111) and (100).

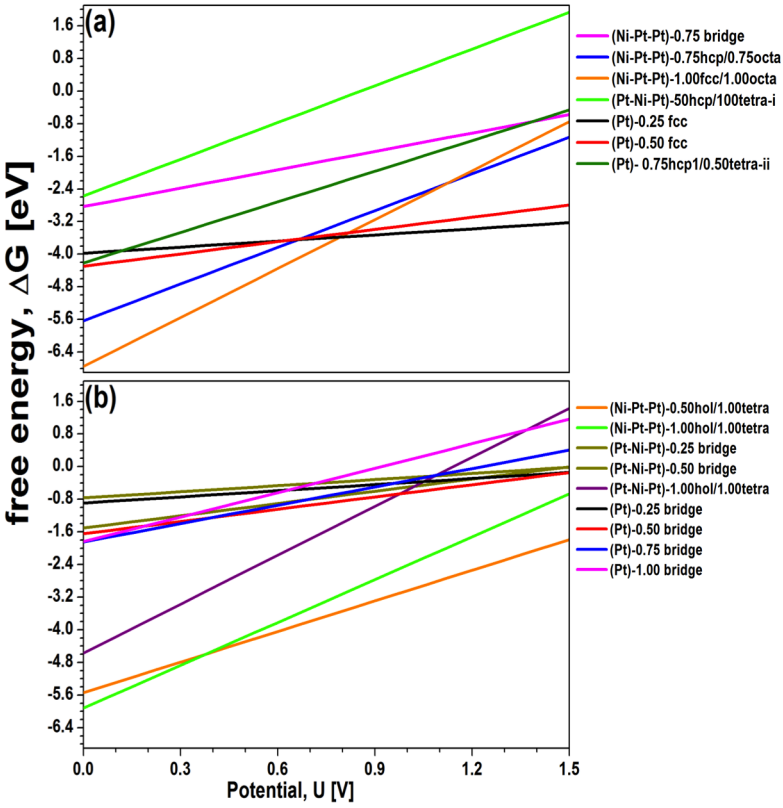

Figure 4.18: Free energy as a function of potential for the PEMFC operating conditions (300K and 1 atm) and for Ni-Pt-Pt, Pt-Ni-Pt and Pt on the (a) (111) and (b) (100) surfaces.

The surface composition changes as the applied potential is increased on the (111) and (100) surfaces. The structures expected to be observed on the catalyst surfaces are Ni-Pt-Pt (1.00 O_{fcc} + 1.00 O_{octa}) (2.00 ML) and Pt (0.25 O_{fcc}) (0.25 ML) on the (111) surface and Ni-Pt-Pt (1.00 O_{hol} + 1.00 O_{tetra}) (2.00 ML) and Ni-Pt-Pt (0.50 O_{hol} + 1.00 O_{tetra}) (1.50 ML) on the (100) surface. The stable structures on the (111) surface switches from the Ni-Pt-Pt to the Pt catalyst surface at 0.79 V while on the (100) surface, it switches at 0.40 V from the Ni-Pt-Pt 2.00 ML to the 1.50 ML. These results suggest that on the (111) surface and as the applied potential is increased, the top layer Ni atoms will leach from the catalyst surface to expose more Pt atoms for the ORR. This is consistent with the cyclic voltammetry experiment carried out between 0.00 V and 0.90 V, which found that Ni

leached from the PtNi catalyst surface exposing 20 % surface Pt.[10] As for the (100) surface, continuous oxygen adsorption on the catalyst surface will block surface sites, leaving fewer sites available for the ORR, thus preventing further reactions from proceeding. This will then lead to the eventual loss of activity and the degradation of the PEMFC.

4.3.5 Electronic Properties

4.3.5.1 Change in Work function, Dipole Moment and *d*-band Centre

Figure 4.19 and Figure 4.20 show the work function change, $\Delta\Phi$, surface dipole moment, μ, and the average d-band centre, ε_d, of the top layer (described in section 2.3.6) with respect to oxygen coverage for the Ni-Pt-Pt and Pt-Ni-Pt at the (111) and (100) surfaces. In addition, a plot showing the average d-band centre, ε_d, and the binding energies are shown for the studied oxygen coverages. The on-surface chemisorptions and the on/sub-surface configurations are evaluated for the most stable structures at the $\theta_{\mathrm{tot}}(0.25 \leq \theta_{\mathrm{tot}} \leq 2.00\mathrm{ML})$. On the Pt-Ni-Pt surface, results for the sub-surface tetra-i absorption site are included, due to its stability at high oxygen coverage.

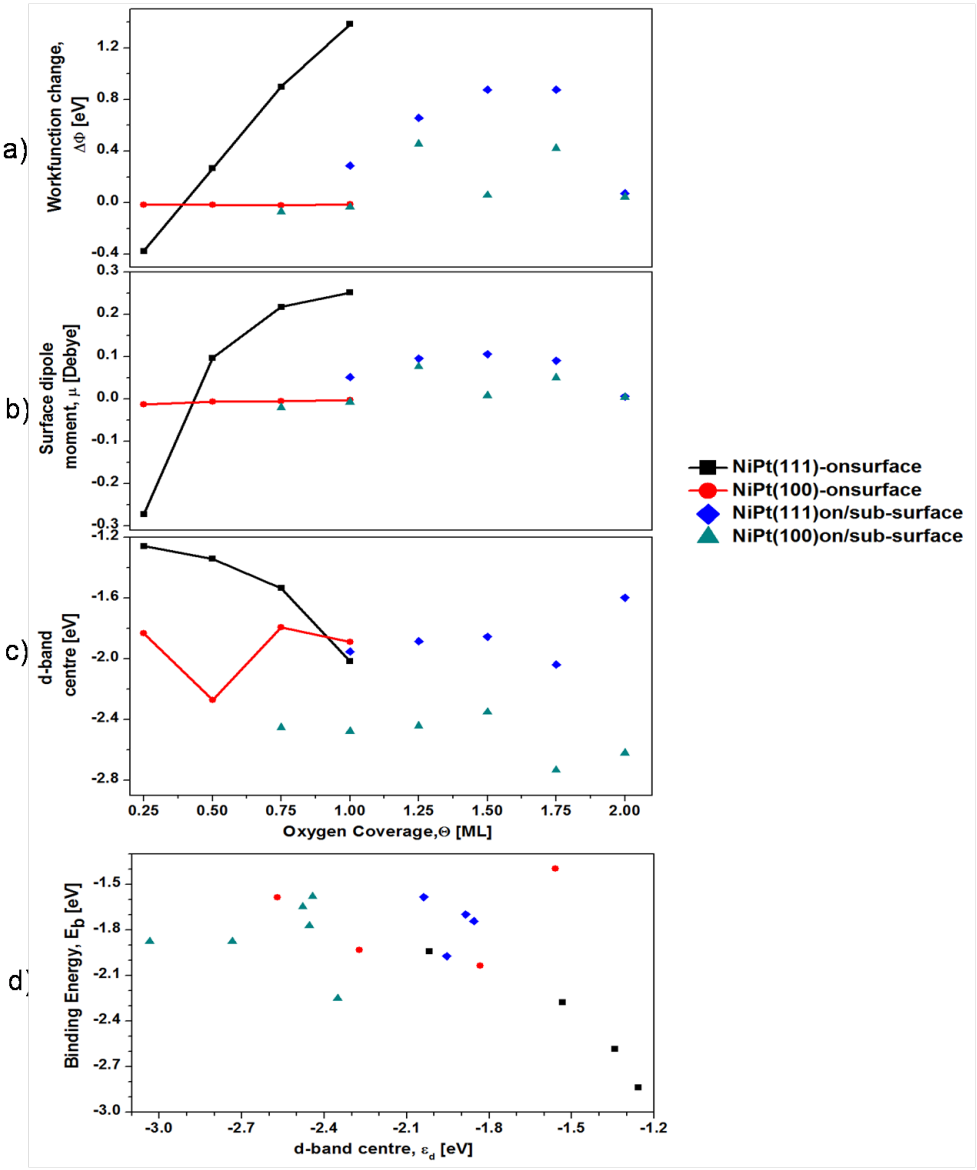

Figure 4.19: Electronic properties of Ni-Pt-Pt (111) and Ni-Pt-Pt (100) surfaces where a) change in the calculated work-function, $\Delta\Phi$, b) surface dipole moment, μ, and c) average d-band centre of the top Ni layer as a function of oxygen coverage for the most stable structures and d) the average d-band centre, ε_d, of the top Ni layer plotted as a function of the binding energies at the studied oxygen coverages.

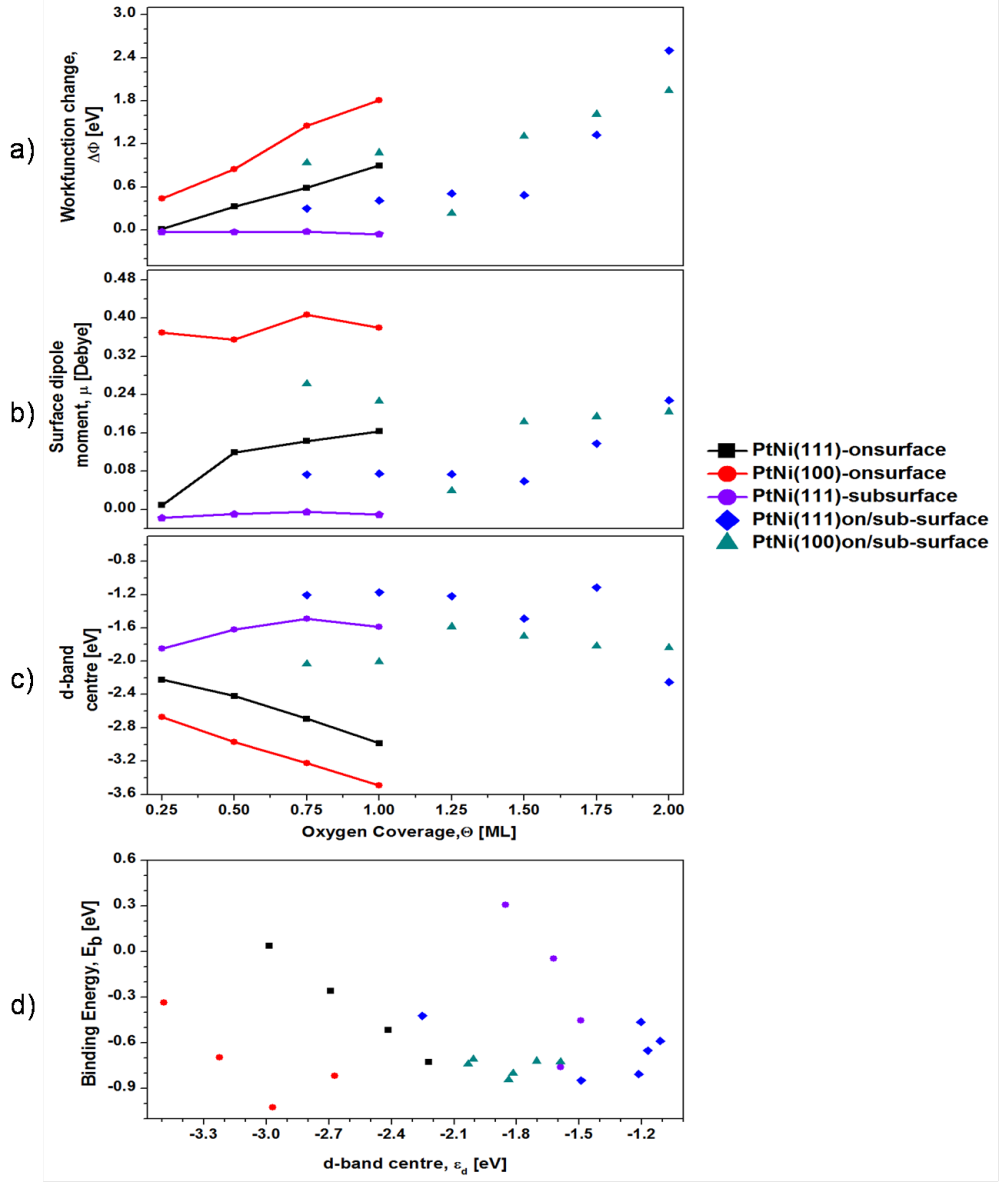

Figure 4.20: Electronic properties of Pt-Ni-Pt (111) and Pt-Ni-Pt (100) surfaces where a) change in the calculated work-function, $\Delta\Phi$, b) surface dipole moment, μ, and c) average d-band centre of the top Pt layer as a function of oxygen coverage for the most stable structures and d) the average d-band centre, ε_d, of the top Pt layer plotted as a function of the binding energies at the studied oxygen coverages.

There is a linear increase in the $\Delta\Phi$ with respect to oxygen coverage for all the on-surface adsorption on Ni-Pt-Pt and Pt-Ni-Pt surfaces except for Ni-Pt-Pt(100) surface (Figure 4.19a and Figure 4.20a). As for Ni-Pt-Pt(100) surface, the $\Delta\Phi$ is constant at the oxygen coverages between 0.25 ML and 1.00 ML. The $\Delta\Phi$ for the on-surface adsorption is higher on the Pt-Ni-Pt surface than on the Ni-Pt-Pt surface on the (111) surface, . As discussed in Section 3.5.1, the general increase in the work function change is mainly due to the electronegativity difference between Pt (2.28), Ni (1.91) and oxygen (3.44), which causes large charge transfer from the top-layer Pt/Ni atoms to the oxygen atoms, thereby yielding a large inward pointing surface dipole moment.[31,32] The constant $\Delta\Phi$ observed on the Ni-Pt-Pt(100) surface suggests that there may be a small charge transfer between the top-layer Ni atoms and the oxygen atoms. As the oxygen coverage increases on the surfaces, the negatively charged oxygens are forced apart to reduce the lateral electrostatic interactions between them, which then lead to a large polarisation (that is an increase in the electron charge transfer).[33] A small decrease in the $\Delta\Phi$ is observed for the sub-surface tetra-i absorption site (Figure 4.20a). This is because an outward pointing surface dipole moment is induced from the charge transfer between the oxygen and the top-layer Pt atoms.[33]

On Ni-Pt-Pt and Pt-Ni-Pt surfaces and at 0.75 ML and 1.00 ML, the $\Delta\Phi$ for the on/sub-surface structures are lower than the on-surface adsorption at the same oxygen coverage. This $\Delta\Phi$ was also observed for the pure Pt surfaces. This reflects the competition for the bonding charge between the sub-surface and on-surface oxygen atoms, which then creates less negatively charged on-surface oxygen atoms.[34] Above 1.00 ML, the workfunction change for the on/sub-surface structures increase steadily with oxygen coverage on the Pt-Ni-Pt surfaces. As for the Ni-Pt-Pt surface, the $\Delta\Phi$ for the on/sub-surface configuration at the (111) surface increases with oxygen coverage but falls at 2.00 ML while the values for the (100) surface are scattered. It is thought that these observations may be due to the direct influence of the Ni atoms present at either the top or sub-layer. Overall, the Pt-Ni-Pt surfaces have larger workfunction change compared to the Ni-Pt-Pt and Pt (Figure 3.12a) surfaces.

The surface dipole moment, μ, (Figure 4.19b and Figure 4.20b), increases with oxygen coverages on the Ni-Pt-Pt and Pt-Ni-Pt (111) surfaces. A constant μ is observed on Ni-Pt-Pt (100) at the oxygen coverages between 0.25 ML and 1.00 ML. On the Pt-Ni-Pt (100) surface, the μ varies for the on-surface adsorption between 0.25 ML and 1.00 ML while it is almost constant on the Pt-Ni-Pt (111) sub-surface tetra-i site. As for the on/sub-surface configurations, the μ slightly increase and decrease with oxygen coverage on the Pt-Ni-Pt (111) and Pt-Ni-Pt (100) surfaces while it somewhat levels off on Ni-Pt-Pt (111) and Ni-Pt-Pt (100) surfaces.

The average d-band centre of the topmost layer, ε_d, moves towards lower energies as the oxygen coverage increases for all the on-surface adsorption except for Ni-Pt-Pt (100) where it shifts to a higher energy above 0.75ML (Figure 4.19c and Figure 4.20c). This d-band centre trend is similar to the results obtained for the Pt surfaces. The on-surface adsorption on the (111) surface is higher on the Ni-Pt-Pt and Pt-Ni-Pt surfaces compared to the Pt surface. The reason for this result may be due to the influence of Ni atoms present and the geometric composition of the surface. The sub-surface tetra-i shows high energy movement with oxygen coverage while the on/sub-surface structures move up and down by a small quantity on both the Ni-Pt-Pt and Pt-Ni-Pt surfaces. Furthermore, there is no linear trend between the ε_d and the binding energies of all the structures (Figure 4.19d and Figure 4.20d). Nevertheless, there is a general correlation in that, the more negative ε_d corresponds to the weaker binding energy of that particular structure. The weakly bound structures are mainly the on-surface adsorption on the Ni-Pt-Pt (111) surface and the on/sub-surface configurations on the Pt-Ni-Pt (111) and Pt-Ni-Pt (100) surfaces. The Pt-Ni-Pt surfaces will bind oxygen more weakly, suggesting that the ORR will occur more easily on this surface compared to the Ni-Pt-Pt surface.

4.3.5.2 Electron density difference and Bader Analysis

In this section, the electron density differences, the Bader charges and the projected density of states (PDOS) for the thermodynamically stable structures are analysed.

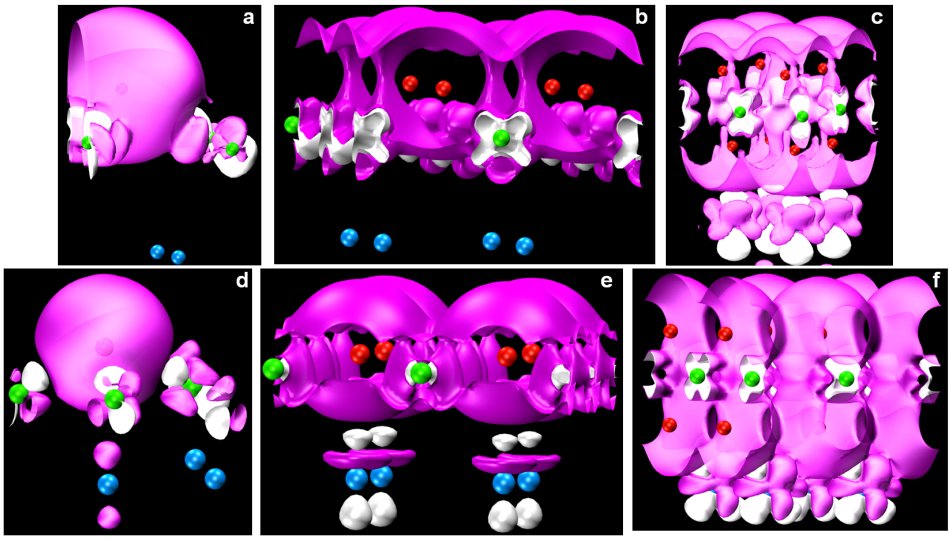

Figure 4.21: Calculated electron density differences for Ni-Pt-Pt (111) surface at a) 0.25 ML and b)1.00 ML on-surface adsorptions and c) (1.00 O_{fcc} + 1.00 O_{octa}) on/sub-surface and for Ni-Pt-Pt (100) surface at d) 0.25 ML and e) 1.00 ML onsurface adsorption and f) (1.00 O_{hol} + 1.00 O_{tetra}) on/sub-surface. The pink and white isosurfaces represent positive and negative electron density differences respectively. The blue, green and red spheres are Pt, Ni and O atoms respectively and the isosurface value is $\pm 0.045\ e\text{Å}^{-3}$.

Similarly to the Pt surfaces, Figures 4.21 and 4.22 illustrate the accumulation of electron charge densities on the oxygen atoms. These electron charge densities have been transferred from the nearest Ni or Pt atoms (showing a depletion of electron charge densities). The bonding interactions for all the on-surface adsorption (0.25 ML and 1.00 ML oxygen coverages) occur mainly with the top-layer Ni or Pt atoms while the sub-surface and on/sub-surface structures involve the second layer atoms. The main orbitals involved in the bonding of the high electronegative

oxygens are $5d$ and $3d$ orbitals present within the Pt and Ni atoms respectively. Overall, large electron charge densities are observed on the (100) for the Ni-Pt-Pt and Pt-Ni-Pt surfaces. This result is similar to the Pt (100) surface (Figures 3.13).

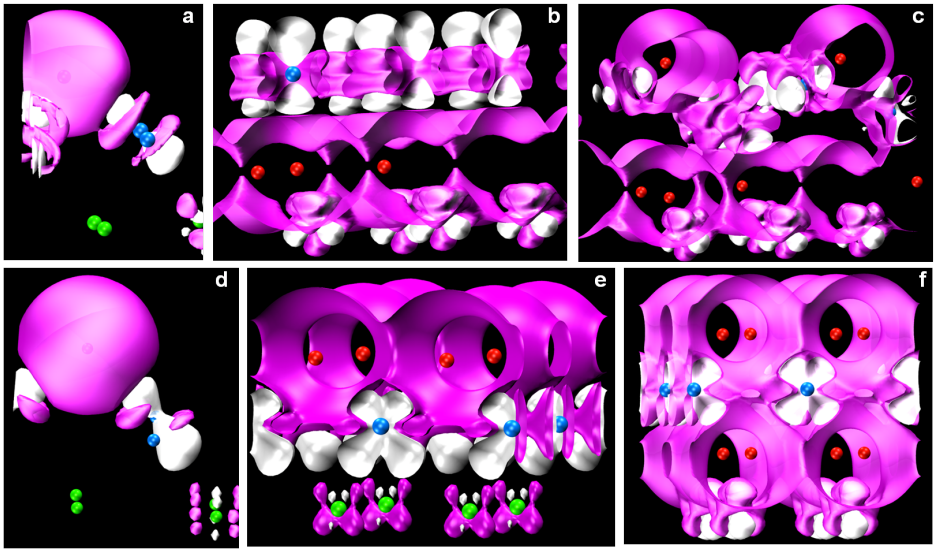

Figure 4.22: Calculated electron density differences for Pt-Ni-Pt (111) surface at a) 0.25 ML on-surface adsorption, b)1.00 ML sub-surface absorption and c) (0.50 O_{hcp} + 1.00 $O_{tetra-i}$) on/sub-surface and for Pt-Ni-Pt (100) surface at d) 0.25 ML and e) 1.00 ML on-surface adsorption and f) (1.00 O_{hol} + 1.00 O_{tetra}) on/sub-surface. The pink and white isosurfaces represent positive and negative electron density differences respectively. The blue, green and red spheres are Pt, Ni and O atoms respectively and the isosurface value is $\pm 0.045\ e\text{Å}^{-3}$.

Table 4.12 shows the Bader charges of the top two layers on the (111) and (100) surfaces for the Ni-Pt-Pt and Pt-Ni-Pt surfaces. The Bader charges for the Pt surfaces were also included for comparison. Generally, there is charge transfer from the transition metals, Pt and Ni onto the O atoms. On both surfaces (Ni-Pt-Pt and Pt-Ni-Pt) and for the clean slab, charges have been transferred from the Ni layer to the Pt layer. As for the on-surface adsorption, charges are transferred onto the O atoms from the Ni layer on the Ni-Pt-Pt surface and from the top two (Pt and Ni) layers on the Pt-Ni-Pt surface. Concerning the on/sub-surface structures, the

charges move from the top two (Pt and Ni) layers to the on-surface and sub-surface oxygens on both the Ni-Pt-Pt and Pt-Ni-Pt surfaces. Compared with the Pt surface, there is no dominant surface with the most charge transfer. However, more charge is moved from the Ni layer compared to the Pt layer. This can be explained by the electronegativity of all the atoms. Ni has the least electronegativity and so it is expected to donate more charge to the O atoms.

Table 4.12: Average Bader charges (e) of the top two layers on the (111) and (100) for Ni-Pt-Pt, Pt-Ni-Pt and Pt surfaces. The average Bader charges for the on-surface oxygen layer, (O_{onsurf}) and the sub-surface oxygen layer ($O_{subsurf}$) layer are also included. The nominal valence charges for Pt, Ni and O are 10, 10 and 6 electrons respectively.

		(111) surface				(100) surface			
		slab	0.25ML	1.00ML	2.00ML	slab	0.25ML	1.00ML	2.00ML
Ni-Pt-Pt	1st layer	9.83	9.58	8.97	8.53	9.79	9.50	8.98	8.70
	2nd layer	10.16	10.16	10.19	9.81	10.17	10.22	10.01	9.39
	O_{onsurf}	-	6.98	6.83	6.90	-	7.07	7.03	7.03
	$O_{subsurf}$	-	-	-	6.79	-	-	-	6.83
Pt-Ni-Pt	1st layer	10.24	10.00	9.79	9.42	10.25	10.02	9.45	8.82
	2nd layer	9.56	9.61	9.10	9.04	9.55	9.57	9.66	9.25
	O_{onsurf}	-	6.79	-	6.81	-	6.76	6.70	6.70
	$O_{subsurf}$	-	-	6.89	6.92	-	-	-	7.00
Pt	1st layer	10.04	9.83	9.20	8.49	10.05	9.85	9.28	9.04
	2nd layer	9.96	9.99	10.05	9.87	9.97	9.98	10.06	9.52
	O_{onsurf}	-	6.74	6.73	6.79	-	6.75	6.67	6.64
	$O_{subsurf}$	-	-	-	6.89	-	-	-	6.79

Figures 4.23 and 4.24 show the PDOS plots for the Ni-Pt-Pt and Pt-Pt-Ni at the (111) and (100) surfaces. The clean surfaces and the 0.25 ML oxygen coverage are examined. The NiPt and PtNi plots show the PDOS for the top two layers on the Ni-Pt-Pt and Pt-Ni-Pt surfaces. The interacting and non-interacting plots are the PDOS for the top two layers which are interacting and not interacting respectively with the O atom. The PtNi-O/O and NiPt-O/O plots illustrate the PDOS of the O atom interacting with the surfaces. Finally the gas phase O is showing the

energy levels of the O atom and the ε_{F} is determined by taking the experimental first ionisation energy of O atom from the highest occupied molecular orbital (HOMO).

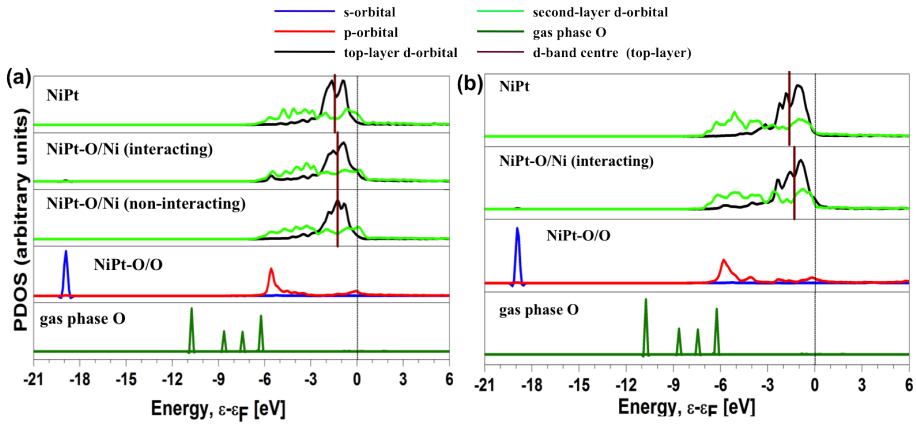

Figure 4.23: Projected density of states (PDOS) for (a) O/Ni-Pt-Pt(111) and (b) O/Ni-Pt-Pt(100) systems at 0.25 ML oxygen coverage. The Fermi energy is indicated by the vertical dotted line.

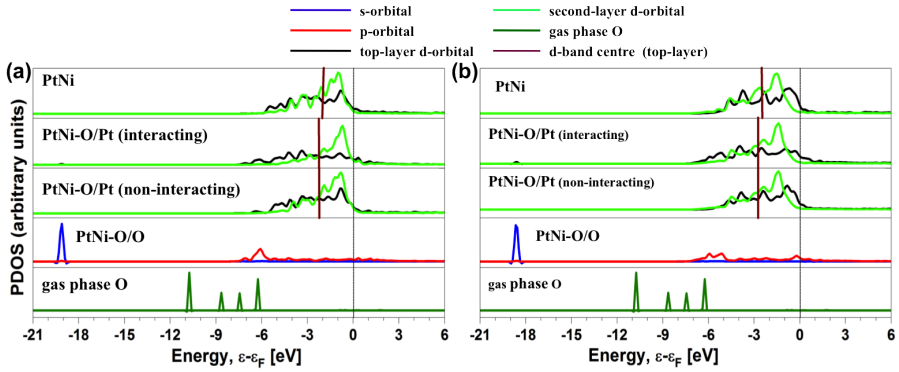

Figure 4.24: Projected density of states (PDOS) for (a) O/Pt-Ni-Pt(111) and (b) O/Pt-Ni-Pt(100) systems at 0.25 ML oxygen coverage. The Fermi energy is indicated by the vertical dotted line.

Similar to the Pt surfaces, a sharp O $2s$ orbital peak is observed on all the NiPt/O and PtNi/O plots at around -19 eV below the Fermi level. In addition, there is a bonding hybridisation between the O $2p$ orbital and the d-orbital from either

the Ni or Pt atoms. This is shown by the broadening of the O $2p$ orbital on the NiPt/O and PtNi/O plots. The O $2p$ orbital on the Pt-Ni-Pt surfaces are wider than the Ni-Pt-Pt surfaces, suggesting that the oxygen interactions on the Pt-Ni-Pt surfaces are weaker. The bonding states on all the surfaces can be found at the energy region between -6.5 eV and -4.5 eV, the lower section of the d-orbital. In all cases, the non-interacting first-layer d-orbital has the same PDOS to its clean counterpart. The second-layer (Pt or Ni) does not take part in the bonding process on all the surfaces except on Pt-Ni-Pt (111), where there is a slight shift of the d-orbital. The d-band centre for the Ni-Pt-Pt oxygen covered surfaces is higher than the clean surface while for the Pt-Ni-Pt, it is lower than the oxygen covered surfaces.

4.3.6 Comparison between Ni-Pt-Pt and Pt-Ni-Pt surfaces

The oxidations of Ni-Pt-Pt and Pt-Ni-Pt surfaces are significantly different from each other. The discussions so far illustrate that the (100) surface binds oxygen more weakly than the (111) surface. In addition, the Pt-Ni-Pt surface will bind oxygen more weakly than the Ni-Pt-Pt surface on both the (111) and (100) surfaces. This suggests that the Pt-Ni-Pt catalyst surface is less blocked by the adsorbed oxygen atom, thereby generating higher ORR activity. This result correlates with experimental and theoretical work, which showed that the Pt-Ni-Pt configuration exhibited increased activity for the ORR because the Pt-Ni-Pt configuration binds atomic oxygen and hydroxyl groups more weakly than pure Pt.[4,22]

The next stage is to understand the surface composition and the stability of binding oxygen to the Ni-Pt-Pt and Pt-Ni-Pt surfaces. This will determine the configuration that will enhance the ORR activity. It is believed that either Pt or Ni will be enriched to the surface in the presence of oxygen.[35] To determine which surface will be present, the surface segregation energy (Eq 2.25) is calculated for the Ni-Pt-Pt and Pt-Ni-Pt surfaces in the presence of oxygen at the studied θ_{tot} between 0.25 ML and 2.00 ML. The stable structures for the on-surface adsorption and the on/sub-surface structures are used for the investigation.

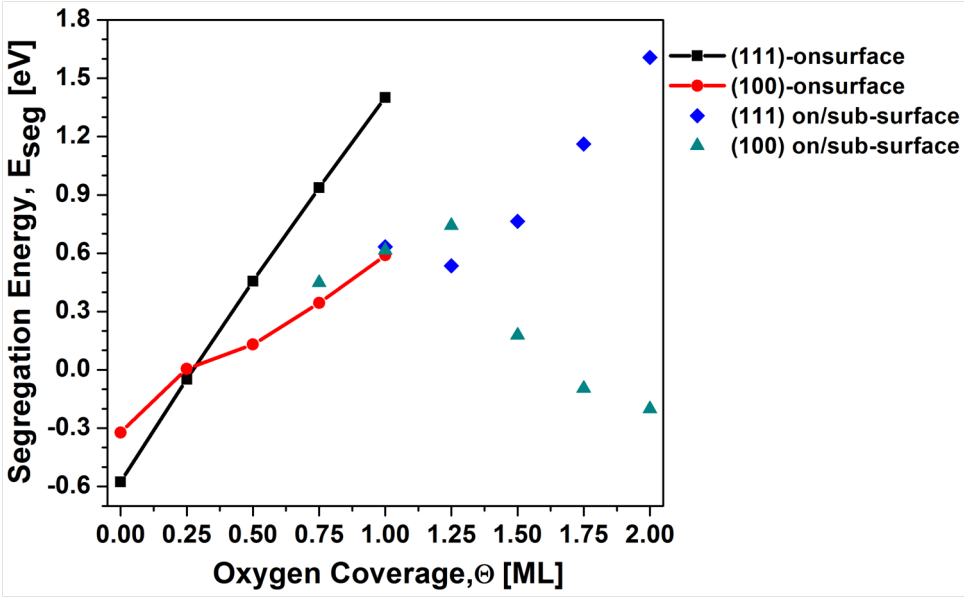

Figure 4.25: The segregation energies between Ni-Pt-Pt and Pt-Ni-Pt for the (111) and (100). Negative segregation energies mean Pt-rich surface while positive segregation energies mean Ni-rich surface.

The graph (Figure 4.25) above illustrates that in the absence of oxygen, a Pt-rich surface is present. At 0.25 ML and for the (111) and (100) surfaces, the segregation energies are negative, revealing a Pt-rich surface. As the oxygen coverage increases above 0.25 ML for the on-surface adsorption, the surface configuration switches to a Ni-rich surface. These results agree with both theoretical calculations and experiments (using AES and HEELS techniques) performed by Menning *et al.* on the (111) and (100) surfaces, which showed that in the absence of oxygen, a Pt-rich surface is observed while at 0.5 ML, a Ni-rich surface is noticed.[22,25] Higher segregation energies are obtained for the on-surface adsorptions on the (111) surface compared those on the (100) surface. As for the on/sub-surfaces, the segregation energies for the (111) surface increase while for the (100) surface, they decrease as the oxygen coverages increases to 2.00 ML. This signifies that the on/sub-surface phases on the (111) surface are Ni-rich while those on the (100) surface become Pt-rich above 1.75 ML. The gradual structural transformation of Pt-Ni-Pt to Ni-Pt-Pt is expected to contribute to the deactivation of the surface catalyst during the PEMFC operations. Although the on/sub-surface

configurations on the (111) surface showed Pt enrichment, it is believed that the surface catalyst will be poisoned because of the significant amount of oxygen atoms present.

4.4 Conclusions and Implications to PEMFC

A theoretical investigation into the stability and structural behaviour of Ni-Pt-Pt and Pt-Ni-Pt monolayer bimetallic alloy surfaces within the oxidising environment showed that these configurations exhibit entirely different characteristics. Similar attributes, however, were observed for the (111) and (100) surfaces of the same monolayer bimetallic alloy configurations. Overall, it was observed that the (100) surface binds oxygen more weakly compared to the (111) surface. For all the on-surface adsorptions, the binding energies decrease as the oxygen coverage increases. This is mainly due to the lateral repulsion interactions between the oxygen atoms. The monolayer bimetallic alloy surfaces are generally unstable when oxygen is purely sub-surface except for the Pt-Ni-Pt (111) surface. On the Pt-Ni-Pt (111) surface, it was observed that critical on-surface oxygen coverage of 0.68 ML is required before oxygen occupy the sub-surface region. Generally, the interaction of oxygen with the Pt-Ni-Pt surfaces showed lower binding energies compared to the Ni-Pt-Pt at the (111) and (100) surfaces. This occurs because the sublayer Ni is influencing the Pt-O bond on the Pt-Ni-Pt surfaces. This Pt-O bond becomes weaker, thereby leading to reduced oxygen poisoning effect and enhanced ORR activity on the surfaces.

The thermodynamic stability does suggest that the on/sub-surface configurations between the oxygen coverages of 1.50 ML and 2.00 ML will be present at the relevant catalytic conditions (300 K and 1 atm). In addition, when potential (0.00 V to 1.50 V) is included, the top layer Ni atoms will leach from the Ni-Pt-Pt (111) catalyst surface to expose more Pt atoms for the oxygen reduction reaction. As for the (100) surface, when the applied potential is increased, continuous oxygen adsorption on the catalyst surface will block the surface sites, thus preventing further

oxygen reduction reactions from proceeding and the eventual loss of activity. For these reasons, both the Ni-Pt-Pt and Pt-Ni-Pt monolayer bimetallic alloy surfaces are not the ideal catalyst to replace Pt for the oxygen reduction reaction because they will cause the eventual degradation of the PEMFC during operation. However, the Ni-Pt-Pt catalyst surface may be acceptable because of the Ni leaching from the surface catalyst.

In the next chapter, the stability and structural behaviour of Pt_3Ni and Pt_3Ni-$Pt_{\mathbf{skin}}$ alloy surfaces will be investigated. The thermodynamically stable surface, (111) will be used to study the effect of the alloying composition and its relative propensity of forming surface oxide film in an oxidising environment.

References

[1] Jacobson, M.; Colella, W.; Golden, D. *Science* **2005**, *308*, 1901–1905.

[2] Zhou, W.; Yang, X.; Vukmirovic, M.; Koel, B.; Jiao, J.; Peng, G.; Mavrikakis, M.; Adzic, R. *Journal of the American Chemical Society* **2009**, *131*, 12755–12762.

[3] Zhang, J.; Vukmirovic, M.; Xu, Y.; Mavrikakis, M.; Adzic, R. *Angewandte Chemie-International Edition* **2005**, *44*, 2132–2135.

[4] Toda, T.; Igarashi, H.; Uchida, H.; Watanabe, M. *Journal of the Electrochemical Society* **1999**, *146*, 3750–3756.

[5] Watanabe, M.; Wakisaka, M.; Yano, H.; Uchida, H. Analyses of Oxygen Reduction Reaction at Pt-Based Electrocatalysts. *Proton Exchange Membrane Fuel Cells 8, Pts 1 and 2*, 2008; pp 199–206, 8th Symposium on Proton Exchange Membrane Fuel Cells, Honolulu, HI, OCT, 2008.

[6] Balbuena, P.; Altomare, D.; Vadlamani, N.; Bingi, S.; Agapito, L.; Seminario, J. *Journal of Physical Chemistry A* **2004**, *108*, 6378–6384.

[7] Paulus, U.; Wokaun, A.; Scherer, G.; Schmidt, T.; Stamenkovic, V.; Markovic, N.; Ross, P. *Electrochimica Acta* **2002**, *47*, 3787–3798.

[8] Yang, H.; Vogel, W.; Lamy, C.; Alonso-Vante, N. *Journal of Physical Chemistry B* **2004**, *108*, 11024–11034.

[9] Balbuena, P.; Altomare, D.; Agapito, L.; J.M., S. *Journal of Physical Chemistry B* **2003**, *107*, 13671–13680.

[10] Paulus, U.; Wokaun, A.; Scherer, G.; Schmidt, T.; Stamenkovic, V.; Radmilovic, V.; Markovic, N.; Ross, P. *Journal of Physical Chemistry B* **2002**, *106*, 4181–4191.

[11] Marković, N.; Gasteiger, H.; Ross, P. N. *Journal of Electrochemistry Society* **1997**, *144*, 1591–1597.

[12] Calvo, S. R.; Balbuena, P. B. *Surface Science* **2007**, *601*, 165–171.

[13] Callejas-Tovar, R.; Balbuena, P. B. *Surface Science* **2008**, *602*, 3531–3539.

[14] Stamenković, V. R.; Mun, B. S.; Arenz, M.; Mayrhofer, K. J. J.; Lucas, C. A.; Wang, G.; Ross, P. N.; Markovic, N. M. *Nature Materials* **2007**, *6*, 241–247.

[15] Hyman, M. P.; Medlin, J. W. *Journal of Physical Chemistry C* **2007**, *111*, 17052–17060.

[16] Xu, Y.; Ruban, A.; Mavrikakis, M. *Journal of the Americal Chemican Society* **2004**, *126*, 4717–4725.

[17] Hartmann, H.; Diemant, T.; Bergbreiter, A.; Bansmann, J.; Hoster, H. E.; Behm, R. J. *Surface Science* **2009**, *603*, 1439–1455.

[18] Kitchin, J. R.; Norskov, J. K.; Barteau, M. A.; Chen, J. G. *Physical Review Letters* **2004**, *93*, 156801.

[19] Stamenković, V.; Schmidt, T. J.; Ross, P. N.; Marković, N. M. *Journal of Electroanalytical Chemistry* **2003**, *554*, 191–199.

[20] Stamenković, V. R.; Fowler, B.; Mun, B. S.; Wang, G.; Ross, P. N.; Lucas, C. A.; Marković, N. M. *Science* **2007**, *315*, 493–497.

[21] Stamenković, V.; Schmidt, T. J.; Ross, P. N.; Marković, N. M. *Journal of Physical Chemistry B* **2002**, *106*, 11970–11979.

[22] Menning, C.; Hwu, H.; Chen, J. *Journal of Physical Chemistry B* **2006**, *110*, 15471–15477.

[23] Fowler, B.; Lucas, C. A.; Omer, A.; Wang, G.; Stamenkovic, V. R.; Markovic, N. M. *Electrochimica Acta* **2008**, *53*, 6076–6080.

[24] Wang, G. F.; Van Hove, M. A.; Ross, P. N.; Baskes, M. I. *Journal of Chemical Physics* **2005**, *122*, 024706.

[25] Menning, C.; Chen, J. *Journal of Chemical Physics* **2008**, *128*, 164703.

[26] Kitchin, J.; Norskov, J.; Barteau, M.; Chen, J. *Journal of Chemical Physics* **2004**, *120*, 10240–10246.

[27] Escaño, M. C.; Nguyen, T. Q.; Nakanishi, H.; Kasai, H. *Journal of Physics-Condensed Matter* **2009**, *21*, 492201.

[28] Escaño, M. C.; Gyenge, E.; Nakanishi, H.; Kasai, H. *Journal of Nanoscience and Technology* **2011**, *11*, 2944–2951.

[29] Caffio, M.; Cortigiani, B.; Rovida, G.; Atrei, A.; Giovanardi, C. *Journal of Physical Chemistry B* **2004**, *108*, 9919–9926.

[30] Bardi, U.; Atrei, A.; Rovida, G.; Ross, P. N. *Surface Science* **1991**, *251*, 727–730.

[31] Benesh, G. A.; Liyanage, L. S. G. *Surface Science* **1992**, *261*, 207–216.

[32] Lide, D. R. *CRC Handbook of Chemistry and Physics*, 89th Edition ed.; CRC Press, 2008.

[33] Attard, G.; Barnes, C. *Surfaces (Oxford Chemistry Primers)*; Oxford University Press Inc., 2006; pp 62–65.

[34] Todorova, M.; Reuter, K.; Scheffler, M. *Physical Review B* **2005**, *71*, 195403.

[35] Greeley, J.; Nørskov, J.; Mavrikakis, M. *Annual Review of Physical Chemistry* **2002**, *53*, 319–348.

Chapter 5

Coverage effects on Pt_3Ni and Pt_3Ni-Pt_{skin} (111) surfaces

5.1 Introduction

This chapter will discuss the results obtained from investigating the oxygen interactions on $Pt_3Ni(111)$ and Pt_3Ni-$Pt_{\mathbf{skin}}(111)$ surfaces. The Pt_3Ni-$Pt_{\mathbf{skin}}$ surface consists of a Pt-rich layer on the Pt_3Ni bulk structure. Pt_3Ni and Pt_3Ni-$Pt_{\mathbf{skin}}$ surfaces have been selected because research indicates a higher catalytic activity on these surfaces compared to the monolayer bimetallic alloy (MBA) surfaces studied in the previous chapter (Chapter 4).[1–3] In addition, the surface composition is believed to affect the oxidation reaction. Experiments have shown that the so-called "$Pt_{\mathbf{skin}}$" forms on most alloy surfaces and have demonstrated excellent ORR activity and durability properties compared to the Pt_3Ni surface.[4,5]

Comparison of the two surfaces is investigated for the on-surface adsorption, on-surface mixed sites adsorption, sub-surface absorption and the tendency for form-

ing thin film surface oxide-like structures. As well as studying the oxygen interaction on these surfaces, the relative thermodynamic stabilities of the surface compositions are examined in relation to oxygen in the gas phase for conditions extending from ultrahigh vacuum to conditions of technological relevance. In addition, the modification of the surfaces due to the Ni alloying element is explored. This is assumed to contribute to the enhanced activities observed on these alloy surfaces.[6,7] From these results, it was found that oxygen interacts on the two surfaces differently. The Pt_3Ni-$Pt_{\mathbf{skin}}$ surface binds oxygen more weakly than the Pt_3Ni surface. In addition, the segregation energy suggests that the Pt_3Ni terminated surface will dominate when the oxygen coverage is increased. This is because there is a thermodynamic tendency for Ni to segregate to the surface in an oxidising environment. Thermodynamically, it is shown that at technological relevant conditions (300 K and 1 atm), the two surfaces exhibit thin surface-like oxide structures.

5.2 Computational Methods

All calculations are performed using DFT as implemented in VASP with the same functional and parameters as the calculations presented in the previous chapters (Sections 3.2.1 and 4.2). Spin polarisation was included in the calculations to take into account the presence of magnetic moments in the system due to the Ni atoms. To be consistent with the Pt and Pt/Ni-MBA surface calculations presented in Chapters 3 and 4, the present calculations were performed within a 2x2 supercell, a five-layer slab of four atoms in each layer with a *k-point* mesh of 8x8x1, which converges the energy to within 0.01 meV. The positions of the atoms in the top three layers were allowed to relax, while the bottom two layers were fixed at the calculated bulk positions and a vacuum thickness of 8 Å separates each successive slab.

In a similar way to previous chapters, the oxygen atoms were allowed to move freely in all directions during the energy minimisation until the lowest energy

configuration was attained. The binding energy, E_b per oxygen atom is defined as Eq. 2.24 and the convergence criteria for the electronic self-consistent energy and the ionic forces are set to 10^{-5} eV and 0.02 eV $Å^{-1}$, respectively.

5.3 Results and Discussion

5.3.1 Clean Pt_3Ni and Pt_3Ni-Pt_{skin} structures on the (111) surfaces

In order to investigate the interactions of oxygen on the Pt_3Ni alloy surfaces, the initial parameters required for further calculations were determined for bulk Pt_3Ni. Bulk Pt_3Ni has been reported experimentally to exhibit a close-packed face-centred cubic (fcc) structure[6] which was then modelled by replacing one of the four Pt atoms in the cubic fcc unit cell with a Ni atom. At a *k-point* grid of 16x16x16, the calculated bulk lattice constant, a_o, (GGA-PBE) is 3.88 Å (neglecting zero-point vibrations), the bulk modulus, B_o, is 2.37 Mbar (obtained using the Murnaghan equation of state) and the cohesive energy, E_o, is -4.51 eV. The calculated lattice constant is the same as other calculated GGA-PBE and GGA-PW91 results[8,9] and agrees with the experimental value of 3.845 Å.[10] These results are also compared to the previously studied (Chapter 3) Pt lattice constant, bulk modulus and cohesive energy, which are 3.98 Å, 2.28 Mbar and -5.90 eV respectively. From these values, there are small differences between the alloyed Pt_3Ni and Pt. This shows that there is a contraction of the Pt_3Ni lattice, which is expected because of the size differences between the Pt and Ni atoms.

The (111) surface was then cleaved from the bulk and two models of the Pt_3Ni alloy were constructed (Figure 5.1). The first model is the Pt_3Ni bulk alloy and contains three Pt atoms and one Ni atom in each layer. The second model is the Pt_3Ni-Pt_{skin} alloy where the first layer consists entirely of Pt atoms; the second

layer is enriched in Ni and contains two Pt atoms and two Ni atoms and the bulk Pt_3Ni alloy compositions for all other layers. This model retains the bulk stoichiometry and accurately models the experimental observation of Pt enrichment and depletion in the first and second layers for many Pt-3d alloys such as Pt-Co and Pt-Fe.[5,10,11]

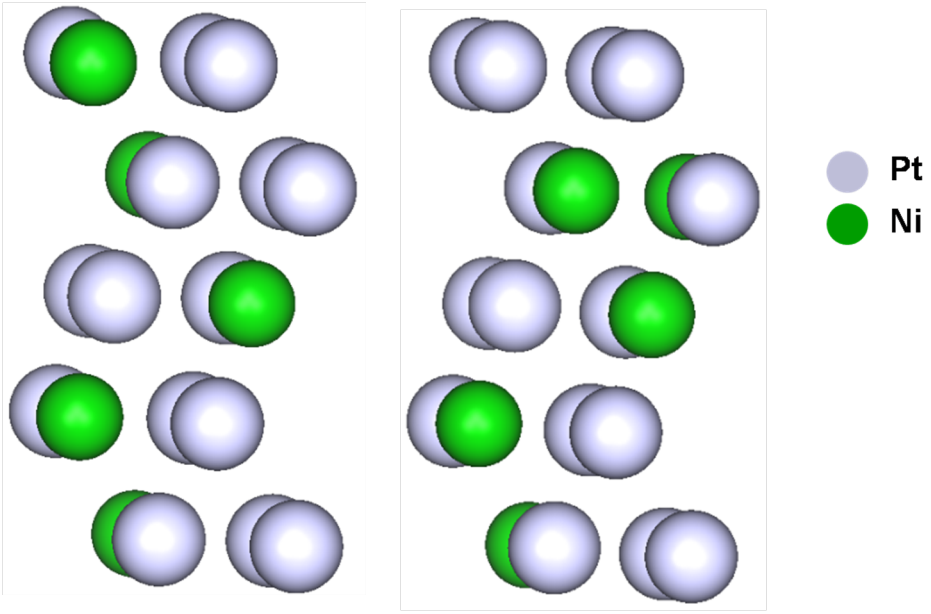

Figure 5.1: Two models of the Pt_3Ni alloy surfaces. Pt_3Ni bulk alloy (left) and Pt_3Ni-$Pt_{\mathbf{skin}}$ alloy (right).

The clean surfaces for the two Pt_3Ni alloy models were allowed to relax to their lowest energy structures. Table 5.1 lists the change in the interlayer spacings, $\delta_{i,j}$, between layers i and j with respect to the bulk interlayer distance, d_0 and also compared the results with the clean Pt (111) surface. On the Pt_3Ni-$Pt_{\mathbf{skin}}$ surface, a more negative change is observed for the δ_{23} compared to those on the Pt_3Ni surface. This change in interlayer spacings may be due to the strong interaction of the mixed second layer with the top Pt-skin layer. The change in interlayer spacings for the Pt(111) surface is similar to the Pt_3Ni-$Pt_{\mathbf{skin}}$ surface but quite different to the Pt_3Ni surface. The differences observed for the interlayer spacings between the Pt_3Ni-alloy surfaces and Pt surface occur because Ni is incorporated into the

present study of the Pt_3Ni-alloy surfaces. The workfunction for the Pt_3Ni surface is slightly smaller than that obtained for the Pt_3Ni-$Pt_{\mathbf{skin}}$ surface. However, the workfunction for the Pt_3Ni-$Pt_{\mathbf{skin}}$ surface is comparable to the clean Pt (111) surface.

Table 5.1: The average change in interlayer spacings (%) and workfunction (eV) of $Pt_3Ni(111)$, Pt_3Ni-$Pt_{\mathbf{skin}}(111)$ and Pt(111) surfaces. d_0(Å) is the bulk Pt_3Ni and Pt interlayer distance (Å), $\delta_{12}(\%)$ is the change in the interlayer spacing between the first and second layer and $\delta_{23}(\%)$ is the change in the interlayer spacing between the second and third layer spacing, Φ(eV) is the workfunction

	Pt_3Ni	Pt_3Ni-Pt_{skin}	Pt
δ_0	2.24		2.30
δ_{12}	-0.27	+0.48	+0.53
δ_{23}	-0.84	-3.18	-1.40
Φ	5.47	5.60	5.67

5.3.2 On-surface Adsorption of Atomic Oxygen on the (111) surfaces of Pt_3Ni and Pt_3Ni-$Pt_{\mathbf{skin}}$ Alloys

The most stable oxygen adsorption sites have been investigated on the Pt_3Ni (111) and Pt_3Ni-$Pt_{\mathbf{skin}}$ (111) surfaces, analogous to those studied on Pt and Pt/Ni-MBA surfaces (Chapters 3 & 4). The binding energies are non-zero-point corrected energies relative to the gas-phase O_2 molecule for the oxygen coverage range of $\theta_{\mathrm{tot}}(0.25 \leq \theta_{\mathrm{tot}} \leq 1.00\mathrm{ML})$. Figure 5.2 shows the high symmetry adsorption sites of an isolated O atom modelled on the two surfaces. The Pt_3Ni alloy surfaces differ from the Pt/Ni-MBA surfaces because there are two different adsorption sites for each high symmetry on-surface site. On the Pt_3Ni and Pt_3Ni-$Pt_{\mathbf{skin}}$ surfaces, there are two different fcc, hcp, bridge and top sites, where the oxygen atom can bind to either the Pt or Ni surface atoms.

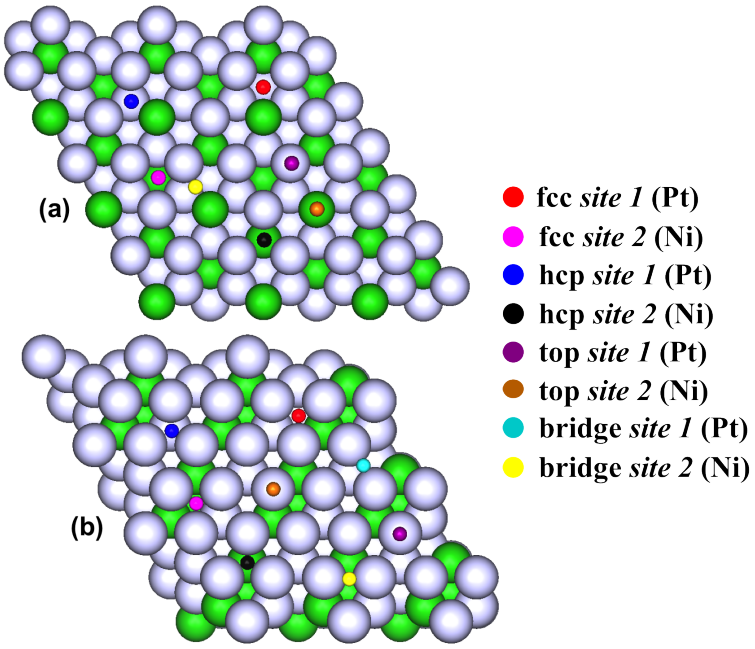

Figure 5.2: Adsobates at adsorption sites on (a) Pt_3Ni (111) and (b) Pt_3Ni-$Pt_{\mathbf{skin}}$(111) surfaces (top views).

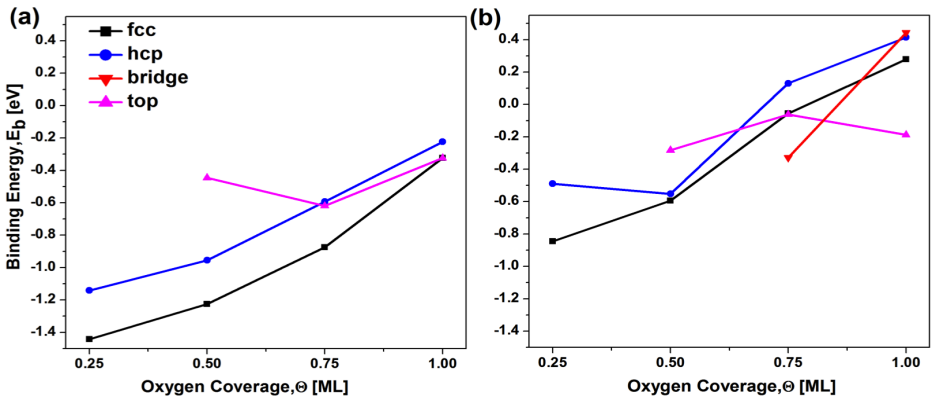

Figure 5.3: On-surface adsorption binding energies of oxygen on (a) Pt_3Ni(111) and (b) Pt_3Ni-$Pt_{\mathbf{skin}}$(111) surfaces at various oxygen coverages.

Figure 5.3 summarises the most stable adsorption energies as a function of oxygen coverage on the two surfaces at 0 K. On the Pt_3Ni surface, the three-fold fcc site is the preferred adsorption site. This is in agreement with other DFT calculations

performed at θ_{tot} of 0.25 ML.[12,13] The observed fcc binding site is also consistent with the Pt(111) and the Pt/Ni(111)-MBA surfaces. As in the case of Pt(111) and Pt-Ni-Pt(111), the bridge site is unstable and oxygen adsorbed on that site relaxes into the neighbouring fcc site. At the θ_{tot} of 0.25 ML, the top site is also unstable towards the nearest hcp site. In addition, at the fcc and hcp adsorption sites, the binding energies decrease steadily as the oxygen coverage increases. As explained in Chapter 3, the decrease in binding energies is mainly due to the metal atom interacting with more oxygen atoms at the same time.

As for the Pt_3Ni-$Pt_{\mathbf{skin}}$ surface, the most stable binding site changes as the oxygen coverage increases. At the θ_{tot} of 0.25 and 0.50 ML, the three-fold fcc-hollow site is the most stable. As the oxygen coverage increases to 0.75 ML, the binding site switches to the two-fold bridge site followed by the top site at 1.00 ML. The adsorption of oxygen at 0.25 ML at the fcc site is in agreement with the DFT calculation performed by Ma *et al.*[12] This result showing changes in the adsorption sites as the oxygen coverage increases is peculiar to the Pt_3Ni-$Pt_{\mathbf{skin}}$ surface. All other surfaces studied within this thesis, showed that the fcc site is the most stable adsorption site. It is interesting to note that the top site at the 1.00 ML is considerably more stable than the other adsorption sites. This could be due to the O_2-like formation [O-O is 1.35 Å] that occurs, thereby stabilising the surface (Figure 5.4).

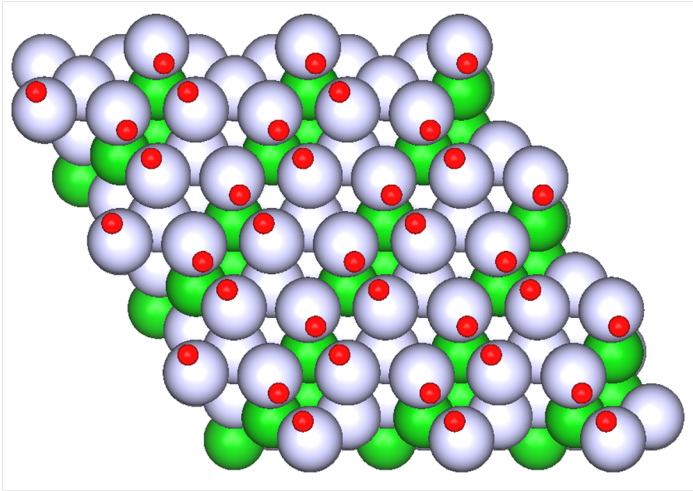

Figure 5.4: Converged 1.00 ML oxygen coverage at the top site and on Pt_3Ni-$Pt_{\mathbf{skin}}$ surfaces.

As mentioned earlier, there are multiple adsorption sites where oxygen can bind to either the Pt or Ni surface atoms (Figure 5.2). Generally, oxygen binding to the Ni atom has stronger binding strength than those binding to the Pt atom, in agreement with Ma *et al.*'s work.[12] On both surfaces and at the fcc site, oxygen prefers to bind to the fcc-Pt atom. Comparatively, the Pt_3Ni-$Pt_{\mathbf{skin}}$ surface binds oxygen more weakly than the Pt_3Ni surface. Furthermore, oxygen adsorption on the Pt_3Ni-$Pt_{\mathbf{skin}}$ surface is weaker than those on the Pt(111) and Ni-Pt-Pt(111) surfaces but stronger than that on the Pt-Ni-Pt(111) surface. The Pt_3Ni surface, on the other hand, binds oxygen more strongly than those on Pt(111) and Pt-Ni-Pt(111) but weaker than on the Ni-Pt-Pt(111) surface. Therefore, the general trend for oxygen adsorption on all studied (111) surfaces (within this thesis) is determined as E_b(Pt-Ni-Pt) $<$ E_b(Pt_3Ni-$Pt_{\mathbf{skin}}$) $<$ E_b(Pt) $<$ E_b(Pt_3Ni) $<$ E_b(Ni-Pt-Pt). The trend for oxygen adsorption agrees with other DFT calculations.[12,14]

Table 5.2: Average bond lengths (Å) and interlayer spacings (%) of atomic oxygen on Pt_3Ni and Pt_3Ni-$Pt_{\mathbf{skin}}$ surfaces at 0.25 ML. $d_{\mathrm{Pt-O}}$(Å) and $d_{\mathrm{Ni-O}}$(Å) are the bond lengths between O and the nearest neighbour atom belonging to the top-layer Pt and Ni atoms respectively, $\delta_{12}(\%)$ is the change in the interlayer spacing between the first and the second layer and $\delta_{23}(\%)$ is the change in the interlayer spacing between the second and the third layer.

	Pt_3Ni		Pt_3Ni-$Pt_{\mathbf{skin}}$	
	fcc	hcp	fcc	hcp
$d_{\mathrm{Pt-O}}$	2.04	2.05	2.06	2.07
$d_{\mathrm{Ni-O}}$	1.88	1.87	-	-
δ_{12}	+1.28	+1.76	+1.30	+2.36
δ_{23}	-0.33	-0.65	-2.91	-2.96

At the θ_{tot} of 0.25 ML, the stable binding sites present on the two surfaces are the fcc and hcp sites. Table 5.2 shows the average bond lengths and the change in interlayer spacings for the fcc and hcp adsorption sites at 0.25ML. The Ni-O bond lengths on the Pt_3Ni surface are shorter than the Pt-O bond lengths at the same adsorption site on the two surfaces. This is in agreement with the bond length observed on the Pt-Ni-Pt and Ni-Pt-Pt surfaces and other DFT calculations.[12,13] As for the change in interlayer spacings, the changes are positive and negative for the δ_{12} and δ_{23} respectively on the two surfaces. These interlayer spacings are similar to those observed on the Pt surface but smaller than those on the Pt-Ni-Pt and Ni-Pt-Pt surfaces.

5.3.3 On-surface Mixed Sites Adsorption of Atomic Oxygen on Pt_3Ni and Pt_3Ni-$Pt_{\mathbf{skin}}$ Surfaces

The on-surface mixed sites configurations with atomic oxygen were investigated on the two most stable high symmetry adsorption sites. These favoured adsorption sites are fcc and hcp sites on the Pt_3Ni surface at the θ_{tot} of 0.25 ML to 0.75 ML and fcc and top sites at the 1.00 ML. As for the Pt_3Ni-$Pt_{\mathbf{skin}}$ surface, the fcc and

hcp sites are stable at the θ_{tot} of 0.25 and 0.50 ML; bridge and top sites at 0.75 ML and finally top and fcc sites at 1.00 ML. Consistently with previous chapters, the oxygen coverage was extended to 2.00 ML so that the mixed configurations can be fully explored.

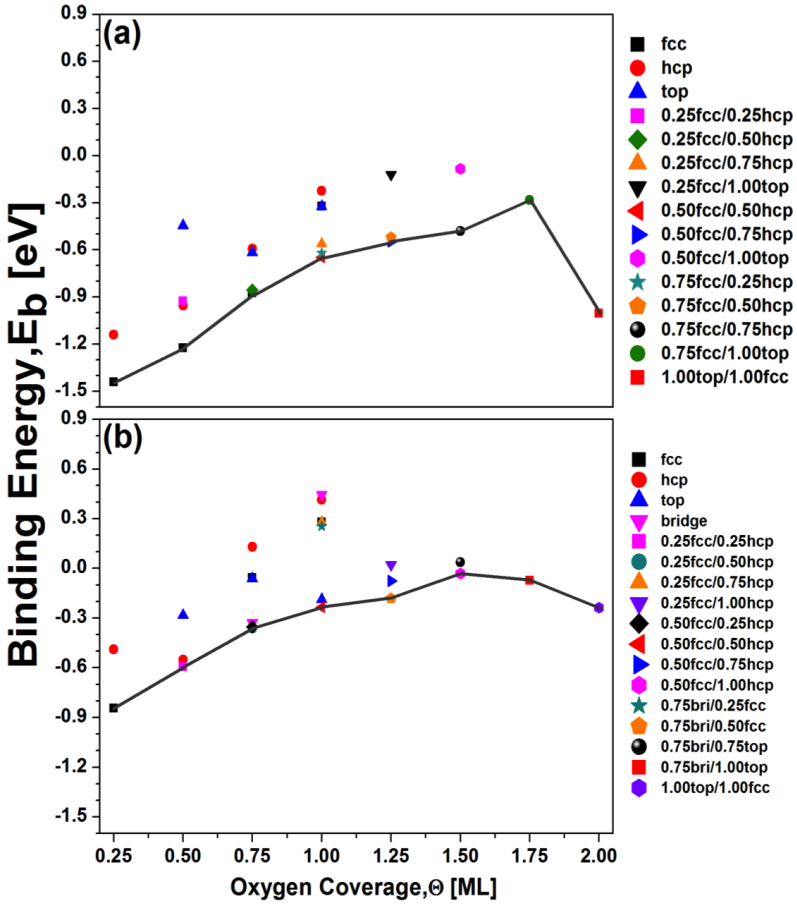

Figure 5.5: Mixed sites binding energies of oxygen adsorbed on (a) $Pt_3Ni(111)$ and (b) $Pt_3Ni\text{-}Pt_{\mathbf{skin}}(111)$ surfaces at various oxygen coverages. Solid black lines highlight the most stable mixed sites at each oxygen coverage.

Figure 5.5 shows the binding energies for the most stable mixed sites configurations along with the on-surface adsorption. It is clear from both graphs that the binding energies decrease steadily as the oxygen coverage increases except at 2.00 ML. The steady decrease in the binding energies is expected due to oxygen

interacting with more than one metal atom at the same time. At 2.00ML, an increase in binding energies was observed particularly on the Pt_3Ni surface. This may be because the short O-O bond distance at the top-site is stabilising the structure. On the Pt_3Ni surface, the high symmetry fcc site is still the energetically favourable adsorption site at the θ_{tot} between 0.25 ML and 0.75 ML while on the Pt_3Ni-$Pt_{\mathbf{skin}}$ surface, the fcc site is only observed at 0.25 ML. These two surfaces are different from all the other studied surfaces, on which the high symmetry fcc site was observed to be stable from 0.25 ML up to 1.00ML oxygen coverage. In the same way as the on-surface adsorption, the binding energies for the mixed adsorption sites on the Pt_3Ni-$Pt_{\mathbf{skin}}$ surface are lower than those on the Pt_3Ni surface.

5.3.4 Sub-surface Absorption of Atomic Oxygen on Pt_3Ni and Pt_3Ni-$Pt_{\mathbf{skin}}$Surfaces

The stability of incorporating oxygen sub-surface is examined theoretically at $\theta_{sub_{tot}}$(0.25 $\leq$ $\theta_{sub_{tot}}$ $\leq$ 1.00 ML). As explained in previous chapters, only the high symmetry absorption sites are considered. On these surfaces, there are two different high symmetry absorption sites for each sub-surface (octa, tetra-i and tetra-ii) site where oxygen absorbs to either the Pt or Ni atoms (Figure 5.6).

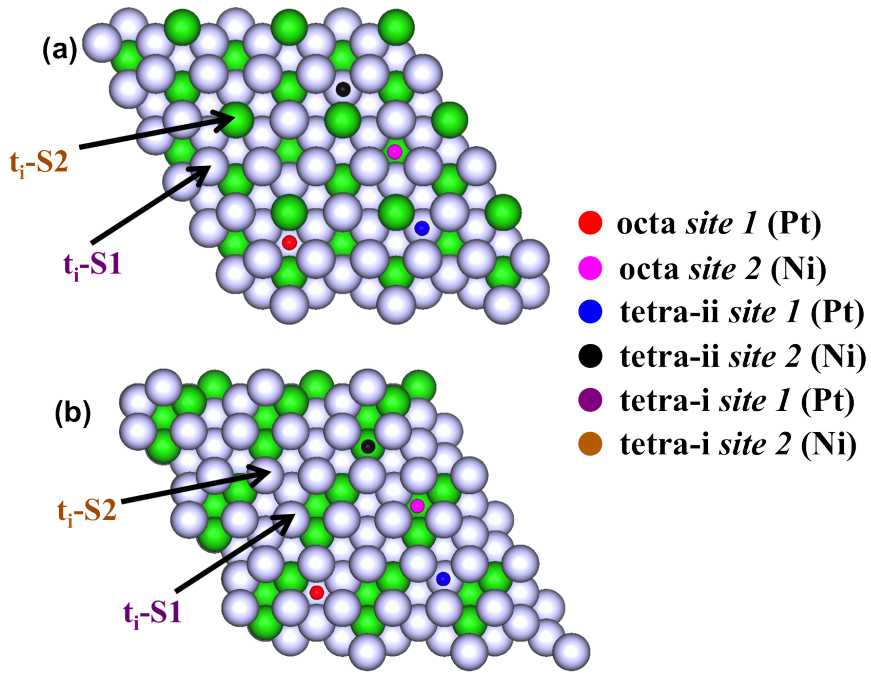

Figure 5.6: Sub-surface Absorption sites on (a) $Pt_3Ni(111)$ and (b) Pt_3Ni-$Pt_{skin}(111)$ surfaces.

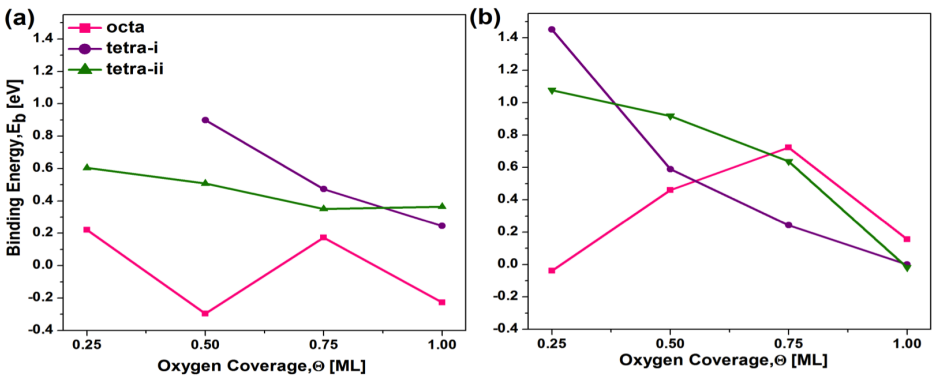

Figure 5.7: Sub-surface binding energies of oxygen absorbed on (a) $Pt_3Ni(111)$ and (b) Pt_3Ni-$Pt_{skin}(111)$ surfaces at various oxygen coverages.

Figure 5.7 illustrates the most stable binding energies for oxygen absorption at each sub-surface site on the two surfaces. On the Pt_3Ni surface, the octa site 1 (Pt) (where oxygen is located beneath the fcc site) is the favoured absorption site at all studied oxygen coverages while on the Pt_3Ni-$Pt_{\mathbf{skin}}$, the octa site 1 (Pt) is only stable at the θ_{tot} of 0.25 ML and 0.50 ML. At 0.75 ML and 1.00 ML on the Pt_3Ni-$Pt_{\mathbf{skin}}$ surface, the preferred absorption sites are tetra-i site 1 (Pt) (where oxygen is located underneath the top site) and tetra-ii site 1 (Pt) (where oxygen is located underneath the hcp site) respectively. At low oxygen coverage, 0.25 ML, the absorption site (octa) observed on the Pt_3Ni and Pt_3Ni-$Pt_{\mathbf{skin}}$ surfaces is the same as those seen on the Pt-Ni-Pt and Ni-Pt-Pt surfaces. On the two surfaces and at all absorption sites, oxygen favours binding to the Pt atoms. In addition, the binding energies of the sub-surface absorption are lower than those for the on-surface adsorption, suggesting that it would be difficult to form the sub-surface structures without on-surface oxygen adsorption.

5.3.5 Interaction of Oxygen with the On/sub-surface Phases

The interaction between the on-surface and sub-surface oxygen are explored in a similar way to those carried out in the previous chapters. This is carried out to determine their tendency to surface oxide formation. The configurations considered on both surfaces, are the two most stable adsorption sites at each oxygen coverage and at all the sub-surface absorption sites, up to a θ_{tot} of 2.00 ML.

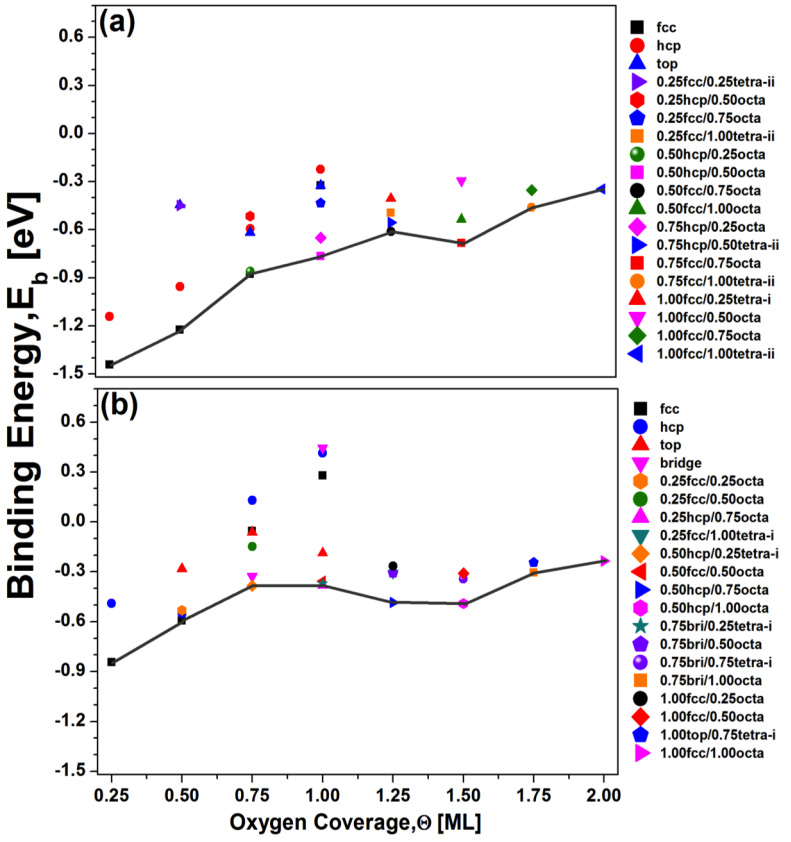

Figure 5.8: The binding energies for the on/sub-surface phases on (a) $Pt_3Ni(111)$ and (b) Pt_3Ni-$Pt_{\mathbf{skin}}(111)$ surfaces at various oxygen coverages. Solid black lines highlight the most stable on/sub-surface phases at each oxygen coverage.

Figure 5.8 shows the binding energies of the most stable on/sub-surface arrangement on the two surfaces along with the on-surface adsorptions. On the Pt_3Ni surface, there is a steady decrease in the binding energies as the oxygen coverage increases. This decrease in binding energy is also observed for the on/sub-surface phases on the Pt and Ni-Pt-Pt surfaces. The on-surface fcc site is the energetically favoured site for the θ_{tot} between 0.25 ML and 0.75 ML. At 0.75 ML, a small binding energy difference of 0.02 eV is observed between the (0.75 O_{fcc}) geometry and the next stable on/sub-surface arrangement, (0.50 O_{hcp} + 0.25 O_{octa}), suggesting that there is a possible coexistence of the (fcc/-) and (hcp/octa) configurations. This possible coexistence of arrangements is similar to those on/sub-surface

structures obtained on the Pt(111) surface, which are (fcc/-) and (fcc/tetra-ii) configurations. Above 0.75 ML, the on/sub-surface configurations are energetically favoured, implying that the surface oxide-like structures will continue to grow on the surface as the oxygen coverage increases. Similarly, to the Pt and Ni-Pt-Pt surfaces interacting with the on/sub-surface structures, the oxygen-oxygen repulsion effect between the electronegative oxygen atoms located on the top and below the metal atom is also causing the weaker interactions of oxygen to the Pt_3Ni surface.

As for the Pt_3Ni-$Pt_{\mathbf{skin}}$ surface, a steady decrease in binding energies is not observed as the oxygen coverage is increased. However, the binding energy trend obtained is similar to those observed on the Pt-Ni-Pt surface (Figure 4.13). The on-surface fcc site is favoured only at the θ_{tot} of 0.25 ML and 0.50 ML. Above 0.50 ML, the on/sub-surface arrangements become favoured. It is interesting to note that the O_2-like formation observed for the stable on-surface top site at 1.00 ML is not present in the on/sub-surface interaction. This may be due to the oxygen-oxygen interaction located on the top and below the metal atom. The oxygen interactions on the Pt_3Ni-$Pt_{\mathbf{skin}}$ surface are less favoured compared to those on the Pt_3Ni surface. Furthermore, the Pt_3Ni-$Pt_{\mathbf{skin}}$ surface binds oxygen more weakly than all other surfaces studied. Therefore, the general trend for on/sub-surface interaction on all studied (111) surfaces (within this thesis) without taking the oxygen coverage into account is determined as $\mathrm{E_b}$(Pt_3Ni-$Pt_{\mathbf{skin}}$) $<$ $\mathrm{E_b}$(Pt) $<$ $\mathrm{E_b}$(Pt_3Ni) $<$ $\mathrm{E_b}$(Pt-Ni-Pt) $<$ $\mathrm{E_b}$(Ni-Pt-Pt). This trend for the on/sub-surface phases on the (111) surfaces is different from the on-surface adsorption, where $\mathrm{E_b}$(Pt-Ni-Pt) is found to be the weakest, suggesting that the surface oxides will be difficult to form on the Pt_3Ni-$Pt_{\mathbf{skin}}$ surface.

Table 5.3: The most stable on/sub-surface phases on all studied (111) surfaces at the oxygen coverages between 0.25 ML and 2.00 ML.

	Oxygen Coverage, θ_{tot} [ML]							
	0.25	0.50	0.75	1.00	1.25	1.50	1.75	2.00
Surfaces	stable sites							
Pt	fcc	fcc	fcc	fcc/tetra-ii	hcp/tetra-ii	fcc/tetra-ii	fcc/octa	fcc/tetra-ii
Pt-Ni-Pt	fcc	fcc	fcc/tetra-i	tetra-i	hcp/tetra-i	hcp/tetra-i	hcp/tetra-i	fcc/octa
Ni-Pt-Pt	fcc	fcc	fcc	fcc/tetra-ii	fcc/tetra-ii	hcp/octa	hcp/octa	fcc/octa
Pt_3Ni	fcc	fcc	fcc	hcp/octa	fcc/octa	fcc/octa	fcc/tetra-ii	fcc/tetra-ii
Pt_3Ni-Pt_{skin}	fcc	fcc	hcp/tetra-i	hcp/octa	hcp/octa	hcp/octa	bri/octa	fcc/octa

Table 5.3 summarises the most stable on/sub-surface sites on all the studied surfaces from the θ_{tot} of 0.25 ML to 2.00 ML. It can be seen that at low oxygen coverages (0.25 ML and 0.50 ML) on all studied surfaces, the on-surface adsorption is favoured. However, as the oxygen coverage increases, the most stable structures are mainly the on/sub-surface. This indicates that all the studied surfaces will form thin surface oxide in oxidising conditions depending on the oxygen coverage. The Pt, Pt_3Ni and Ni-Pt-Pt surfaces will form the thin surface oxides at larger oxygen coverage.

The geometric structures, change in interlayer spacings and the average bond lengths for the stable on/sub-surface configurations at the θ_{tot} of 0.75, 1.00 and 1.25 ML are examined further for the Pt_3Ni surface (Table 5.4 and Figure 5.9) and the Pt_3Ni-Ptskin surface (Figure 5.10 and Table 5.5).

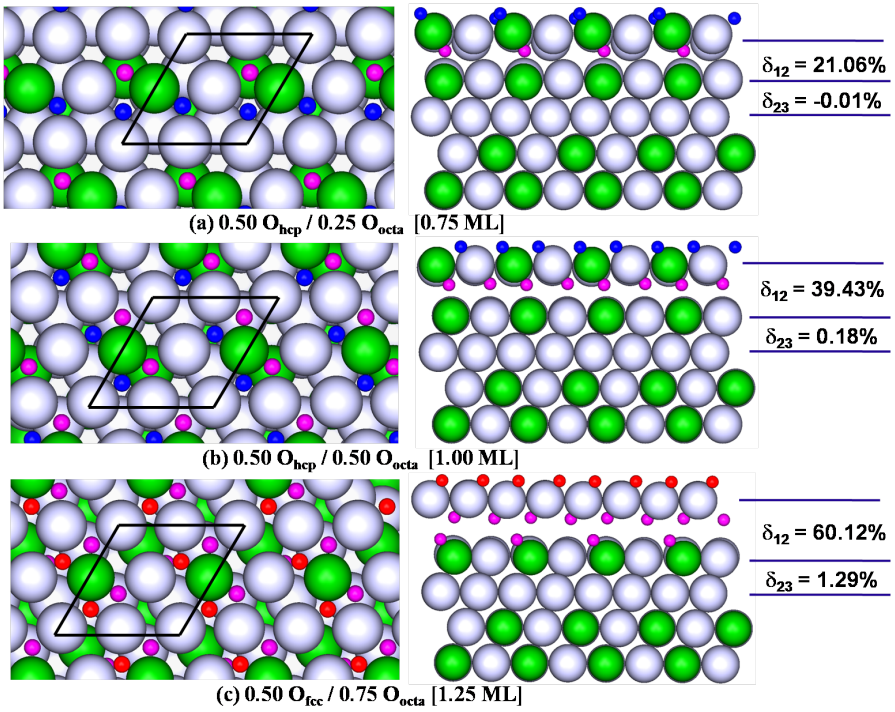

Figure 5.9: Top and side views of the most stable oxygen on/sub-surface configurations on the Pt_3Ni surface, calculated using a (2x2) surface unit cell at a total oxygen coverage of (a) 0.75 ML, (b) 1.00 ML and (c) 1.25 ML. The average change in interlayer spacings, (%), δ_{12}, between the first and second layer and δ_{23}, between the second and third layer, with respect to the bulk Pt_3Ni value is given to the right of the figures. The large sky blue and green spheres represent Pt and Ni atoms, the small red and blue spheres represent the on-surface O atoms at the fcc and hcp sites and the small purple spheres represent the sub-surface O atoms at the octa sites.

Table 5.4: The calculated (average) bond lengths (Å) for the most stable on/sub-surface configurations on the Pt_3Ni surface at the θ_{tot} of 0.75, 1.25 and 1.50 ML. $d_{\mathrm{O_{onsurf}-Pt/Ni}}$(Å) is the distance between the on-surface oxygen and the nearest-neighbour first layer Pt/Ni atom, $d_{\mathrm{Pt/Ni-O_{sub}}}$(Å) is the distance between the nearest-neighbour first layer Pt/Ni atom and sub-surface oxygen, $d_{\mathrm{O_{sub}-Pt/Ni}}$(Å) is the distance between the sub-surface oxygen and the nearest-neighbour second layer Pt/Ni atom and $d_{[\mathrm{Pt_3Ni}]_{12}-[\mathrm{Pt_3Ni}]_{23}}$(Å) is the distance between the nearest neighbour atoms belonging to the first and second layers for the most stable on/sub-surface configuration.

	0.75 ML	1.00 ML	1.25 ML
$d_{\mathrm{O_{onsurf}-Pt/Ni}}$	1.91	1.93	1.99
$d_{\mathrm{Pt/Ni-O_{sub}}}$	1.88	1.97	2.22
$d_{\mathrm{O_{sub}-Pt/Ni}}$	1.88	2.01	2.18
$d_{[\mathrm{Pt_3Ni}]_{12}-[\mathrm{Pt_3Ni}]_{23}}$	3.07	3.47	3.88

On the Pt_3Ni surface, a small buckling is observed in the first layer of the (0.50 O_{hcp} + 0.25 O_{octa}) structure while a positive change is noticed for the δ_{12} on the (0.50 O_{hcp} + 0.50 O_{octa}) and (0.50 O_{fcc} + 0.75 O_{octa}) structures (Figure 5.9). The buckling in the first layer is similar to that observed on the Pt surface. The positive change observed for the δ_{12} is comparable to the on/sub-surface geometries observed on the Ni-Pt-Pt surface. The average bond lengths for the Pt/Ni-O and the Pt_3Ni-Pt_3Ni layers are similar, regardless of the oxygen coverage (Table 5.4). Comparing other studied surfaces, the observed bond lengths are shorter on these surfaces than those seen on the Pt and Pt-Ni-Pt surfaces but slightly longer than the Ni-Pt-Pt surface.

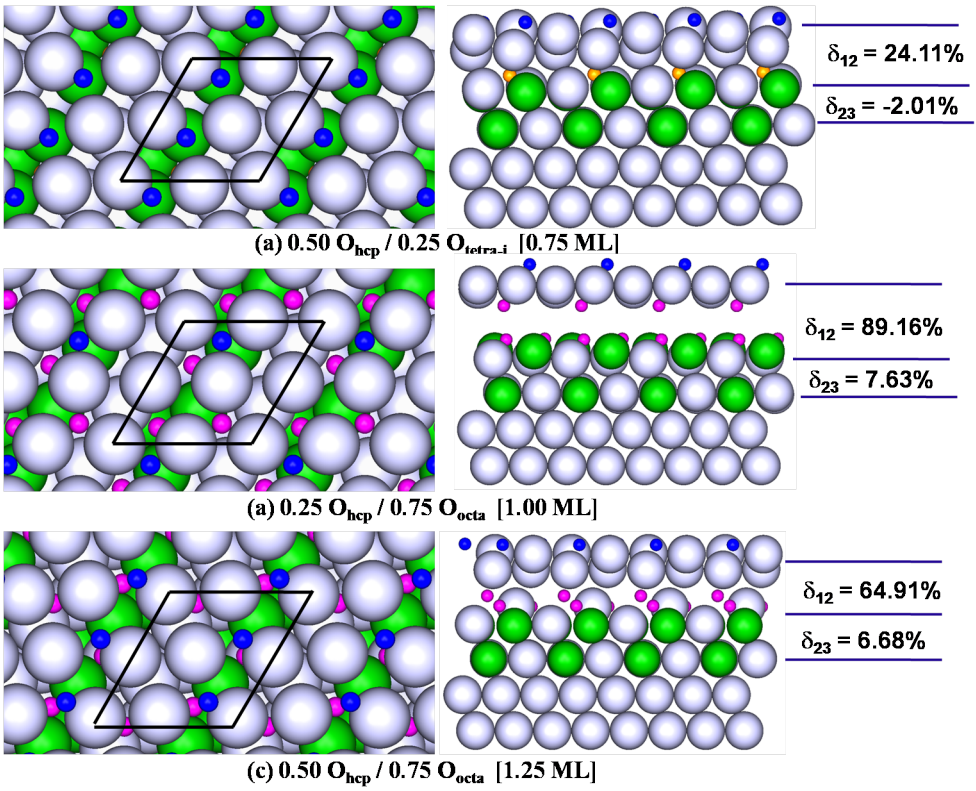

Figure 5.10: Top and side views of the most stable oxygen on/sub-surface configurations on the Pt_3Ni-Pt_{skin} surface, calculated using a (2x2) surface unit cell at a total oxygen coverage of (a) 1.00 ML, (b) 1.25 ML and (c) 1.50 ML. The average change in interlayer spacings, (%), δ_{12}, between the first and second layer and δ_{23}, between the second and third layer, with respect to the bulk Pt_3Ni value is given to the right of the figures. The large sky blue and green spheres represent Pt and Ni atoms, the small red and blue spheres represent the on-surface O atoms at the fcc and hcp sites and the small orange and purple spheres represent the sub-surface O atoms at the tetra-i and octa sites.

Table 5.5: The calculated (average) bond lengths (Å) for the most stable on/sub-surface configurations on the Pt_3Ni-$Pt_{\mathbf{skin}}$ surface at the θ_{tot} of 0.75, 1.25 and 1.50 ML. $d_{\mathrm{O_{onsurf}-Pt}}$(Å) is the distance between the on-surface oxygen and the nearest-neighbour first layer Pt atom, $d_{\mathrm{Pt-O_{sub}}}$(Å) is the distance between the nearest-neighbour first layer Pt atom and sub-surface oxygen, $d_{\mathrm{O_{sub}-Pt/Ni}}$(Å) is the distance between the sub-surface oxygen and the nearest-neighbour second layer Pt/Ni atom and $d_{[\mathrm{Pt_3Ni-Pt_{skin}}]_{12}-[\mathrm{Pt_3Ni}]_{23}}$(Å) is the distance between the nearest neighbour atoms belonging to the first and second layers for the most stable on/sub-surface configuration.

	0.75 ML	1.00 ML	1.25 ML
$d_{\mathrm{O_{onsurf}-Pt}}$	2.01	2.03	2.02
$d_{\mathrm{Pt-O_{sub}}}$	2.69	3.06	2.72
$d_{\mathrm{O_{sub}-Pt/Ni}}$	1.93	1.95	1.97
$d_{[\mathrm{Pt_3Ni-Pt_{skin}}]_{12}-[\mathrm{Pt_3Ni}]_{23}}$	3.01	4.69	3.94

Continuing onto the Pt_3Ni-$Pt_{\mathbf{skin}}$ surface, significant buckling is observed in the first two layers of all the stable structures. For the (0.25 O_{hcp} + 0.75 O_{octa}) arrangement, coupled with the bucklings, a large positive change for the δ_{12} is also seen (Figure 5.10b). The observed buckling in the first two layers of the structure is only specific to this surface. This is because, on all other surfaces, the buckling is seen only in the first layer of the on/sub-surface structures. The interlayer spacing observed on the Pt_3Ni-$Pt_{\mathbf{skin}}$ surface is considerably larger than those seen on all other surfaces. The Pt-O bond lengths for the sub-surface oxygens are substantially longer than the on-surface oxygens (Table 5.5). These were also noticed for the Pt-O bond lengths on the Pt-Ni-Pt surface. The bond lengths for the first two layers, ($d_{[\mathrm{Pt_3Ni-Pt_{skin}}]_{12}-[\mathrm{Pt_3Ni}]_{23}}$) are large and the 1.00 ML structure is shown to have the longest bond length. Overall, the bond lengths observed on the Pt_3Ni-$Pt_{\mathbf{skin}}$ surface are longer than those seen on all other surfaces, which correlates well with the binding energies.

As in the case of the Pt/Ni-MBA surfaces, there is no literature data to compare the binding energies of the studied oxygen interactions except for the on-surface adsorption. A general observation is that the interaction of oxygen with the Pt_3Ni-

$Pt_{\mathbf{skin}}$ surface is weaker than that with the Pt_3Ni and Pt surfaces. This is consistent with the on-surface adsorption literature that observed lower binding energies on the Pt_3Ni-$Pt_{\mathbf{skin}}$ surface, hence enhanced ORR activity.[5,12,14] This enhanced ORR activity is attributed to the surface structure where the Pt enrichment and Ni depletion is observed in the first two layers.

5.3.6 Statistical Thermodynamic Model

The statistical thermodynamic model is used on the surfaces, to generate the (T, p) phase diagrams. As in previous chapters, the required surface free energies are calculated from low pressures up to the real catalysis conditions using the approximation discussed in Section 2.4. This approximation involves using only the most stable binding energies calculated at each oxygen coverage from $\theta_{\mathrm{tot}}(0.25 \leq \theta_{\mathrm{tot}} \leq 2.00\mathrm{ML})$. The surface free energies were then calculated over a temperature range of 100 K to 1000 K and a pressure range from 10^{-5} atm to 10^{5} atm. Figure 5.11 illustrates the (T, p) phase diagrams of Pt_3Ni and Pt_3Ni-$Pt_{\mathbf{skin}}$ surfaces while Table 5.6 summarises the temperature at which the oxygen coverage changes phase at the UHV, real catalytic condition and high pressures.

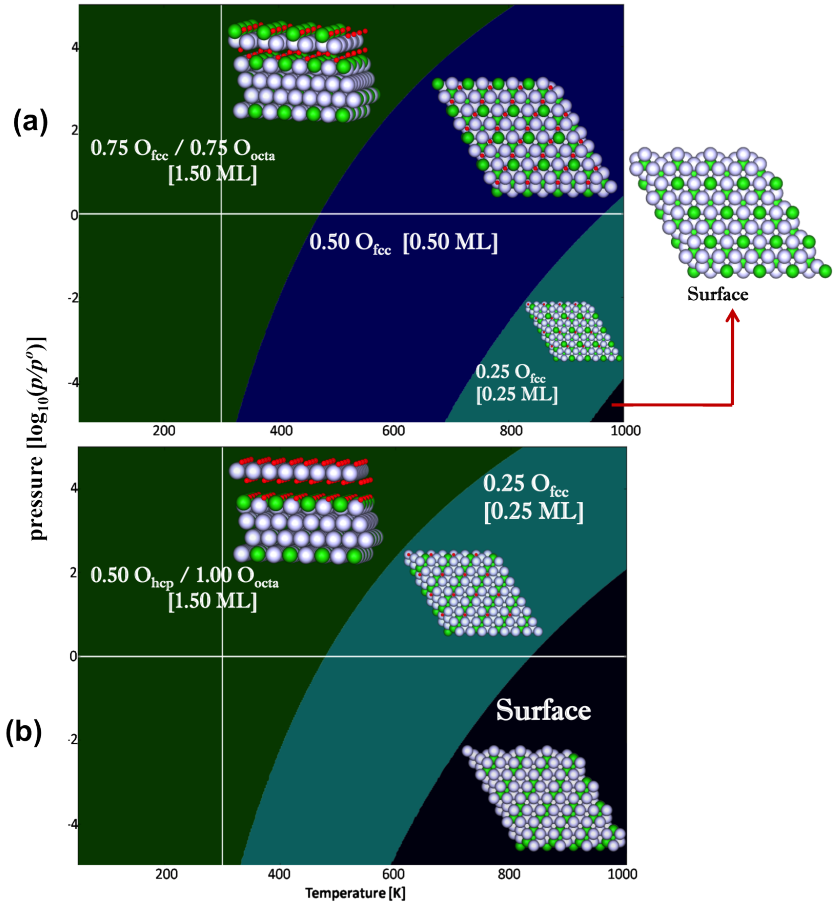

Figure 5.11: Phase diagram of (a) $Pt_3Ni(111)$ and (b) Pt_3Ni-$Pt_{\mathbf{skin}}(111)$ surfaces in equilibrium with O_2 gas phase. PEMFC operating conditions are labelled as 1 atm (horizontal white line) and 300 K (vertical white line).

Table 5.6: The temperatures (K) at which the oxygen coverage changes phase from the (T, p) thermodynamics phase diagram on the Pt_3Ni and Pt_3Ni-Pt_{skin} surfaces at at low pressure (10^{-5} atm), real catalytic condition (1 atm) and high pressure (10^5 atm).

		pressure [atm]		
	phase change [ML]	10^{-5}	1	10^5
		Temperature [K]		
Pt_3Ni	1.50 → 0.50	324	470	810
	0.50 → 0.25	688	964	> 1000
	0.25 → surface	940	> 1000	-
Pt_3Ni-Pt_{skin}	1.50 → 0.25	330	478	822
	0.25 → surface	590	834	> 1000

It can be seen that at low temperature and at all considered pressures, the on/sub-surface structures are observed on the two surfaces. These on/sub-surface oxygens gradually desorb from the surfaces as the temperature increases until a completely clean surface is exposed. The temperature at which the initial oxygen coverage changes phase is relatively close on the two surfaces and at all studied pressures. The (T, p) phase diagram for the Pt_3Ni surface is similar to that observed on the Pt(111) surface (Figure 3.10 (top)). In addition, the identified structures on the Pt_3Ni surface at 0.50 ML (2x1) and 0.25 ML (2x2) are identical to those observed on the Pt(111) surface. The main difference between the Pt_3Ni and Pt(111) surfaces is that, higher desorption temperatures are predicted on the Pt_3Ni surface at all considered pressures.

At the operating pressure, 1 atm (indicated by the horizontal white line), a complete desorption of oxygen occurred on the Pt_3Ni-Pt_{skin} surface at a temperature of 834 K, lower than that on the Pt_3Ni surface. At the operating temperature of 300 K (indicated by the vertical white line), the surface oxide-like structures are likely to be present on both surfaces. These surface oxide-like structures are

expected to desorb from the surfaces as the temperature increases compared to those on the Pt/Ni-MBA surfaces, where the surface oxide-like are observed at all considered temperature range. These results suggest that the presence of surface oxide will lead to fewer available sites for the ORR, thereby preventing the reaction from taking place. However, a smaller quantity of the thin film surface oxides will form on the Pt_3Ni and Pt_3Ni-$Pt_{\mathbf{skin}}$ surfaces, compared to those on the Pt/Ni-MBA surfaces.

5.3.6.1 Free Energy as a Function of Potential

The free energy as a function of potential is analysed for the PEMFC operating conditions of 300 K and 1 atm, for the thermodynamically stable structures determined on the Pt_3Ni and Pt_3Ni-$Pt_{\mathbf{skin}}$ surfaces. The free energies identify the most likely structures to be found on the catalyst surface when a potential (between 0 V and 1.5 V) is applied. Figure 5.12 shows the free energy as a function of potential on the two surfaces combined with those on the Pt surface.

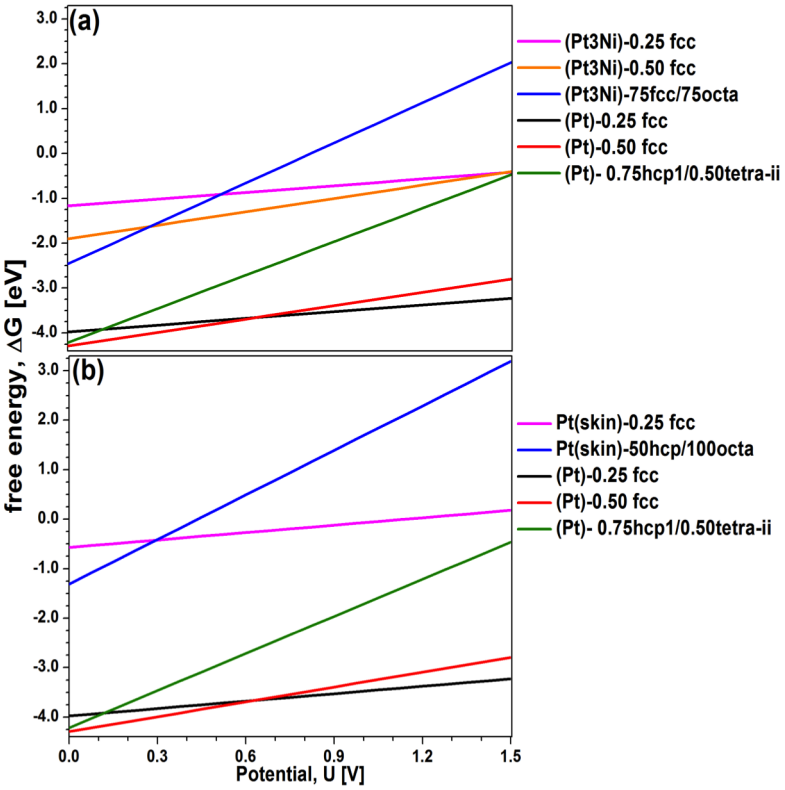

Figure 5.12: Free energy as a function of potential for the PEMFC operating conditions (300 K and 1 atm) on (a) $Pt_3Ni(111)$ and (b) Pt_3Ni-$Pt_{\mathbf{skin}}(111)$ surfaces coupled with those on the Pt surface. The PEMFC operating conditions (300K and 1 atm)

The free energies observed on the Pt_3Ni and Pt_3Ni-$Pt_{\mathbf{skin}}$ surfaces are less stable than those noticed for the Pt surface. The free energies for the Pt_3Ni-$Pt_{\mathbf{skin}}$ surface are lower than those on the Pt_3Ni surface. The observed Pt surface structures on the two surfaces suggest that when potential is included, a Pt-rich surface would be expected and the structures change from 0.50 ML at low potential to 0.25 ML at high potential. This oxygen coverage structure switches at 0.63 V on the two surfaces, identical to those seen on the Pt surface.

5.3.7 Electronic Properties

5.3.7.1 Change in Work function, Dipole Moment and d-band Centre

Figure 5.13 illustrates the work function change, $\Delta\Phi$, surface dipole moment, μ, and the average d-band centre of the first layer (described in section 2.3.6) with respect to the oxygen coverage for the Pt_3Ni and Pt_3Ni-$Pt_{\mathbf{skin}}$ surfaces. In addition, the plot between the average d-band centre, ε_d, of the first layer and the binding energies are shown for the studied oxygen coverages. In the same way as the previous chapters, the stable fcc on-surface and the on/sub-surface configurations are evaluated for the most stable structures at the $\theta_{\mathrm{tot}}(0.25 \leq \theta_{\mathrm{tot}} \leq 2.00\mathrm{ML})$.

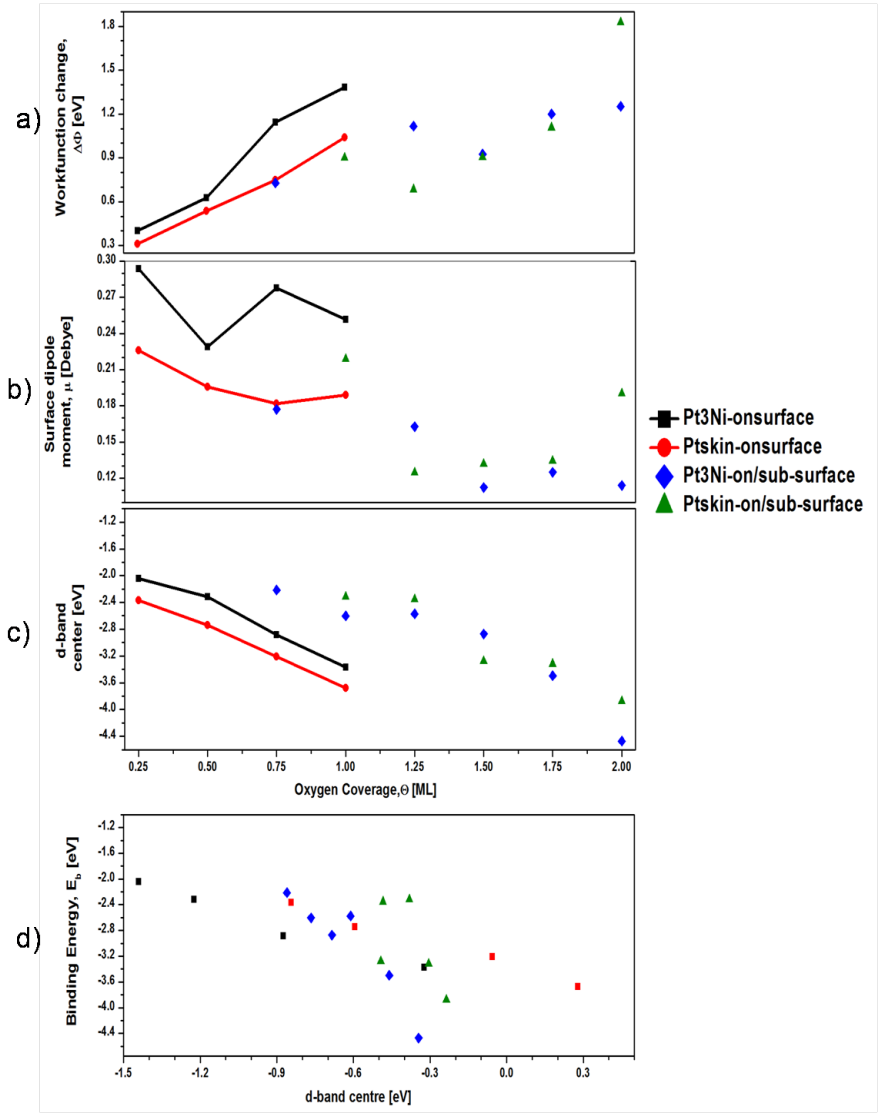

Figure 5.13: Electronic properties of the most stable structures identified on the $Pt_3Ni(111)$ and $Pt_3Ni\text{-}Pt_{\mathbf{skin}}(111)$ surfaces. a) work-function change, $\Delta\Phi$, b) surface dipole moment μ, c) average d-band centre, ε_d, of the topmost layer as a function of oxygen coverage and d) average d-band centre, ε_d, of the topmost layer, plotted as a function of binding energies at the studied oxygen coverages.

The workfunction change, $\Delta\Phi$, for the on-surface adsorptions (Figure 5.13a) increases linearly as the oxygen coverage increases on the two surfaces. This $\Delta\Phi$ is higher on the Pt_3Ni surface than on the Pt_3Ni-$Pt_{\mathbf{skin}}$ surface. This is mainly due to the influence of the Ni within the top-layer surface. In addition, the increased $\Delta\Phi$, is also observed on all the studied (111) surfaces, however, the biggest change is seen on the Pt_3Ni-$Pt_{\mathbf{skin}}$ surface. As expected, the $\Delta\Phi$ for the on/sub-surface structures at 0.75ML and 1.00ML are lower than the on-surface adsorption at the same oxygen coverage. This is also observed on all the other studied surfaces. As explained in previous chapters, the lower $\Delta\Phi$ occurs because there is competition for the bonding charge between the sub-surface and on-surface oxygen atoms which creates a slightly less negative charge on-surface oxygen atoms.[15]

The surface dipole moment, μ, (Figure 5.13b), observed on the Pt_3Ni-$Pt_{\mathbf{skin}}$ surface is similar to that seen on the Pt surface, suggesting that the Ni atoms in the second layer are not involved in the bonding. The decrease seen on the two surfaces for the on-surface adsorption and on/sub-surface structures, occurs as a result of the strong depolarisation which arises from the electron charge transfer from the top-layer atoms to more than one adsorbing O atom.[16] In the same way as the $\Delta\Phi$, the μ observed on the Pt_3Ni surface is higher than those seen on the Pt_3Ni-$Pt_{\mathbf{skin}}$ surface.

Next, the average d-band centre of the topmost layer, ε_d, (Figure 5.13c) moves towards lower energies as the oxygen coverage increases on the two surfaces and for the on-surface adsorptions and the on/sub-surface configurations. This observation is comparable to all other studied (111) surfaces within this thesis. In addition, the average d-band centre of the topmost layer on the Pt_3Ni-$Pt_{\mathbf{skin}}$ surface is lower in energy compared to those on the Pt_3Ni surface. Figure 5.13d shows that the weaker binding energy corresponds to higher average d-band centre. This is also consistent with all the studied surfaces within this thesis and with the general theory of the d-band centre. Furthermore, from Figure 5.13d, it can be seen that the Pt_3Ni on-surface oxygen adsorptions are much weaker than those on the Pt_3Ni-$Pt_{\mathbf{skin}}$ surface.

5.3.7.2 Electron density difference, Bader Analysis and Density of States

In this section, the electron density differences and the projected density of states (PDOS) are analysed. Figure 5.14 shows that in all cases, there is an accumulation of electron density on the oxygen atoms. This is similar to the electron density differences obtained on the Pt and Pt/Ni-MBA surfaces. The observed electron densities have been transferred from the nearest Pt or Ni atoms (showing a depletion of electron charge densities). The bonding interactions on the on-surface adsorptions (0.25 ML and 1.00 ML) take place with the top-layer Pt or Pt/Ni atoms, in the same way as all other studied surfaces. As for the on/sub-surface phases, the top two layers for the two surfaces are involved with the bonding of the on-surface and sub-surface oxygens. Large electron density depletion is seen on the $Pt_3Ni\text{-}Pt_{\mathbf{skin}}$ on/sub-surface phase (Figure 5.14f). This may be due to the second layer atoms (two Pt and two Ni atoms) attempting to transfer their electrons to the sub-surface oxygen but being influenced by the top layer Pt atoms.

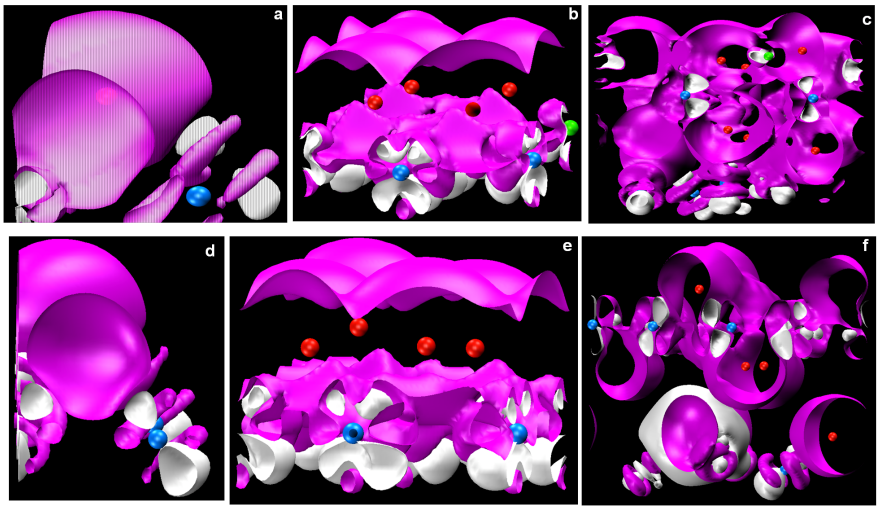

Figure 5.14: Calculated electron density differences for structures on the Pt_3Ni surface at a) 0.25 ML and b) 1.00 ML on-surface adsorption sites and c) (0.75 O_{fcc} + 0.75 O_{octa}) on/sub-surface and on the Pt_3Ni-$Pt_{\mathbf{skin}}$ surface at d) 0.25 ML and e) 1.00 ML on-surface adsorption and f) (0.50 O_{hcp} + 1.00 O_{octa}) on/sub-surface. The pink and white isosurfaces represent positive and negative electron density differences respectively. The blue, green and red spheres are Pt, Ni and O atoms respectively and the isosurphase value is $\pm 0.045\ e\text{Å}^{-3}$.

Table 5.7 summarises the average Bader charges for the two outer layers and the corresponding on-surface and sub-surface oxygens. On the clean surfaces, the charge transfer within the outer two layers is larger on the Pt_3Ni surface than on the Pt and Pt_3Ni-$Pt_{\mathbf{skin}}$ surfaces. This is mainly because there is a Ni atom in each layer that would donate more charge to the Pt atoms. As expected, the charges observed for the oxygen coverages were transferred from the transition metals (Pt or Ni atoms) onto the O atoms. This is shown by the increase of the charges on all the oxygen atoms. As for the on/sub-surface structures, the charge transfer from the Pt_3Ni surface is also larger than the Pt_3Ni-$Pt_{\mathbf{skin}}$ surface. The charge transfer observed on the Pt surface is comparable to those observed on the Pt_3Ni-$Pt_{\mathbf{skin}}$ surface. This suggests that the Ni atoms in the second layer of the Pt_3Ni-$Pt_{\mathbf{skin}}$ surface are not involved in the charge transfer.

Table 5.7: Average Bader charges (e) of the top two layers, (O_{onsurf}), of the on-surface oxygen layer and (O_{onsurf}), of the sub-surface oxygen layer on the Pt_3Ni and Pt_3Ni-$Pt_{\mathbf{skin}}$ surfaces. The nominal valence charges for Pt, Ni and O atoms are 10, 10 and 6 electrons respectively.

		(111) surface			
		slab	0.25ML	1.00ML	1.50ML
Pt_3Ni	1st layer	9.89	9.47	9.13	8.97
	2nd layer	9.81	9.82	9.87	9.53
	O_{onsurf}	-	6.85	6.75	6.83
	$O_{subsurf}$	-	-	-	6.91
Pt_3Ni-Pt_{skin}	1st layer	10.11	9.89	9.33	9.21
	2nd layer	9.86	9.88	9.92	9.53
	O_{onsurf}	-	6.77	6.70	6.82
	$O_{subsurf}$	-	-	-	6.85
Pt	1st layer	10.04	9.83	9.20	8.84
	2nd layer	9.96	9.99	10.05	9.89
	O_{onsurf}	-	6.74	6.73	6.81
	$O_{subsurf}$	-	-	-	6.93

Figure 5.15 shows the PDOS plots for the two surfaces. The clean surfaces and the 0.25 ML oxygen coverage are examined. The Pt_3Ni plot shows the PDOS for the top layer Pt and Ni atom while the Pt_3Ni-$Pt_{\mathbf{skin}}$ plot illustrates the PDOS for the top Pt layer. The interacting and non-interacting plots are the PDOS of the top layer atoms (Pt or Pt/Ni) which are interacting and not interacting respectively with the O atom. The Pt_3Ni-O/O and Pt_3Ni-$Pt_{\mathbf{skin}}$-O/O plots show the PDOS of the O atom interacting with the surfaces. Finally, the gas phase O is showing the energy levels of the O atom and the ε_{F} is determined by taking the experimental first ionisation energy of O atom from the highest occupied molecular orbital (HOMO).

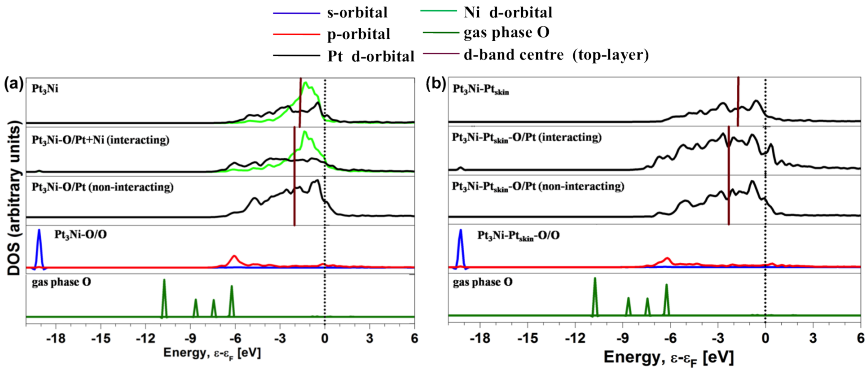

Figure 5.15: Projected density of states (PDOS) of (a) O/Pt_3Ni (111) and (b) O/Pt_3Ni-$Pt_{\mathbf{skin}}$ (111) at 0.25 ML oxygen coverage. The Fermi energy is indicated by the vertical dotted line.

As expected, a sharp O $2s$ orbital is observed on the Pt_3Ni-O/O and Pt_3Ni-$Pt_{\mathbf{skin}}$-O/O plots at about 19 eV below the Fermi level. In addition, the broadening of the O $2p$ orbital is due to the bonding hybridisation between the O $2p$ orbital and the d-orbital from either the Ni or Pt atoms. Similarly to other surfaces, the bonding (at about 6.5 eV below the Fermi level) and anti-bonding states (above the Fermi level) are observed on the two surfaces (Pt_3Ni-O/O and Pt_3Ni-$Pt_{\mathbf{skin}}$-O/O). The average d-band centre for the oxygen coverage surfaces is lower than that of the clean surfaces. There are differences in the PDOS for the non-interacting surfaces and the clean surfaces, which may be due to the influence of Ni within the surfaces.

5.3.8 Surface Segregation

The segregation energy between Pt_3Ni and Pt_3Ni-$Pt_{\mathbf{skin}}$ surfaces are analysed using Eq 2.25 for the studied θ_{tot} between 0.00 ML and 2.00 ML. This will determine which surface structure will dominate in an oxidising environment. Figure 5.16 presents the segregation energies of the two surfaces for the stable on-surface oxygen adsorption and the on/sub-surface structures. The segregation energies for the Pt/Ni(111)-MBA surfaces are also shown for comparison.

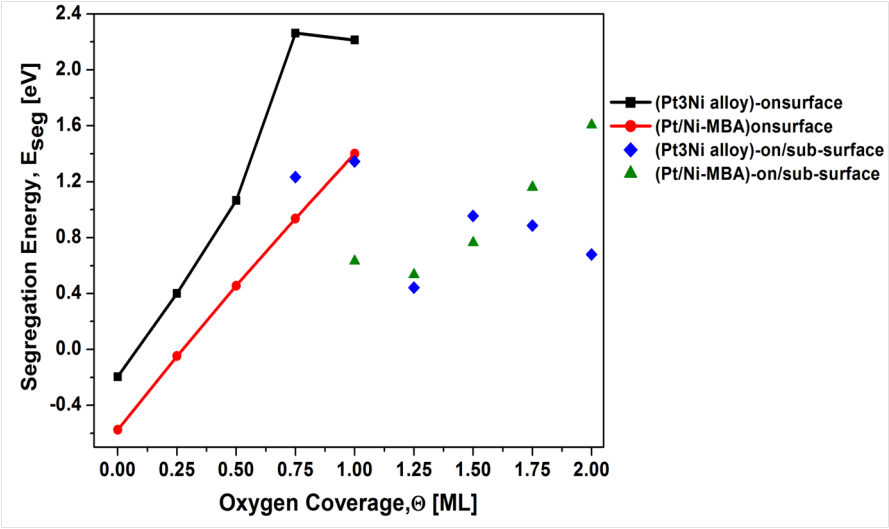

Figure 5.16: Segregation energies between $Pt_3Ni(111)$ and $Pt_3Ni\text{-}Pt_{\mathbf{skin}}(111)$ surfaces. Negative segregation energies mean $Pt_3Ni\text{-}Pt_{\mathbf{skin}}$-rich surface while the positive segregation energies mean Pt_3Ni-rich surface.

In the absence of oxygen (clean surface), the $Pt_3Ni\text{-}Pt_{\mathbf{skin}}$ surface is favoured indicating a Pt-rich surface. This is in agreement with both experimental and theoretical calculations, which suggest a Pt-rich surface.[11,17–19] As oxygen begins to interact with the surface from 0.25 ML up to 2.00 ML oxygen coverage, the stability switches to the Pt_3Ni surface. This also agrees with the theoretical results performed by Ma *et al.*,[20] which showed that the $Pt_3Ni\text{-}Pt_{\mathbf{skin}}$ surface is generally not thermodynamically favoured at the most stable adsorption sites and at 0.25 ML. For the on-surface adsorption, the segregation energies increase linearly as the oxygen coverage increase except for 1.00 ML where there is a small decrease of 0.05 eV. In general, higher segregation energies are observed on Pt_3Ni surfaces compared to the Pt/Ni(111)-MBA surfaces for the on-surface adsorptions, suggesting that the Pt/Ni(111)-MBA surfaces (in particular, the Ni-Pt-Pt surface) will dominate. In the case of the on/sub-surfaces, there is no correlation for the segregation energies with increasing coverage, though the Pt_3Ni surface composition is the most stable at all coverages.

5.4 Conclusions and Implications to PEMFC

A theoretical investigation into the stability and structural behaviour of the Pt_3Ni and Pt_3Ni-$Pt_{\mathbf{skin}}(111)$ surfaces within an oxidising environment showed different characteristics. Firstly, the oxygen binding energies on the Pt_3Ni-$Pt_{\mathbf{skin}}$ surface are lower than those obtained on the Pt_3Ni surface. This suggests that the Pt_3Ni-$Pt_{\mathbf{skin}}$ surface will be less easily oxidised, thereby leading to increased ORR activity. Similarly to what is observed in the previous chapters, the binding energies for all the on-surface adsorptions are observed to decrease as the oxygen coverage increases. This is mainly due to the metal atom interacting with more oxygen atoms at the same time. At 1.00 ML oxygen coverage on the Pt_3Ni-$Pt_{\mathbf{skin}}$ surface, an O_2-like structure is formed at the top adsorption site, thereby stabilising the surface.

At the technological relevant conditions (300 K and 1 atm), the thermodynamic stabilities illustrate that the on/sub-surface structures of 1.50 ML oxygen coverage should be observed. This suggests that thin-film surface oxide will form on the surfaces under oxidising conditions, thereby, leading to fewer surface atoms available for the ORR and also, lower ORR activity. As the temperature increases on the two surfaces, the formation of the surface oxide structures becomes more difficult.

Notably, it is shown that both the Pt_3Ni and Pt_3Ni-$Pt_{\mathbf{skin}}(111)$ surfaces are not ideal catalysts to replace Pt for the oxygen reduction reaction because they will cause the eventual degradation of the PEMFC during operation. However, the Pt_3Ni alloy surfaces (particularly the Pt_3Ni-$Pt_{\mathbf{skin}}$ surface) are better catalysts compared to the Pt/Ni-monolayer bimetallic alloy surface. This is because Ni prefers to be on the surface of the catalyst and will bind oxygen more strongly. In addition, the formation of the thin-film surface oxides occurs more slowly on the Pt_3Ni alloy surfaces.

References

[1] Colón-Mercado, H. R.; Popov, B. N. *Journal of Power Sources* **2006**, *155*, 253–263.

[2] Min, M. K.; Cho, J. H.; Cho, K. W.; Kim, H. *Electrochimica Acta* **2000**, *45*, 4211–4217, 3rd Electrocatalysis Meeting (ECS 99), Portoroz, Slovenia, 1999.

[3] Mukerjee, S.; Srinivasan, S. *Journal of Electroanalytical Chemistry* **1993**, *357*, 201–224.

[4] Ramirez-Caballero, G. E.; Balbuena, P. B. *Chemical Physics Letters* **2008**, *456*, 64–67.

[5] Stamenković, V. R.; Fowler, B.; Mun, B. S.; Wang, G.; Ross, P. N.; Lucas, C. A.; Marković, N. M. *Science* **2007**, *315*, 493–497.

[6] Mukerjee, S.; Srinivasan, S.; Soriaga, M. P.; McBreen, J. *Journal of the Electrochemical Society* **1995**, *142*, 1409–1422.

[7] Jalan, V.; Taylor, E. J. *Journal of the Electrochemical Society* **1983**, *130*, 2299–2301.

[8] Yang, Z.; Wang, J.; Yu, X. *Chemical Physics Letters* **2010**, *499*, 83–88.

[9] Pillay, D.; Johannes, M. D. *Journal of Physical Chemistry C* **2008**, *112*, 1544–1551.

[10] Gauthier, Y.; Baudoingsavois, R.; Bugnard, J. M.; Bardi, U.; Atrei, A. *Surface Science* **1992**, *276*, 1–11.

[11] Mun, B. S.; Watanabe, M.; Rossi, M.; Stamenkovic, V.; Markovic, N. M.; Ross, P. N. *Journal of Chemical Physics* **2005**, *123*, 204717.

[12] Ma, Y.; Balbuena, P. B. *Journal of Physical Chemistry C* **2008**, *112*, 14520–14528.

[13] Yang, Z. X.; H., Y. X.; W., M. D. *Acta Physico-Chimica Sinica* **2009**, *25*, 2329–2335.

[14] Xu, Y.; Ruban, A.; Mavrikakis, M. *Journal of the Americal Chemican Society* **2004**, *126*, 4717–4725.

[15] Todorova, M.; Reuter, K.; Scheffler, M. *Physical Review B* **2005**, *71*, 195403.

[16] Pang, Q.; Zhang, Y.; Zhang, J.-M.; Xu, K.-W. *Applied Surface Science* **2011**, *257*, 3047–3054.

[17] Gauthier, Y.; Joly, Y.; Baudoing, R.; Rundgren, J. *Physical Review B* **1985**, *31*, 6216–6218.

[18] Stamenković, V.; Schmidt, T. J.; Ross, P. N.; Marković, N. M. *Journal of Physical Chemistry B* **2002**, *106*, 11970–11979.

[19] Ma, Y.; Balbuena, P. B. *Surface Science* **2008**, *602*, 107–113.

[20] Ma, X.; Deng, H.; Yang, M.; Li, W. *Journal of Chemical Physics* **2008**, *129*, 244711.

Chapter 6

Conclusions and Implications to PEMFC

The main aim of this thesis was to determine the relative propensity of surface oxide film forming on Pt and Pt/Ni alloys by means of *Density Functional Theory* (DFT) and a statistical thermodynamic model. Both experimental and theoretical studies have shown that Pt is the preferred transition metal catalyst for the oxygen reduction reaction because it produces the highest catalytic activity under the proton exchange membrane fuel cells' (PEMFC) operating conditions.[1] The oxygen reduction reaction (ORR) kinetics are, however, sluggish, which prevents them from being commercialised. One explanation for this is the "so called place exchange mechanism" between the oxygen and the platinum which eventually leads to the formation of thin surface oxide film on the catalyst surface, preventing the ORR from proceeding. For this reason, Pt alone does not present satisfactory activity for the ORR, which has led to the alloying of Pt with a secondary transition metal. Pt/Ni alloys have been shown to exhibit improved activity. However, their relative propensity of forming surface oxide films has not been investigated.

In this thesis, electronic structure calculations were employed to investigate the interaction of the catalyst surfaces with the oxidising environment and to determine the effect of the overall alloy composition. The catalyst surfaces studied were the active low index (111) and (100) surfaces for Pt (Chapter 3) and the Pt-Ni monolayer bimetallic alloys (Chapter 4) and the (111) surfaces for the Pt_3Ni alloys (Chapter 5).

In Chapter 3, it was revealed that for oxygen on-surface adsorption and at oxygen coverages between 0.25 ML and 1.00 ML, the fcc and bridge sites are the most stable adsorption sites for Pt(111) and Pt(100) surfaces respectively. In addition, it was shown that the Pt(100) surface binds oxygen more strongly than the Pt(111) surface, suggesting that lower catalytic activity will be observed. The surface oxide-like structures are more likely to form on the Pt(111) surface and the on-surface oxygen coverage required before oxygen starts to penetrate subsurface is 0.75 ML. As for the Pt(100) surface, an oxygen coverage of more than 1.00 ML will be required to form the surface oxide-like structure.

Subsequently, in Chapter 4, it was found that the oxygen interactions on the Ni-Pt-Pt (Ni incorporated at the top layer of the surface) and Pt-Ni-Pt (Ni incorporated in the sub-layer of the surface) monolayer bimetallic alloy surfaces exhibited entirely different characteristics. However, similar attributes were observed for the (111) and (100) surfaces of the same alloy configurations. In addition, the alloy surfaces are generally unstable when oxygen is purely subsurface except for the Pt-Ni-Pt(111) surface. On the Pt-Ni-Pt (111) surface, it was observed that critical on-surface oxygen coverage of 0.68 ML is required before oxygen occupy the subsurface region. This is at a lower oxygen coverage compared to the Pt(111) surface, indicating that the surface is more easily poisoned. Generally, the interaction of oxygen with the Pt-Ni-Pt surfaces showed lower binding energies compared to the Ni-Pt-Pt at the (111) and (100) surfaces.

The effect of the alloy composition was further investigated on the Pt_3Ni and Pt_3Ni-$Pt_{\mathbf{skin}}$ surfaces. The results show that the oxygen binding energies on the

Pt_3Ni-$Pt_{\mathbf{skin}}$ surface are lower than those obtained on the Pt_3Ni surface, suggesting that Pt_3Ni-$Pt_{\mathbf{skin}}$ will be less easily oxidised, thereby leading to increased oxygen reduction reaction activity. At 1.00 ML oxygen coverage on the Pt_3Ni-$Pt_{\mathbf{skin}}$ surface, an O_2-like structure is formed at the top adsorption site, thereby stabilising the surface.

Following the electronic structure calculations, a statistical thermodynamic model was applied to the DFT data to bridge the temperature and pressure gap between DFT and the technological relevant conditions of 300 K and 1 atm. These studies revealed that the most likely structures to be found on the Pt surfaces are 0.50 ML (fcc) on the Pt(111) surface and 0.75 ML (bridge) on the Pt(100) surface. As for the monolayer bimetallic alloy and Pt_3Ni alloy surfaces, the on/sub-surface configurations between the oxygen coverages of 1.50 ML and 2.00 ML will be present on all the (111) and (100) surfaces. This suggests that a thin-film surface oxide will form on the Pt/Ni alloy surfaces under oxidising conditions, thereby, leading to fewer surface atoms available for the ORR and then the eventual loss of catalytic activity.

Overall, this project has provided valuable information about the relative propensity of forming surface oxide on the catalysts studied. It was observed that none of the alloy surfaces studied are the ideal catalyst to replace Pt for the oxygen reduction reaction. This is because Ni has a thermodynamic tendency to leach from the catalyst surface to expose the Pt atoms ($\sim 20\%$).[2] The leached Ni atoms binds oxygen more strongly and so lead to the eventual degration of the PEMFC during operation. Of all the alloys studied, a stable Pt_3Ni-$Pt_{\mathbf{skin}}$ alloy surface may prove to be a better catalyst because the formation of thin-film surface oxides, on this surface termination, is thermodynamically less favourable.

6.1 Future Research Work

It has been discovered that Ni is not an adequate alloying element with Pt as a catalyst replacement for the PEMFC. Therefore, a useful extension of the present investigation would be to explore other alloying elements to determine their relative propensity of forming surface oxide film. As discussed in the introduction chapter, several alloying elements (e.g. Fe, Co, V, *etc.*) have been shown to exhibit improved oxygen reduction reaction activity[2–4] and so, the approach here is to use DFT calculations to identify interesting candidates that can be then further tested experimentally. In order to find an optimum catalyst for the PEMFC, it is expected that the catalyst with less surface oxide formation will eventually give the maximum catalytic activity.

Although not presented in this thesis, the surfaces of some interesting alloying elements (Ti, Zr, Hf and Pd) were modelled and compared to the studied Pt metal and the Ni alloying element. The surface considered is the thermodynamically low index (111) surface. Figure 6.1 shows the surface segregation in the absence of oxygen. It can be seen that the segregation energies are negative, indicating that the alloying elements will be enriched to the surface.

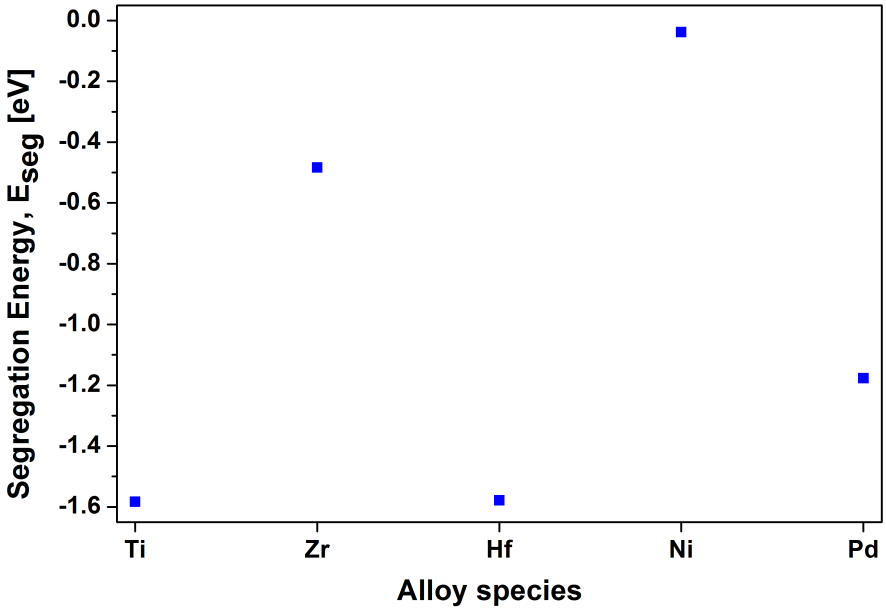

Figure 6.1: Segregation energies between the alloying elements (Ti, Zr, Hf, Ni and Pd) and Pt surfaces without the present of oxygen. Negative segregation energies mean alloying element surface enrichment while the positive segregation energies mean Pt-rich surface.

Following the segregation energies, the study was extended to determine the effect of increasing the oxygen coverage ($\theta_{\mathrm{tot}}(0.25 \leq \theta_{\mathrm{tot}} \leq 1.00\mathrm{ML})$) at the fcc adsorption site on the monolayer bimetallic alloy surfaces for each alloying element. The fcc adsorption site was chosen because it was the favoured site for most of the studied alloy compositions (within this thesis). It can be seen from Figure 6.2 that the adsorption energies decrease as oxygen coverage increases. In addition, oxygen binds strongly to the alloying element that is positioned at the top layer. Therefore, they are not useful catalysts for the oxygen reduction reaction. The obtained information are consistent with the results discussed in Chapter 4 of this thesis, which showed that O binds more strongly to the Ni-Pt-Pt surfaces. Furthermore, when the alloying element is subsurface, it can be seen that when either Ni or Zr are the alloying element we have prefential binding charachteristics to Pt, therefore, suggesting further study of Zr is warranted.

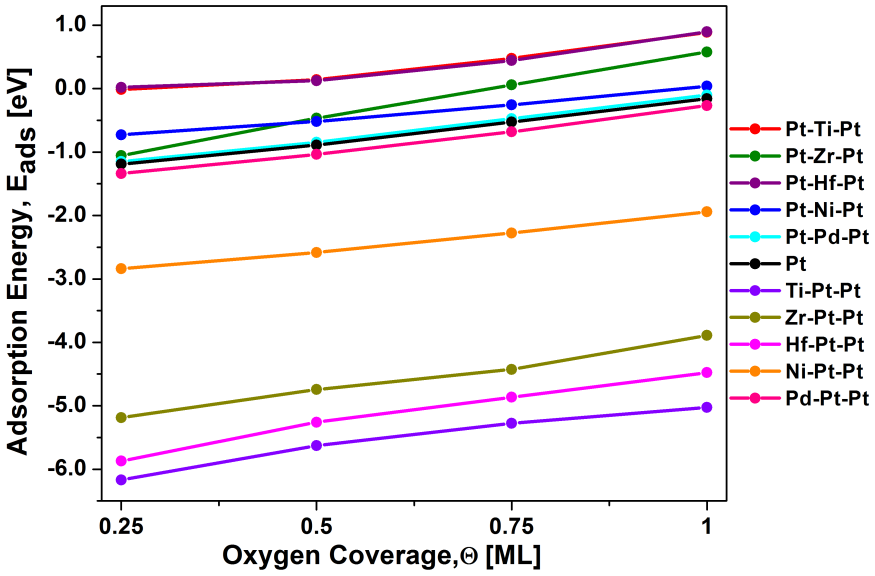

Figure 6.2: On-surface adsorption binding energies of oxygen adsorbed at the fcc site on the bimetallic monolayer alloy surfaces at various oxygen coverages. Both alloy composition (X-Pt-Pt and Pt-X-Pt) are investigated. X means alloying element.

It would be interesting to determine what happens to the segregation energies in the presence of oxygen. Future calculations will include the effect of absorbing oxygen sub-surface and the on/sub-surface oxygen interactions.

References

[1] Nørskov, J.; Rossmeisl, J.; Logadottir, A.; Lindqvist, L.; Kitchin, J.; Bligaard, T.; Jonsson, H. *Journal of Physical Chemistry B* **2004**, *108*, 17886–17892.

[2] Paulus, U.; Wokaun, A.; Scherer, G.; Schmidt, T.; Stamenkovic, V.; Radmilovic, V.; Markovic, N.; Ross, P. *Journal of Physical Chemistry B* **2002**, *106*, 4181–4191.

[3] Mukerjee, S.; Srinivasan, S. *Journal of Electroanalytical Chemistry* **1993**, *357*, 201–224.

[4] He, T.; Kreidler, E.; Xiong, L.; Luo, J.; Zhong, C. J. *Journal of the Electrochemical Society* **2006**, *153*, A1637–A1643.

Appendix A

Convergence Tests

At the beginning of the project, a series of convergence test calculations were performed to determine the parameters for future calculations. The first of these is to determine the lattice constant. In this test, the volume is varied while keeping the lattice parameter constant. The resulting (E, V) points are fitted to the Birch-Murnaghan equation of state

$$E(V) = E_0 + B_0 V_0 \left[\frac{1}{B_0'(B_0' - 1)} \left(\frac{V_0}{V} \right)^{B_0' - 1} + \frac{1}{B_0'} \left(\frac{V}{V_0} \right) - \frac{1}{B_0' - 1} \right] \quad \text{(A.1)}$$

where V_0 is the equilibrium volume, E_0 is the energy at that volume, B_0 is the bulk modulus at the equilibrium volume, and B_0 is its pressure derivative at that point. This essentially determines the bulk modulus and the lattice constant required for further calculations.

The next convergence test is to determine the number of required *k*-points, where the *k*-points are varied from 3x3x3 grid to 9x9x9 grid using the 2x2 supercell. Figure A.1 shows the *k*-points convergence for the Pt (111) surface. It can be seen that the *k*-point was converged at the 8x8x8 grid. This is the lowest number of *k*-points needed to provide a balance between accuracy and computing time.

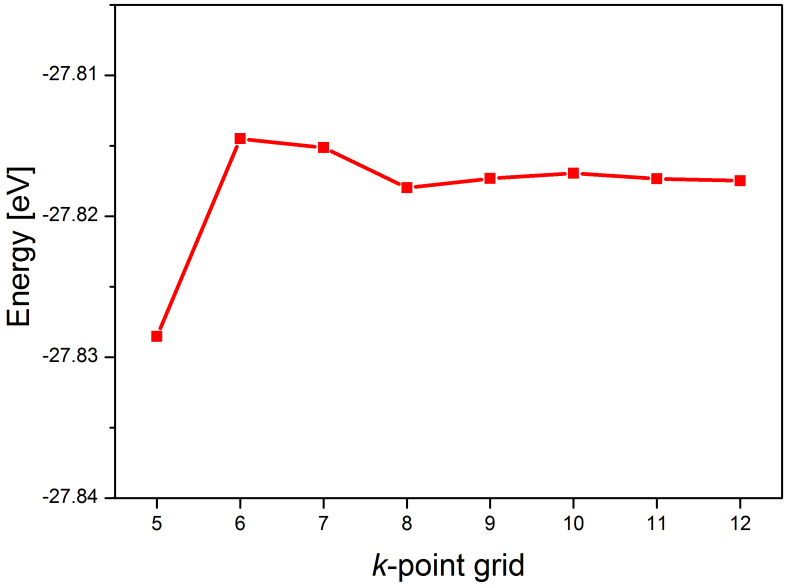

Figure A.1: Convergence test for the *k*-point grid.

Next, a convergence test is carried out to determine the vacuum gap. This will give the approximate vacuum required to avoid the interactions from other periodic slabs. Figure A.2 shows this convergence for Pt (111) surface. A vacuum gap of 8 Å was applied to all further calculations.

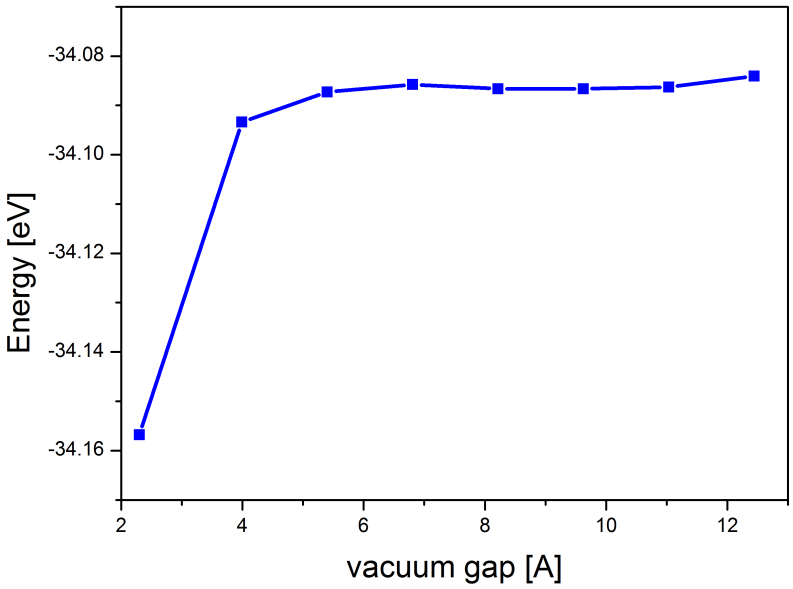

Figure A.2: Convergence test for the vacuum gap.